UNIVERSITY OF
BIRMINGHAM

HYDROGEN STORAGE IN ZEOLITES: ACTIVATION OF THE PORE SPACE THROUGH INCORPORATION OF GUEST MATERIALS

by

Matthew Simon Turnbull

Supervisor: Dr Paul A. Anderson

A Thesis submitted to the University of Birmingham
for the degree of Doctor of Philosophy

School of Chemistry
College of Engineering and Physical Science
The University of Birmingham

March 2010

ABSTRACT

Solid state hydrogen storage materials have become a key area of research over the past 20 years. In this work, the potential of zeolites to occlude hydrogen storage materials as guests to make composite materials was explored.

Lithium borohydride was successfully loaded in zeolites NaA, NaX and NaY; showing a two phased system. Desorption of hydrogen from the occluded lithium borohydride was 5℃ lower than that of bulk lithium borohydride, but with slower kinetics, implying diffusion effects of occlusion into the host. Adsorption showed reduced uptakes of hydrogen at 77 K compared with the host zeolite, which was consistent with the degree of loading. Limited hydrogenation was achieved with milder conditions at 350℃ at 15 bar hydrogen of the desorbed lithium borohydride. Heats of adsorption were estimated for the samples both before and after high temperature desorption of hydrogen.

Lithium borohydride was also loaded into zeolitic carbons and lithium, copper (II) and ammonium ion-exchanged zeolites. Copper exchanged zeolite catalysed desorption of hydrogen from lithium borohydride was most promising and occurred at room temperature. Lithium and ammonium exchanged zeolite showed a 10℃ reduction in desorption temperature, the ammonium system showing the best diffusion kinetics, with a sharp desorption similar to the bulk lithium borohydride.

NaA and NaX were occluded with ammonia borane and lithium borohydride amide [$Li_4BH_4(NH_2)_3$]. NaY containing occluded sodium was found to hydrogenate at room temperature at pressures up to 15 bar. This was accompanied with trapping of hydrogen and an increased adsorption of hydrogen at low temperature, exceeding the gravimetric absorption value for zeolite NaY.

ACKNOWLEDGEMENTS

I wish to start by thanking Paul for his support through the long haul. Many thanks go to the research group of Dr David Book in Materials and Metallurgy at the University of Birmingham, for the use of equipment. Special mention within this group goes to Dr Allan Walton, Dr Dan Reed, Dr Vicky Mann and Steve Tedds. Each in their own way has helped me with various pieces equipment and their running, certainly when things seemed to go awry!

Thanks to Dr Robert Mokaya and his group at the University of Nottingham for the synthesis of the zeolitic carbons.

Special thanks goes to the members of the Anderson group: Dr Phil for always being there, from the first day to the last; Alvaro for providing the moral support on zeolite science amidst the crazy hydrogen storage people; Martin; Jim, Alex, Ian, Dave, Ivan and Tom for being constant sources of entertainment in the lab.

Thanks to those on floor five and others at the school of chemistry for their constant support in the form of staff house and the occasional beer.

Final thanks goes to those who supported me personally in one way or another over the years of madness. My Parents; my brothers Frank and Andy; Mich Antonik for her support and Karen for her continuing patience. Sam West for rescuing me when I needed it.

CONTENTS

CHAPTER 1
THE HYDROGEN ECONOMY

1.1 Global Energy Trends

Current global trends for energy consumption are increasing and with dwindling resources the solution has become a universal concern; developments through science and new technology are striving to deliver alternatives[1]. One accepted consensus is that future energy sources should be sustainable with minimal impact on the environment[2]. Efforts are being made so that alternatives can be found without a noticeable sacrifice in lifestyle and culture. Energy production, both stationary and mobile, at present is primarily based on fossil fuels. These have two key problems: the environmental effects of their use and the finite nature of the resource.

The finite nature of these resources, suggests a more sustainable energy source is required[2,3]. Fossil fuels provide the vast majority of our energy supply, approximately 86% globally. Renewable sources (such as solar, wind, wave and hydrothermal power) could provide a viable long term solution for global energy, however, government initiatives suggest the use of other non-renewable sources[4,5], such as nuclear energy for the shorter term.

The burning of fossil fuels has had an environmental impact due to the products of combustion, in particular CO_2. CO_2 is a greenhouse gas, responsible for absorbing radiation from the sun causing the surface temperature of the earth to increase. The greenhouse effect is a natural process, but excessive production has lead to an anthropogenic greenhouse effect, causing an unwanted further warming effect.

A correlation has been shown between surface temperature and increase in CO_2, which started after the industrial revolution[6]. CO_2 is not the only greenhouse gas caused by human endeavours; other examples include methane. Automobiles are responsible for a substantial proportion of this emission. A high proportion of CO_2 is naturally sequestered in the oceans of the earth, but the solubility decreases with an increase in temperature. Increasing surface temperatures would only help to exacerbate the problem.

A method should be found where energy can be produced in a useful form, without the detrimental effect to the environment. Total independence from fossil fuels would be ideal, but difficult to achieve and necessary to overcome this problem. Changing national power generation to renewable resources is a key step, but it also important to consider mobile applications. Different technological approaches would be required for small scale power devices[7]. Rechargeable batteries have been prominent power supply to small devices. Another possible method would involve hydrogen as an energy carrier.

1.2 The Hydrogen Economy

The suitability of hydrogen as an energy carrier comes from the sole combustion product of water. Hydrogen is the most abundant element in the universe, it does not exist in its elemental form and must be obtained from compounds, of which water is the most readily abundant. This makes hydrogen an energy carrier rather than a primary fuel, similar to electricity, and requiring a process of generation, storage, and conversion.

The use of hydrogen in mobile applications is often envisaged as a means of overcoming the limitations of batteries, which have been widely used in mobile applications for a number of years. Recent developments in lithium-ion battery technology have made these prevalent in many modern devices, due to good energy densities. Some problems associated with batteries are: loss is experienced due to self-discharge; length of time required to completely recharge; safety and stability concerns.

The explosive nature of hydrogen sometimes leads to concern about its mass usage, but its light and diffusive nature minimises the chances of an explosive mix being achieved[1,3]. A comparison with currently used fuels reveals that the lower explosive limit is much larger than natural gas and gasoline[3].

To properly use hydrogen as an energy medium, a necessary change to infrastructure is required. Some moves to provide hydrogen refilling stations have tentatively begun. The construction of infrastructure for delivering petrol to the populace took a 30 year period; a similar time might be envisaged before hydrogen could hope to achieve market dominance.

Three key areas of research for the use of hydrogen are: generation; conversion and storage.

1.2.1 Generation

At present the synthesis of molecular hydrogen occurs mostly by non sustainable methods such as steam reformation of natural gas or gasification of coal. These form CO_2 as a major product, but their wide use and large scale production make them a cheap method[1,8].

More sustainable methods which do not directly produce CO_2 are also being implemented. Such methods include: electrolytic splitting of water from renewable resources; thermolytic splitting of water using heat from nuclear reactors; photolytic splitting using catalysts. Biomass could be used in a similar fashion to coal to generate hydrogen; with a carbon neutral cycle, this would not have the environmental impact of natural gas or coal, whilst keeping costs low.

1.2.2 Conversion

Hydrogen as an energy carrier needs to be converted, whether used in stationary applications, such as back-up generators in hospitals, or mobile applications, such as transportation.

Fuel cells can be used in both circumstances through the reaction of hydrogen with oxygen[9]. A wide range of types with different operating conditions are already employed in the generation of electricity. The lower temperature fuel cells, such as polymer exchange membrane (PEM) and Alkaline fuel cells, are quite susceptible to gas stream impurities. Alternatively, conventional automobiles already use an internal combustion engine, which can be adapted to use hydrogen as a fuel. In general, the efficiencies of fuel cells, even at low temperatures, exceed those of combustion engines.

1.3 Hydrogen Storage Materials

Safe and convenient hydrogen storage is the key to making a hydrogen economy work. Methods need to be produced to cater for both mobile and stationary needs.

Various government agencies have outlined what would constitute a suitable material[2,10]. Guidelines include storage capacity (by weight for mobile applications), operational temperatures, and ability for re-use (rehydrogenation cycles). An example is shown in table 1.1 for the U.S. Department of Energy's requirements for vehicles. In the case for all materials, several targets may have been achieved, yet others remain unviable.

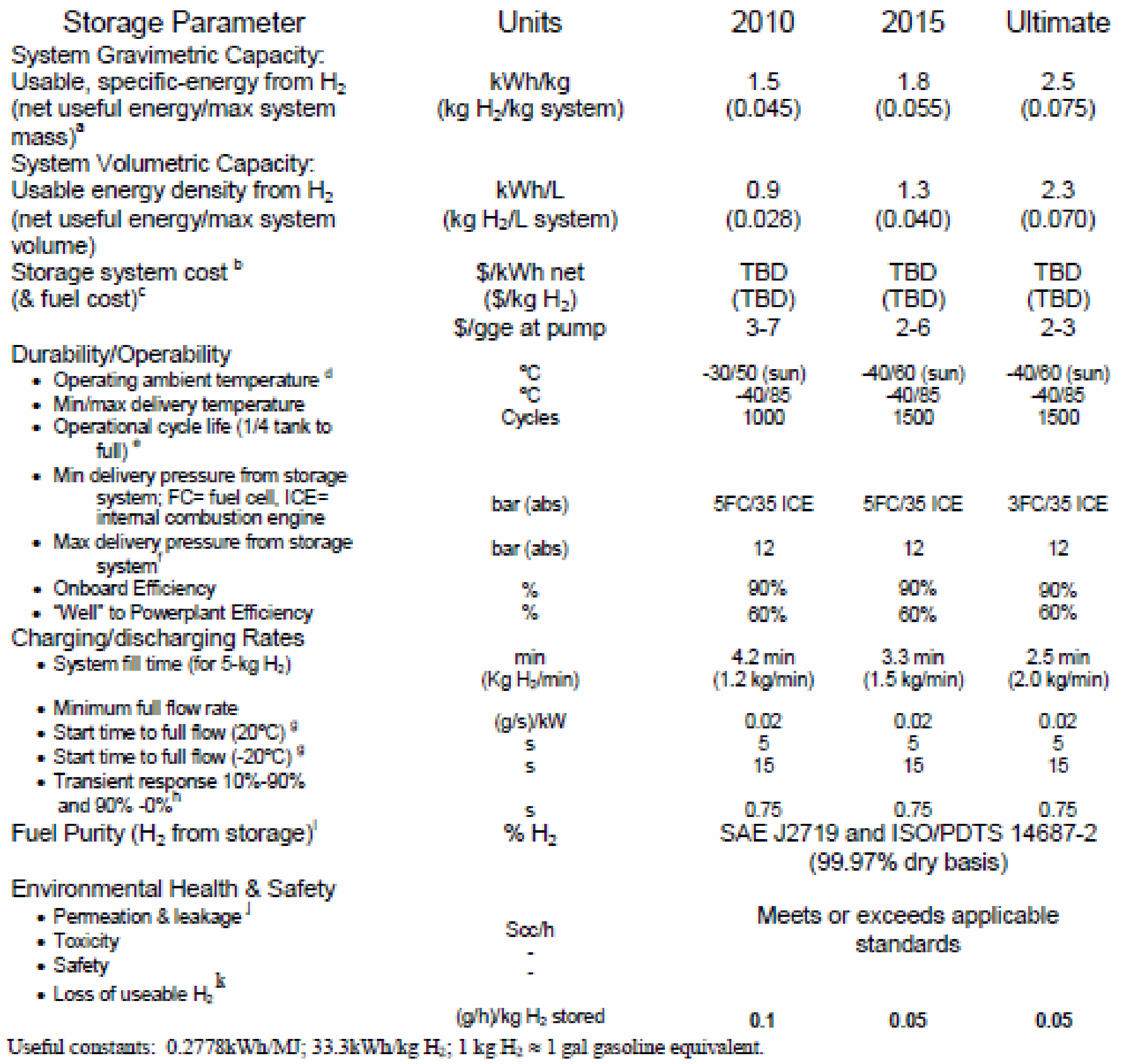

Storage Parameter	Units	2010	2015	Ultimate
System Gravimetric Capacity: Usable, specific-energy from H_2 (net useful energy/max system mass)[a]	kWh/kg (kg H_2/kg system)	1.5 (0.045)	1.8 (0.055)	2.5 (0.075)
System Volumetric Capacity: Usable energy density from H_2 (net useful energy/max system volume)	kWh/L (kg H_2/L system)	0.9 (0.028)	1.3 (0.040)	2.3 (0.070)
Storage system cost [b] (& fuel cost)[c]	\$/kWh net (\$/kg H_2) \$/gge at pump	TBD (TBD) 3-7	TBD (TBD) 2-6	TBD (TBD) 2-3
Durability/Operability				
• Operating ambient temperature [d]	°C	-30/50 (sun)	-40/60 (sun)	-40/60 (sun)
• Min/max delivery temperature	°C	-40/85	-40/85	-40/85
• Operational cycle life (1/4 tank to full) [e]	Cycles	1000	1500	1500
• Min delivery pressure from storage system; FC= fuel cell, ICE= internal combustion engine	bar (abs)	5FC/35 ICE	5FC/35 ICE	3FC/35 ICE
• Max delivery pressure from storage system[f]	bar (abs)	12	12	12
• Onboard Efficiency	%	90%	90%	90%
• "Well" to Powerplant Efficiency	%	60%	60%	60%
Charging/discharging Rates				
• System fill time (for 5-kg H_2)	min (Kg H_2/min)	4.2 min (1.2 kg/min)	3.3 min (1.5 kg/min)	2.5 min (2.0 kg/min)
• Minimum full flow rate	(g/s)/kW	0.02	0.02	0.02
• Start time to full flow (20°C) [g]	s	5	5	5
• Start time to full flow (-20°C) [g]	s	15	15	15
• Transient response 10%-90% and 90% -0%[h]	s	0.75	0.75	0.75
Fuel Purity (H_2 from storage)[i]	% H_2	SAE J2719 and ISO/PDTS 14687-2 (99.97% dry basis)		
Environmental Health & Safety				
• Permeation & leakage [j]	Scc/h	Meets or exceeds applicable standards		
• Toxicity	-			
• Safety	-			
• Loss of useable H_2 [k]	(g/h)/kg H_2 stored	0.1	0.05	0.05

Useful constants: 0.2778kWh/MJ; 33.3kWh/kg H_2; 1 kg H_2 ≈ 1 gal gasoline equivalent.

Table 1.1 – U.S. Department of Energy's requirements for hydrogen storage material in light-duty vehicles.

1.3.1 Cryogenic Storage

Hydrogen liquefies at 21.2 K. To achieve these temperatures a Joule–Thompson cycle is required[3,11], which pre-cools the hydrogen with liquid nitrogen, before compressing, heat exchanging and then isoenthalpically expanding to generate some liquid hydrogen, with the remaining vapour being recycled. Due to the combination of two protons and two electrons, hydrogen exists in two forms, ortho- and para-. The energetic difference between the two states at cryogenic temperatures exceeds the heat of vaporisation, leading to some boil-off. The hydrogen is able to self convert from ortho- to para-; rates are typically slow at 21.2 K, but the effect can be profound over time. Metal catalysts and activated charcoal have been used to catalyse the ortho- to para- conversion to minimise the boil-off. With adequate insulation the external heating can be minimised to prevent further vaporisation. The combination of the low temperatures required and constant boil-off make this an inefficient and potentially inconvenient method.

1.3.2 Pressurised Storage Systems

Pressurised cylinders have been routinely used for gas storage. Composite cylinders are formed of multiple layers and display the tensile strength of steel whilst reducing the weight. The improvements made using composite materials have allowed for pressures of 700 bar to be achieved; typical stainless steel cylinders are often pressurised to 200 bar[3,11]. Care has to be taken at connections between the storage tank and the rest of the fuel delivery system to avoid leaking due to the diffusive nature of hydrogen. Pressurised cylinders have already been used in some commercial systems. In spite of this, safety concerns about using high pressure storage, and concerns over total weight, may limit its use.

1.3.3 Metal Hydride and Complex Metal Hydride Materials

Chemically bound hydrogen shows great potential with high gravimetric capacities in complex metal hydrides. Metal hydrides often have a lower decomposition temperature. The transition metals often show the best of results, but low amounts of hydrogen, gravimetrically, are stored. Complex metal hydrides offer improvements, but suffer from higher temperatures to desorb the hydrogen, and poor reversibility. High pressures and temperatures are routinely required for rehydrogenation.

Systems involving $NaBH_4$ have exploited hydrolysis as a method to obtain hydrogen[11], controlling the desorption using dilute alkaline solutions and catalysts. These systems suffer from the high energy cost of regeneration after use.

$LiBH_4$, as an example of a complex hydride, provides a high weight storage (13.9 wt% available), but desorbs at 320ºC above its melting point of 278 ºC[12]. At present rehydrogenation requires elevated temperatures and pressures, 600ºC at 155 bar[13].

1.3.4 Porous Storage Materials

Porous materials have shown that their high surface areas are useful in the physisorption of hydrogen[14,15]. Typically, physisorption occurs at cryogenic temperatures and elevated pressures. It occurs by van der Waals interactions, aided by capillary condensation in small channels or pores. A correlation has been found between surface areas and quantity adsorbed, emphasising the importance of interactions between the surface and hydrogen. Typical materials include: porous carbon materials[15,16] whose adsorptions can reach 6.9 wt% in zeolitic carbons; metal organic frameworks (MOFs)[17] achieving 2.47 wt% in Cu-MOF (MOF-505); and zeolites[18] achieving up to 2.19 wt% (all values at 15 bar and 77 K). These material types absorb a small amount at room temperature and ambient pressures, meaning there would be an incurred energy cost from maintaining low temperatures and elevated pressures in use. They could be used to enhance pressurised storage systems, and clearly low weight frameworks such as those of carbon or MOF's would be most beneficial. The chemical tuning available in MOFs and zeolites could allow for improved binding of hydrogen.

1.3.5 Chemisorption *versus* Physisorption

Chemisorption and physisorption of hydrogen offer viable solutions to the hydrogen storage problem. Chemisorption allows formation for stable compounds which can be indefinitely stored at ambient conditions. Coupled with high weight percentages, they make viable candidates for mobile applications. Chemisorption does suffer from reversibility, not all the systems can be readily regenerated. Some systems show multiple desorption pathways which further complicate regeneration and provide an impure source of hydrogen.

Physisorption does not achieve the same gravimetric storage as chemisorbed hydrogen, a minority achieve the weight percentages outlined by the U.S. Department of Energy. Suggesting they are not as viable for mobile applications, though they can still be considered for stationary storage applications. Physisorption requires low temperatures, or elevated pressures to maintain the degree of adsorption, which could be used to enhance storage in pressurised or cryogenic systems. Regeneration of sample is not a problem with physisorption, as with chemisorption. Similarly purity of the desorbed gas is not a problem for physisorbed systems.

1.4 Obstacles to the Hydrogen Economy

Whilst the introduction of a hydrogen economy could provide a solution to some difficult problems, there are several obstacles in a variety of disciplines that still need to be overcome before its implementation could be considered, and other problems which are shared with any potential energy system.

The technical problems for the use of hydrogen are the ability to generate the required levels of hydrogen from renewable sources, with most at present coming from natural gas reformation. At present no suitable storage material is available to provide adequate storage at near room temperature. The inefficiency and safety concerns of liquid and pressurised systems make then undesirable for long term solutions.

The continued requirement for mining of resources, could compromise overall sustainability even if energy were produced sustainably. The hydrogen storage materials, as well as fuel cells, require raw minerals as a starting point. This is inherent in all energy systems, but the introduction of a new major usage could exhaust the ability of the planet's resources to meet the needs of a new technological revolution. This could be alleviated through proactive recycling. Unexpected environmental problems may also accompany 'sustainable' methods hydrogen production. As explained earlier it can be obtained from the splitting of water, but the quantities that would be involved on a global scale would be immense. As a car would need at least 4 kg of hydrogen to give it the equivalent range of a petrol car, the quantities of water required are large if hydrogen alone were used as a mobile energy carrier. This could have further anthropological effects on the environment, with reduced water tables, with associated ability to sequester CO_2, not to mention an increase in atmospheric oxygen. The global effects of this could be as bad as the effects observed from combustion of fossil fuels.

The final problem may arise from more social aspects. Whilst new technology can be quite attractive to the consumer, a large amount of investment in infrastructure would be required for the widespread introduction of hydrogen. Without public understanding and acceptance of the need to solve the problems associated with fossil fuel consumption that change is unlikely to occur.

1.5 References

1. Edwards P. P., Kiznetsov V. L., David W. I. F., *Phil. Trans. R. Soc. A*, **2007**, 365, 1043
2. Jamasb T., Nuttall W., Pollitt M., *Future Technologies for a Sustainable Electricity System*, **2005**
3. Zuttel A., *Mater. Today*, **2003**, 6, 24
4. European Energy Commission. http://ec.europa.eu/energy/index_en.htm
5. Solomon B. D., Banerjee A., *Energy Policy*, **2006**, 34, 781
6. Core writing team, Pachauri R. K., Reisinger A., *Climate Change 2007: Synthesis Report*, **2007**, IPCC
7. Schlapbach L., Züttel A., *Nature*, **2001**, 414, 353
8. Thomas G., Jones R. H., *J. Mater.*, **2007**, 59, 50
9. Jain I. P., *Int. J. Hydrogen Energy*, **2009**, 34, 7368
10. Department of Energy, USA. http://www.hydrogen.energy.gov/index.html
11. Felderhoff M., Weidenthaler C., von Helmolt R., Eberle U., *Phys. Chem. Chem. Phys.*, **2007**, 9, 2643
12. Züttel A., Rentsch S., Fisher P., Wenger P., Sudan P., Mauron Ph., Emmenegger Ch., *J. Alloys Comp.*, **2003**, 356-357, 515
13. Mauron P., Buchter F., Friedrichs O., Remhof A., Bielmann M., Zwicky C. N., Zuttel A., *J. Phys. Chem. B*, **2008**, 112, 906

14. Fichtner M., *Adv. Eng. Mater.*, **2005**, 7, 443
15. Langmi H. W., McGrady G. S., *Coord. Chem. Rev.*, **2007**, 251, 925
16. Yang Z., Xia Y., Mokaya R., *J. Am. Chem. Soc.*, **2007**, 129, 1673
17. Hirscher M., Panella B., *Scripta Materialia*, **2007**, 56, 809
18. Walker G., *Solid-state hydrogen storage: Materials and chemistry.*, Woodhead Publishing, **2008**

CHAPTER 2
ZEOLITES

2.1 Introduction

Zeolites are a group of crystalline microporous aluminosilicate compounds, both of natural and synthetic origin, with defined cavity- and channel-type pore structures of molecular dimensions. Zeolites were first described by the Swedish mineralogist Baron Axel Cronstedt in 1756. They derive their name from the Greek *zeo*, to boil, and *lithos* meaning stone, due to a simple observation that when heated these stones hissed and bubbled, as if boiling.

The general formula for the composition of zeolites is:

$$M_{x/n}[(AlO_2)_x(SiO_2)_y].mH_2O$$

where the negative charge of the framework is balanced by the cations M of valence n, usually alkali or alkaline earth metals but these can be exchanged. The framework is formed from corner sharing $[SiO_4]^{4-}$ and $[AlO_4]^{5-}$ tetrahedra which define the cavities and channels, in which the cations can be found coordinating to framework oxygens and/or water molecules. These crystalline structures have found modification through the replacement of tetrahedral sites with gallium, titanium and phosphorus, for example[1-2].

This chapter will briefly cover some of the general information associated with zeolites, such as: structure, properties and applications, with attention given to their potential role in hydrogen storage.

2.2 Structure and Nomenclature

The method of referring to zeolites by name often comes down to context[3-4]. At the simplest level they are often referred to by a simple letter or character e.g. Zeolite A, X or Ω. These were often allocated by the people who carried out the initial synthesis. They may also, if possible, be referred to by their relation to a natural zeolite.

The final and widely used method of nomenclature introduced by the International Zeolite Association Structure Commission is a three letter code which is used to label structures of similar framework topology[4], often using the natural mineral as the source of the abbreviation. The structures need not necessarily have the same complete connectivity or composition, and it is very common for different topologies to be generated from the same building units. For example zeolite A is of the IZASC group LTA (Linde Type 4A), whereas zeolites X and Y both have the structure of faujasite, a naturally occurring mineral, and are denoted as FAU. All three are formed of β- or sodalite cages[5-6].

The structure of the zeolite is defined by its corner sharing tetrahedra of $[SiO_4]^{4-}$ and $[AlO_4]^{5-}$, these are called secondary building units (SBU's) illustrated in figure 2.1. The SBU's are regarded as the building blocks for the 3-dimensional structures. These form the basis of very simple polyhedra, which can then continue to connect and build up to give different framework structure types. In some cases the same SBU can be used to give different frameworks using different connectivity. For example, single 6-rings (S6R) and single 4-rings (S4R), which are 2 of the 24 categorised SBU's. The S6R and S4R can each connect to form a double version of themselves a double 6- ring (D6R) and double 4- ring (D4R), respectively. The S6R and S4R can also connect to form a β-cage or sodalite cage, which is a truncated octahedron. This forms the basis for the 3 zeolites being used in this work: zeolites A, X and Y.

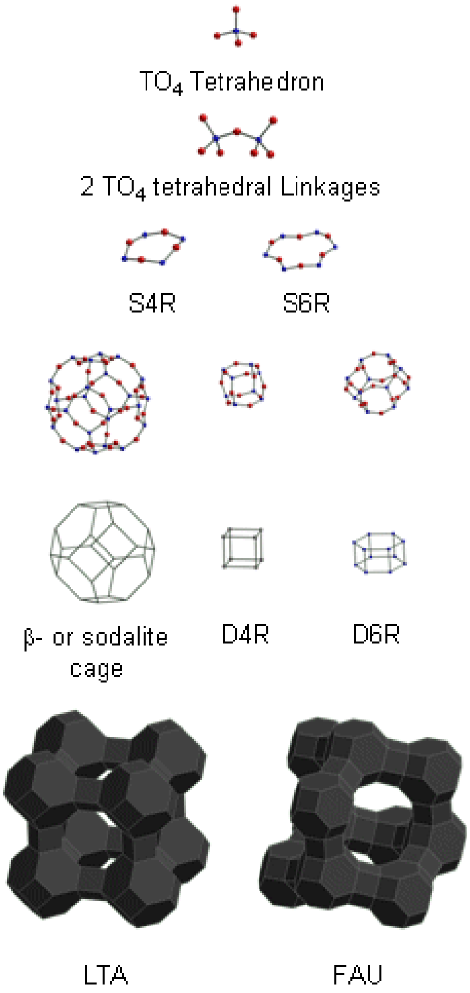

Figure 2.1 – Primary building units and secondary building units leading to the structures of zeolites A (LTA), and X and Y (FAU)

2.3 Applications

Inherent in this type of regular pore structure are exploitable properties. One previously mentioned is ion exchange *i.e.* replacement of the charge balancing cations. In practice most s-block metals can readily exchange, so long as the cation size is not too great. First row d-block metals do not often fully exchange into zeolites, and may, if pH isn't adequately controlled, lead to collapse of the framework. The ability for cations to be exchanged arises from their accessible location and mobility within the zeolite pores, partly coordinated to framework windows and partly to zeolitic waters.

The pore structure in zeolites normally contains water and, when dehydrated there is a considerable strain on the lattice. To minimise this strain the framework will often readily absorb ionic or molecular species into its pore structure.

The final truly exploitable characteristic is down to the frameworks themselves, with such a variety of composition, pore size and pore connectivity. Using these characteristics we have a medium for size- and shape-selectivity, whilst also offering functionality in the form of framework acid sites.

2.4.4 Petrochemicals and Catalysis

Companies such as Exxon-Mobil, Linde, Chevron, to name but a few, have invested heavily in the use of zeolites in these areas. For example, the alkylation of toluene with methanol was modified using zeolite to produce para-xylene as an exclusive product[2,7]. Through use of the large variety of topologies available, increased surface areas can also be harnessed to improve catalysis through use of precious metals (Pt, Ag, Cu and Ni, for example)[8-10]. Using these, preferential cracking to light oil fractions can occur, and the narrower pore structures can be employed to generate linear alkyl chains. Similarly their capacity to provide strong acid sites (in the form of H-zeolites), also provides diverse applications[3].

2.4.5 Desiccants and Molecular Sieves

The pore structure of zeolites, which is of molecular dimensions, and the charged nature of the framework and exchangeable cations affords a system, which can be used to adsorb polar gases and liquids[11-12]. Zeolites are readily used as desiccants as the adsorption of water into the framework is reversible. By tuning with selective cations preferential absorption of undesired waste gases from chimney stacks is also possible[13], whilst thin films of molecular sieves have been employed in the separation of gases through selective adsorption[14]. The use of zeolites as “molecular sieves” exploits the shape and size selectivity of the zeolite pore structure, allowing preferential adsorption of simple hydrocarbons in reaction streams whilst allowing larger aromatic structures to be collected separately[2].

2.4.6 Water Softeners and Ion-exchangers

Due to the relative pore diameter in most zeolites compared with that of the cationic species, there is a great degree of mobility[15]. Zeolite NaA is known for being used as a large scale softener as a result of its ability to remove calcium from solution, to be replaced by sodium. As with the desiccant application, the initial zeolite can be regenerated making it a long lasting and environmentally sound water softener. For this reason zeolites have been employed in washing powders, though not in a regenerative application[16]. They have also found use in the nuclear waste industry for clean up and isolation of radioactive wastes[17-18].

2.5 Occlusion of Guest Materials in Zeolites

Use of the internal pore volume to host guest materials has been explored in a variety of areas. Whilst the previous section outlined uses of the pore volume, none in reality used it as a storage medium. Here materials occupy the pore volume and an intimate mixture at the nanoscale is formed.

It has been shown that zeolites containing nitrates and phosphates can be used as fertiliser additives[19-22]. The placement of these ions in zeolites allows for a slow release mechanism as the zeolites are rehydrated; the phosphates and nitrates diffuse out and into the external environment. This slow diffusion has reduced the amount of leaching of these nutrients into local water bodies, where in great quantity they could have detrimental effect on aquatic life[21].

Other examples of slow release systems have been studied using drug molecules as the occluded material. Again this has the advantage of providing a slow release mechanism for drugs that potentially have a very quick uptake by the body[23]. As many zeolites are non-toxic this can also provide a useful method to avoid difficulties in drug pill formulation and potential problems with crystallographic polymorphs. The research showed that a variety of different pore apertures could be used as a control of the diffusion mechanism.

In the area of nuclear waste, ion-exchange has shown a great degree of success in capturing anionic and cationic species[17]. Iodide, for example, has also been successfully trapped, through incorporation of silver iodide in zeolite A. This allows for a thermal decomposition to sodalite, trapping the iodide within a β-cage, which immobilises it. This was shown through leach testing under acidic and basic conditions.

The pore volume of zeolites has been used to produce negative replicas, by impregnation with glucose. This is followed by pyrolysis of the glucose under air and then dissolution of the framework leaves a porous “zeolitic” carbon[24-25]. These have potential as hydrogen storage materials, with the rationale being to provide the high surface areas and free volumes in zeolites, with the weight advantage seen in carbon nanostructures.

The encapsulation of transition metal sulfides in zeolite Y was used to try and provide suitable catalytic sites for hydro-processing[26]. Usually the catalysts are mounted on alumina or carbon surfaces and it was postulated that there should be an optimal cluster size to provide good activation towards the desired reactions. It was found though that the zeolite-based catalysts showed less favourable results, than the material being supported on a host surface. This was deemed to be down to formation of clusters within the pores of unknown local structure.

Buhl et al.[27] took a known hydrogen storage material, in the form of sodium borohydride, and added it to the solvothermal synthesis gel of a zeolite. This allowed the incorporation of the borohydride unit, for example, into the sodalite framework as a bound template. This work expands on different templating agents being used for improved synthesis of the frameworks, as observed with the use of tetramethyl ammonium species, for example. A complete change of binding and environment offers a change in desorption and adsorption properties. In the case of the encapsulated borohydride there was an increase in the temperature of desorption from 838 K in bulk sodium borohydride; a broad absorption with onset approximately 898 K, peaking at around 943 K, was observed for the ‘clathrate’ borohydride, showing that the encapsulation nominally stabilises the borohydride. The addition of framework water had a detrimental effect by causing the oxidation of the borohydride; this change was monitored through IR and NMR.

The formation of clusters in zeolite pores has been studied extensively[28], with a variety of different metals being incorporated, including most alkali metals as well as cadmium and silver. This research was primarily carried out for magnetic and electronic properties. It was found that electronic structures were altered often yielding paramagnetic species. Other research has identified small metallic clusters suitable for use as catalysts. Clusters in zeolites are also important in dyes and pigments.

As a final example, it has been shown recently that zeolites loaded with silver or copper salts, can act as precursors for the growth of metallic nanowires, under electron beam radiation[29-30]. The wires were formed from all the metal ions present in the framework, both those introduced through ion exchange and through incorporation of the salt, providing a route to bimetallic and alloy nanowires. The growth of the wires was also found to be controllable through reaction conditions and loading levels.

2.7 Hydrogen Storage in Zeolites

The interest in zeolites as hydrogen storage materials arises from some of the same basic attributes that have been exploited in other fields. Their pore structure offers a high internal surface area, which is a useful attribute for the physisorption of hydrogen. One of the potential advantages of using zeolites as hydrogen storage materials is their thermal and chemical stability, which has been shown to be useful in catalytic applications. This is exemplified by their lack of combustibility both in air and, in particular, in a hydrogen atmosphere. The presence of exchangeable cations allows tuning of characteristics, for instance transition metals could be used to improve the binding of hydrogen within the zeolite, whilst the size of the cation could, in principle, be used to tune pore aperture and the free pore space. The use of different exchangeable cations could offer a different thermodynamic heat of adsorption. This might allow the zeolite to be “tuned” to provide improved adsorption of hydrogen at higher temperatures. The storage of hydrogen in zeolites can be categorised into two separate regimes: room to elevated temperature under pressure (encapsulation) and cryogenic.

Hydrogen storage in zeolites has been studied since the 1970’s, with initial research focused on room and high temperature, high pressure encapsulation of hydrogen in zeolite cages. The kinetic diameter of the hydrogen molecule is 2.89 Å, so it cannot access to certain void spaces in zeolites. The aperture of the 6-ring is approximately 2.3 Å preventing the diffusion of hydrogen into a sodalite cage under ambient conditions. The 8-ring, which can act as access to an α-cage on the other hand, is 4.2Å in diameter so can accommodate this freely under ambient conditions. Larger cations which normally occupy these rings, allow a better trapping of hydrogen than smaller cations, although their larger ionic radii causes them to occupy more space reducing the available volume. In the case of NaA an uptake of approximately 0.1 wt% was observed at room temperature at 10 bar, this value was closer to 0.4 wt% at 60 bar. It was concluded that capacities could be as high as 1.2 wt% of hydrogen at 700 bar at room temperature[31-33].

The retention and encapsulation of hydrogen once returned to ambient conditions wasn’t found to be as good in the case of the sodium zeolites. Comparatively, potassium exchanged zeolite lost 46% of the encapsulated hydrogen over 45 hours at 25°C; replacement with caesium resulted in a loss of only 7% at 25°C over 5 days. On partial substitution of sodium with caesium in zeolite A it was observed that using a combination of sodium and caesium the loading could be up to 3 fold greater than the fully sodium sample and almost twice that of the caesium sample, approximately 0.6 wt% at 300℃ and 917 bar. This effect was ascribed to controlled diffusion pathways, with the caesium ions preferentially taking up sites blocking some of the 8-rings. This minimises the diffusion from α-cages directly to α-cages, and replaces it primarily with diffusion through β-cage to α-cages, allowing an increase in the trapping effect. Effects of trapping have also been observed in faujasite structures suggesting the trapping is not solely occurring in the α-cages of zeolite A.

One study showed the generation of occluded palladium clusters, by ion-exchange and reduction under hydrogen, in NaY[34]. At low enough loadings these were largely restricted to the internal surface; at higher loadings nanoparticles aggregated on the zeolite surface. It was expected that low loadings kept the pore apertures free for hydrogen diffusion. Significant improvements were seen in room temperature isotherms: a negligible uptake was observed for the parent NaY, yet a sample prepared with 1 wt% palladium saw a 5-fold increase at 25℃ and 1 bar hydrogen. Higher loadings showed uptake akin to that of powdery bulk palladium, probably due to formation of bulk palladium.

Lately there has been great interest in porous materials for hydrogen storage at cryogenic temperatures[35]. Zeolites were considered due to their thermal and chemical stability providing a distinct advantage over MOF's and nano-structured carbon[36], in spite of the latter showing a greater degree of adsorption. Under cryogenic conditions physisorption occurs through van der Waals interactions. Also at these temperatures the access through the smaller pores is unavailable in contrast to the earlier high pressure encapsulations. This occurs due to a lack of vibrational flexibility in the zeolite framework, but also because hydrogen behaves as a pseudo-quantum particle near its liquefaction temperature, increasing its perceived diameter to as high as 4.089 Å.

Studies of cryogenic hydrogen storage in zeolites for true application purposes started in the 1990's. Early analysis of several structures of hydrogen exchanged zeolites showed a strong correlation of the zeolite pore size and volume to the uptake at low pressures. An uptake of around 0.7 wt% was observed up to 0.65 bar in the case of H-mordenite, which was better than H-ZSM-5 and H-Y[37,38]. Further studies[39] which outlined that the uptake in ZSM-5 was greater than that of zeolite L and ferrierite helped corroborate the necessity for large pore volumes as a driving factor for increased storage. It was concluded that a good porous material for hydrogen storage should contain a large pore structure with adequately sized pore windows to afford easy diffusion[40].

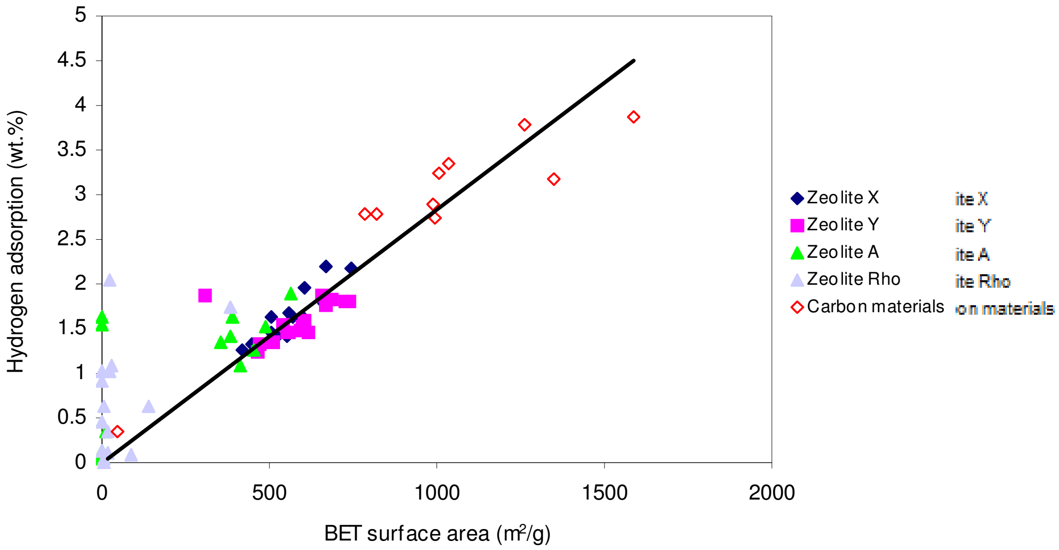

Figure 2.2 – Correlation between the hydrogen adsorption at 77 K and 15 bar and BET surface area for some zeolite and high surface area carbon materials[41-42].

Extensive studies were also performed on ion-exchanged materials of zeolites A, X, Y and Rho[41-44]. Rather than pore size and volume, this work found a strong correlation between uptake and internal surface area. This correlation has been found to be apply much more generally to various high surface area materials including carbons (figure 2.2) and MOFs[45]. These studies also showed that the general trend of increasing cation size can have the effect of pore blocking causing a reduction in the observed uptake[41-44]. The uptakes observed ranged from negligible to vast improvements compared with the original sodium zeolite at 77 K up to 15 bar. The negligible uptakes were largely observed in zeolites where exchange with a larger cation causes pore blocking, such as CsA. In more open frameworks we can see an improvement in uptake, the highest recorded was in CaX at 2.19 wt%. As with encapsulation, there was a competing effect, with changing to a larger cation reducing the available pore volume, and in some cases blocking access to certain cavities. The selected ion-exchanged cation could also in some cases improve the binding strength to hydrogen. When ion-exchanged from monovalent to divalent cations, the cations can sit preferentially in the 6-membered rings, rather than the 8-membered rings. As the number of cations is also reduced the net effect is of a more accessible pore volume. With increase of monovalent cation size, the effect is that of blocking the rings in which the cations are bound.

It is largely accepted that the strongest binding sites for hydrogen are the exchangeable cations and comparisons between zeolites X & Y showed that lower Si/Al ratios yielded higher uptakes. The binding sites and their location are important in the fine tuning of hydrogen storage properties.

IR spectroscopy has also been used in determining the possible enthalpies of adsorption for hydrogen in a variety of systems. Values have been observed between

−3.5 and −18.2 kJ mol^{-1}, dependent on cation and framework. It has been suggested that a value of approximately −15 kJ mol^{-1} would be ideal in the case of physisorption[45-46]. Higher values could maximise the quantity adsorbed, whilst lower values maximise the ease of release.

The weight percent uptakes of zeolites will always be low due to their heavy framework. Noticeable improvements have been seen through increased pressure measurements to values as high as 2.55 wt%[48].

One type of material that offers a possible solution to this problem are zeolite templated carbons, formed from pyrolysis of glucose within the zeolite pores, followed by dissolution of the aluminosilicate framework. Zeolitic carbons based on the faujasite structure saw uptakes of 6.9 wt% at 77 K and 20 bar[24-25].

Zeolites will never be considered an ideal storage medium for hydrogen as the relatively heavy framework, compared with carbon or MOF’s (where carbon, nitrogen and oxygen make the bulk of the structure) put them at a distinct disadvantage for mobile applications. They may have some potential for cheap bulk stationary storage, where the gravimetric advantage is negated, and their lack of flammability may bring safety advantages. From a scientific point of view, considerable interest resides in exploiting the tunable properties in an attempt to generate a material which can either trap or bind hydrogen at temperatures much nearer to ambient than other porous solids. With the wealth of different zeolites and possible alterations that can be made, this work should at least provide valuable insights into the interaction of hydrogen with solids of this type.

2.8 Thesis Outline

This thesis covers the attempted incorporation of several hydrogen storage materials into either zeolite A, X and Y. These materials were lithium borohydride [$LiBH_4$], ammonia borane [NH_3BH_3], lithium borohydride amide [$Li_4BH_4(NH_2)_3$] and sodium metal. Lithium borohydride was also tested on some ion-exchanged zeolites and zeolitic carbons.

2.9 References

1. Xiao F.-S., Qiu S., Pang W., Xu R., *Adv. Mater.*, **1999**, 11, 1091
2. Davis M. E., *Ind. Eng. Chem. Res.*, **1991**, 30, 1675
3. Dyer A., *An Introduction to Zeolite Molecular Sieves*, Wiley, Chichester, **1988**
4. Baerlocher Ch., Meier W. M., Olson D. H., *Atlas of Zeolite Framework Types*, **2001**
5. Olson D. H., *J. Phys. Chem.*, **1970**, 74, 2758
6. Breck D. W., Reed T. B., *J. Am. Chem. Soc.*, **1956**, 78, 5972
7. Yashima T., Sato K., Hayasaka T., Hara N. J., *J. Catal.*, **1972,** 26, 303
8. De Vos D. E., Dams M., Sels B. F., Jacobs P. A., *Chem. Rev.*, **2002**, 102, 3615
9. Díaz E., Ordóñez S., Vega A., Coca J., *App. Catal. B: Environ.*, **2005**, 56, 313
10. Armor J. N., *Micropor. Mesopor. Mater.*, **1998**, 22, 451
11. Hoshi U. D., Joshi P. N., Tamhankar S. S., Joshi V. V., Shiralkar V. P., *J. Colloid Interface Sci.*, **2001**, 235, 135
12. Fraenkel D., *J. Chem. Soc. Faraday Trans. I*, **1981**, 77, 2041
13. Hoshi U. D., Joshi P. N., Tamhankar S. S., Joshi V. P., Idage B. B., Joshi V. V., Shiralkar V. P., *Thermochim. Acta*, **2002**, 387, 121
14. Kayiran S. B., Dakrim F. L., *Surf. Interface Anal.*, **2002**, 34, 100

15. Santikary P., Yashonath S., *J. Phys. Chem.*, **1994**, 98, 9252
16. Inglezakis V. J., *J. Colloid Interface Sci.*, **2005**, 281, 68
17. Hyatt N. C., Hriljac J. A., Choudhry A., Malpass L., Sheppard G. P., Maddrell E. R., *Scientific Basis for Nuclear Waste Management XXVII*, *Mater. Res. Soc. Symp. Ser.*, **2004**, 807, A132
18. Logar N. Z., Kaučič V., *Acta Chim. Slov.*, **2006**, 53, 117
19. Park M., Kim J. S., Choi C. L., Kim J.-E., Heo N. H., Komarneni S., Choi J., *J. Controlled Release*, **2005**, 106, 44
20. Park M., Komarneni S., *Zeolites*, **1997**, 18, 171
21. Park M.,Shin S. C., Choi C. L., Lee D. H., Lim W. T., Komarneni S., Kim M. C., Choi J., Heo N. H., *Micropor. Mesopor. Maters.*, **2001**, 50, 91
22. Bansiwal A. K., Rayalu S. S., Labhasetwar N. K., Juwarkar A. A., Devotta S., *J. Agric. Food Chem.*, **2006**, 54, 4773
23. Horcajada P., Márquez-Alvarez C., Rámila A., Pérez-Pariente J., Vallet Regí M., *Solid State Sciences*, **2006**, 8, 1459
24. Yang Z., Xia Y., Sun X., Mokaya R., *J. Phys. Chem. B*, **2006**, 110, 18424
25. Yang Z., Xia Y., Mokaya R., *J. Am. Chem. Soc.*, **2007**, 129, 1673
26. Hensen E. J. M., van Veen J. A. R., *Catal. Today*, **2003**, 86, 87
27. Buhl J.-Ch., Gesing Th. M., Rüscher C. H., *Micropor. Mesopor. Mater.*, **2005**, 80, 57
28. Anderson P. A., *Mol. Sieves*, **2002**, 3, 307
29. Anderson P. A., Edmondson M. J., Edwards P. P., Gameson I., Meadows P. J., Johnson S. R., Zhou W., *Z. Anorg. Allg. Chem.*, **2005,** 631, 443
30. Mayoral A., Anderson P. A., *Nanotechnology*, **2007,** 18, 165708
31. Fraenkel D. Shabtai J., *J. Am. Chem. Soc.*, **1977**, 99, 7074

32. Fraenkel D., *J. Chem. Soc. Faraday Trans. I*, **1981**, 77, 2029
33. Yoon J.-H., *J. Phys. Chem.*, **1993**, 97, 6066
34. Nishimiya N., Kishi T., Mizushima T., Matsumoto A., Tsutsumi K., *J. Alloys Comps.*, **2001**, 319, 312
35. Walker G., *Solid-state hydrogen storage: Materials and chemistry.*, Woodhead Publishing, **2008**
36. Makarova M. A., Zholobenko V. L., Al-Ghefalli K. M., Thompson N. E., Dewing J., Dwyer J., *J. Chem. Soc.*, *Faraday Trans.*, **1994**, 90, 1047
37. Ruthven D. M., Farooq S., *Chem. Eng. Sci.*, **1994**, 49, 51
38. Lin X., Jia J., Zhao X., Thomas M., Blake A. J., Walker G. S., Champness N. R., Hubberstey P., Schröder M., *Angew. Chem. Int. Ed.*, **2006**, 45, 7358
39. Nijkamp M. G., Raaymakers J. E. M. J., van Dillen A. J., de Jong K. P., *Appl. Phys. A.*, **2001**, 72, 619
40. Dong J., Wang X., Xu H., Zhao Q., Li J., *Int. J. Hydrogen Energy.*, **2007**, 32, 4998
41. Langmi H. W., *Hydrogen Storage in Zeolites and Carbon Materials*, Thesis awarded by the University of Birmingham, **2004**
42. Harris I. R., Book D., Anderson P. A, Edwards P. P., *Fuel Cell Rev.*, **2004**, *1*, 17
43. Langmi H. W., Book D., Walton A., Johnson S. R., Al-Mamouri M. M., Speight J. D., Edwards P. P., Harris I. R., Anderson P. A., *J. Alloys Comps.*, **2005**, 404-406, 637
44. Langmi H. W., Walton A., Al-Mamouri M. M., Johnson S. R., Book D., Speight J. D., Edwards P. P., Gameson I., Anderson P. A., Harris I. R., *J. Alloys Comps.*, **2003**, 356-357, 710
45. Hirscher M., Panella B., *Scripta Materialia*, **2007**, 56, 809
46. Palomino G. T., Carayol M. R. L., Areán C. O., *J. Mater. Chem.*, **2006**, 16, 2884

47. Areán C. O., Manoilova O. V., Bonelli B., Delgado M. R., Palomino G. T., Garrone E., *Chem. Phys. Letts.*, **2003**, 370 ,631

48. Du X. M., Wu E. D., *Chin. J. Chem. Phys.*, **2006**, 19, 475

CHAPTER 3
EXPERIMENTAL TECHNIQUES

3.1 Introduction

This chapter contains a description of the experimental procedures used during the course of this work. The synthetic techniques include zeolite synthesis, ion-exchange and reactions with guest material. The characterisation techniques are of three types: structural, including crystallographic techniques such as powder x-ray diffraction, and scanning electron microscopy; the spectroscopic techniques of infra-red, Raman and electron spin resonance spectroscopy; and other methods of characterisation that focus on desorption and adsorption properties using an intelligent gravimetric analyser, pycnometer, thermo-gravimetric analyser coupled with mass spectrometry and thermal desorption under vacuum with a residual gas analyser.

3.2 Synthetic Techniques

3.2.1 Zeolite Synthesis

Zeolites are natural volcanic minerals, often formed under pressure and temperature[1]. The synthetic formation of zeolites, which was initially studied in the 1950's, uses hydrothermal conditions similar to those found in nature often with highly alkaline solutions. These alkaline conditions are such that dissolution of both aluminium and silicon sources can be achieved. Whilst many features of the mechanism of zeolite growth remain uncertain, it is believed that the nucleation of aluminate and silicate species occurs around hydrated cations. This was further developed using larger templating agents allowing different frameworks to be developed[1,2].

3.2.1.1 NaA by Hydrothermal Preparation

Zeolite NaA was prepared via the verified method[2,3]. 1.48 g of sodium hydroxide (NaOH 99% Fischer Scientific) was dissolved in 80 ml deionised water. This was then split into two equal measures in polypropylene beakers. To the first beaker 30.96 g of sodium metasilicate ($Na_2SiO_3.5H_2O$ 99.9% Sigma-Aldrich) was added under gentle mixing and heating. 16.52 g of sodium aluminate ($Na_2O.Al_2O_3$ 99.9% Strem) was added to the second half of the sodium hydroxide solution and dissolved under gentle mixing. These two solutions were then transferred to a 250 ml polypropylene bottle and mixed vigorously till homogenous. The homogenous mixture was placed into a preheated hydrothermal oven at 100℃ for 5 hours. During the first 45 minutes it was re-homogenised to afford a consistent temperature for crystallisation. The sample was then removed and allowed to cool to room temperature. During the synthesis process of zeolites the gel mixtures separated to leave a clear supernatant liquid and crystalline precipitate. The latter was collected by vacuum filtration and thoroughly washed with deionised water. Finally the sample was dried overnight at 50℃. The synthesis yielded approximately 25 g of product.

3.2.1.2 NaX by Hydrothermal Preparation

Zeolite NaX was synthesised by a modified method[3]. Two solutions were prepared in separate polypropylene beakers. The first had 1.23 g of sodium hydroxide (NaOH 99% Fischer Scientific) dissolved in 116 ml of deionised water with gentle mixing; to this solution 5.69 g of sodium aluminate ($Na_2O.Al_2O_3$ 99.9% Strem) was added and dissolved. The second solution was initially prepared with 1.23 g of sodium hydroxide (NaOH 99% Fischer Scientific) was dissolved in 104 ml of deionised water with gentle mixing; to this 27.08 g of sodium metasilicate ($Na_2SiO_3.5H_2O$ 99.9% Sigma-Aldrich) was added using gentle heat and mixing. When both were dissolved they were added to a 500ml polypropylene bottle and agitated for an hour to afford a completely homogenous mixture. The sample was then placed into a preheated hydrothermal oven at 90℃ for 20 hours. Manual agitation was employed during the first 3 hours to ensure a consistent reaction mixture. Again the precipitate was collected by vacuum filtration, washed copiously with deionised water and then be dried overnight at 50℃. This synthesis yielded approximately 12 g of product.

3.2.2 Ion exchange

A few ion exchanges were carried out during this study. An ion exchange occurs when the cations present in the zeolite are exchanged for other cations present externally[2,4]. This concept is exploited in the use of zeolites as water softeners. There are three ways of exchanging the ions: vapour phase, solution mediated and in the solid state. In this case only solution based ion exchanges were performed. The selected ions for exchange were copper (II), lithium and ammonium salts[3].

Copper

For the copper exchange, 0.5875 g of copper (II) nitrate ($Cu(NO_3)_2.2.5H_2O$ 98% Sigma-Aldrich) were dissolved in 250 ml of deionised water to make a 0.01 M solution, to which 4 g of zeolite was added. The ion exchange was performed at room temperature over a

24 hour period and the zeolite was vacuum filtered and replaced into a fresh solution. This was repeated three times. The solute was then washed once with deionised water. The final solid was again vacuum filtered and dried at 50℃ overnight.

Lithium

For the lithium exchange, 17.235 g of lithium nitrate ($LiNO_3$ >99% Sigma-Aldrich) were dissolved in 250 ml of deionised water to make a 1 M solution, to which 10 g of zeolite was added. The ion exchange was performed at 90℃ over a 24 hour period and the zeolite was vacuum filtered and replaced into a fresh solution. This was repeated five times. The final solid was again vacuum filtered and dried at 50℃ overnight.

Ammonium

For the ammonium exchange, 1.3398 g of ammonium chloride (NH_4Cl >99% Fluka Analytical) was dissolved in 250 ml of deionised water to make a 0.1 M solution, to which 4 g of zeolite was added. The ion exchange was performed at 80℃ over a 24 hour period and the zeolite was vacuum filtered and replaced into a fresh solution. This was repeated three times. The solute was then washed once with deionised water. The final solid was again vacuum filtered and dried at 50℃ overnight.

3.2.3 Reactions with Guest Materials

Traditionally the occlusion of salts in zeolites has been achieved through heating near to or above the melting point, but as some hydrogen storage materials are known to desorb from melts, it is necessary to understand their desorption profiles to develop an informed methodology for incorporation in the host. The occlusion of inorganic salts has been extensively studied[1].

Furthermore, on account of the possibility of hydrogen gas desorption from lithium borohydride and ammonia borane near their melting points, it was necessary to prepare the samples by one of two different methods: in sealed evacuated tubes or under a flowing inert atmosphere. In both cases, the use of an inert atmosphere glove box was required due to the reactive nature of the guest materials and the hygroscopic behaviour of dried zeolites. In all cases the glove box operated under an argon atmosphere.

3.2.3.1 Sealed Vacuum Reactions

Initial preparations involved cleaning with water and then baking out a quartz reaction tube, usually between 20 and 30 cm in length, at 350℃ for an hour to dry the tube. The dried tube was introduced to an inert atmosphere glovebox. The reaction mixture was prepared and placed at the bottom of the tube. It was then sealed from the atmosphere by an Ultra-torr fitting and right-angled glass adaptor with Young’s tap. Figure 3.1 shows the experimental setup for the evacuation process.

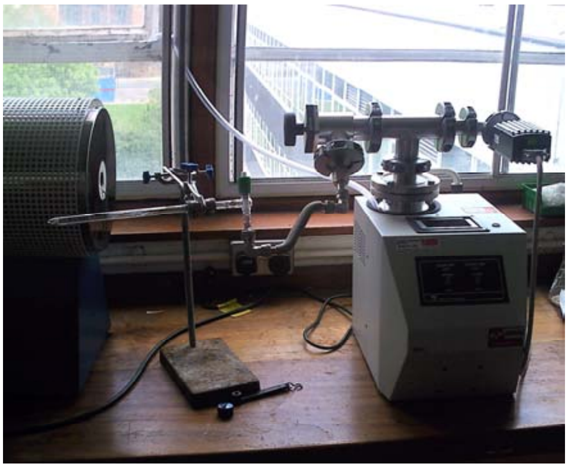

Figure 3.1 – Setup for evacuation of a sample for sealed reaction.

On removal from the glove box the tube was attached to a vacuum pump, initially evacuated under a fore or rough pump (either diaphragm or rotary pump), then followed by evacuation by turbo pump to high vacuum (1 x 10^{-6} mbar) for 18 hours. The sample was then sealed at the Young's tap and removed from the vacuum system. The glass tube was sealed by a gas torch approximately 4 inches away from the sample. This sample was then ready to undergo reaction. After the reaction was complete, the sample was returned to the glove box, and was collected by safely snapping the glass tube.

3.2.3.2 Flowing Inert Gas Reactions

The flowing inert gas reactions were prepared in the glovebox in the same way as the sealed vacuum reactions. Here the sample mixture was loaded and sealed from the atmosphere via an Ultra-torr and Young's tap fixture in a "T" configuration. The experimental set up is shown below in figure 3.2.

Figure 3.2 – Set-up for sample preparation in flowing inert gas.

The reaction tube was connected by the T-piece to a gas cylinder via acid bubblers, flexible piping and a manifold to regulate flow. When the T-piece was attached the piping was flushed with argon gas for several minutes prior to opening the Young's tap and starting the reaction. Again the sample was collected inside the glove box.

3.2.3.3 Lithium Borohydride ($LiBH_4$)

$LiBH_4$ has a well defined decomposition pathway, in which hydrogen is evolved[5]. Melting at 278℃, there is no significant evolutionof hydrogen until 320℃. A slight weight loss (~0.3wt%) is observed at 100℃, occurring due to a structure change.

The following method was used for sodium, copper and lithium zeolites and zeolitic carbons, in evacuated sealed tubes. Between 0.1 g and 0.75 g of degassed host material was intimately mixed with between 0.01 g and 0.5 g of lithium borohydride (>95% purity Sigma-Aldrich) depending on loading concentration, and sealed in quartz tubes as outlined in section 3.2.3.1. The samples were then heated at 250℃ for up to 24 hours.

In the case of ammonium exchanged zeolites, NH_4-Y for example, it was necessary to perform the reactions at reduced temperatures. Above 150℃ there is a weight loss associated with deammoniation in the sample and its dehydration. For this reason it was decided to explore, whether reactions at 100℃ were viable. There were two conditions under which the NH_4-Y was dehydrated at: 75℃ for 72 hours under vacuum, initially at 1 x 10^{-3} bar, but ultimately to 1 x 10^{-7} bar; and initially at 120℃ for 12 hours and on to 350℃ for 72 hours under the same vacuum conditions. Between 0.1 and 0.5 g of dried zeolite was added to between 0.01 and 0.2 g lithium borohydride and mixed intimately.

Samples were prepared at 100, 150 and 250℃ in either sealed tube or flowing gas as outlined in sections 3.2.3.1 and 3.2.3.2, respectively.

3.2.3.4 Lithium Borohydride Amide ($Li_4BH_4(NH_2)_3$)

($Li_4BH_4(NH_2)_3$) melts at 220℃ with desorption starting at 260℃[6]. Reactions were performed at either 200℃ or 250℃. 0.1 g to 0.5 g of dehydrated zeolite was intimately mixed with between 0.01 g and 0.5 g of lithium borohydride amide, depending on loading concentration, and prepared as outlined in section 3.2.3.1.

3.2.3.5 Ammonia Borane (NH_3BH_3)

Ammonia borane has been shown to desorb hydrogen on melting between 77 and 112℃[7]. Reactions between sodium zeolites and ammonia borane were performed under both flowing gas and in evacuated sealed tubes, at 60, 70 and 80℃.

Between 0.1 g and 0.75 g of dehydrated zeolite was intimately mixed with between 0.01 g and 0.5 g of ammonia borane, (Sigma Aldrich, >90% purity) depending on loading required, and prepared as outlined in section 3.2.3.1 for sealed tube, or 3.2.3.2 for flowing gas.

3.3 Structural Characterisation Techniques

3.3.1 Crystallography

Solid materials, like most others, are often defined by their microscopic and macroscopic properties. When considering structural features, the microscopic details relate to the connectivity of the individual species. These can be broadly described as either crystalline or amorphous. Amorphous materials exhibit no long range ordering of atoms and molecules, but it is possible for local ordering to occur.

Crystalline materials are described as having a bulk structure that is a regular and ordered. They are defined by a single motif, which when repeated infinitely in 3 dimensions yields a bulk material with long range order. This motif is referred to as the unit cell. The unit cell can be classified into several geometric structure types (cubic, hexagonal, orthorhombic, etc.), which represent different crystal symmetries

Although the unit cell can be regarded as an intrinsically microscopic descriptor of a bulk crystalline material, during analysis it generally represents an average of the bulk material. This can be explained by the occurrence of defects. Defects can be either random in nature, representing statistical anomalies over the bulk material, or inherent defects synthesised into a compound either by absence or substitution. The latter can often alter the bulk properties of the materials.

3.4.2.2 Powder X-ray Diffraction (PXRD)

Powder X-ray diffraction is often the first screening method in the characterisation of solid samples.

Diffraction is the effect observed in the propagation of waves, when the waves meet an obstacle or series of obstacles. Bragg diffraction (or scattering) is observed in crystal structures, when the wavelengths of incident radiation are similar to the spacings observed between atoms, allowing a crystalline material to behave similar to a diffraction grating. Bragg modelled the process by considering that the regular array of atoms in a crystal behaved like a series of semitransparent parallel planes, that each reflected a proportion of the incident radiation. The extra distance travelled by the x-ray radiation between two planes generates a discrepancy in the wave phase. When this discrepancy is of an integral number of wavelengths, the waves interfere constructively, as illustrated in figure 3.3.

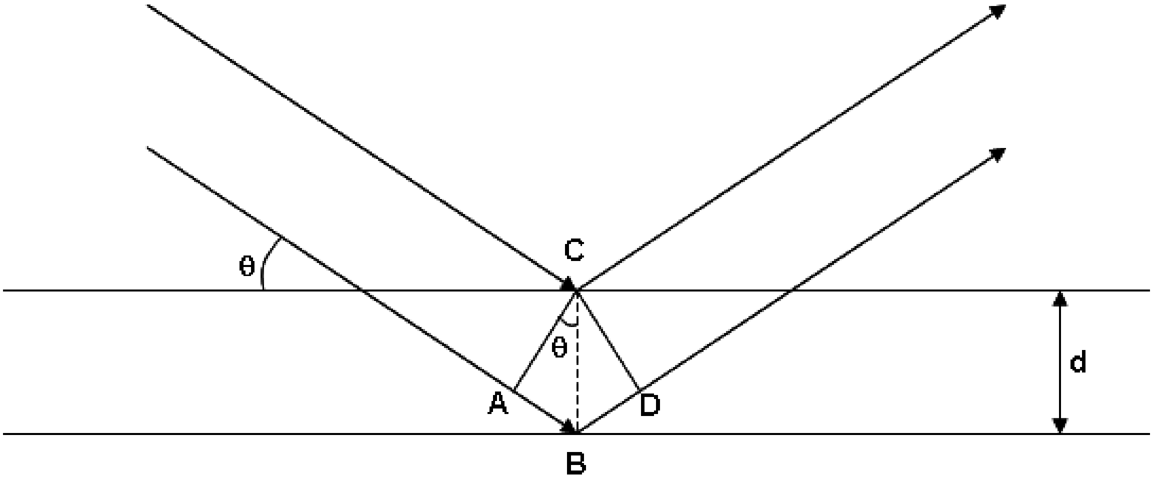

Figure 3.3 – Schematic representation of the path difference derivation for Bragg's law.

From figure 3.3, the condition for this is given by:

$$n\lambda = 2d_{hkl}\sin\theta$$

where: $n\lambda$ is the phase difference between the waves; $2d_{hkl}\sin\theta$ is the distance between AB and BD; d_{hkl} defines the interplanar distance, CB, given respective miller indices h, k, and l.

The miller indices represent the planes by which the radiation is diffracted. When taken as their reciprocal, they represent the fractional intercept of the plane from within the unit cell, given lattice directions a, b and c to the miller indices h, k, l respectively, examples shown in figure 3.4 below.

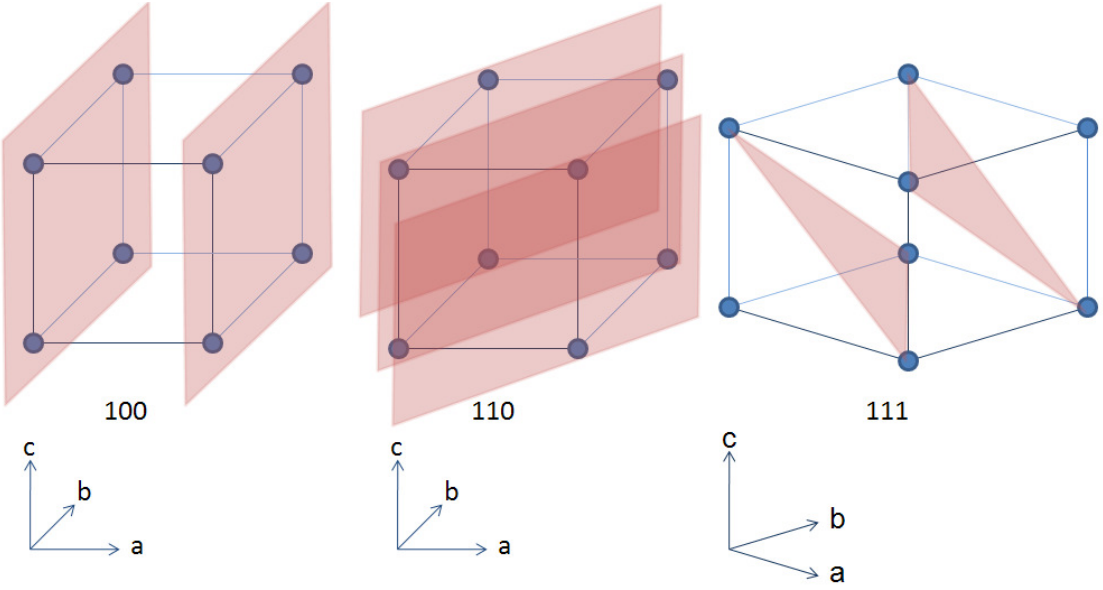

Figure 3.4 – Schematic representation of lattice planes according to their miller indices.

As the d-spacing at a given miller index represents the distance between the two planes, allowing information of the unit cell to be inferred from the diffraction pattern. The lattice parameters for an orthorhombic crystal structure and the relationship to the d-spacing are as follows:

$$\frac{1}{d^2} = \frac{h^2}{a^2} + \frac{k^2}{b^2} + \frac{l^2}{c^2}$$

The intensity of these peaks can be defined as:

$$I_{hkl} = K_{exp} M_{hkl} F_{hkl}^2 K_{samp} L_x P_x$$

This is a simplified view of a diffraction peak, but captures the key contributing factors to peak intensities:

K_{exp} – the constant peak intensity due to the experimental set-up, including: the initial intensity, distance to sample, x-ray wavelength, the effect of electron interaction based on its radius and the phase alignment within the x-rays; it also covers the change in intensity based on diffraction angle and any corrections due to the monochromator;

M_{hkl} – the multiplicity of the given reflection, hkl;

F_{hkl} – the structure factor, which has the greatest effect over the intensity; it defines the scattering of the x-ray by individual atoms based on their scattering ability given their location within the unit cell and the occupancy of the site; also the thermal factor for the atom, a reduction observed due to vibration which is directly affected by temperature;

K_{samp} – the effects of the sample on diffraction intensity, such as the absorption factors of the sample, the fractional amount of phase present, thickness and preferred orientation effects.

L_x – the Lorentz Factor accounts for the variation in probability of a reflection occurring at any given diffraction angle.

P_x – the polarisation factor accounts for the polarisation of the x-ray beam. X-ray and samples interact most when the electronic vector is parallel and antiparallel to the sample.

Within a diffractometer we look at 3 key areas: The source; the sample and the detector. The detector and source are diffractometer dependent.

A laboratory based diffractometer generates x-rays by way of a high energy electron beam, from a high temperature filament, striking a metal surface. All the diffractometers used during the course of this work used a copper source. Two different x-ray radiation profiles are generated through this method. The first referred to as “white-body” radiation or Bremsstrahlung radiation arises from the loss of energy of electrons through deceleration, which gives a characteristic broad curve. The second is caused by relaxation of bound electrons into the copper 1s orbital, yielding sharply defined wavelengths. The incident electron beam causes ionisation of copper 1s electrons. This causes electrons in higher orbitals drop into the vacancy to reduce the energy of the system. The 2p and 3p relax to the 1s causing emission of the $K\alpha$ (a doublet) and $K\beta$ at the wavelengths of 1.5406, 1.5433 and 1.3922 Å, respectively.

The X-rays are often 'filtered' using a metal foil, nickel in this case, to yield monochromatic radiation at $K_{\alpha 1}$ of 1.5406 Å. The position sensitive detectors (PSD) count the intensity over a range of θ values, with a given step size ~ 0.02°, averaging the intensity.

Laboratory Data Collection

A Siemens D5000 was used for all samples at room temperature, both air-sensitive and prepared in atmosphere. Data was collected between 5 and 50° 2θ. Copper $K_{\alpha 1}$ radiation from a copper source and germanium monochromator was used, with the resulting X-ray beam being setup in transmission geometry with a mobile PSD and rotating sample. The setup is shown in figure 3.5, also showing $\theta - \theta$ transmission geometry.

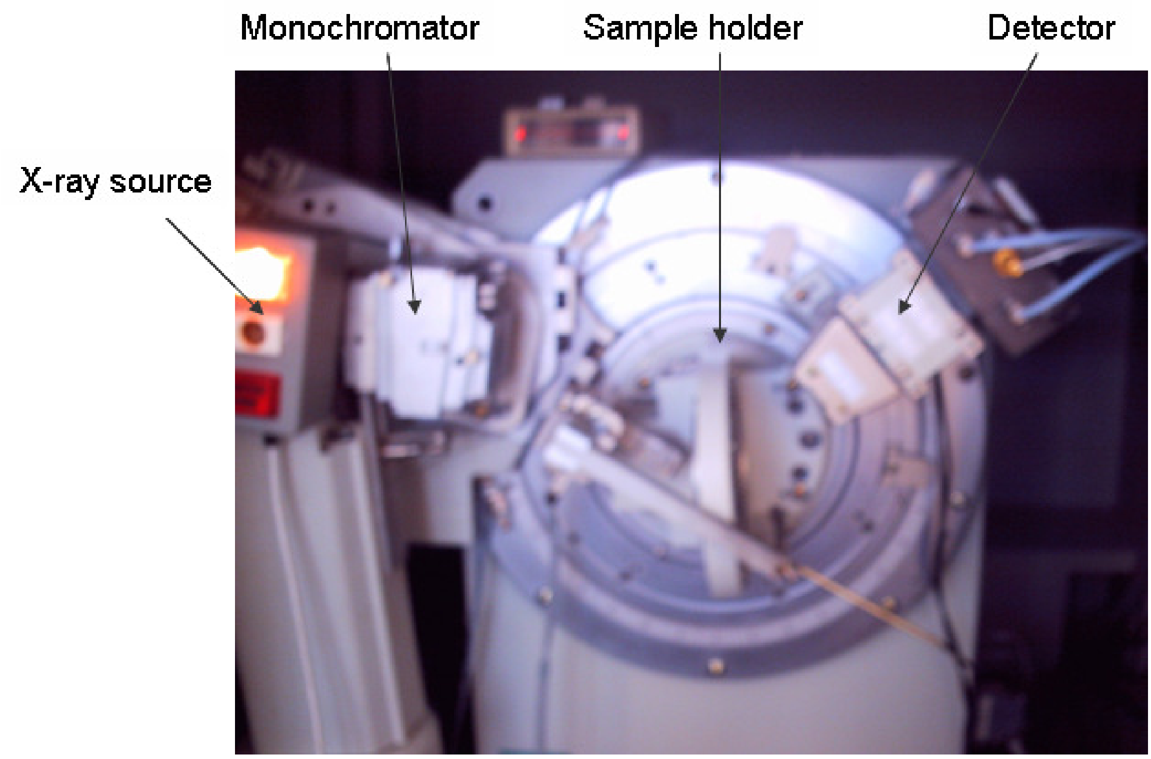

Figure 3.5 – Bruker D5000 powder X-ray diffractometer in transmission geometry.

$\theta - \theta$ reflectance geometry setups were used for specific inert atmosphere measurements. A Bruker D5005 with Anton-Parr cell, provided variable temperature measurements. It was used with flowing nitrogen to afford an inert environment under which to perform diffraction under desorption conditions. Data was collected between 5 and 60° 2θ.

Initial analysis of this data was performed using the peak diffraction database present with the EVA software provided by Bruker[8]. This was used to determine phases present by diffraction. Analysis of the key phases was performed using Chekcell[9], which is a least squares minimisation based program using peak positions. This compares observed $\sin^2 \theta$ values with those calculated from a starting lattice parameter and a space group, to refine the lattice parameters and/or angles.

In some cases, Rietveld analysis, which is also a least squares minimisation method, was performed using Topas[10]. The observed pattern is compared to a mathematically modelled one, based on parameters that describe the unit cell size, shape, atomic positions, occupancies and thermal factors. Peak profile and background are also accounted for. This was used to get an approximation of phase compositions in samples.

3.4.2.3 Scanning Electron Microscopy (SEM)

SEM is used to obtain information about the morphologies and sample surfaces.

When a beam of electrons is incident to a material under vacuum conditions several different interactions can take place. These are schematically represented in figure 3.6.

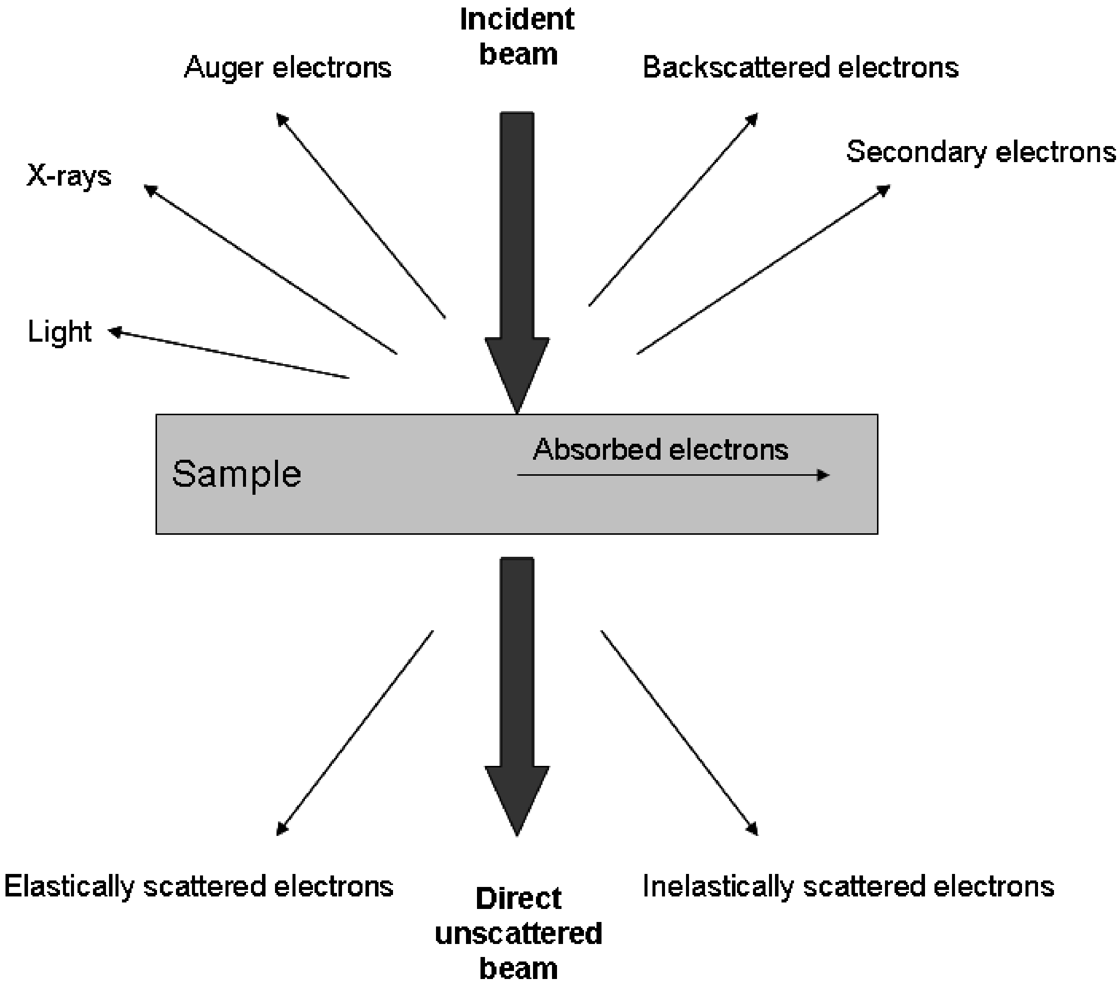

Figure 3.6 – Schematic of the interactions between the electron beam and sample within an electron microscope.

The vacuum is necessary to minimise interaction between the electrons and gaseous species, allowing for a focused beam of electrons. These electrons are typically generated by an electrically heated tungsten filament and accelerated towards the sample by applying a large potential difference. The interaction between electron beam and sample generates secondary electrons. These electrons when processed are converted into electrical signals, but are only indicative of a single point on the sample. By scanning in a rastered fashion this information can be obtained for an area of sample. The electric signal is processed and displayed as an image, either by cathode ray tube (CRT) or charge-coupled device (CCD). The intensity of the signal, from the quantity of secondary electrons, is directly related to the incident angle with the surface of the sample. The image observed reflects the topology of the sample observing the three-dimensional surface of the material over the rastered area.

The experimental data were collected on a JEOL 7000. Samples were placed uniformly on to carbon disks and placed in a Kilner jar until measured. Brief exposure to atmosphere occurred during the loading, but the samples were evacuated quickly within the SEM.

3.4.3 Spectroscopy

One of the most useful spectroscopic probes of solid state materials is vibrational spectroscopy. This can prove useful in determining changes in the local structure of crystalline species, whilst also confirming the presence of guest species. To obtain vibrational information wavelengths in the mid-infrared (IR) are used. Raman spectroscopy yields information by exciting at a known wavelength and observing the energy emitted as the state relaxes, whilst filtering those closest to the incident radiation. The difference gives information about the vibrational state. Wavelengths in the visible region of the electromagnetic spectrum are used.

3.4.3.2 Fourier Transformed Infrared Spectroscopy (FTIR)

A Thermo Nicolet 8600 fitted with Specac golden gate was used to obtain the FTIR spectroscopic data. The Specac golden gate was fitted with an inert die using an o-ring seal. The cell was purged using nitrogen to remove traces of atmospheric gases (water and carbon dioxide, for example), which interfere with the spectra. Data was collected between 500 and 4000 cm^{-1}.

3.4.3.3 Raman Spectroscopy

A Renishaw InVia Reflex with an Instec HCS621V was used with a wavelength of excitation of 488 nm. The Instec stage was loaded with several samples and sealed from atmosphere. The Instec stage can be used with flowing gas, but in this case it was left under a static pressure of argon, with the inlet and outlet sealed.

3.4.3.4 Electron Spin Resonance Spectroscopy (ESR)

Electron spin resonance or electron paramagnetic resonance (EPR) is related to nuclear magnetic resonance (NMR) which is a commonplace analytical technique within the chemical community. ESR requires unpaired electrons and is, therefore suitable only for paramagnetic species.

ESR exploits the interaction of unpaired electrons with magnetic fields. Insertion of the electron into a magnetic field produces a splitting in the otherwise degenerate electron spin energy levels proportional to the magnetic moment and the magnitude of the magnetic field. The measurement using an ESR spectrometer operates at a fixed frequency; the ESR spectrum is generated as a function of linear variation in the magnetic field.

Contributions to peak position and shape come from interactions with nuclei, spin-orbit coupling and the external magnetic field. The first two are sample specific. The g-value of a free electron is 2.00231, and whilst the value within compounds is frequently approximately 2, electrons are very sensitive to their local environment and it can be determined quite accurately.

Sample data was collected on a Bruker ESP-300 spectrometer operating at X-band frequencies of approximately 9.5 GHz. Spectra were collected both at room temperature and at 77 K.

3.5 Desorption and Adsorption Techniques

Hydrogen storage materials require direct measurement to ascertain their suitability for their purpose. In this work, the intrinsic nature of a host-guest system means that two different possible regimes needed to be considered. Measurements to assess the hydrogen uptake of porous materials are done using accurate volumetric and gravimetric measurements at low temperatures. The physisorption properties of the hosts and some composites were measured using an intelligent gravimetric analyser (IGA).

The guest materials often have desorption properties in higher temperature regimes to those of the hosts. Similarly their rehydrogenation (if any) to regenerate the starting material would occur at higher pressures and temperatures. The desorption properties of the guests within the hosts were obtained using TPD. Some rehydrogenation experiments were attempted using an IGA.

3.5.1 Intelligent Gravimetric Analysis (IGA)

The analysis of adsorption properties was performed on a Hiden IGA-001. The IGA or intelligent gravimetric analyser is an accurate microbalance which has a sample container hung against a counterbalance. Accurate control of gas pressure is achieved through the use of motorised inlet and outlet valves. A furnace or liquid dewars provide access to temperatures up to 500℃ or as low as 77 K. The microprocessor unit of the IGA controls the pressure and temperature and is then linked to a PC. The PC also provides a point for data collection of the system parameters through the IGASwin software. The system schematic and actual image are shown in figure 3.7.

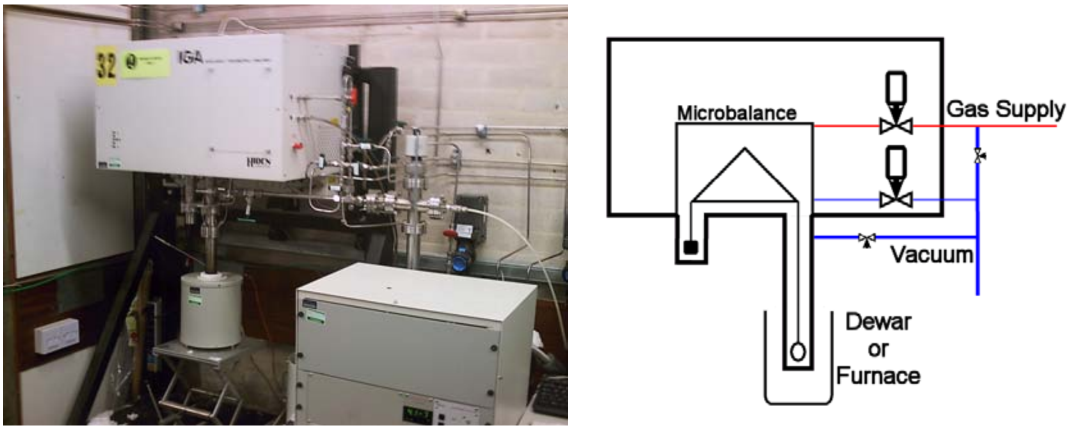

Figure 3.7 – Image and schematic of the IGA.

The use of the computer and microprocessor system allows for corrections to be made for buoyancy. As the samples are exposed to increasing pressures of gas the change in observed mass is due to a buoyancy effect. The mass of sample (and fittings) becomes a function of the change in volume and gas density.

The data collected can yield a variety of information on adsorption properties, from the actual adsorptive properties to intrinsic information about the system such as the adsorption mechanisms or even data on the internal pore structure. Mechanisms may often be deduced simply from the variation with mass at given pressure over time. Surface areas can be estimated at low temperatures using mobile gases. The use of variable temperatures and their correlation with uptake and pressures allow for the determination of the heats of adsorption. Several methods can be used to model the mechanism of adsorption. The program Solver[11] in Microsoft Excel was used to minimise the differences between the modelled values and the experimentally collected data through alteration of the fitting constants within the models. The fitted data at 77 and 87 K were then used with the Clausius-Clapeyron equation to derive a heat of adsorption at any given coverage.

The sample runs performed on the IGA were all inertly loaded. The antechamber was attached and purged 100 times with argon before 70 – 100 mg of sample was loaded onto the IGA. This was done to minimise the exposure to atmosphere. Then the IGA sample chamber was sealed to the antechamber and purged with hydrogen (99.9995% purity) to ensure that no argon remained in the system. The antechamber was removed and the samples were outgassed. In most cases the initial outgas was performed at room temperature. Elevated temperatures were used where the dehydrogenated form of the sample was required. Isothermal plots were favoured at the lower temperatures regimes, where the sample had been outgassed and the pressures were increased at constant temperature. Data were recorded at 77, 87 or 298 K. Isobaric plots were favoured at elevated temperatures, where an initial pressure of 18 bar hydrogen was introduced into the sample cell and then the temperature was ramped over a period of time to observe changes in the mass, with corrections to buoyancy. All runs involving hydrogen used a liquid nitrogen trap for the hydrogen line. Between measurements the samples were evacuated again.

After sample runs were completed, the samples were inertly unloaded with a flushing of the antechamber for 1 hour with Argon. This allowed the integrity of the sample to be assessed by XRD.

3.5.2 Thermogravimetric Analysis with Mass Spectrometry (TGA-MS)

Thermal analysis of hydrogen storage samples is invaluable in determination of desorption properties. Thermogravimetric analysis (TGA) is the most common method used. The analysis itself shows a change in mass over a given temperature regime, a typical plot looking like that in figure 3.8, showing data for Whewellite (Calcium Oxalate monohydrate), a TGA standard.

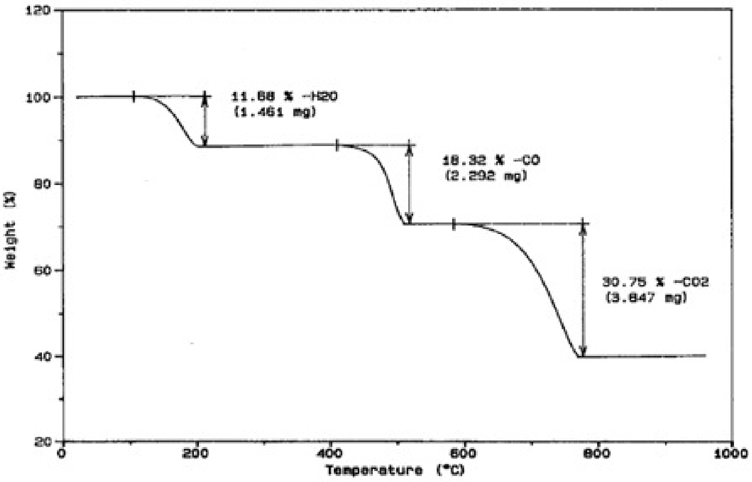

Figure 3.8 – TGA trace of Whewellite.

Onsets of mass loss events can be seen such as at 118°C, where the progression of time brings an increase in temperature and loss of weight. This will continue until the event has finished such as 180°C, after which the temperature continues to increase but the mass remains the same. A different type of measurement is an isothermal point. This is where a temperature is selected at which time progresses and the mass may drop until the system reaches thermodynamic equilibrium, without a change in temperature.

TGA measurements were carried out on a Netzsch TG209. The TGA was located inside an argon filled glove box, allowing accurate measurement of inert samples without exposure to atmospheric gases. This TGA functioned with a top pan balance arrangement, whereby the sample was loaded on top of the balance. This contrasts with the IGA which functioned with a hang down balance. The TGA system is shown below in figure 3.11.

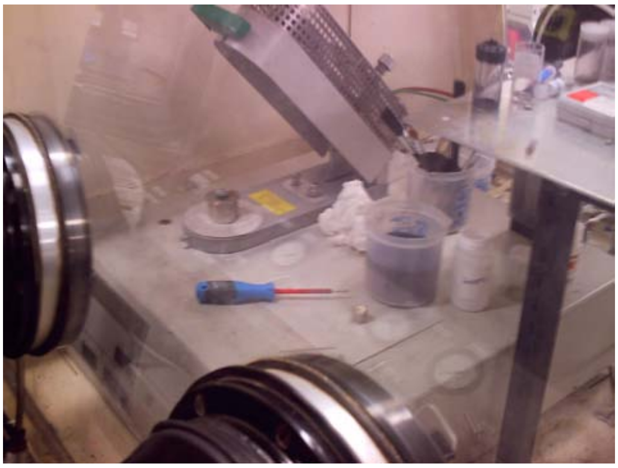

Figure 3.9 – Image of the inert Netzsch TG209.

The samples were analysed in one of the following regimes. The first was a ramp from 30 to 600℃ at 2℃ per minute; the system used a 40 ml per minute flow of Argon as a protective gas. The second was a ramp from 30 to 420℃ with a 2 hour isothermal point at the final temperature, and again a 40 ml per minute flow of Argon as a protective gas. In each case a blank run was performed and this was used as a buoyancy correction. Approximately 25 mg of the sample was loaded into an alumina crucible for the sample run. The exhaust vent on the TGA was piped into an inlet feed on to a vacuum pumping system and then onto the mass spectrometer.

3.5.2.1 Mass Spectrometry

Mass spectrometry is an analytical technique often used in organic chemistry for determining elemental composition or structural details such as connectivity. In this field of research gas streams from thermal analysis methods (including thermogravimetric) can be analysed to determine gaseous species present. With appropriate calibration it can be used to determine quantitatively the amount of gaseous species present.

Mass spectrometry has three key functions: ionisation; mass analysis and detection. As the species to be analysed in this case were already gaseous no vaporisation step was required. The pressure was above atmospheric for the gas stream so the mass spectrometer sampled the gas stream through the use of vacuum systems to achieve low partial pressures.

The gaseous species were ionised using electron beam ionisation to yield ions which could then be manipulated by the mass analyser. The mass analyser used was a quadrupole mass analyser. This uses an oscillating electrical field to choose a specific mass-to-charge ratio (m/z). The quadrupole field causes the paths of the ions to either stabilise and be sent to the detector or destabilise and collide with the rods generating the electrical field. Altering the potential of the electrical field allows for different m/z ratios to be selected. Either a full sweep of ions can be accurately determined, or specific ions can be analysed over a given period.

A Faraday-type detector was used, which operates by measuring an electrical current. This current is generated by the ions striking the detectors surface and becoming neutralised. The number of ions that strike the surface over a given time is proportional to the charge. The data produced records the number of ions against the m/z ratio.

The outlet gas stream of the TGA was monitored using a Hiden Analytical HAL IV quadrupole mass spectrometer

3.5.3 Vacuum Temperature Programmed Desorption (TPD) with Residual Gas Analyser (RGA)

Small samples were heated up under vacuum and the gaseous desorption products were analysed by a residual gas analyser (an MKS products microvisionplus RGA with quadrupole analyser with process eye software for analysis). Heating was provided by a large bore Lenton furnace. Unlike the TGA, no gravimetric data is obtained by this method. The schematic and picture in figure 3.10 show its design.

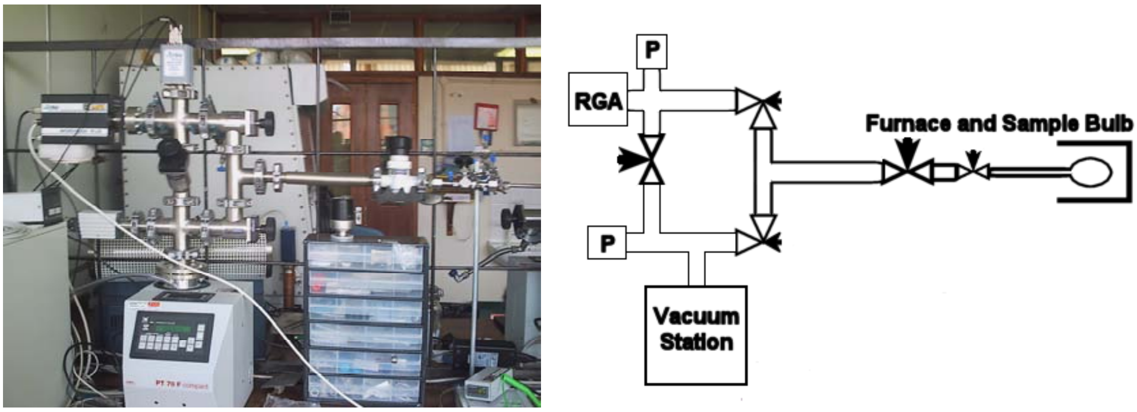

Figure 3.10 – Image and schematic for vacuum TPD.

The RGA functions identically to a mass spectrometer, again with the m/z being determined by a quadrupole analyser. The limiting factor was that no m/z above 50 could be measured, though in this study, predominantly of hydrogen desorption, few species were expected above this value.

The sample holder went through two different incarnations. Initially samples were prepared in two quartz glass tubes: the larger quartz tube (12 mm external diameter and 20 cm in length) was present to contain the actual sample tube, but also allow its connection to the vacuum rig and the sample being heated; the sample tube was 4 mm in diameter and 11 cm in length. The second incarnation used a stainless steel bulb to replace the larger quartz tube. This change in design was due to concerns over leaking into the vacuum system, which became apparent. These leaks occurred at the Ultra-torr fittings which connect the glass tube to the valve system. The steel sample bulb was attached with Swagelok fittings and piping. The use of a gasket resolved the problem with leaks. One phenomenon sometimes observed at low pressures was sympathetic gas flow, where the increase gas flow from a major desorption caused false fluctuations in the baseline of species not being desorbed.

A desorption run started with the sample tube and bulb (or the large quartz tube plus sample tube) being baked out to 500℃ over 18 hours whilst under vacuum, initially with the diaphragm pump to approximately 1 x 10^{-3} bar, then with a turbo pump to approximately 1 x 10^{-8} bar. During this process the RGA was isolated from the vacuum system to ensure any desorbed products from the cleaning of the sample holder did not coat the RGA filament. Once a suitable pressure was reached the RGA section was reopened to the vacuum pumps to ensure it remained as clean as possible. Once the sample bulb and tube were at room temperature the vacuum was sealed from the tube/piping and the holder was removed whilst sealed from the atmosphere and placed in an argon recirculating glove box. Here the sample was loaded carefully into the internal glass tube, with minimal handling. The sample quantities required were no more than 0.9 mg for high weight percentage hydrogen storage materials such as ammonia borane or lithium borohydride. The occluded compounds often contained much less hydrogen, approximately 4%, and in practice 2.5 mg could be used. Once the sample was loaded, the smaller tube was reinserted into the bulb or larger quartz tube and again sealed from the atmosphere by the tap. This was then reattached to the rig, and the sample holder was again evacuated whilst the RGA section was isolated. Once the pressure had settled the RGA section was reopened. Once the pressure had settled again the RGA was initialised and after a brief spike the pressure settled quickly. A furnace was manoeuvred over the sample, as well as an external thermocouple which was clamped in place on the tube or bulb. The furnace was programmed and started and the sample was ready to be measured. Normally a ramp rate of 2℃ per minute to 450℃ was employed for lithium borohydride. In some cases a dwell of 8 hours was required to reach thermodynamic stability.

3.5.4 Pycnometer

The density of systems can give an insight into possible changes in structure. In solid samples densities are obtained through gas expansion pycnometry. The gas used is important as any interaction with the surface will affect the perceived change in volume. Also the gas must be as permissible as possible to allow for measurements of pore structures. For these reasons helium is generally used. Strictly speaking this is a volumetric measurement, with two chambers of calibrated volume: the reference and sample cell. By dosing a known pressure into the reference cell and then expanding this into the sample cell we obtain a pressure difference, allowing us to determine the second volume. As the sample is placed into the cell, it displaces part of the known volume, this will be accounted for in a different pressure change on dosing. The quantities are related by the equation:

$$V_s = V_c + \frac{V_r}{1 - \left(\frac{P_1}{P_2}\right)}$$

where V_s is the volume of the sample, V_c is the volume of the sample cell, V_r is the volume of the reference cell and P_1 is the dosing pressure and P_2 is the expanded pressure. The density is then calculated as the mass per unit volume, where the mass of the sample is measured externally from the pycnometer.

Density measurements were obtained through helium gas pycnometry using a Micromeritics AccuPyc II 1340 system. The operation of the pycnometer was in an argon glove box, in which samples were placed. Samples were weighed (between 0.17 and 0.30 g), and placed in the sample cell. Sample runs consisted of 30 purge cycles, followed by a 50 cycle run, whereby the volume is calculated 50 times and then averaged to reduce error.

3.6 References

1. Dyer A., *An Introduction to Zeolite Molecular sieves*, Wiley, Chichester, **1988**
2. Robson H., *Verified Syntheses of Zeolitic Materials 2nd Edition*, Elsevier Science, **2001**
3. Langmi H. W., *Hydrogen Storage in Zeolites and Carbon Materials*, PhD Thesis awarded by the University of Birmingham, **2004**
4. Inglezakis V. J., *J. Colloid Interface Sci.*, **2005**, 281, 68
5. Züttel A., Rentsch S., Fisher P., Wenger P., Sudan P., Mauron Ph., Emmenegger Ch., *J. Alloys Comp.*, **2003**, 356-357, 515
6. Chater P. A., David W. I. F., Johnson S. R., Edwards P. P., Anderson P. A., *Chem. Commun.*, **2006**, 2439
7. Baitalow F., Baumann J., Wolf G., Jaenicke-Rößler K., Leitner G., *Thermochim. Acta*, **2005**, 430, 9
8. Bruker AXS Diffracplus EVA, http://www.bruker-axs.de/eva.html

9. CHEKCELL, developed at Laboratoire des Matériaux et du Génie Physique Ecole Nationale Supérieure de Physique de Grenoble (INPG), France

10. Bruker AXS Diffracplus Topas, http://www.bruker-axs.de/topas.html

11. Microsoft Excel Solver, http://office.microsoft.com/en-au/excel-help/about-solver-HP005198368.aspx

CHAPTER 4
THE OCCLUSION OF LITHIUM BOROHYDRIDE IN SODIUM ZEOLITES A, X & Y.

4.1 Introduction

Over recent years interest has been shown in the nano-scaling of hydrogen materials to improve the kinetics associated with hydrogen diffusion through solids, as well as increased surface areas for hydrogenation[1-5]. Concurrently, similar ideas were being applied to the thermodynamics of systems to take poorly reversible storage materials and hopefully improve thermodynamics. The effect of particle size reduction can show improvements in the kinetics of systems, suggesting that improved hydrogenation could occur at smaller scales [1-7].

The methods by which this scale down process has largely been occurring are mechanical milling[2,5,7], some thin layers by vapour deposition[7] and use of nanoporous materials as hosts[8-15].

Mechanical milling, whilst a well established method for synthesis of hydrogen storage materials, can yield a broad range of particle sizes[2,7]. In spite of this range of sizes the process does lead to improved kinetics, with thermodynamics often remaining unaltered. Vapour deposition techniques[16] on the other hand can yield uniform film thicknesses. This would suggest a vast improvement in kinetic diffusion over shorter distances. The typical thicknesses are often between nanometer and micrometer in scale. This can lead to a closer representation of the bulk thermodynamics than that expected of clusters[6,7].

The final method outlined is that of incorporation into nanoporous host materials to provide the size constraint. In practice a variety of results are obtained over an equally varied range of systems. Some systems such as ammonia borane incorporated in mesoporous silica MCM-41 have been shown to give a lower onset temperature for hydrogen desorption and also remove the unwanted decomposition product borazine[14]. Recent studies using magnesium as the store have shown improved kinetics and thermodynamics when using carbon aerogels as host materials[10]. These show lower onset temperatures as well, but the synthesis involves wet impregnation using nickel or copper and rehydrogenation; this in itself will show improved kinetics owing to the catalytic nature of the initial metal loading. The majority of work in this area has been done in mesoporous materials; zeolites may offer the next step in particle size reduction.

Normal methods for the loading of guest materials into porous hosts involve either: solvent impregnation[9,14,15]; thermal occlusion of a guest[8,9-13] or direct synthesis routes[17]. Routes involving direct synthesis often yield new products where the guest material is incorporated into the actual host framework, and as such behave quite differently to the initial guest material. Solvent mediated impregnation is often used when the pore size is large enough to accommodate solvent–guest adducts and allow enough “space” to allow the solvent to be drawn off without affecting the guest material. It is also worth considering that in smaller pore apertures there may be competing effects as to whether either solvent or guest are occluded.

For this reason thermal occlusion is a valid technique for some hydrogen storage guest materials. Thermal occlusion reactions work best from a melt or near the melting point to make use of capillary effects. They will require materials that are known to not desorb near their melting points, but in principle a partly or completely desorbed product could be introduced and then rehydrogenated[10].

This chapter explores the thermal occlusion of lithium borohydride in zeolites NaA (LTA), NaX and NaY (FAU), with analysis was carried out via several methods..

4.2 Experimental

Samples NaA and NaX were synthesised as detailed in the experimental chapter; NaY (13Y) and $LiBH_4$ (>90%) were obtained from Sigma-Aldrich.

Sample preparation began by dehydrating the zeolites (NaA, NaX and NaY); initially they were heated at 60°C per hour to 120°C and held for 12 hours, followed by a further ramp at 120°C per hour to 450°C where they were held for 48 hours, all under vacuum. Dried zeolites were then transferred to an argon glove box to ensure that the zeolites did not rehydrate and allow for intimate mixing with the lithium borohydride, which oxidizes in air. Mixtures were formed in increments of 32 $LiBH_4$ units per unit cell (PUC) from 32 – 256. For NaA the $Fm\bar{3}c$ space group with a 24 Å unit cell was used, and for NaX and NaY the $Fd\bar{3}m$ space group with a unit cell parameter of approximately 25 Å was used for determination of unit cell loadings[18-20]. Samples were prepared as outlined in section 3.2.3.3.

The samples were characterized using powder X-ray diffraction (PXRD). Raman and IR data were collected. SEM images were recorded. Density information was obtained using a pycnometer.

4.3 Results and Discussion

This section is broken down into three parts with each zeolite being independently analysed in turn. It will become apparent that similar effects are observed in all three zeolites to a greater or lesser degree. These differences are indicative of the differences between the frameworks.

4.3.1 NaA with Lithium Borohydride

The synthesis of NaA yielded an off white compound with indexed powder pattern, using the space group $Fm\overline{3}c$, shown in figure 4.1.

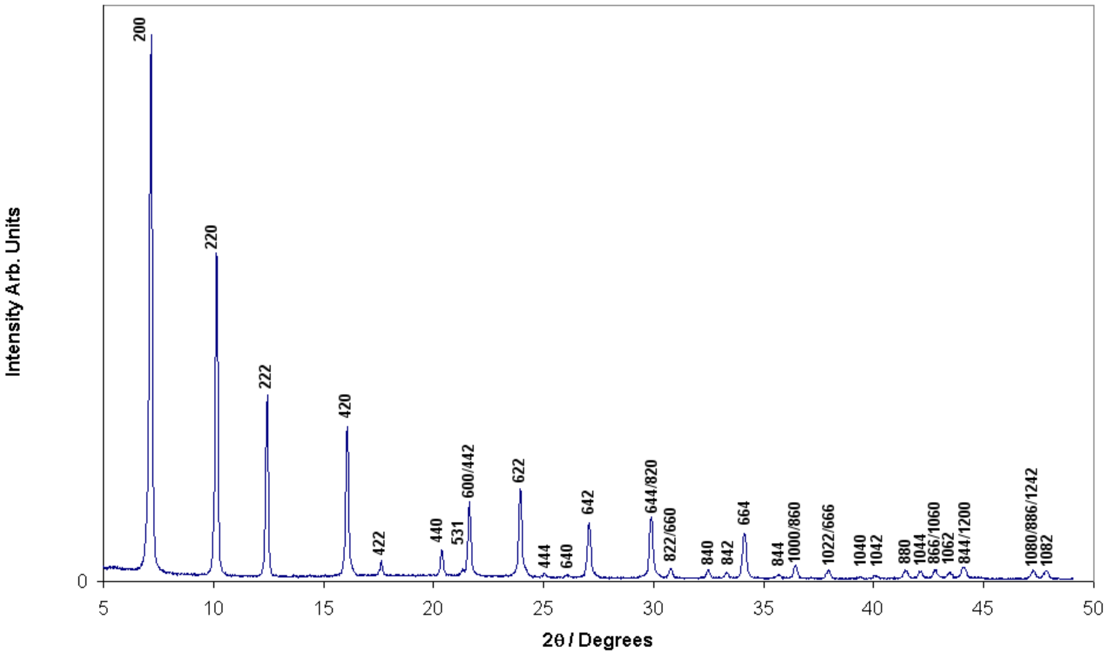

Figure 4.1 – Powder XRD pattern for NaA indexed in space group Fm-3c.

When the dehydrated zeolite NaA (white powder) was heated with lithium borohydride (white crystalline solid), a light grey/off white ‘electrostatic’ powder was collected. A key observation from the initial reaction at 250°C was that no pressure was generated inside the sealed quartz tube, in spite of the expected desorption of ~0.3 wt% of lithium borohydride with its structural transition from the orthorhombic to tetragonal phase[21]. Previous studies had shown that on mixing with silica the decomposition of lithium borohydride could be reduced in temperature, and it was thought that the aluminosilicate framework might behave as a catalyst in the same fashion. With no decomposition observed in the initial reaction further reactions were prepared at different loadings.

4.3.1.1 Powder X-ray Diffraction

Initial analysis of a heated sample, 96 $LiBH_4$ per unit cell (PUC) referred to as $(LiBH_4)_{96}.NaA$, using PXRD is shown in figure 4.2

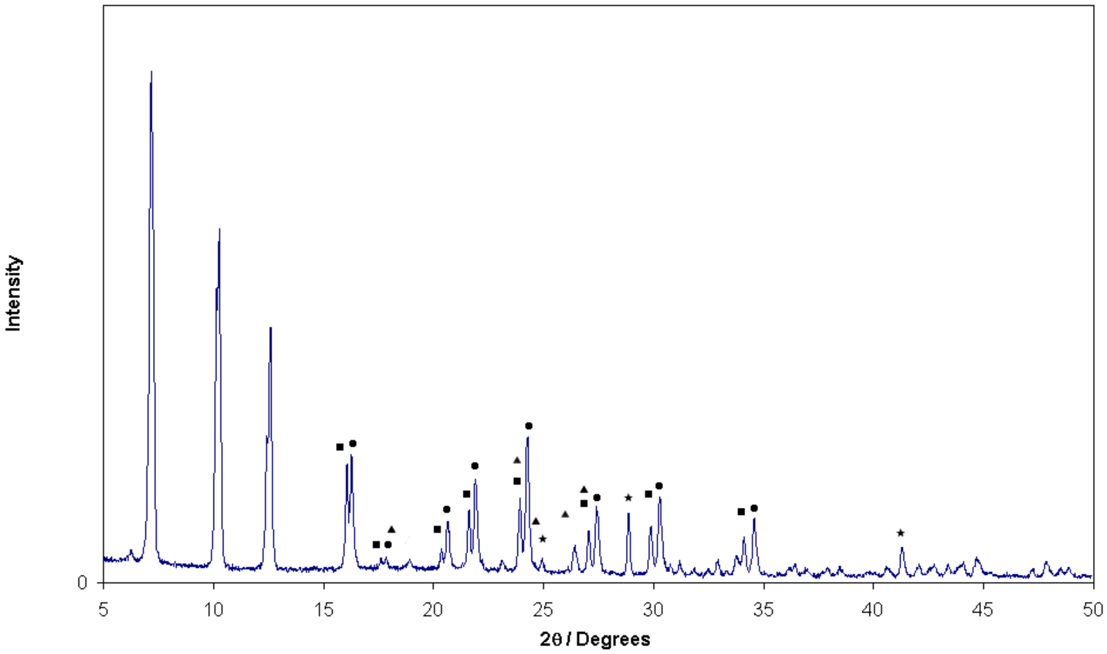

Figure 4.2 – Powder XRD pattern showing $(LiBH_4)_{96}$.NaA after reaction at 250°C for 12 hours. (■) Dehydrated NaA; (●) "loaded" NaA and (✱) $NaBH_4$. The position of $LiBH_4$ peaks, if present, is also marked (▲).

On synthesis a second phase, with the same basic diffraction pattern as that of dehydrated NaA was observed but with all peaks shifted to higher 2θ, indicating a reduction in lattice parameter. Lithium borohydride peaks had all but disappeared whilst peaks due to sodium borohydride had appeared.

Figure 4.3 shows that the relative ratios between the two zeolite phases changed. As more lithium borohydride was added to the reaction mixture the proportion of the higher two-theta phase increased.

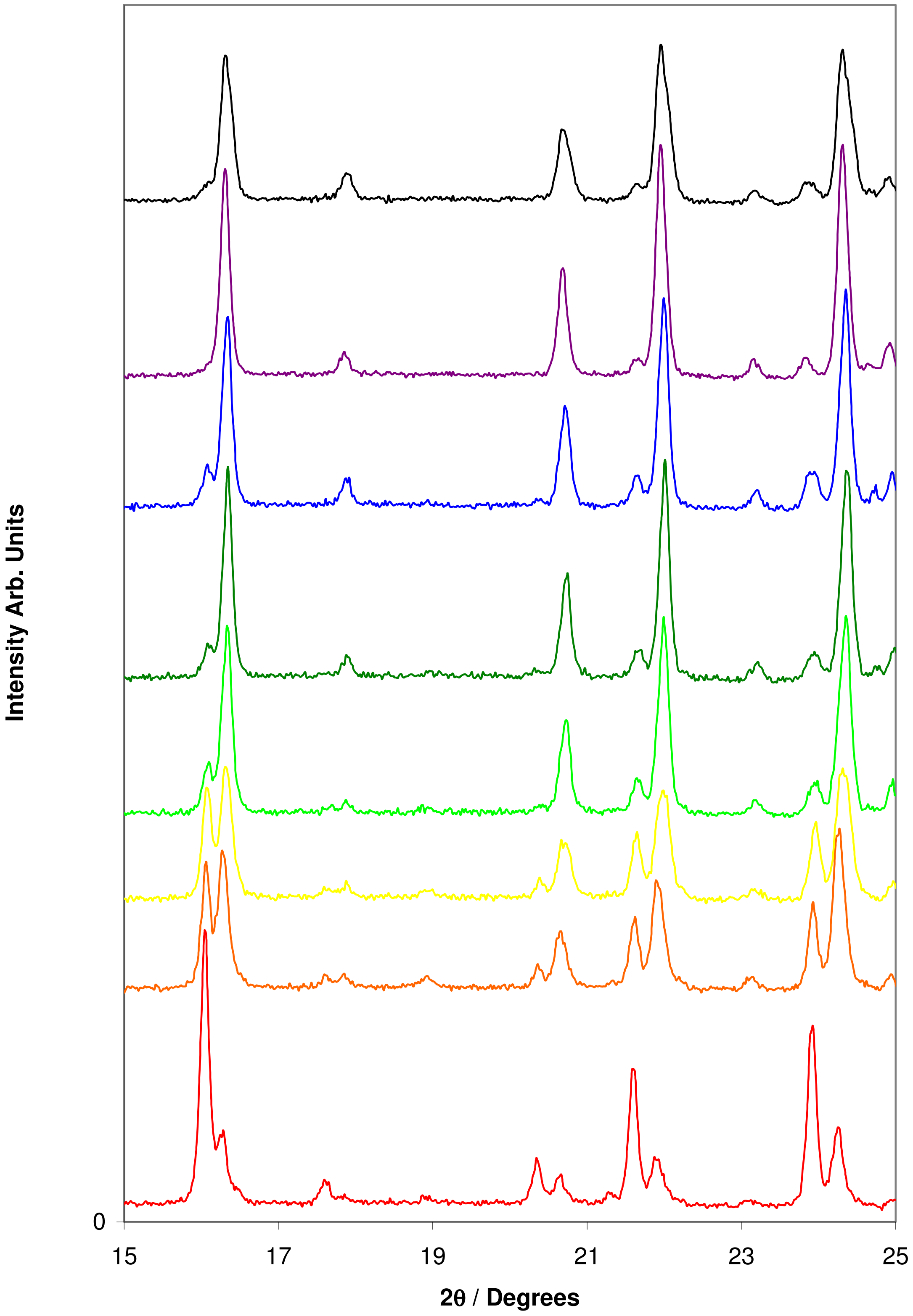

Figure 4.3 – A stacked XRD plot from 15 and 25º 2θ at different loadings of $(LiBH_4)_x$.NaA, where x is: (-) 32; (-) 64; (-) 96; (-) 128; (-) 160; (-) 192; (-) 224; and (-) 256.

This is unusual behaviour in zeolites as countless studies have been performed on zeolites concerning their inclusion chemistry, yet only in a few sodalites have two-phase systems resulted. Generally it could be understood that on loading of compounds into the host framework, as the guest is incorporated, it is, after sufficient time to allow for diffusion, distributed evenly throughout the whole crystallite to minimise intrapore strain. Here the opposite is observed; it appears that lithium borohydride is preferentially accommodated at a certain stoichiometry.

The lattice parameters for these products are shown in figure 4.4. Increased errors in the lattice parameter were observed in each phase when in the minority due to the inability to resolve most peaks except the major zeolite reflections.

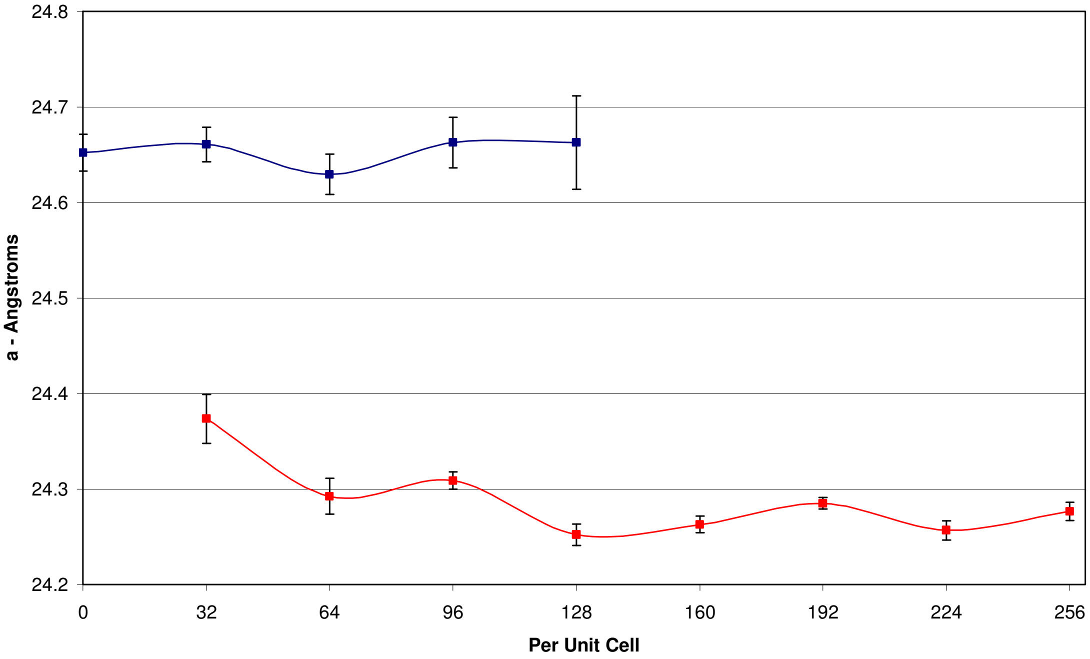

Figure 4.4 – The change in lattice parameter of NaA with loading concentration of $LiBH_4$, showing the dehydrated phase (-) and "loaded" phase (-); error bars show 3 ESD's.

It was observed that values for the phase at low two-theta resembled that of the dehydrated zeolite and remained unloaded. The second phase can be presumed to be a “loaded” zeolite phase. Both of these phases tend towards a single value for the lattice parameter within error.

The only other new phase which appeared was $NaBH_4$, a by-product of solid state ion-exchange in the reaction mixture. Despite this solid state ion-exchange it is worth noting that the lattice parameters for neither zeolite phase matched that of LiA, which is 24.018(3) Å, so exchange was not complete.

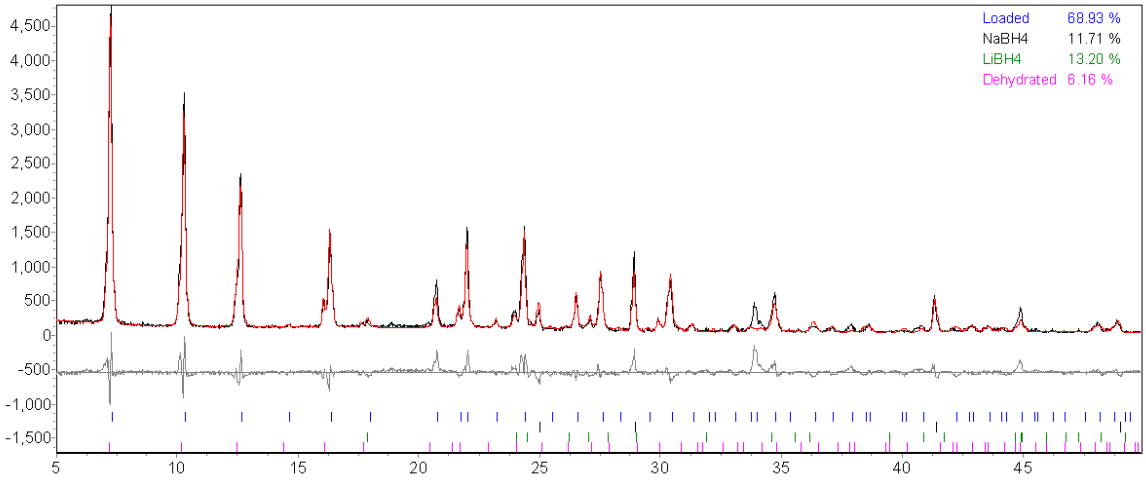

Figure 4.5 – Rietveld fit for $(LiBH_4)_{128}$.NaA. The phases fitted are the loaded and dehydrated zeolite as well as $NaBH_4$ and $LiBH_4$. (-) denotes the raw data; (-) the fitted line.

A Rietveld analysis, shown in figure 4.5, on the powder XRD pattern from the $(LiBH_4)_{128}$.NaA sample suggests that there was approximately 11.7% of $NaBH_4$ present in the system, based on diffraction. The starting mixture contained 26.05% by mass of $LiBH_4$. This sample was selected because the higher two-theta phase was at its most dominant, with some of the other phase still present. This fit, having an R_{wp} of 25.864, is not expected to be highly accurate as it used the dehydrated NaA as the model for one of the zeolite phases and hydrated NaA as the model for the second. As one phase was expected to contain lithium borohydride in the zeolite pores, the hydrated zeolite was used as a model to give an appropriate electron density within the pore. The hydrated model used water to model the occlusion compounds, rather than altering for Li^+/BH_4^-, with freedom to the occupancy and location within the pores. These values would suggest a theoretical hydrogen capacity of 3.65 wt% remaining in the lithium borohydride within the zeolite.

A Reitveld analysis was performed across the composition range, with the results shown in table 4.1. It is possible to see that as concentration of lithium borohydride increased, the loaded phase increased coupled with a decrease in the dehydrated phase. Above $(LiBH_4)_{128}$.NaA lithium borohydride and sodium borohydride dominated the composition implying that the occlusion was completed leaving only ion-exchange and unreacted lithium borohydride.

	Percentage composition in Reitveld analysis				
Occupancy / PUC	% Loaded Phase	% Dehydrated Phase	% $LiBH_4$	%$NaBH_4$	Rwp
32	38.78	52.69	5.03	3.5	20.086
64	64.49	24	5.05	6.46	19.456
96	45.17	22.05	24.46	8.32	18.721
128	68.93	6.16	13.2	11.71	25.864
160	44.51	7.61	36.17	11.72	17.333
192	38.64	15.44	29.33	16.59	18.991
224	11.78	0.91	49.08	38.23	19.08
256	33.78	5.69	37.35	23.19	17.724

Table 4.1 – Reitveld composition data for different concentrations of $LiBH_4$ with NaA.

Above a loading of $(LiBH_4)_{128}$.NaA the powder XRD patterns visibly began to show $LiBH_4$ in the heated mixture; this can be used as an estimate of the maximum loading for NaA, taking into account that there is a small amount of $NaBH_4$ that is always generated. In further studies a half loaded sample was used as a comparison, particularly for adsorption measurements. The sample of $(LiBH_4)_{64}$.NaA was used as it seemed to have an equal proportion of unloaded and loaded phase.

Within the PXRD patterns a change in the relative intensities associated with the Bragg reflections of the host zeolite was also observed. As the intensity of the reflections depends on the distribution of the electron density present we can get an idea of the changes occurring in the framework cavities between the unloaded and loaded phase. This becomes more noticeable with the reflections at higher 2 theta where zeolites usually have poor intensity.

Two examples are shown in figures 4.6 and 4.7 showing the ratios of the Bragg reflections 222 to 200 and 600 to 200 respectively.

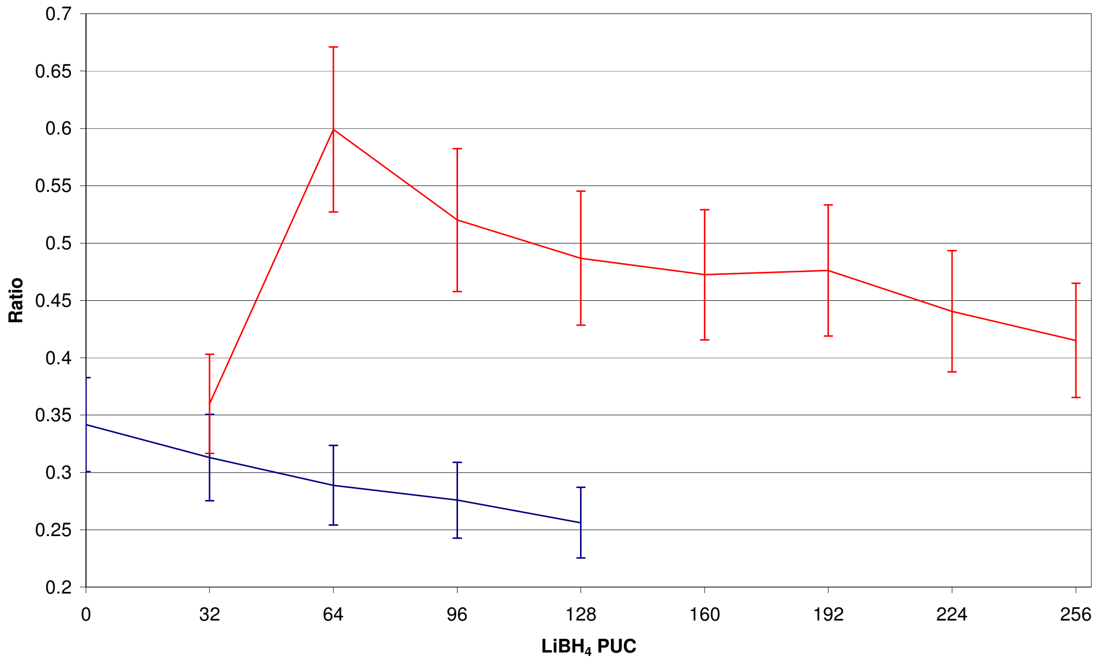

Figure 4.6 – The change in ratio of the intensity of the 222 peak relative to the 200 peak over the composition range of ($LiBH_4$)x.NaA: (-) the dehydrated zeolite phase; (-) the loaded phase.

The loaded phase, in general had a higher ratio than the unloaded zeolite, in both figures 4.6 and 4.7. This indicates that the lower angle (high d-spacing) peaks had a lower relative intensity, which is often an indication of an increase in electron density within the void pore structure, which would reduce the contrast in scattering density between the centre of the zeolite cages and the cage walls. Another noticeable factor is the consistency of the unloaded zeolite ratios, which follows the trend outlined by the lattice parameters in figure 4.4. Small changes in composition may be causing the fluctuation in relative intensities, which would go unnoticed by the change in lattice parameters

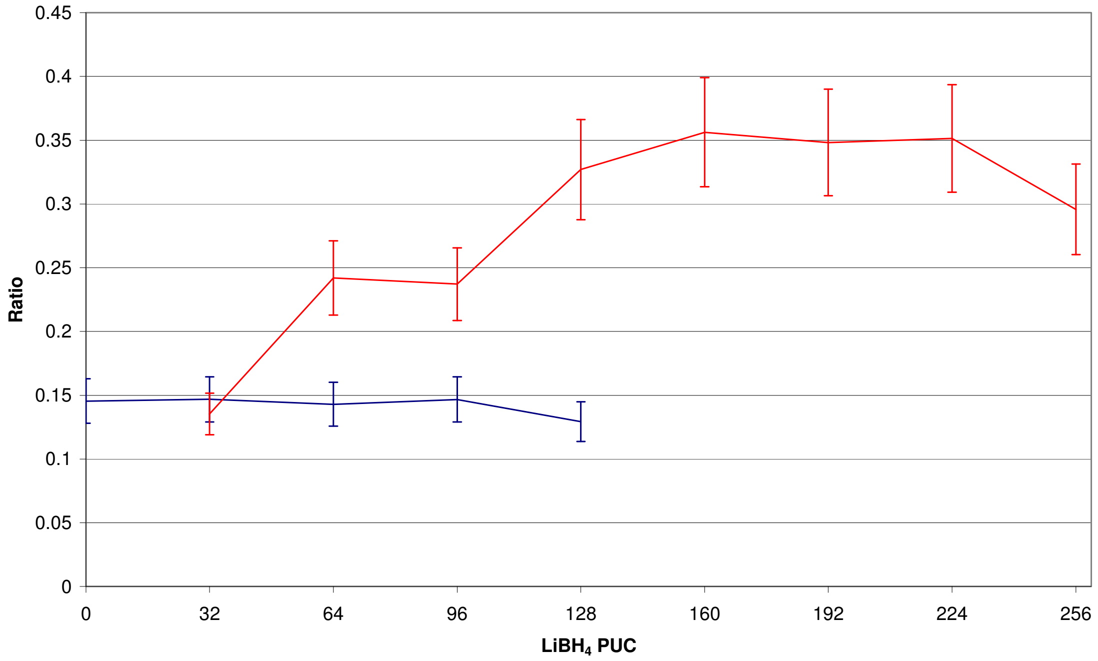

Figure 4.7 – The change in ratio of the intensity of the 600 peak relative to the 200 over the composition range of $(LiBH_4)_x$.NaA: (-) the dehydrated zeolite phase; (-) the loaded phase.

4.3.1.2 Sample Densities

An analysis of densities was performed on the samples using a pycnometer. This gave information about the changes occurring within the sample as the loading occurred. Rather interestingly a decrease in measured density was observed as the sample loading increased. Lithium borohydride, and through ion exchange possibly sodium borohydride (0.666 and 1.074 g/cm^3 respectively) are the materials having the greatest effect in changing the density of this system through occlusion. The parent zeolite when hydrated had a density of 1.990 g/cm^3; this is likely to be that of the framework only with helium permeating some of the pore structure. The total density of the sample may be treated as a summed average of the component densities. We would expect the relationship of loading against density to be linear. The total density is defined as:

$$\rho_{Total} = n_{Zeo}\rho_{Zeo} + n_{Occ}\rho_{Occ} + n_{Li}\rho_{Li} + n_{Na}\rho_{Na}$$

Within the sample, n_x is the fractional percentage of phase x in the sample and ρ_x is the density of the phase x, which can be: dehydrated zeolite (Zeo); loaded zeolite (Occ); lithium borohydride (Li) and sodium borohydride (Na). As we increase the loading we can assume $n_{Na}\rho_{Na}$ to be reasonably constant as XRD has shown very little change in its intensity relative to that of the zeolite, though the percentage value dropped slightly with increasing amounts of lithium borohydride in the system, and increased slightly at lower loadings. Similarly the effect of $n_{Li}\rho_{Li}$ should not become a significant factor until after the sample composition had reached that of maximum occupancy. The term $n_{Zeo}\rho_{Zeo}$ should decrease its contribution as the loading level increases, until the maximum occupancy was reached when it should reach zero. The final term is that of the loaded phase ($n_{Occ}\rho_{Occ}$), which should increase as the dehydrated zeolite term decreased to yield its maximum value at the point where $LiBH_4$ reappeared and the dehydrated zeolite disappeared. This results in three different equations across the phase composition: before the maximum occlusion limit (1), at the maximum occlusion value (2), and with an excess of lithium borohydride (3).

$$\rho_{Load} = n_{Zeo}\rho_{Zeo} + n_{Occ}\rho_{Occ} + n_{Na}\rho_{Na} \qquad 1$$

$$\rho_{Max} = n_{Occ}\rho_{Occ} + n_{Na}\rho_{Na} \qquad 2$$

$$\rho_{Excess} = n_{Occ}\rho_{Occ} + n_{Li}\rho_{Li} + n_{Na}\rho_{Na} \qquad 3$$

This analysis implies that there are should be two different lines of fit to the density data, rather than one.

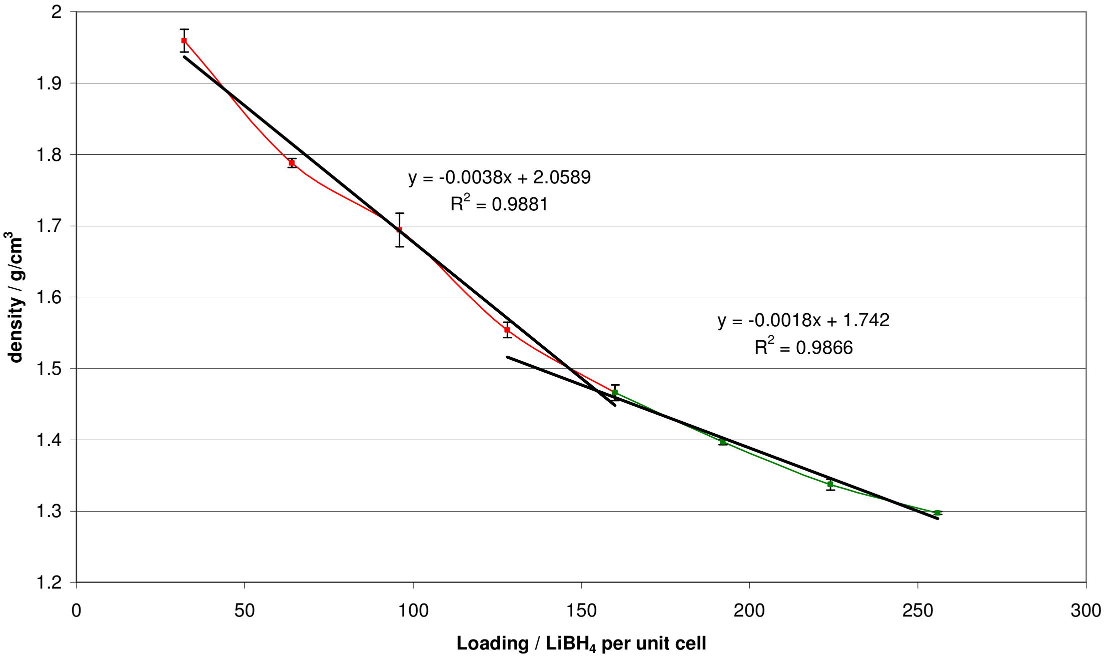

Figure 4.8 – Plot showing the density of samples at various loadings of NaA by LiBH$_4$, split into two sections. The trend lines and formulae are shown.

Whilst figure 4.8 appears to show two distinct regions, the exact relationship between the loading and density may not be linear in the “excess” region of the diagram. The fluctuation and error observed within the lattice parameters upon loading suggest that there may be discrepancies of composition within the sample and some unloaded pore may be encapsulated by loaded parts to the diffusion of the pycnometer gas. The fact that the point of intersection appeared at 158 ± 2 LiBH$_4$ PUC is a good indication that this is in fact maximum loading; this was consistent with powder XRD where LiBH$_4$ reappearing between 128 and 160 PUC.

4.3.1.3 Vibrational Spectroscopy

Spectroscopic methods were used to determine changes to the borohydride environment upon occlusion; the tetrahedral borohydride anion (BH_4^-) is both Raman and IR (infra-red) active and table 4.2 outlines the particular modes of vibration[23-24]. Also shown are the values from IR and Raman which have been collected experimentally in this work.

	Literature Values at 80 K		Experimental Values at RT	
Assignment	Raman Frequencies / cm^{-1}	Infra-red Frequencies / cm^{-1}	Raman Frequencies / cm^{-1}	Infra-red Frequencies / cm^{-1}
ν_1	2300		2296	
ν_2	1287	1284	1286	1290
ν_2'	1325	1323	1317	1311
ν_3	2274	2277	2271	2273
ν_3'	2309	2307	2315	2300
ν_3''		2350		
$^{10}\nu_4$		1099		
ν_4		1089		1091
ν_L		418		
T_1		391		
T_2		324		
T_3		274		
T_4		232		
T_5		175.5		
T_6		162.5		
$\nu_2' + \nu_4$		2423		2402
$\nu_2 + \nu_4$		2387		
$2\nu_4$		2176		2184
$3\nu_L$	1253	1254		1238

Table 4.2 – Infra-red and Raman spectroscopic data for $LiBH_4$ with both literature and experimental values (in cm^{-1})

A close correlation was found between literature data and our IR and Raman data for lithium borohydride.

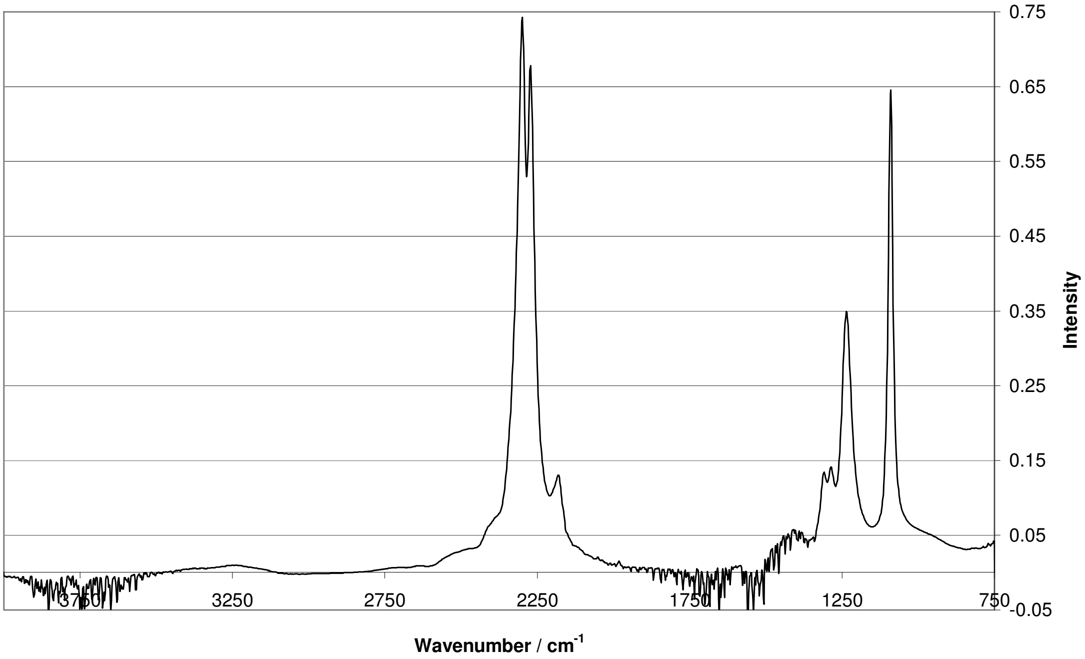

Figure 4.9 – IR spectrum of LiBH$_4$.

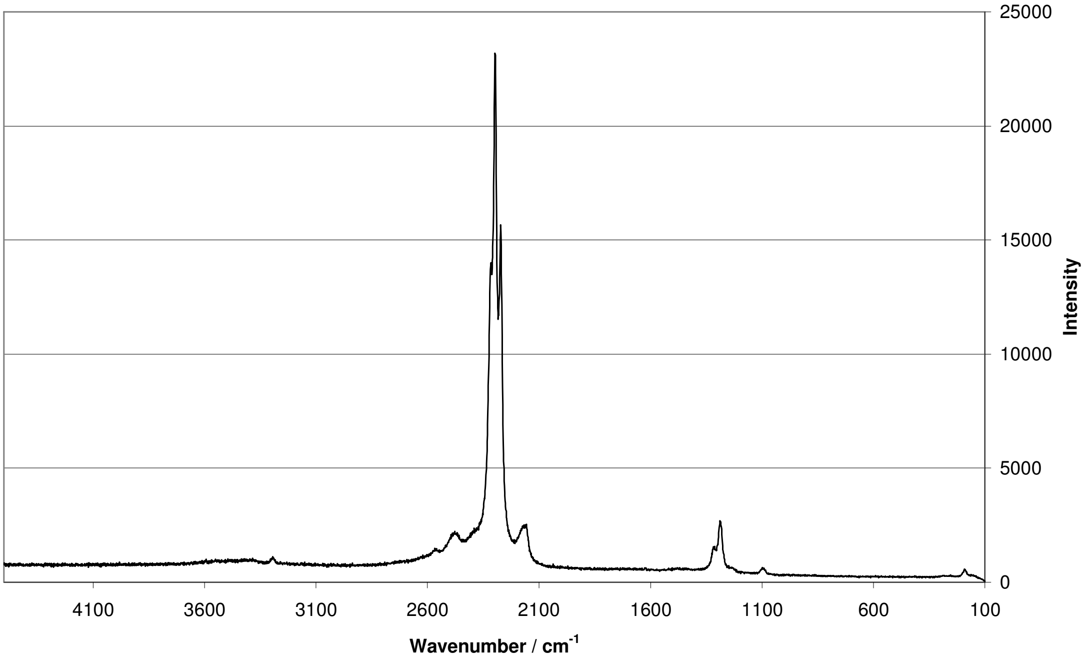

Figure 4.10 – Raman spectrum of LiBH$_4$.

As we can see there are several modes which overlap between Raman and IR, specifically around 2300 cm^{-1}, allowing us a degree of comparability between the two methods. In general zeolite vibrations have varied frequencies determined by their composition and linking. Table 4.3 shows some of the regions for vibrational modes from literature[25-26], as well as some of our observed data for NaA. The IR data were collected between 600 and 4000 cm^{-1}; the Raman data were collected between 100 and 4000 cm^{-1}.

	Literature Values	Experimental Observations	
Assignment	/ cm^{-1}	Raman Frequencies / cm^{-1}	Infra-red Frequencies / cm^{-1}
Internal Linkages			
Asymmetric Stretch	1250-920	960, 1031, 1085	955
Symmetric Stretch	720-650	691	686
T-O Bend	500-420	490	
External Linkages			
Double Ring	650-500		621
Pore Opening	420-300	333, 393	
Asymmetric Stretch	1150-1050		1140 (sh)
Symmetric Stretch	870-750		

Table 4.3 – Infra-red and Raman vibrations for NaA collected experimentally and general zeolite lattice vibrations from the literature (in cm^{-1}).

In addition to these peaks, there are peaks associated with cation interactions which occur between 50 and 250 cm^{-1}. The cations are also known to cause alterations in other vibrational modes of the framework. Hydroxyl peak positions are typically around 3600 cm^{-1}, though they can largely be ignored as they should not be present in dehydrated samples[25-26]. Again similarities between these values and the IR and Raman spectra for hydrated NaA are easily observed.

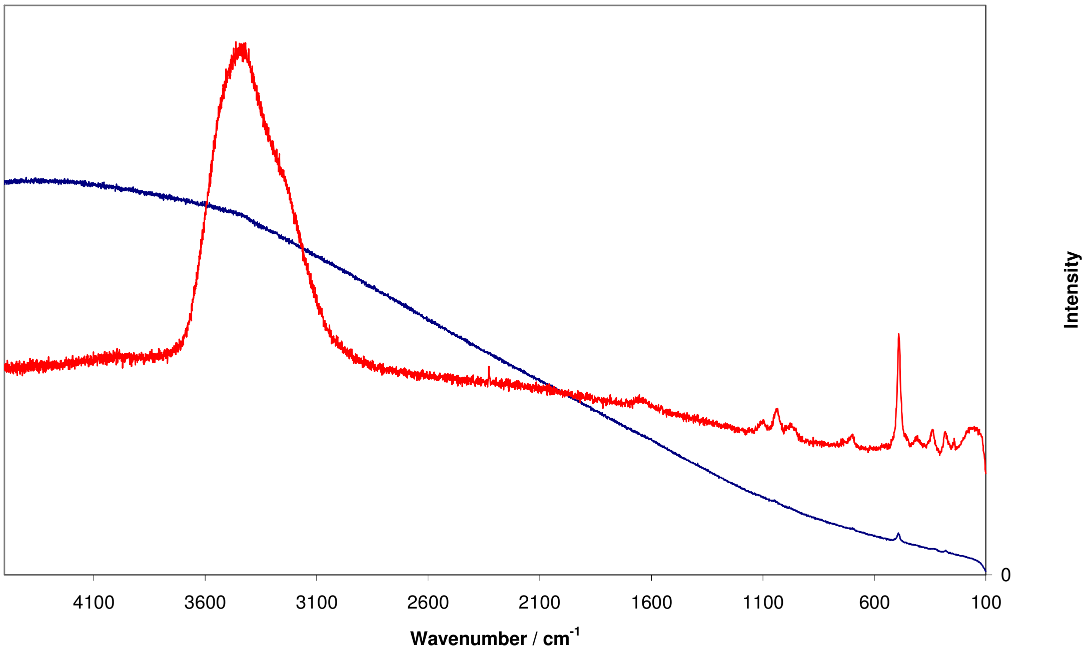

Figure 4.11 – Raman spectra of NaA Hydrated (-) and NaA Dehydrated (-).

On dehydration, shown in figure 4.11, we note that almost all the Raman signals have disappeared. It is likely that these bands are broadened considerably by framework strain on dehydration.

With the IR data, shown in figure 4.12, it was observed that on occlusion of $LiBH_4$ there was a reduction in the borohydride signal, although experimentally, this could be masked by atmospheric CO_2 which has a peak at 2350 cm^{-1}. There was some noise between 1500 and 1750 cm^{-1} which is down to the ν_2, the bending mode of atmospheric water. The sample remained inert, but the path of laser between sample and detector itself was still exposed to small amounts of atmosphere due to the method of gas purging.

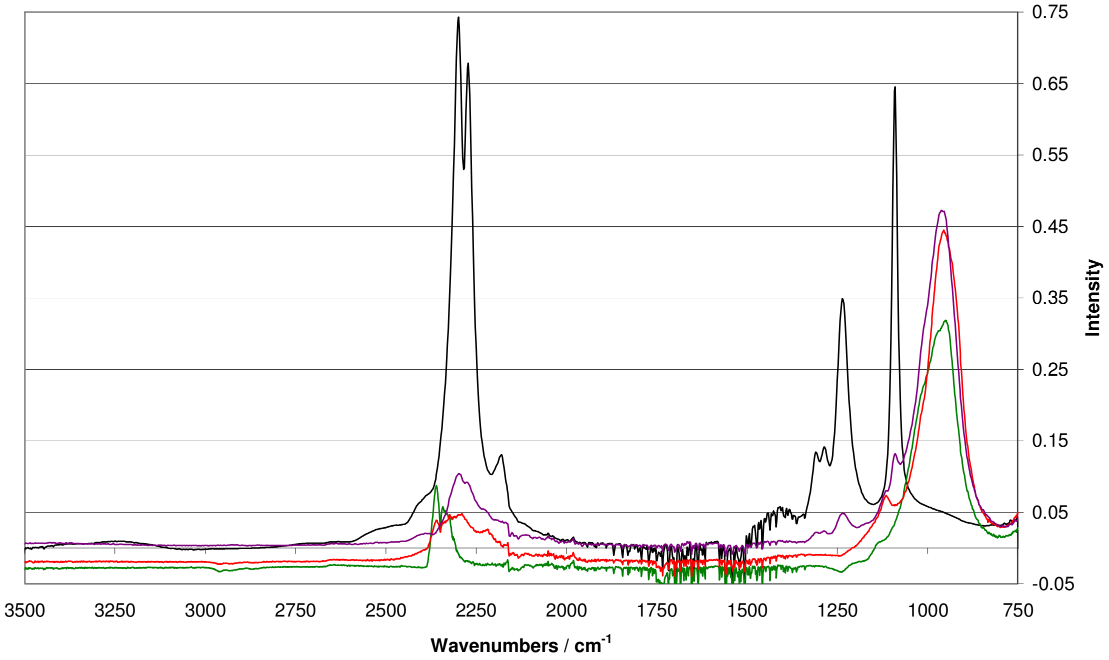

Figure 4.12 – IR spectra of $LiBH_4$ (-), a mixture of $LiBH_4$ and NaA (-), $(LiBH_4)_{128}$.NaA (-), and NaA dehydrated (-).

There was a change to the main framework peak at around 958 cm^{-1}, which showed a shift on occlusion to 960 cm^{-1}. A slight shoulder which was present on the main framework peak at 1140 cm^{-1} became more accentuated on occlusion and shifted to 1121 cm^{-1}. This corresponds to the region suggesting external asymmetric stretches of the zeolite. The stretch is “external” to that of the framework, suggesting that the interactions with species in the pore space give this peak its character. The inclusion of a guest material could give the peak greater intensity and a shift in position due to a change in chemical environment compared with the dehydrated zeolite, which has vacant pores. The region between 2150 and 2400 cm^{-1} containing the borohydride stretches, shows that between the mixture and the compound containing occluded $LiBH_4$ the peaks were retained but broadened into an indefinable stretch.

Figure 4.13, showing $(LiBH_4)_{64}$.NaA, gave a similar picture for the region of 2150 to 2400 cm^{-1}, the diminished peak heights in comparison to $(LiBH_4)_{128}$.NaA due to there being less borohydride present. In contrast, the zeolite peak at 960 cm^{-1} remained in the same location after loading.

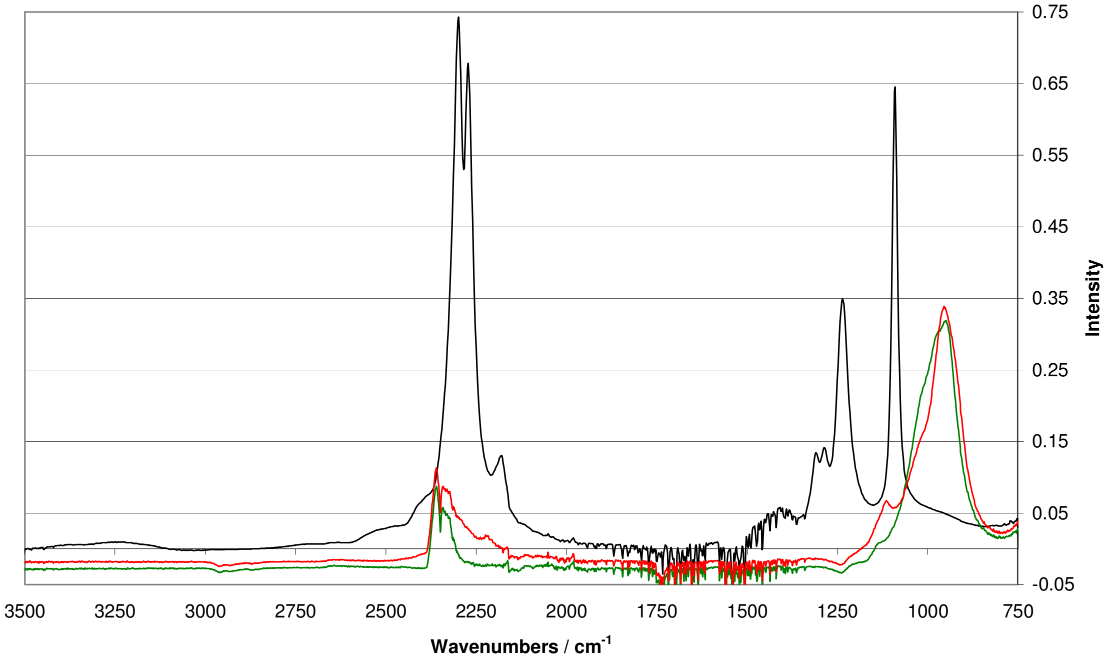

Figure 4.13 – IR spectra of $LiBH_4$ (-), $(LiBH_4)_{64}$.NaA (-), and NaA dehydrated (-).

In contrast to the Raman data there was very little change in the framework peaks. One peak at 494 cm^{-1}, which was marginally above the background increased in intensity on occlusion of lithium borohydride.

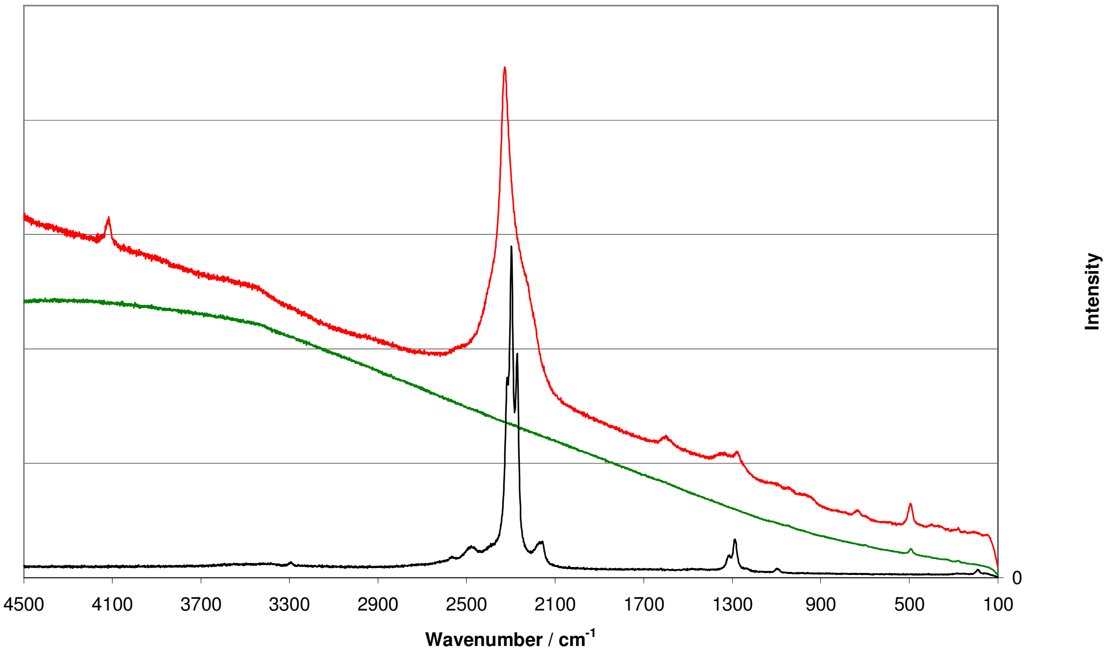

Figure 4.14 – Raman spectra of $LiBH_4$ (-), $(LiBH_4)_{128}$.NaA (-), and NaA dehydrated (-).

Another noticeable difference after reaction was that the 3 distinct peaks of lithium borohydride at 2315, 2296 and 2271 cm^{-1} became a broad feature with a dominant peak at 2325 cm^{-1}. It could be argued that with the production of sodium borohydride (figure 4.15 for the Raman spectra) that this could result from a summation of the two borohydrides. With sodium borohydride having a dominant peak at 2330 cm^{-1}, the new peak formed was between those of the lithium and sodium compounds. It is likely, however, that in a mixture some of the peaks would be resolved. It is also likely that within the zeolite the lithium borohydride is no longer in the same chemical environment as in the bulk crystalline form. Such a variation of chemical environments as offered by the zeolite pores could lead to a greater range of different environments for the borohydride, which in turn would lead to a broader signal.

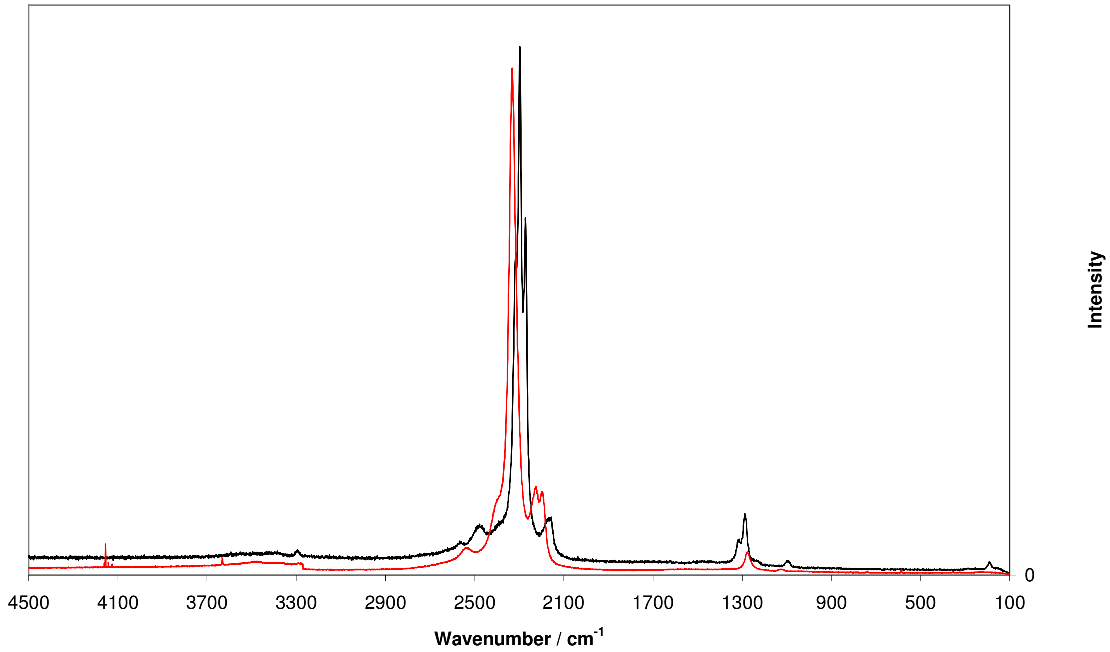

Figure 4.14 – Raman spectra of $LiBH_4$ (-) and $NaBH_4$ (-)

Similar results were observed in $(LiBH_4)_{64}$.NaA to those observed in the fully loaded $(LiBH_4)_{128}$.NaA. The framework peak at 494 cm^{-1}[24] in figure 4.16 became more noticeable on reaction. The broad borohydride feature had a peak maximum at 2328 cm^{-1}.

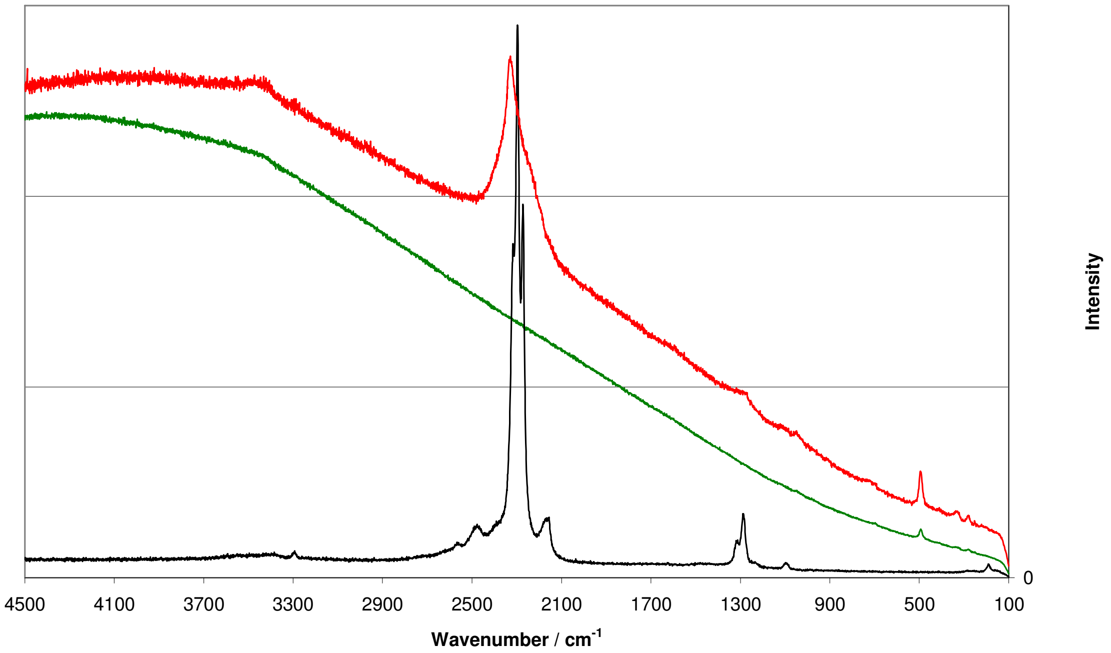

Figure 4.16 – Raman spectra of $LiBH_4$ (-), $(LiBH_4)_{64}$.NaA (-), and NaA dehydrated (-).

4.3.1.4 Microscopy

SEM images of dehydrated zeolite NaA show the regular cubic morphology expected. In $(LiBH_4)_{128}$.NaA we see that the morphology was retained, although some aggregation was observed in both cases (figure 4.17).

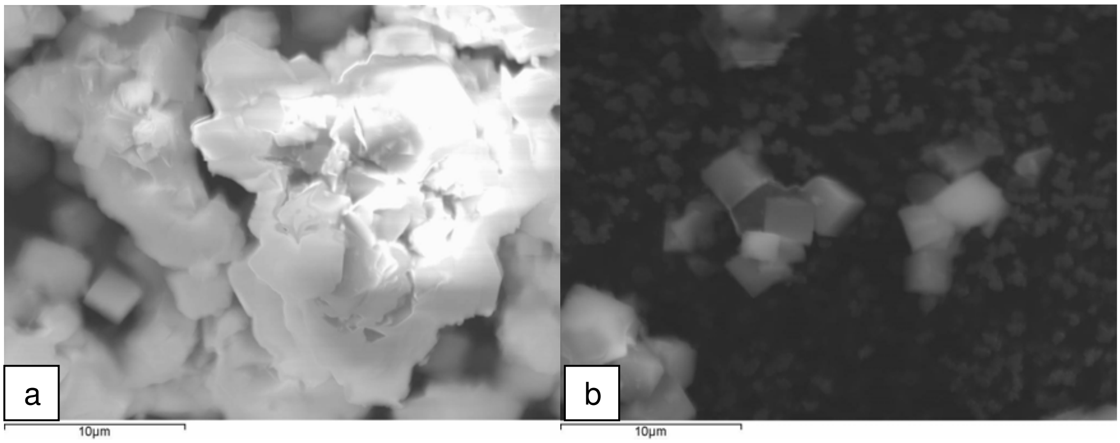

Figure 4.17 – SEM images of (a) NaA dehydrated and (b) $(LiBH_4)_{128}$.NaA

When the same analysis was performed on $(LiBH_4)_{64}$.NaA we again observed that the morphology was retained and aggregation was present, figure 4.18a and b.

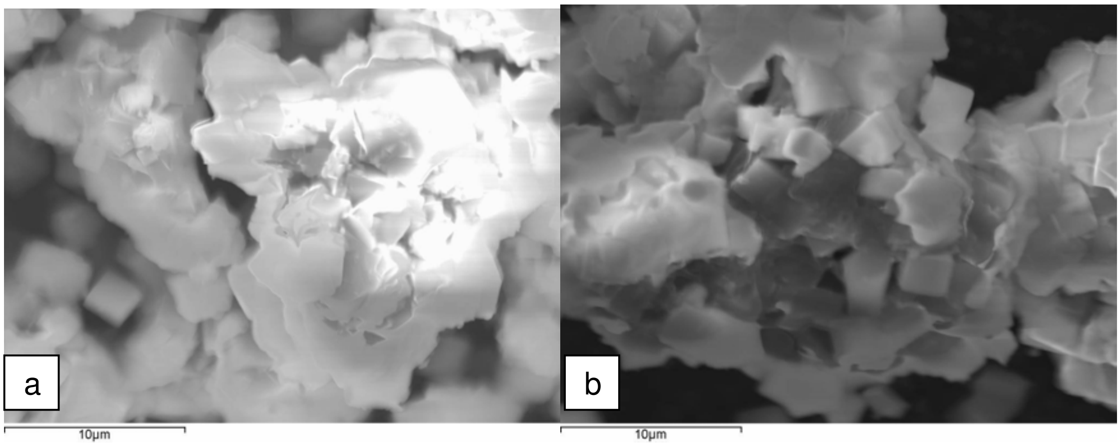

Figure 4.18 – SEM images of (a) NaA dehydrated and (b) $(LiBH_4)_{64}$.NaA

No changes occurred on occlusion suggesting that the reaction is not destructive to the zeolite.

4.3.2 NaX with Lithium Borohydride

Synthesis of NaX produced an off-white powder sample with the following indexed pattern, using the space group $Fd\overline{3}m$.

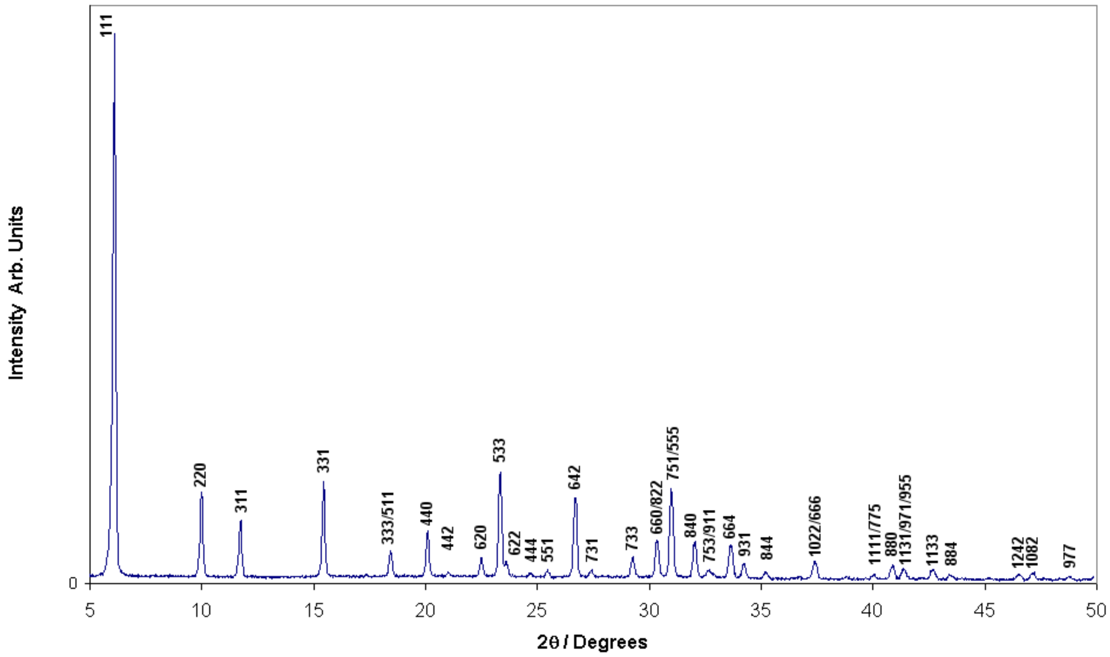

Figure 4.19 – Powder XRD pattern for NaX indexed in space group Fd-3m.

Like NaA, NaX (an off-white powder) when heated with the white crystalline lithium borohydride at 250℃, afforded an off-white sample. Again as before no pressure build up was observed under these conditions.

4.3.2.1 Powder X-ray Diffraction

On synthesis a second phase, with the same basic diffraction pattern as that of dehydrated NaX was observed but with all peaks shifted to higher 2θ, indicating a reduction in lattice parameter.

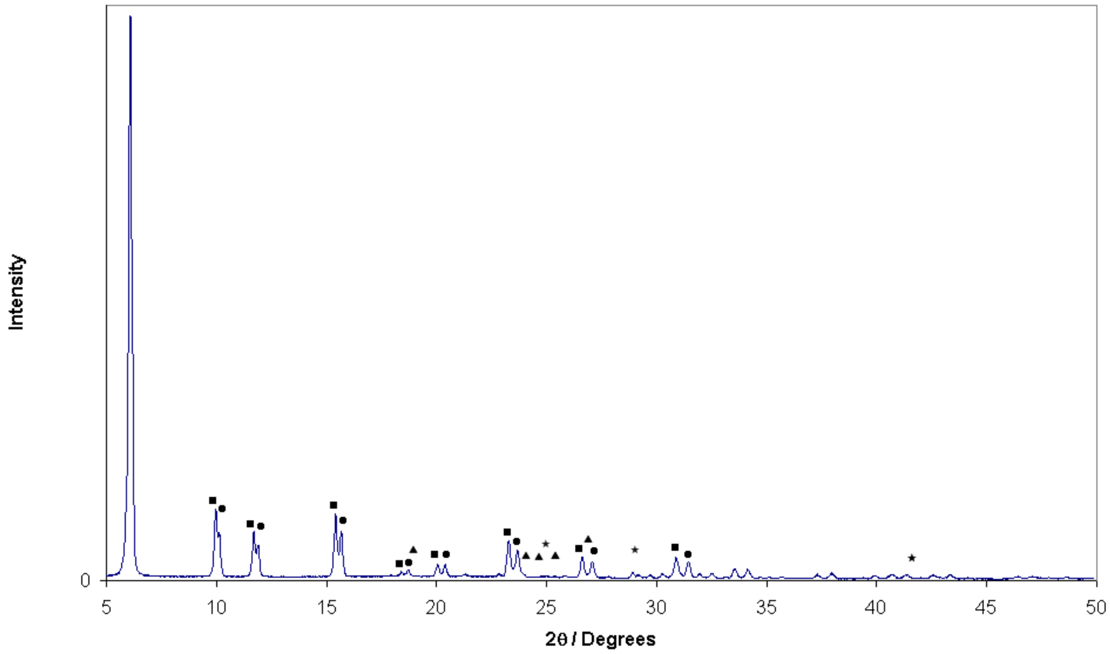

Figure 4.20 – Powder XRD Pattern showing $(LiBH_4)_{64}$.NaX after reaction at 250°C for 12 hours. (■) Dehydrated NaX; (●) "loaded" NaX; and (✱) $NaBH_4$. The position of $LiBH_4$ peaks, if present, is also marked (▲).

Figure 4.20 shows that with an increase of the loading level there was an increase in the proportion of this secondary phase suggesting, as observed with NaA, that this phase could be a "loaded" phase.

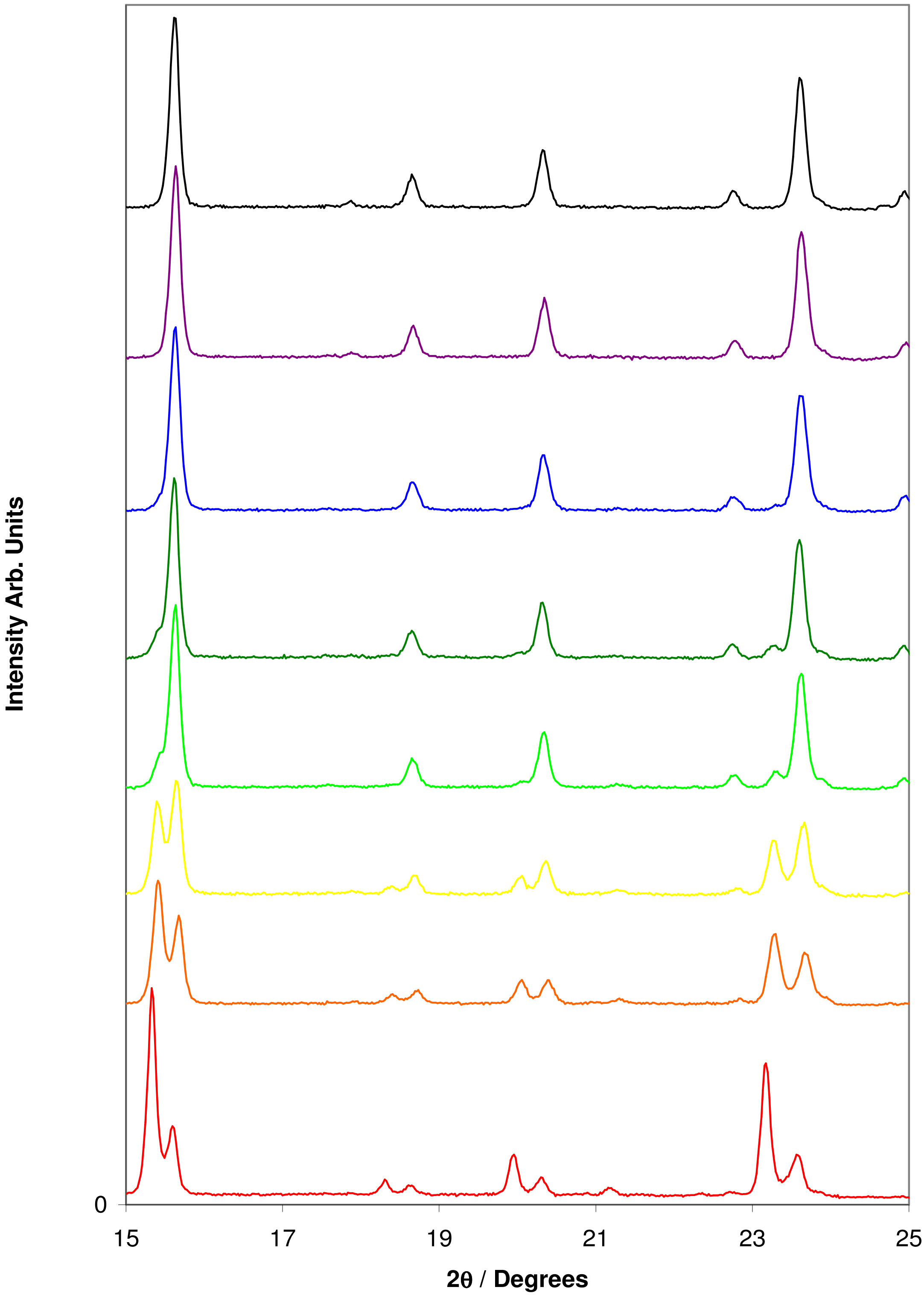

Figure 4.21 – A stacked powder XRD plot from 15 and 25º 2θ at different loadings of $(LiBH_4)_x$.NaX, where x is: (-) 32; (-) 64; (-) 96; (-) 128; (-) 160; (-) 192; (-) 224; and (-) 256.

The lattice parameters, shown in figure 4.22, of the “loaded” phase were similar within error across the composition range, with the exception of around 64 and 96 $LiBH_4$ PUC, where smaller values were observed.

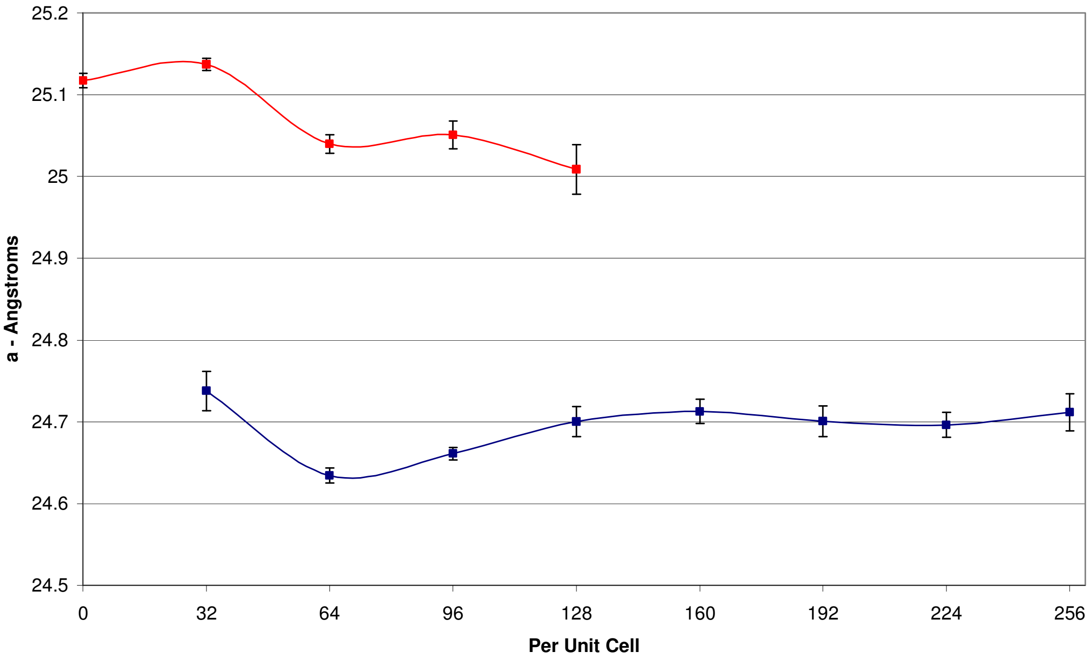

Figure 4.22 - The change in lattice parameter versus loading level for NaX with $LiBH_4$ showing the dehydrated phase (-) and "loaded" phase (-); error bars show 3ESD’s.

In contrast to NaA, the lattice parameter of the “dehydrated zeolite” or unloaded phase was not consistent but decreased at loading levels above 32 PUC. As was the case with NaA some $NaBH_4$ was observed in the diffraction pattern. The ion-exchange that is occurring may cause the lattice parameter reduction for the unloaded zeolite. Partial exchanges might tend the lattice parameter value towards that of LiX, 24.780(4) Å. This could also be caused by partial occlusion into the unloaded phase.

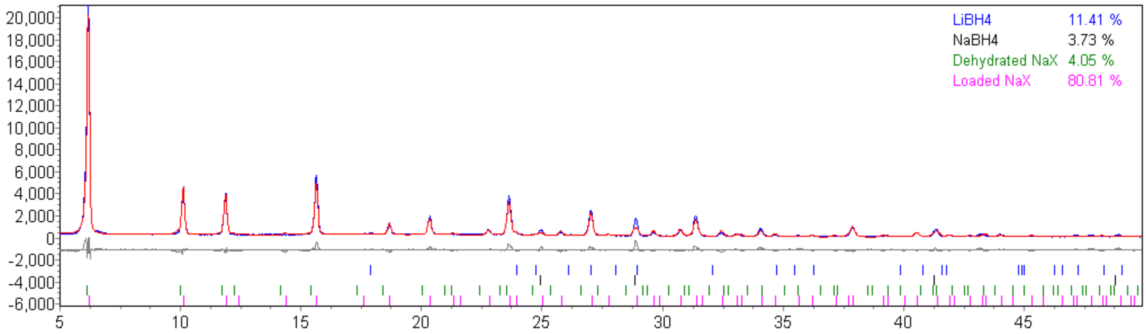

Figure 4.23 – Rietveld fit for $(LiBH_4)_{224}$.NaX. The phases fitted are the loaded and dehydrated zeolites as well as $NaBH_4$ and $LiBH_4$. (-) denotes the raw data; (-) the fitted line.

Figure 4.23 shows that $NaBH_4$ constitutes 3.73% of the diffraction pattern; this is quite low, and given a reasonable fit (Rwp 16.540) would suggest that it is unlikely much of the lithium has ion-exchanged. Removal of $NaBH_4$ from the refinement causes the R factor to increase. NaX acted as the model for one of the zeolite phases and hydrated NaX as the model for the second. As one phase was expected to contain lithium borohydride in the zeolite pores, the hydrated zeolite was used as a model to give an appropriate electron density within the pore. As $NaBH_4$ did not appear to change much in relative intensity to that of the NaX diffraction pattern across the composition range either, this may suggest that there was a degree of occlusion occurring in the unloaded zeolite, a result of the more open framework of NaX compared with NaA.

A Reitveld analysis was performed across the composition range, with the results shown in table 4.4. As the loading level of lithium borohydride is increased the phase composition shows an increase of the loaded phase, with the dehydrated phase decreasing. Lithium borohydride decreased up to $(LiBH_4)_{192}$.NaX, to then increase above this loading, the amount of sodium borohydride seemed consistent across the composition range.

	Percentage composition in Reitveld analysis				
Occupancy / PUC	% Loaded Phase	% Dehydrated Phase	% $LiBH_4$	%$NaBH_4$	Rwp
32	57.98	36.06	0	5.95	17.834
64	51.39	33.86	8.95	5.8	16.223
96	52.46	26.57	16.63	4.34	14.122
128	59.74	20.59	7.84	11.83	14.598
160	72.03	17.95	0.01	10.02	11.262
192	82.97	4.6	0.99	11.44	11.692
224	80.81	4.05	11.41	3.73	16.54
256	78.67	3.53	11.73	6.07	15.81

Table 4.4 – Reitveld composition data for different concentrations of $LiBH_4$ with NaX.

As the loading was increased it became apparent above $(LiBH_4)_{224}$.NaX that $LiBH_4$ was reappearing noticeably in the diffraction pattern, suggesting that this could be the effective maximum loading. $(LiBH_4)_{96}$.NaX was used as an approximate “half-loaded” zeolite NaX for the purpose of comparison when observing adsorption and desorption effects.

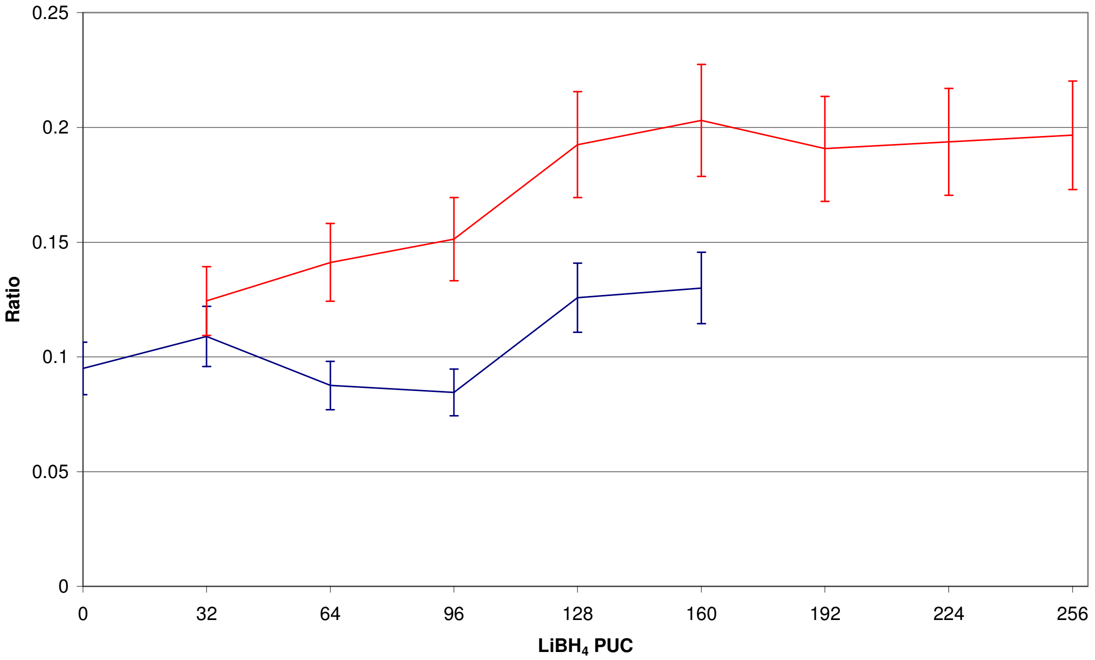

Figure 4.24 – The change in ratio of the 311 to the 111 peak over the composition range of $LiBH_4$ PUC of NaX: (-) the dehydrated zeolite phase; (-) the loaded phase.

Figures 4.24 and 4.25 show the variation of relative intensities as the loading was changed. As with NaA, a change in relative intensities of the "loaded" zeolite peaks with increased loading is an indication of increasing amounts of occluded material within the zeolite.

Noticeably both loaded and unloaded phases showed variation in the relative intensities. The change in the unloaded phase may again be an indication of ion-exchange. In general, distinct ratios were observed for the loaded and dehydrated zeolites. The change in electron density within the zeolite is further evidenced by the appearance of higher 2θ peaks in the powder XRD pattern, which were not readily visible in the parent zeolite. The unloaded ratio could be changing due to slight occlusion.

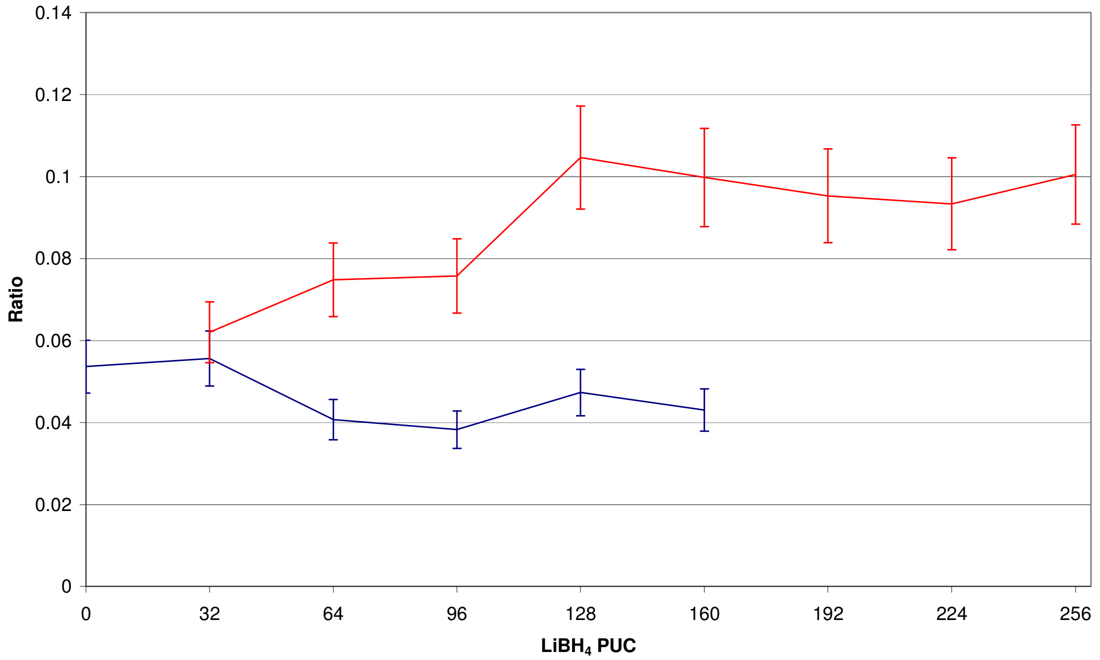

Figure 4.25 – The change in ratio of the 555 to the 111 peak over the composition range of $LiBH_4$ PUC of NaX: (-) the dehydrated zeolite phase; (-) the loaded phase.

4.3.2.2 Vibrational Spectroscopy

Spectroscopic methods again were used to monitor the changes to $LiBH_4$ on occlusion.

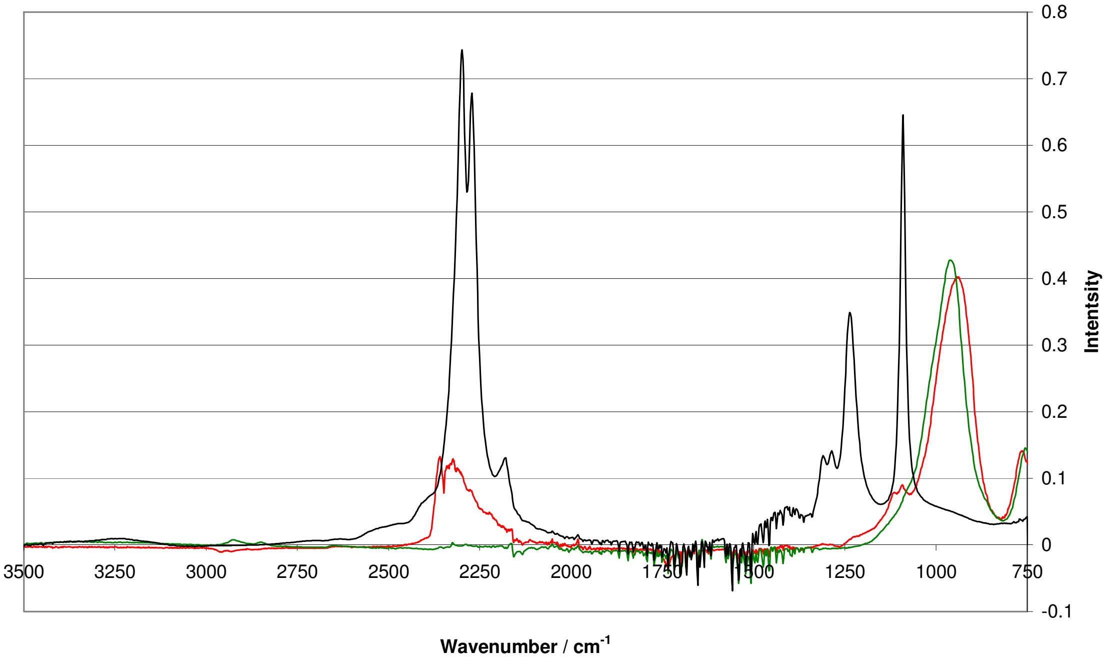

Figure 4.26 – IR spectra of $LiBH_4$(-), $(LiBH_4)_{224}$.NaX (-), and NaX dehydrated (-).

Figure 4.26 shows the IR spectrum of $(LiBH_4)_{224}$.NaX. The borohydride stretches at 2300 cm^{-1} and 2271 cm^{-1} appeared to be partially masked by atmospheric CO_2, although the FTIR was flushed with nitrogen.

Again the framework peaks were broader and appeared to be shifted slightly, the peak maxima being 945 and 966 cm^{-1}, for the loaded and dehydrated zeolite respectively. Two new peaks appeared on loading of $(LiBH_4)_{224}$.NaX as shoulders on the main zeolite peak: one at 1128 cm^{-1}, which is a zeolite vibration associated with framework interactions with pore species. The other noticeable peak was that at 1098 cm^{-1}, which matches the ν_4 of lithium borohydride.

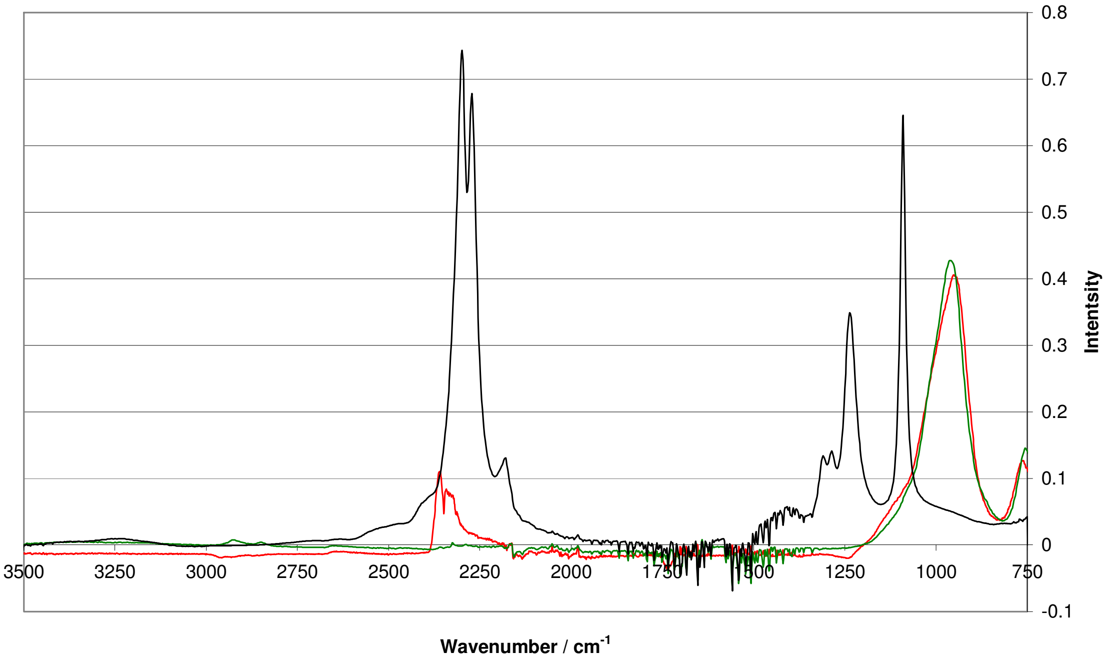

Figure 4.27 – IR spectra of $LiBH_4$ (-), $(LiBH_4)_{96}$.NaX (-), and NaX dehydrated (-).

The spectrum of $(LiBH_4)_{96}$.NaX (figure 4.27) showed the same initial shift upon occlusion from 966 to 945 cm^{-1} of the framework peak. The borohydride stretches at 2300 cm^{-1} and 2271 cm^{-1} were affected by atmospheric CO_2, as with $(LiBH_4)_{224}$.NaX. Noticeably there were no shoulder peaks at ~1100 cm^{-1}.

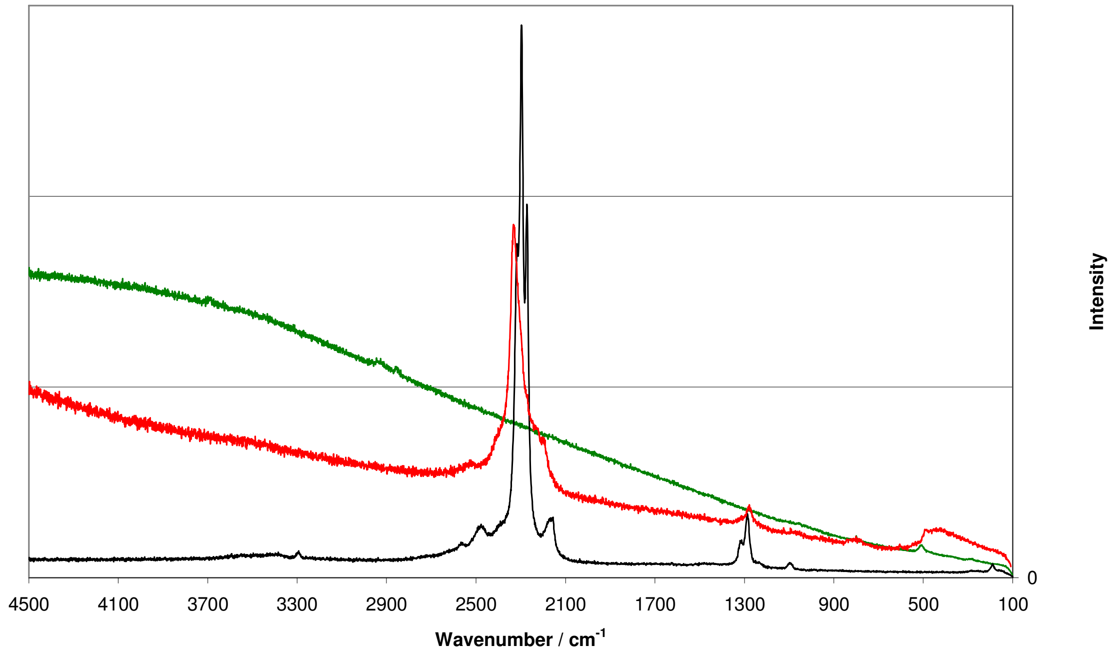

Figure 4.28 – Raman spectra of $LiBH_4$ (-), $(LiBH_4)_{224}$.NaX (-) and NaX dehydrated (-).

Raman spectroscopy has been shown to provide better spectra of the borohydride stretching area than IR, and for $(LiBH_4)_{224}$.NaX a broadening of the main stretch at 2300 cm^{-1} was seen in figure 4.28, with the peak maximum being 2327 cm^{-1}. A single framework peak at 500 cm^{-1} was shown to be more pronounced but broader after occlusion, in $(LiBH_4)_{224}$.NaX.

In $(LiBH_4)_{96}$.NaX (Figure 4.29) the borohydride stretches show two broader peaks at 2323 and 2265 cm^{-1}. The intensity of the framework peak was much increased with a large shift to 542 cm^{-1}. The observation of this peak, present even though the Raman spectra of dehydrated zeolites are generally featureless, is strong evidence that material was incorporated into the zeolite pores.

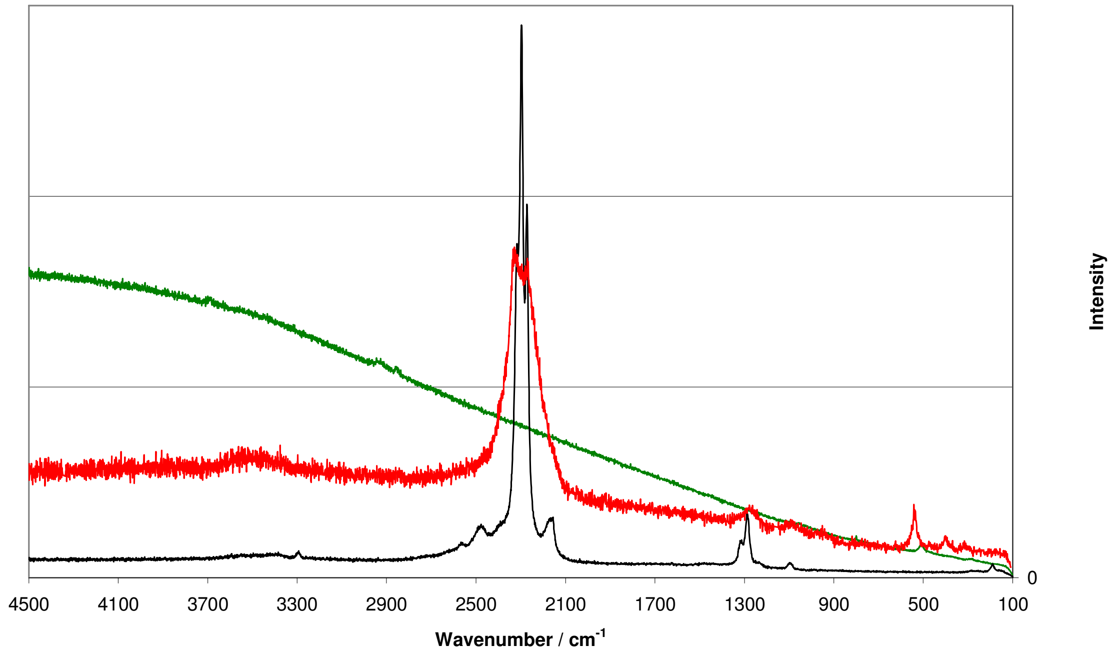

Figure 4.29 – Raman spectra of $LiBH_4$ (-), $(LiBH_4)_{96}$.NaX (-) and NaX dehydrated (-).

4.3.2.3 Microscopy

On analysis of SEM images of $(LiBH_4)_{224}$.NaX, it was observed that the octahedral morphology of the crystals was retained on occlusion, figure 4.30a and b. The crystals were all well ordered and of a fairly uniform size. Though some material was coating the surface, this may be $LiBH_4$ or $NaBH_4$.

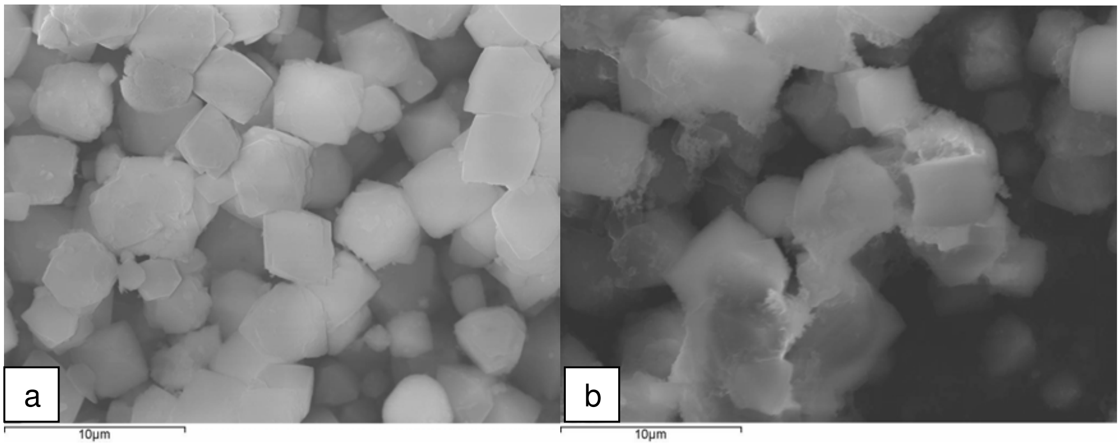

Figure 4.30 – SEM images of (a) NaX dehydrated and (b) $(LiBH_4)_{224}$.NaX

On analysis of $(LiBH_4)_{96}$.NaX, figure 4.31b, we observed again the regular octahedral morphologies which appeared to be retained on occlusion.

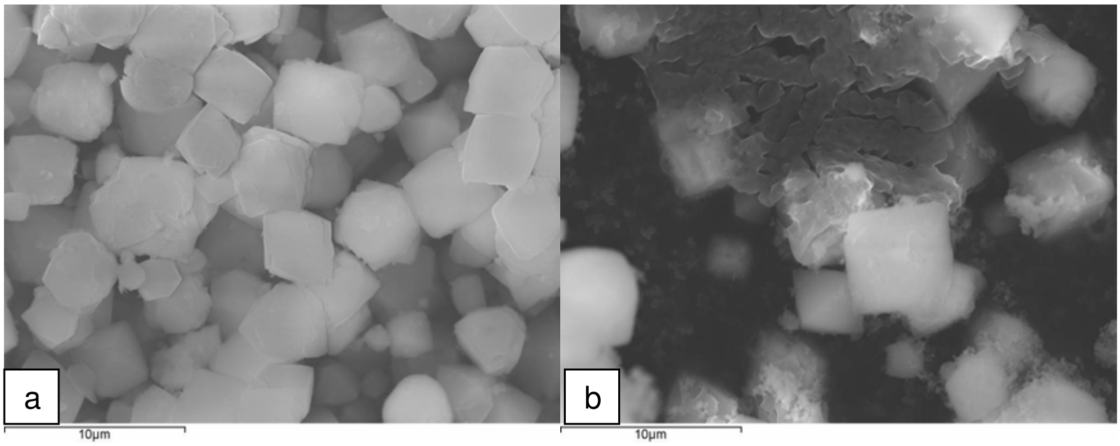

Figure 4.31 – SEM images of (a) NaX dehydrated and (b) $(LiBH_4)_{96}$.NaX.

4.3.3 NaY with Lithium Borohydride

NaY was obtained from Sigma-Aldrich, as a white powder. A powder XRD pattern was recorded and indexed in space group $Fd\bar{3}m$.

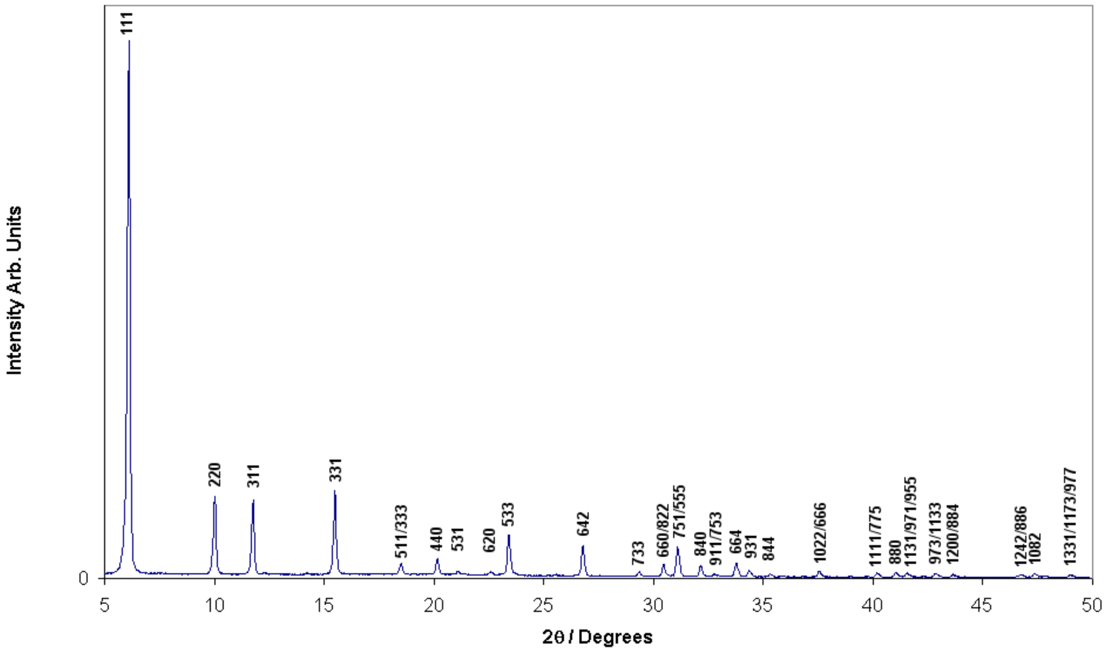

Figure 4.32 – Powder XRD pattern for NaY indexed in space group Fd-3m.

As with the previous zeolites the reaction of NaY (an off-white powder) with the white crystalline lithium borohydride at 250°C afforded an off-white sample. Again as before no pressure build up was observed under these conditions and preparations at different loadings were carried out.

4.3.3.1 Powder X-ray Diffraction

On reaction, as with the other zeolites in this chapter, a second phase at higher 2θ with the same diffraction pattern as the parent zeolite was observed.

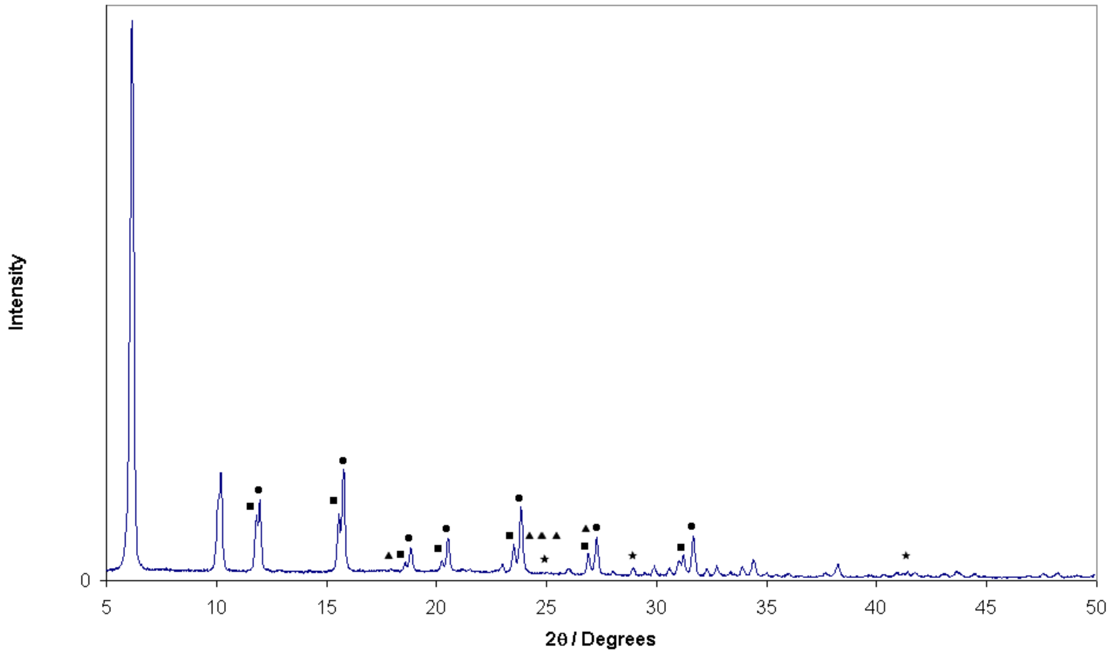

Figure 4.33 – XRD Pattern showing $(LiBH_4)_{96}$.NaY after reaction at 250℃ for 12 hours. (■) Dehydrated NaY; (●) "loaded" NaY; (▲) location for $LiBH_4$ and (✱) $NaBH_4$.

The amount of second phase present was dependent on the concentration of $LiBH_4$, suggesting it was a "loaded" phase.

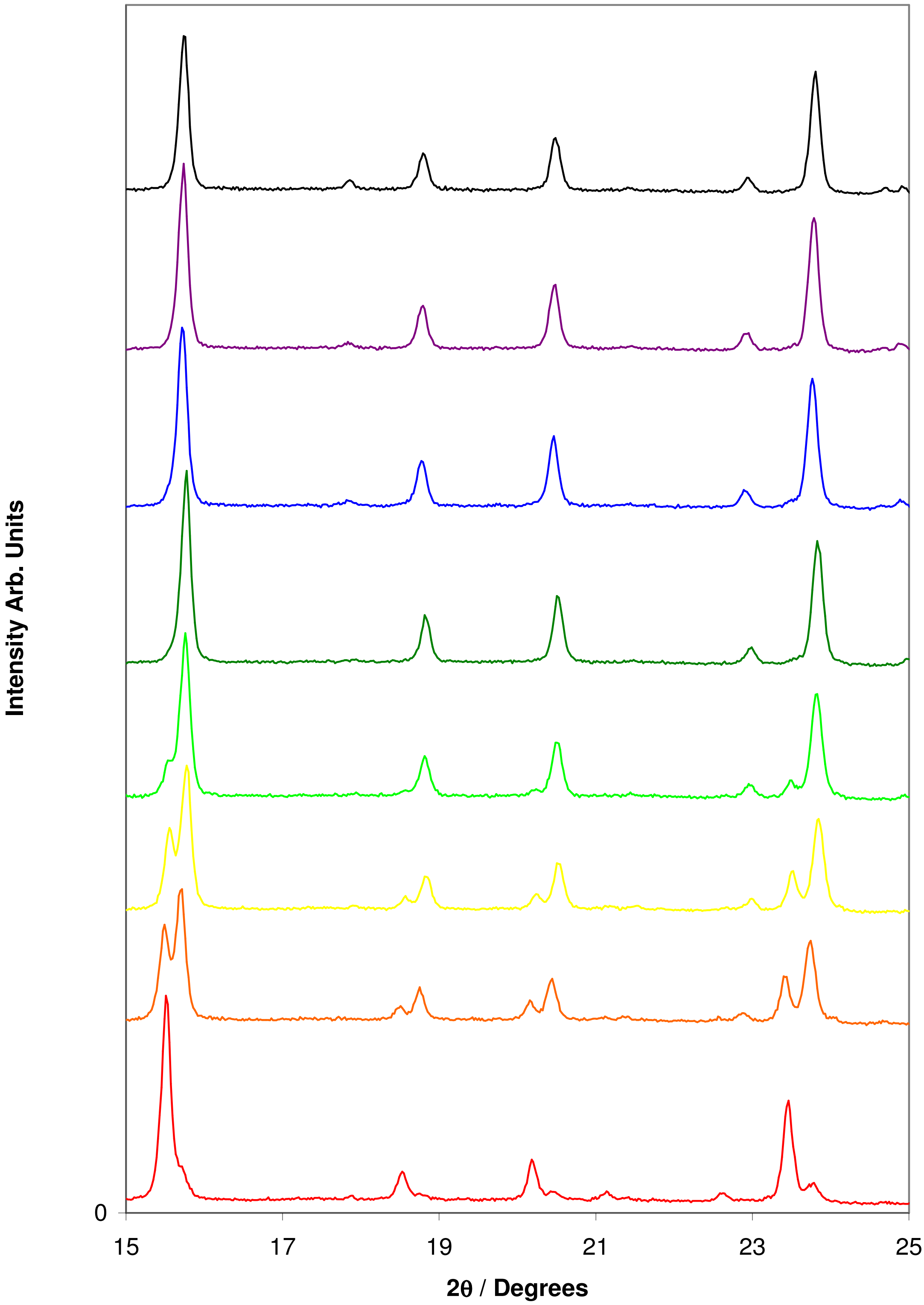

Figure 4.34 – A stacked powder XRD plot from 15 and 25º 2θ at different loadings of $(LiBH_4)_x$.NaA, where x is: (-) 32; (-) 64; (-) 96; (-) 128; (-) 160; (-) 192; (-) 224; and (-) 256.

Where two zeolite phases were present the lattice parameters were distinct, with the larger lattice parameter corresponding well with that of dehydrated NaY.

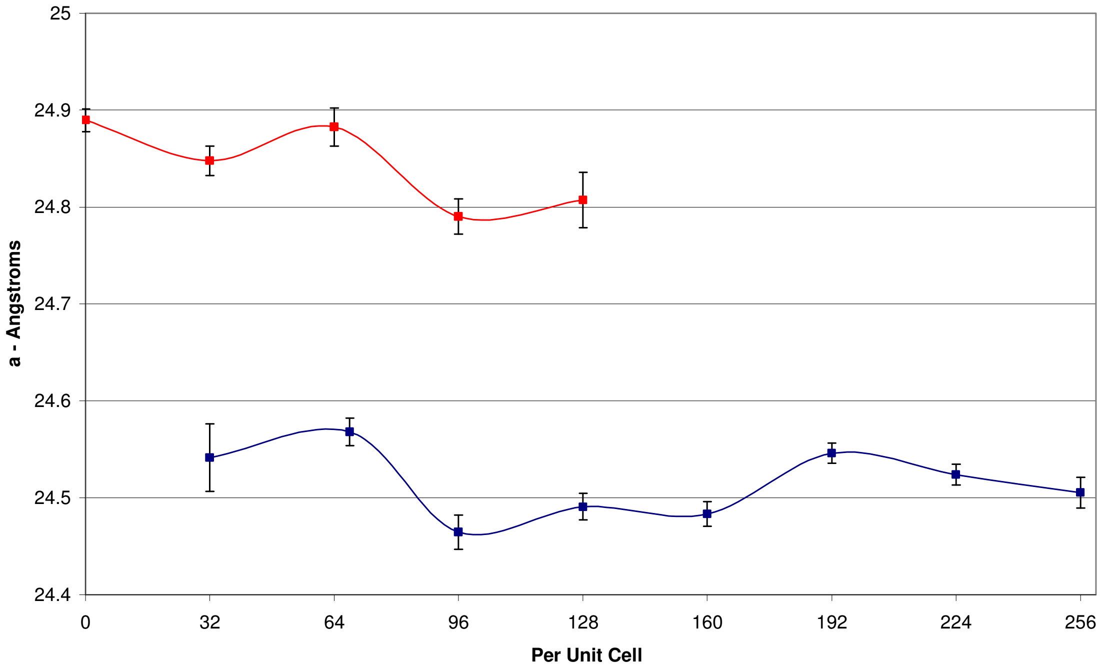

Figure 4.35 - The change in lattice parameter for NaY with concentration of $LiBH_4$ showing the “dehydrated” phase (-) and "loaded" phase (-); error bars show 3ESD’s.

The lattice parameter, shown in figure 4.35, of the “loaded phase” had a similar value with only slight variation over the composition range. The “dehydrated” phase was not constant with composition change, which could indicate either ion exchange or partial occlusion. This could suggest that sodium borohydride was also present, but was not as prevalent as in the case of the other zeolites. At loadings above $(LiBH_4)_{192}$.NaY it was observed that substantial amounts of lithium borohydride reappeared in the XRD pattern.

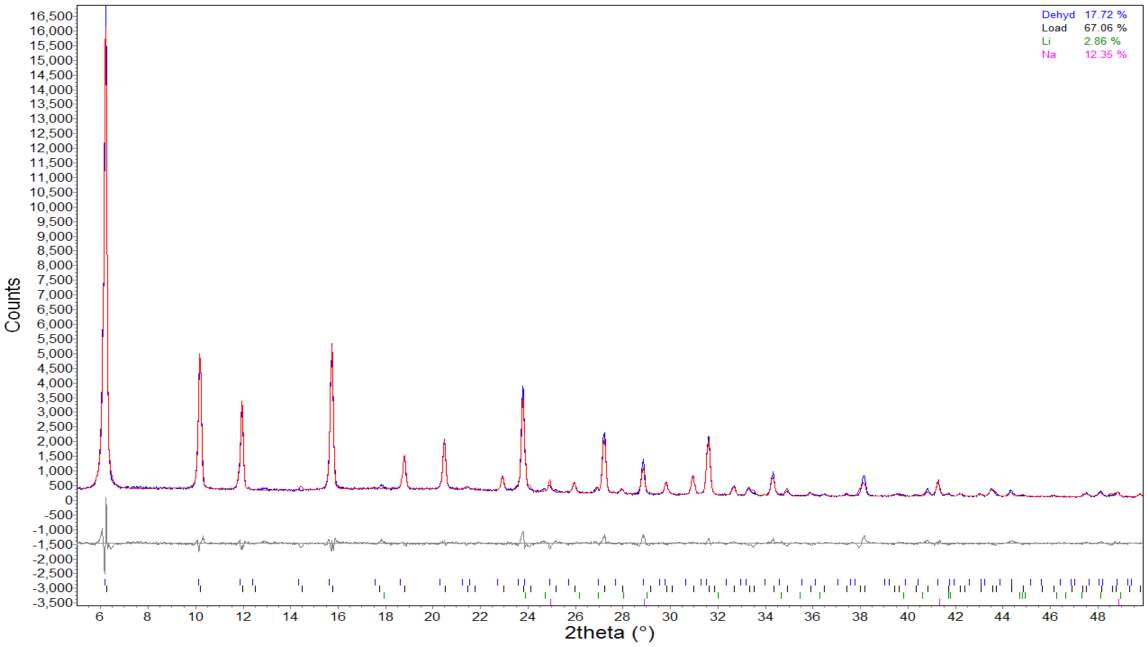

Figure 4.36 – Rietveld fit for $(LiBH_4)_{128}$.NaY. The phases fitted are the loaded and dehydrated zeolite as well as $NaBH_4$ and $LiBH_4$. (-) denotes the raw data; (-) the fitted line.

The phase fraction of sodium borohydride present in the pattern of $(LiBH_4)_{128}$.NaY was 12.35%. NaY acted as the model for one of the zeolite phases and hydrated NaY as the model for the second. As one phase was expected to contain lithium borohydride in the zeolite pores, the hydrated zeolite was used as a model to give an appropriate electron density within the pore. This would suggest a loading of around 3.97 wt% hydrogen in the host–guest material, given the amount of ion-exchange observed.

A Reitveld analysis was performed across the composition range, with the results shown in table 4.5. Again the loaded phase replaced the dehydrated phase as the concentration on lithium borohydride increased. Lithium borohydride was constant up to $(LiBH_4)_{192}$.NaY, above which it appeared to increase. Sodium borohydride appeared constant across the composition range.

	Percentage composition in Reitveld analysis				
Occupancy / PUC	% Loaded Phase	% Dehydrated Phase	% $LiBH_4$	%$NaBH_4$	Rwp
32	11.78	77.2	8.92	2.1	15.828
64	46.13	40.25	12.11	1.51	9.89
96	56.63	26.95	12.77	3.64	9.61
128	61.01	24.7	8.1	6.18	9.345
160	73.22	11.39	6.9	8.49	9.845
192	67.99	8.21	17.37	6.42	11.24
224	67.06	17.72	2.86	12.35	9.64
256	57.23	3.6	34.73	4.45	9.729

Table 4.5 – Reitveld composition data for different concentrations of $LiBH_4$ with NaY.

Another change on loading was the relative intensities of the peaks. This was most simply illustrated with the observation of higher intensity diffraction peaks at higher angle in the reacted sample powder XRDs, such as figure 4.33.

The values for selected relative peak intensities are shown in figures 4.37 and 4.38. Ratios for the dehydrated phase appeared constant across the loading range, whilst increased loading caused changes to the relative intensities of the loaded phase, although at low loadings the values were similar to those of the unloaded phase.

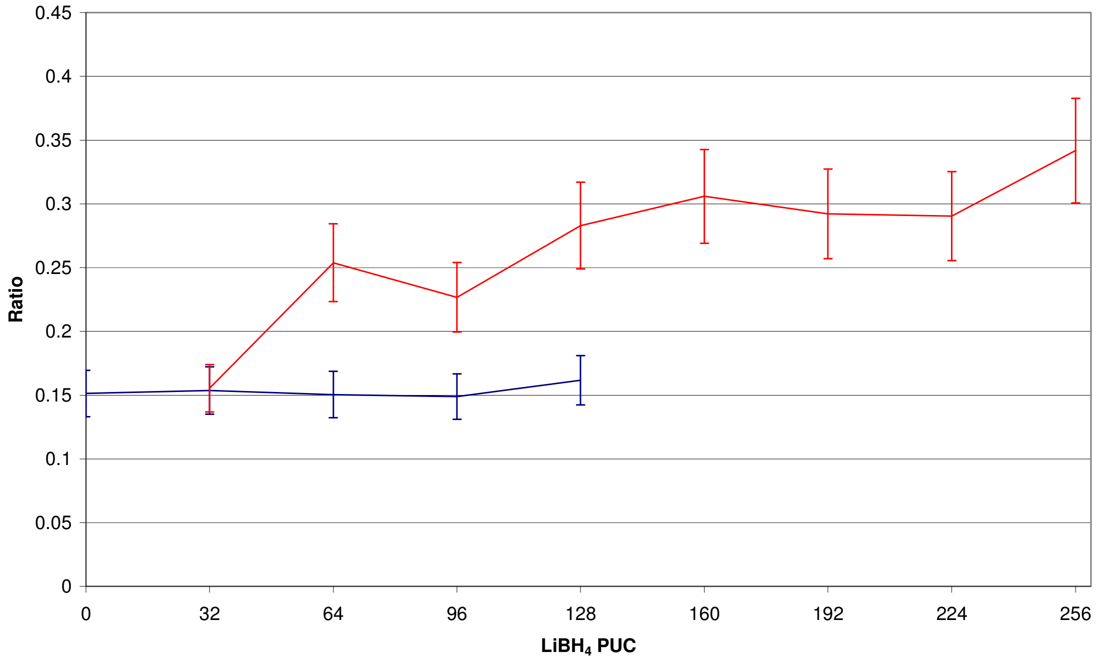

Figure 4.37 – The ratio of the intensities of the 220 to the 111 peaks over the composition range of $LiBH_4$ in NaY: (-) the dehydrated zeolite phase; (-) the loaded phase.

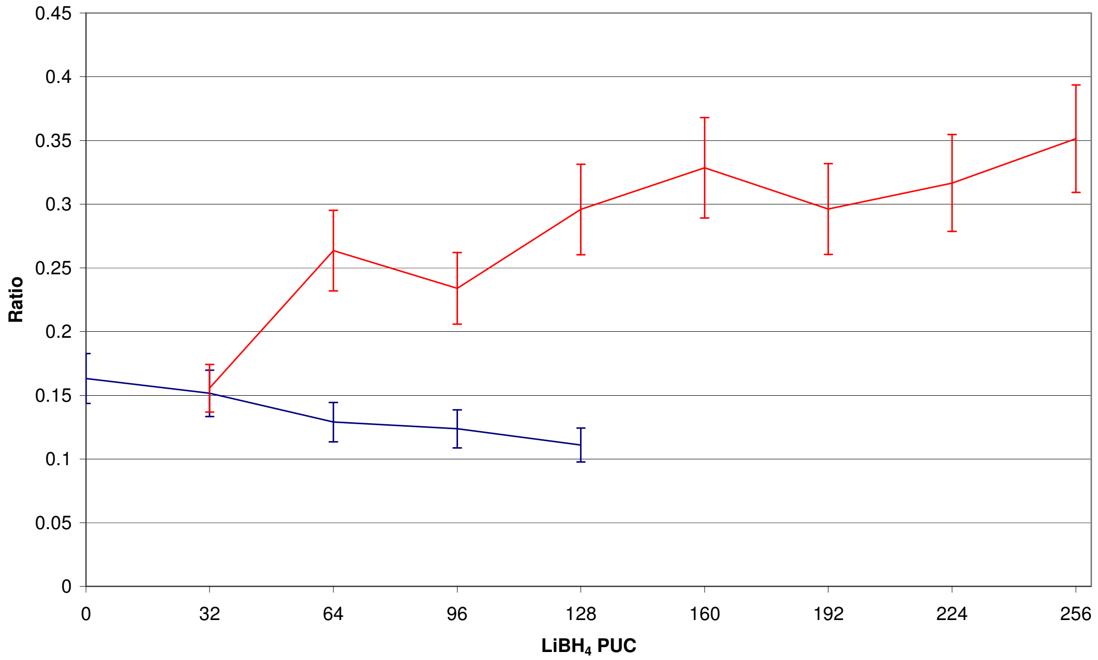

Figure 4.38 – The ratio of the intensities of the 331 to the 111 peaks over the composition range of $LiBH_4$ in NaY: (-) the dehydrated zeolite phase; (-) the loaded phase.

4.3.3.2 Vibrational Spectroscopy

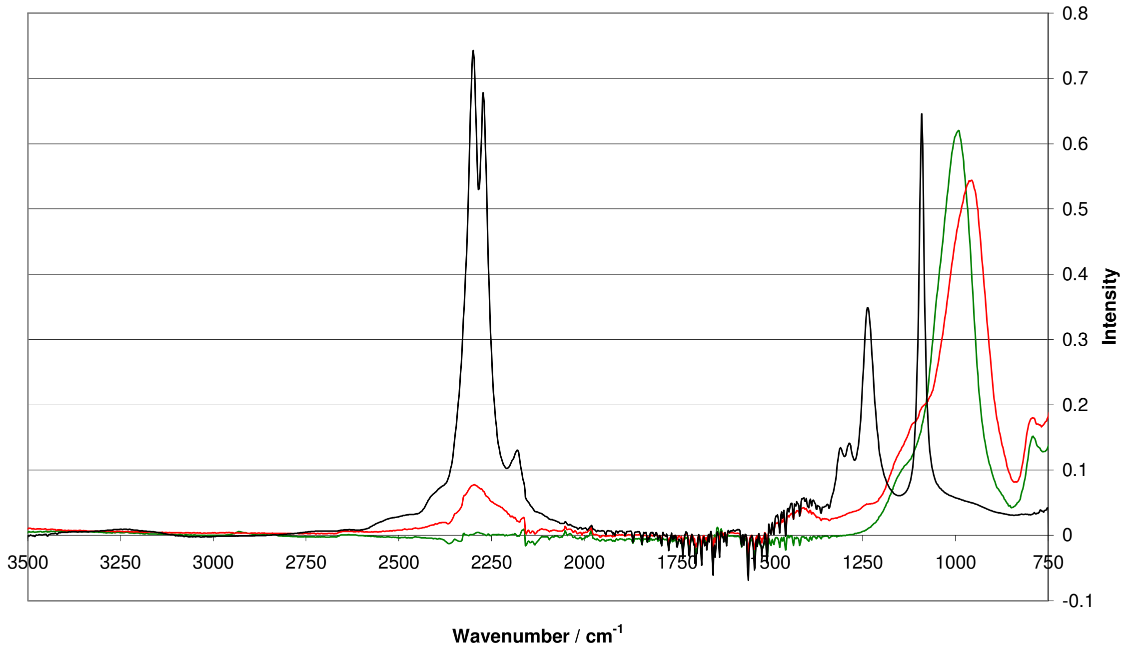

Figure 4.39 – IR spectra of $LiBH_4$ (-), $(LiBH_4)_{192}$.NaY (-), and dehydrated NaY (-).

Figure 4.39 shows IR spectra of $(LiBH_4)_{192}$.NaY before and after reaction. Again a change was observed in the framework peak at 999 cm^{-1} of the dehydrated zeolite, which was shifted to 966 cm^{-1} and broadened. There was also a broad borohydride feature peaking at 2310 cm^{-1}.

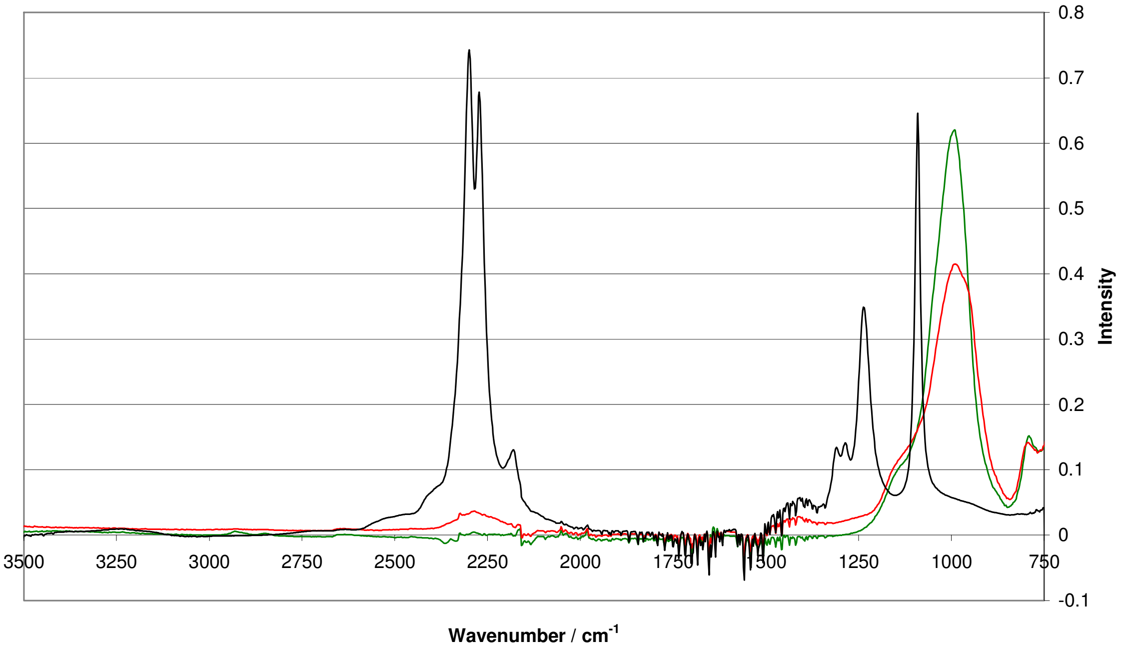

Figure 4.40 – Showing IR spectra of $LiBH_4$ (-), $(LiBH_4)_{96}$.NaY (-) and dehydrated NaY (-).

$(LiBH_4)_{96}$.NaY showed a similar set of effects in figure 4.40. The feature at 2300 cm^{-1} was caused by the occlusion of borohydride. A shift occurred on occlusion to 991 cm^{-1} from 999 cm^{-1} in the main dehydrated zeolite band.

The Raman spectra (Figures 4.41 & 4.42) of the zeolite Y samples were in agreement with those of the other zeolites, with the borohydride feature broadened on occlusion. Similarly there were no features on the dehydrated zeolite spectrum, but on occlusion a weak peak was obtained in the region of 495 cm^{-1}, which is a zeolite framework stretch, providing evidence of loading. The main borohydride peak was at 2325 cm^{-1}, again close to the value expected for sodium borohydride.

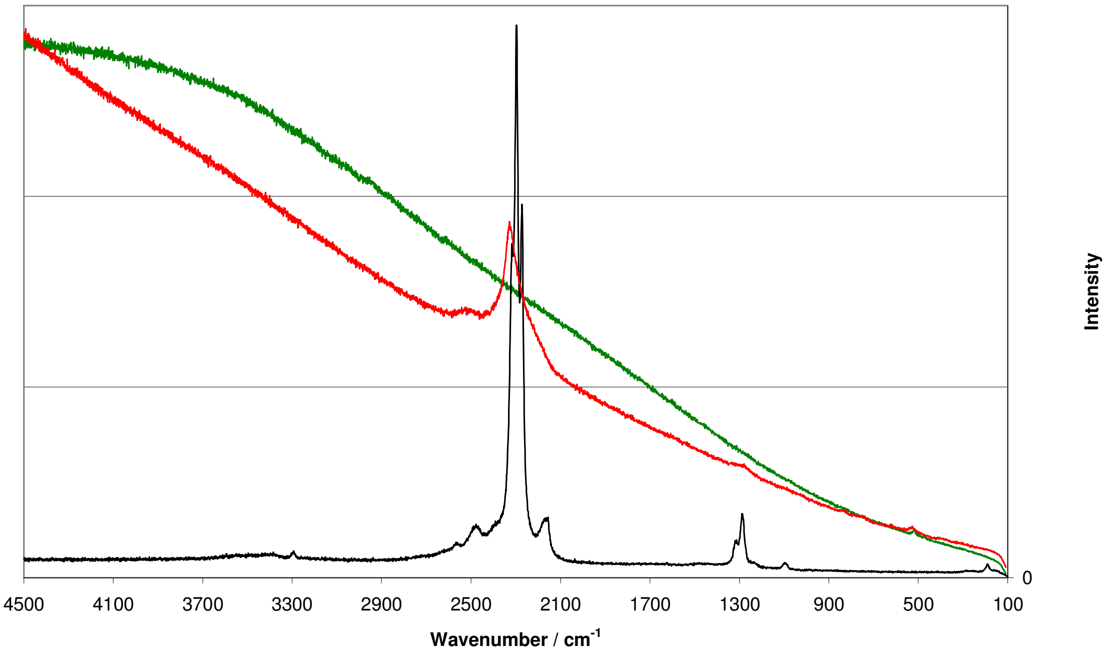

Figure 4.41 – Raman spectra of $LiBH_4$ (-), $(LiBH_4)_{192}$.NaY (-) and dehydrated NaY (-).

The $(LiBH_4)_{96}$.NaY sample in contrast to the all the other samples showed only a small broad feature at 2300 cm^{-1}. The 495 cm^{-1} framework peak was also more pronounced on occlusion.

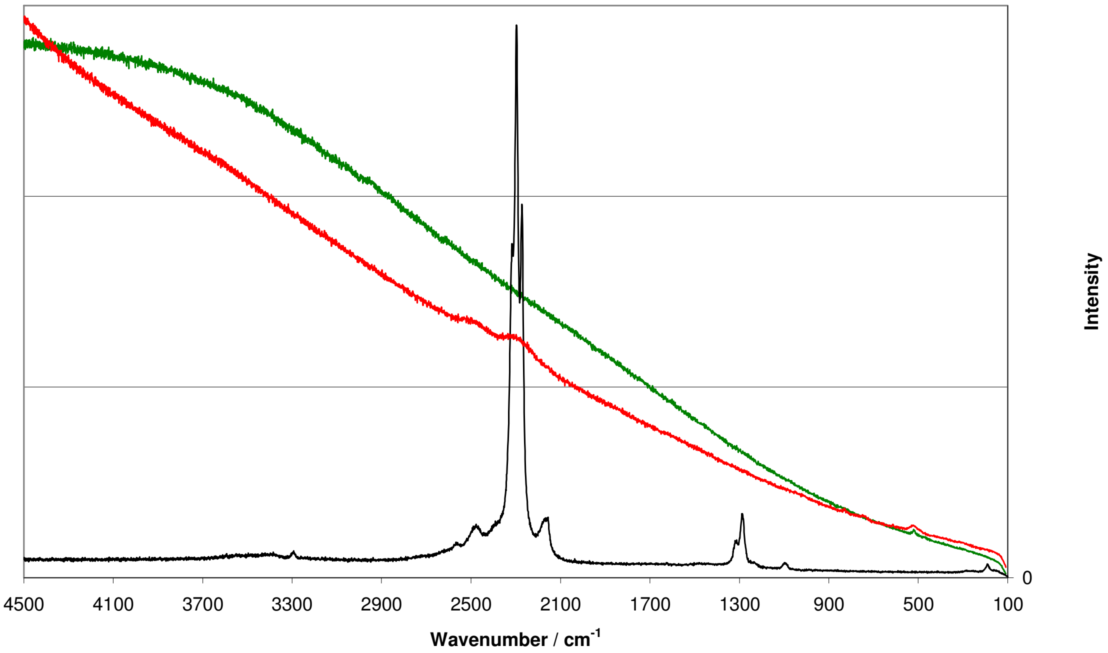

Figure 4.42 – Raman spectra of $LiBH_4$ (-), $(LiBH_4)_{96}$.NaY (-) and NaY dehydrated (-).

4.3.3.3 Microscopy

SEM images (Figure 4.43) showed fine octahedral particles as expected from a faujasite-type zeolite, with very fine particles of approximately one micron.

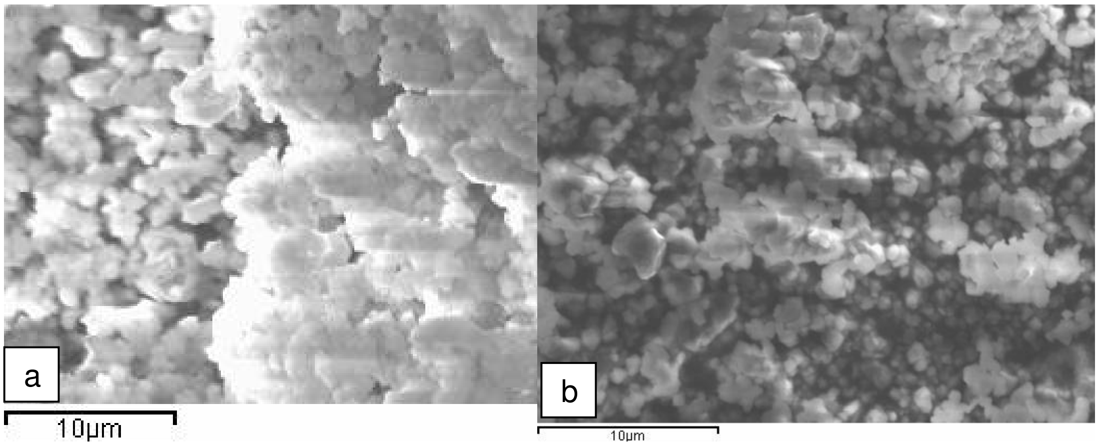

Figure 4.43 –SEM images of (a) NaY dehydrated and (b) $(LiBH_4)_{192}$.NaY.

For the fully loaded samples occlusion appears to have left the morphologies unaltered. The small particle size makes it uncertain whether material has aggregated on the surface.

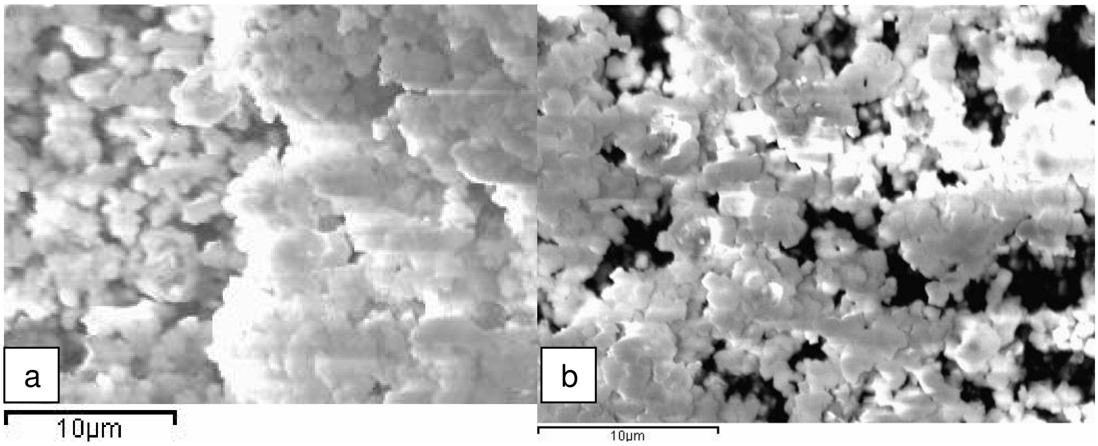

Figure 4.44 –SEM images of (a) NaY dehydrated and (b) $(LiBH_4)_{96}$.NaY.

Analysis of the half loaded sample $(LiBH_4)_{96}$.NaY showed similar results in figure 4.44, the morphologies appear retained on occlusion.

4.4 Conclusion

Lithium borohydride has successfully been incorporated into zeolites NaA, NaX and NaY. In all three cases the reactions initially resulted in two phases that could be indentified as loaded and unloaded.

NaX and NaY share the same framework type, and the same pore volume. NaY appears to occlude more lithium borohydride. This may be due to the difference in framework composition.

The effect of loading on the zeolite framework was apparent in IR spectra, which showed a shift and broadening in the framework peaks on loading. Raman spectra, on the other hand, showed a broadening of the borohydride stretches and a noticeable increase in the intensity of the zeolite's external asymmetric framework stretch, as a result of interaction with the cage contents.

SEM analysis showed that the morphologies of the host crystals remained largely unchanged during the loading.

Analysis of sample densities in the case of NaA showed that the change in density relative to the level of loading can give a more accurate estimate of the loading limit.

4.5 References

1. Fichtner M., *Adv. Eng. Mater.*, **2005**, 7, 443
2. Vajo J. J., Olson G. L., *Scripta Materialia*, **2007**, 56, 829
3. Suzuki Y., Haraki T., Uchida H., *J. Alloys Comp.*, **2002**, 330-332, 488
4. Fichtner M., *Nanotechnology*, **2009**, 20, 204009
5. Bormann R., Barkhordarian G., Eigen N., Dornheim M., *Adv. Eng. Mater.*, **2006**, 8, 377
6. Kim K. C., Dai B., Johnson J. K., Sholl D. S., *Nanotechnology*, **2009**, 20, 204001
7. Fujii H., Orimo S.-I., *Physica B*, **2003**, 328, 77
8. Gross A. F., Vajo J. J., Van Atta S. L., Olson G. L., *J. Phys. Chem. C*, **2008**, 112, 5651
9. Fichtner M, Zhao-Karger Z., Hu J., Roth A., Weilder., *Nanotechnology*, **2009**, 20, 204029
10. Gross A.F., Ahn C. C., Vajo J. J., Van Atta S. L., Liu P., *Nanotechnology*, **2009**, 20, 204005
11. Stephens R. D., Gross A. F., Vajo J. J., Van Atta S. L., Pinkerton F. E., *Nanotechnology*, **2009**, 20, 204018

12. Wu H., Zhou W., Wang K., Udovic T. J., Rush J. J., Yildirim T., Bendersky L. A., Gross A. F., Vajo J. J., Van Atta S. L., Pinkerton F. E., Meyer M. S., *Nanotechnology*, **2009**, 20, 204002
13. Zhang Y., Zhang W.-S., Wang A.-Q., Sun L.-X., Fan M.-Q., Chu H.-L., Sun J.-C., Zhang T., *Int. J. Hydrogen Energy*, **2007**, 32, 3976
14. Gutowska A., Li L., Shin Y., Wang C. M., Li X. S., Linehan J. C., Smith R. S., Kay B. D., Schmid B., Shaw W., Gutowski M., Autrey T., *Angew. Chem. Int. Ed.*, **2005**, 44, 3578
15. Feaver A., Sepehri A., Shamberger P., Stowe A., Autrey T., Cao G., *J. Phys. Chem. B.*, **2007**, 111, 7469
16. Weber J., Singhal R., Zekri S., Kumar A., *Int. Mater. Rev.*, **2008**, 53, 235
17. Buhl J.-Ch., Gesing Th. M., Rüscher C. H., *Micropor. Mesopor. Mater.*, **2005**, 80, 57
18. Olson D. H., *J. Phys. Chem.*, **1970**, 74, 2758
19. Breck D. W., Reed T. B., *J. Am. Chem. Soc.*, **1956**, 78, 5972
20. Baerlocher Ch., Meier W. M., Olson D. H., *Atlas of Zeolite Framework Types*, **2001**
21. Züttel A., Rentsch S., Fisher P., Wenger P., Sudan P., Mauron Ph., Emmenegger Ch., *J. Alloys Comp.*, **2003**, 356-357, 515
22. Breck D. W., Eversole W. G., Milton R. M., Reed T. B., Thomas T. L., *J. Am. Chem. Soc.*, **1956**, 78, 5963
23. Harvey K. B., McQuaker N. R., *Canadian J. Chem.*, **1971**, 49, 3282
24. Gomes S., Hagemann H., Yvon K., *J. Alloys Comp.*, **2002**, 346, 206
25. No K. T., Seo B. H., Jhon M. S., *Theor. Chim. Acta*, **1989**, 75, 307
26. Auerbach S. M., Carrado K. A., Dutta P. K., *Handbook of Zeolite Science and Technology*, **2003**.

CHAPTER 5
THERMAL DESORPTION OF SODIUM ZEOLITES A, X & Y, CONTAINING LITHIUM BOROHYDRIDE.

5.1 Introduction

Chapter 4 demonstrated the successful loading of lithium borohydride into zeolites NaA, NaX and NaY. Here we explore the desorption of lithium borohydride after its incorporation into the zeolite, and the physisorption properties of the composite $LiBH_4$–zeolite materials, before and after desorption.

5.2 Experimental

Samples NaA and NaX were synthesised as detailed in the experimental chapter; NaY (13Y) and $LiBH_4$ (>90%) were obtained from Sigma-Aldrich.

Sample preparation was carried out as outlined in Section 4.2. The samples were desorbed by heating to 420℃ at a rate of 120℃ per hour and holding for up to 24 hours under flowing argon.

The samples were characterized using powder X-ray diffraction (PXRD). Raman spectra and IR data was collected, SEM images were recorded. Thermogravimetric data were collected with temperature runs either from 30 – 600℃, or 30 – 420℃ followed by a 4 hour isothermal step, both at a ramp rate of 2℃ per minute; the TGA data was when available coupled with mass spectrometry collecting m/z for hydrogen, water (OH^- and H_2O), diborane, nitrogen, oxygen and argon. The products of thermal desorption into vacuum were analysed by a residual gas analyser, with a thermal ramp of 2℃ per minute in the temperature range 30 - 450℃.

5.3 Results and Discussion

This section is broken down into three parts with each zeolite being independently analysed in turn, through a variety of structural and gas adsorption/desorption methods.

5.3.1 NaA with Lithium Borohydride

5.3.1.1 Desorption

Initial desorption studies by TGA-MS ran from 30℃ to 600℃ at 2℃ per minute with the results shown in figure 5.1. The mass loss data for $(LiBH_4)_{128}$.NaA showed a total desorption of 4.0 wt% which started at around 275℃ and continued until above 450℃. A slight shoulder at 420℃ suggests that a second desorption step may have occurred. This would be consistent with the major desorptions observed for bulk lithium borohydride, and this is corroborated by the mass spectrometer trace. Noticeably, the mass loss percentage value came out higher than the estimated value, for hydrogen, obtained from the Rietveld refinement performed in section 4.3.1.1 (3.65 wt%).

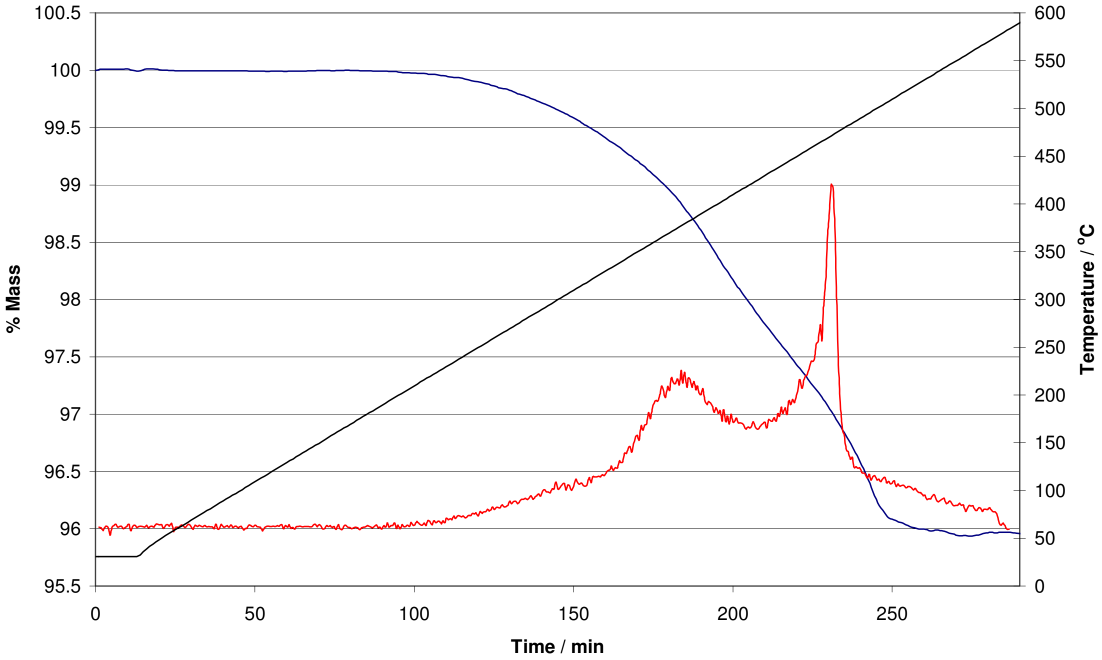

Figure 5.1 – TGA-MS desorption trace of $(LiBH_4)_{128}$.NaA from 30 to 600℃: temperature (-); % of initial mass (-). MS trace for hydrogen evolved (-) scaled to fit.

5.3.1.2 Powder X-ray Diffraction

A sample of $(LiBH_4)_{128}$.NaA was prepared at 250℃. This sample was placed inertly onto the heating stage. The initial run, for which the powder patterns are shown in figure 5.2, was performed from 30 to 600℃, but it was found that above temperatures of 450℃, the zeolite structure began to collapse to the glassy sodium aluminosilicate nepheline, which remained up to 600℃. On cooling, NaA was no longer present as a product. This contrasts with the parent zeolite which starts to decompose around 800℃ to a similar glassy phase[1].

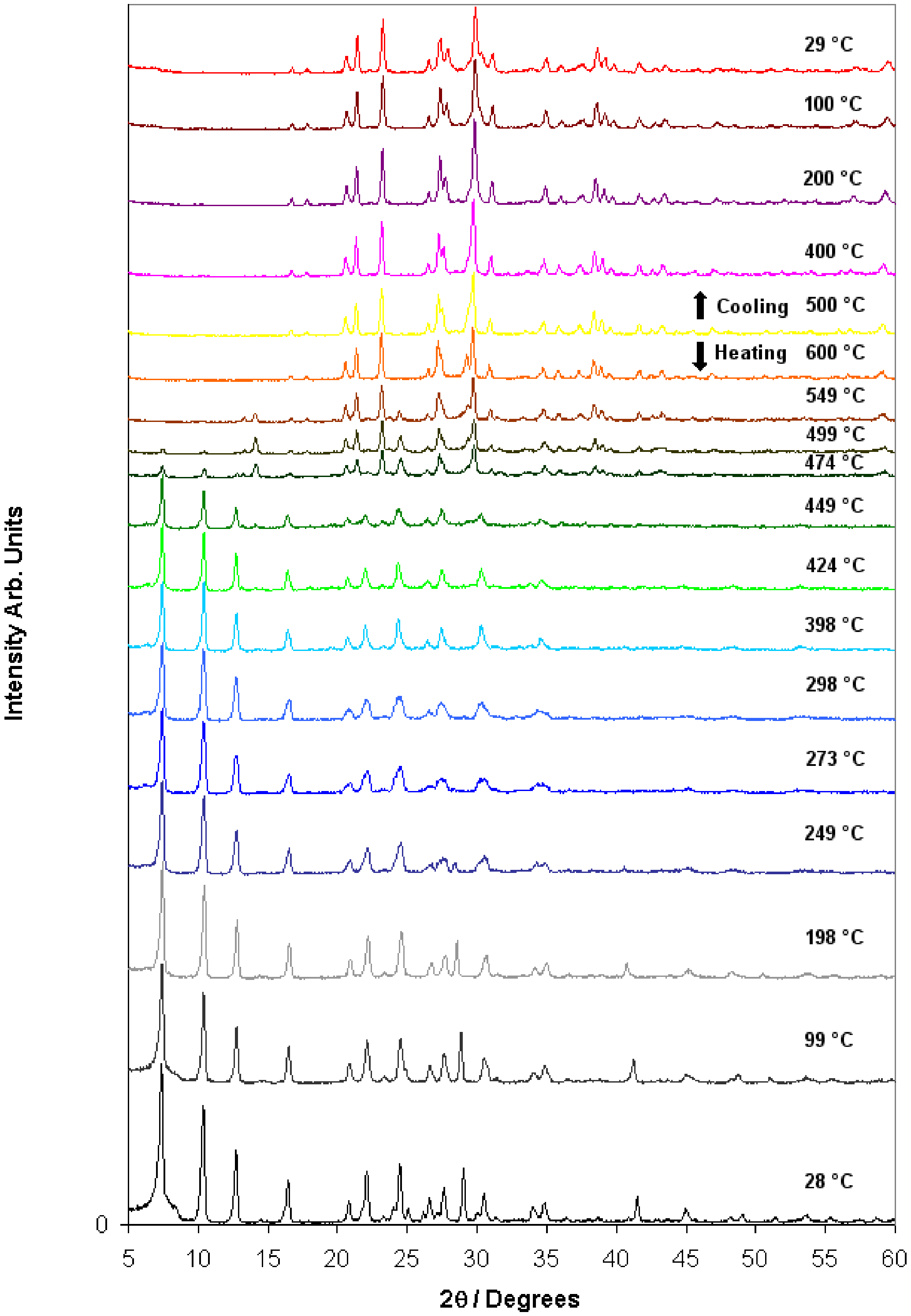

Figure 5.2 – A stack plot of powder XRD patterns of $(LiBH_4)_{128}$.NaA, heated to and cooled from 600°C.

Analysis of the lattice parameters, in figure 5.3, showed that the values all remained very similar, with any deviation masked by the errors.

This experiment was then repeated with an initial ramp to 450℃ where the temperature was held for several hours. This time it was found that the final product at this temperature contained both an NaA-type phase and nepheline; both phases persisted on cooling, as observed in figure 5.4. The drop in temperature at which NaA converts to nepheline is dependent on the inclusion of lithium borohydride as a guest, and is probably affected by loading level.

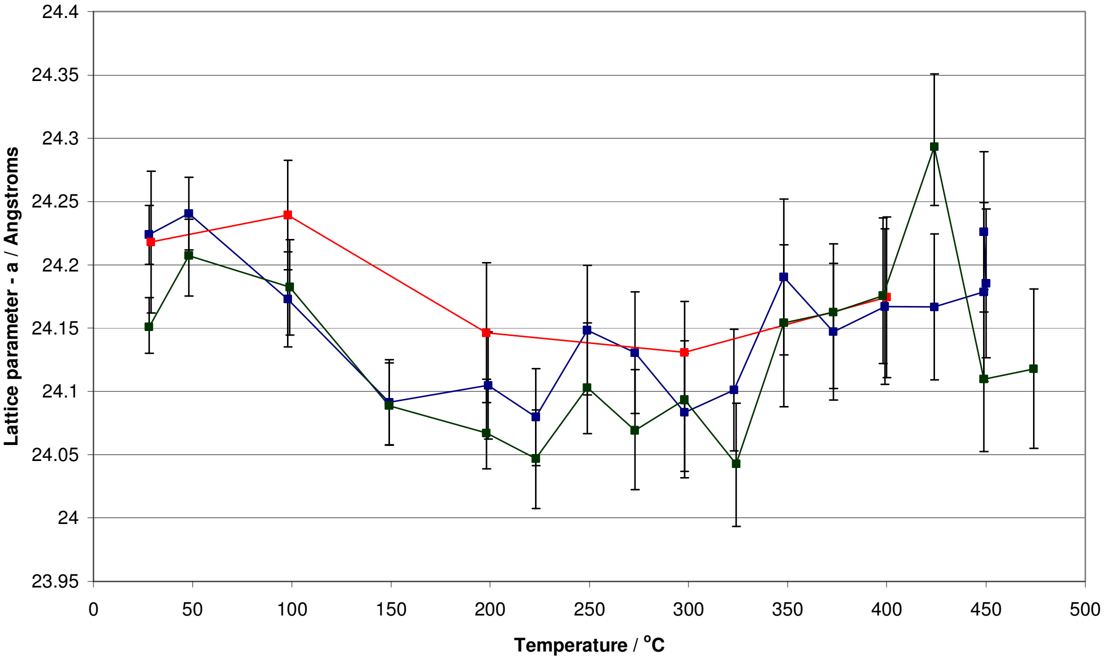

Figure 5.3 - Lattice parameters for $(LiBH_4)_{128}$.NaA on heating and cooling, showing the initial run to 600℃ (-), and the heating (-) and cooling (-) cycles of the 450℃ run, with error bars displaying 3 ESD's.

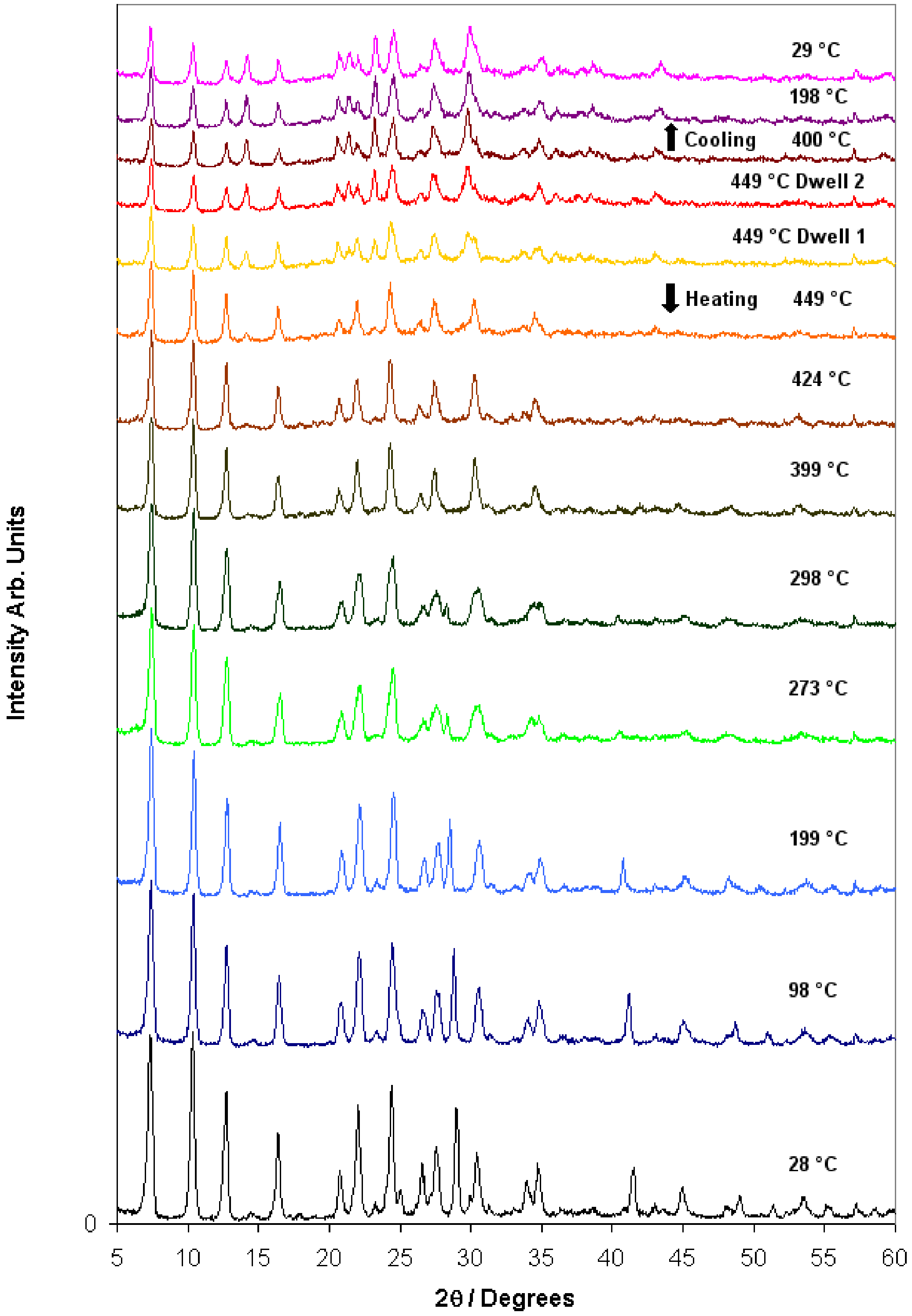

Figure 5.4 – A stack plot of powder XRD patterns of $(LiBH_4)_{128}$.NaA, heated to 450°C with 2 hours dwell before cooling to room temperature.

In figure 5.4 the high temperature runs clearly showed that temperatures above 425℃ resulted in partial collapse of the framework, as both nepheline and NaA were present. There are changes in the region 20-30° 2θ, which can be attributed to the phase transition in lithium borohydride. These peaks are reduced and then disappear above 298℃ above the melting temperature for lithium borohydride.

When $LiBH_4$ containing samples were heated under flowing argon gas in a furnace at 420℃ for 18 hours, the framework was shown to remain intact with no nepheline phase observed. Dehydrogenated samples of $(LiBH_4)_{128}$.NaA and $(LiBH_4)_{64}$.NaA were prepared in this fashion for further analysis by other means. Powder XRD showed a change in lattice parameters from 24.252(3) and 24.292(6) Å, to 24.33(1) and 24.36 (1) Å, respectively. This expansion of the lattice parameter is presumed to be due to expansion of the guest material. The value tends towards that expected for the dehydrated zeolite.

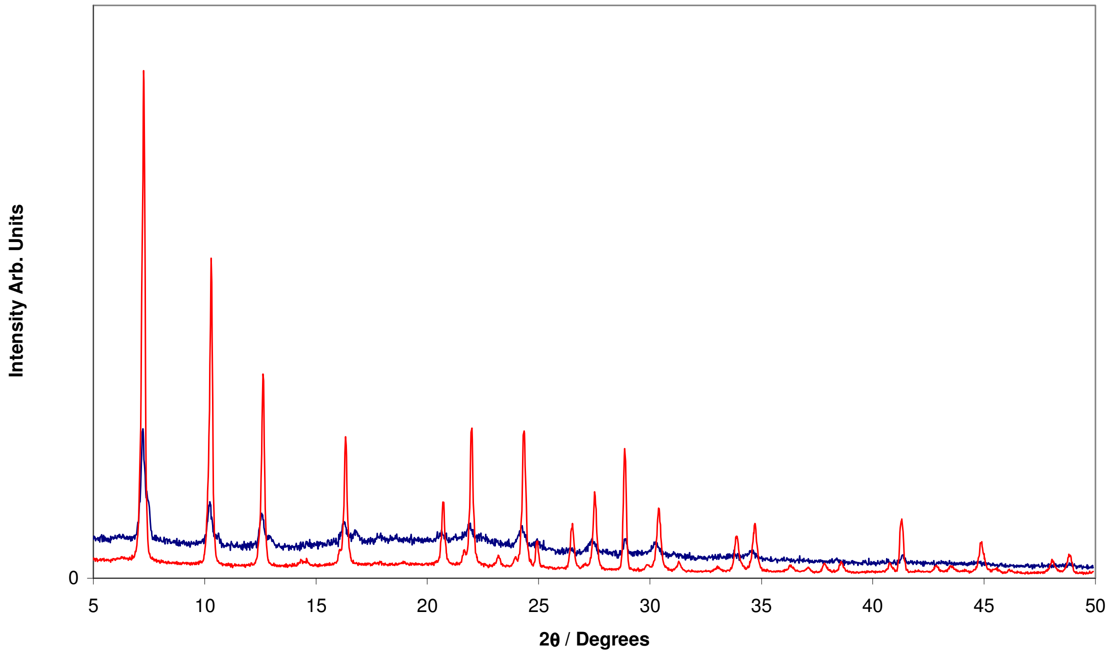

Figure 5.5 – XRD Pattern showing $(LiBH_4)_{128}$.NaA (-) and (-) after desorption at 420ºC.

Figure 5.5 shows that the final product had much broader peaks with poorer intensities at high two-theta. These are usually indicative of a lack of long range order. So whilst the sample may appear to have some zeolitic peaks, these are caused by short range order. This poorer diffraction may be caused by the presence of amorphous materials from the dehydrogenation, or distortion of the framework damaging the frameworks long range connectivity.

The half loaded sample, shown in figure 5.6, also showed some peak asymmetry, which could indicate that some of the contents of the internal pore structure were homogenised during its desorption process.

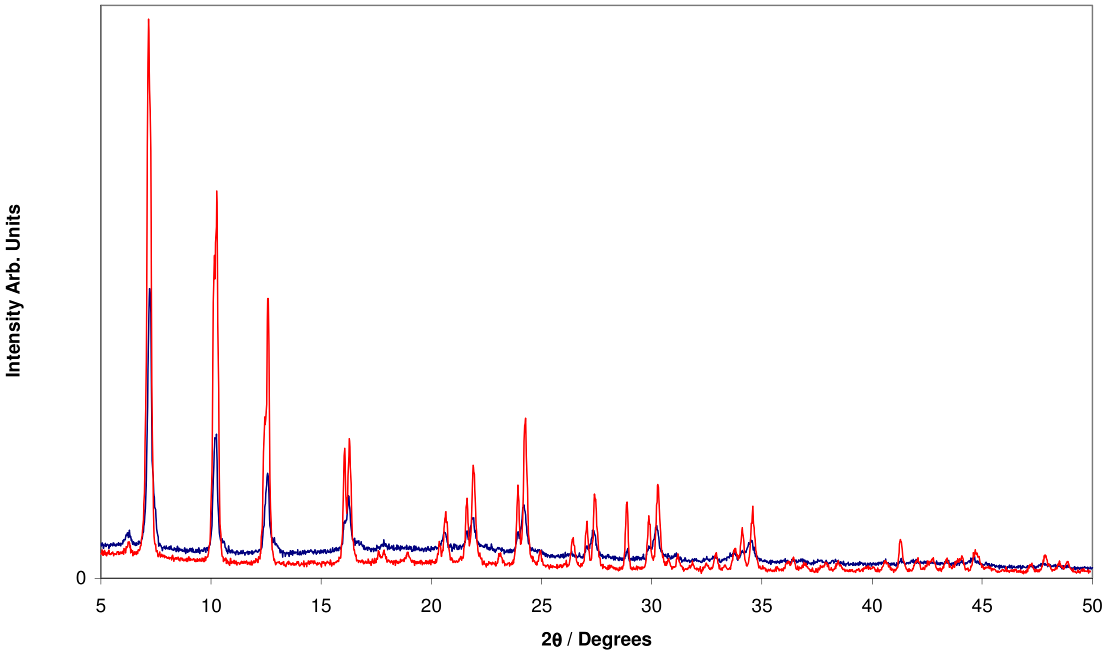

Figure 5.6 – Powder XRD pattern showing $(LiBH_4)_{64}$.NaA (-) and (-) after desorption at 420ºC.

The colour change observed was from a light grey powder to a brown/orange powder; amorphous boron is a dark brown coloured powder. Amorphous boron being one of the final desorption products from lithium borohydride.

5.3.1.3 Further Desorption

Figure 5.7 shows data from a separate TGA desorption experiment from 30 to 420°C with a 2 hour isothermal point at the end, which showed only one distinct desorption. The temperature was chosen to minimise decomposition of the framework. The mass loss observed equates to around 2.25 wt%, which is approximately half that of the higher temperature run. This corresponds well with quantity of hydrogen expected to be desorbed the 1st and 2nd desorptions[2] observed in bulk lithium borohydride shown in equations 1 and 2. The first desorption occurs with the structural transition at approximately 105℃; the second desorption of bulk lithium borohydride starts at 320℃; with the third starting around 400℃ and peaking at about 500℃, and coming to completion by 600℃. Lithium hydride remains stable up to 900℃.

$$LiBH_4 \rightarrow LiBH_{4-\varepsilon} + \tfrac{1}{2}\varepsilon H_2 \qquad (1)$$

$$LiBH_{4-\varepsilon} \rightarrow \text{"}LiBH_2\text{"} + B + \tfrac{1}{2}(1-\varepsilon)H_2 \qquad (2)$$

$$\text{"}LiBH_2\text{"} \rightarrow LiH + B + \tfrac{1}{2}H_2 \qquad (3)$$

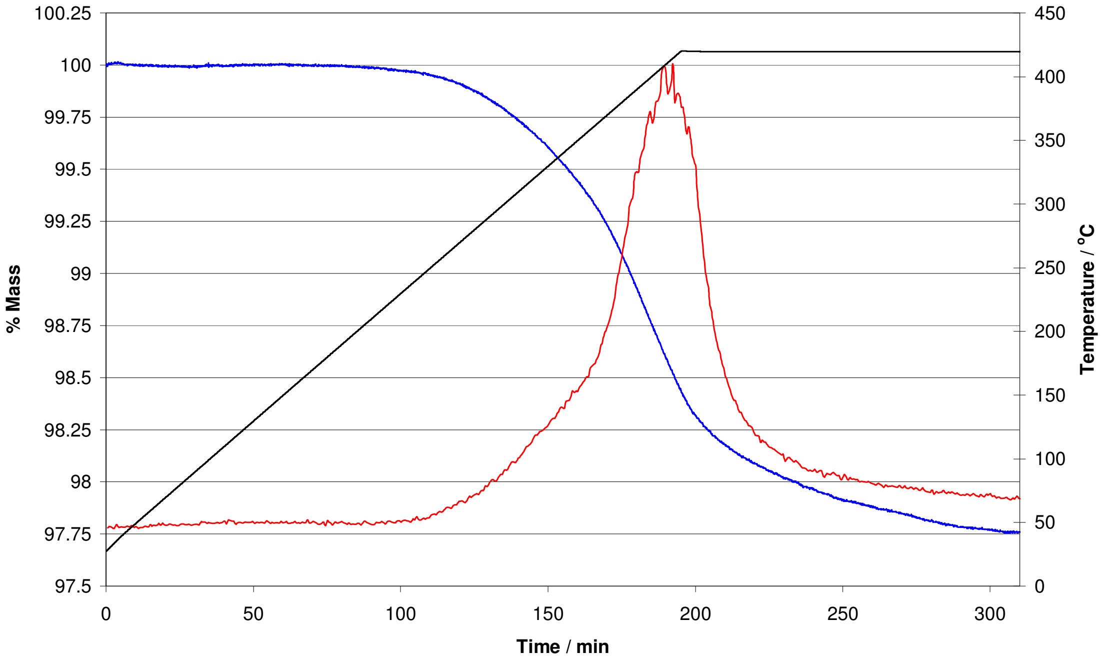

Figure 5.7 – TGA-MS desorption trace of $(LiBH_4)_{128}$.NaA from 30 to 420℃ with 2 hour dwell: temperature (-); %of initial mass (-). MS trace of hydrogen evolved (-) scaled to fit.

As expected, the mass spectrometer trace showed that at these temperatures the desorbed products were exclusively hydrogen.

With $(LiBH_4)_{64}$.NaA the same desorption temperatures were observed as with $(LiBH_4)_{128}$.NaA, although the shoulder at 420ºC was less pronounced in the half loaded sample. That may be an indication that the loading of the sample directly affects the diffusion kinetics.

The second peak from the MS trace in figure 5.1 showed a sharp profile. This shows the final desorption step, possibly represented by equation (3), may correspond with the collapse of the framework to the glassy aluminosilicate phase, nepheline, observed in high temperature powder XRD. The samples collected after desorption at 420℃ showed through powder XRD, figures 5.5 and 5.6, that this was far more pronounced in $(LiBH_4)_{128}$.NaA than in $(LiBH_4)_{64}$.NaA.

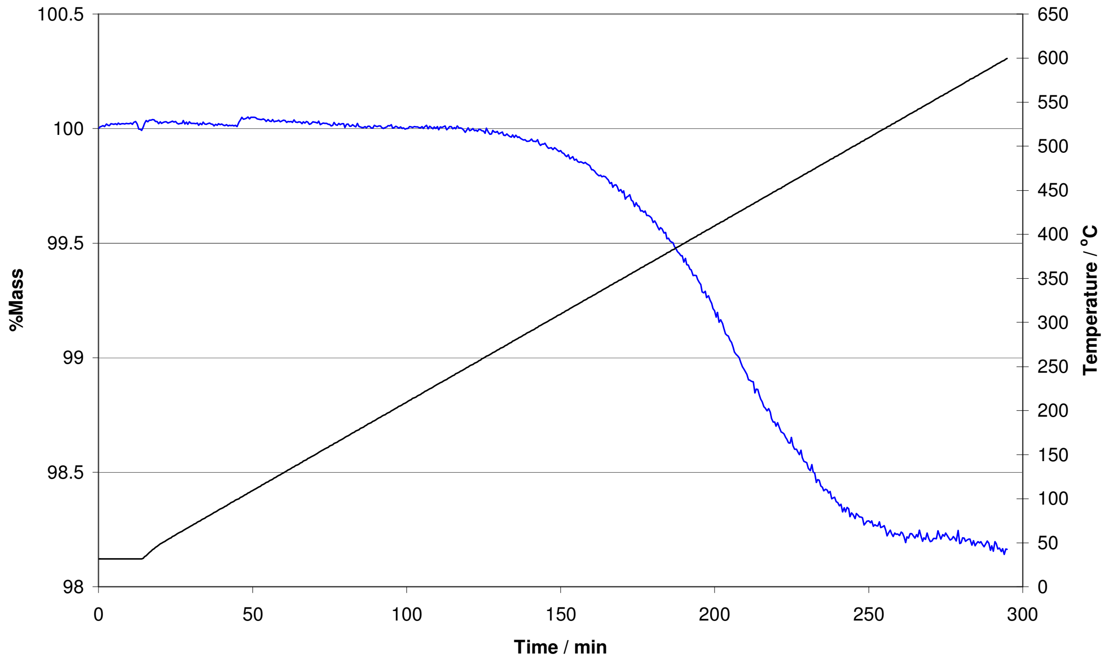

Figure 5.8 – TGA desorption trace of $(LiBH_4)_{64}$.NaA from 30 to 600℃: temperature (-); % of initial mass (-).

During desorption of bulk $LiBH_4$, approximately 9 wt% is desorbed in equations (1) and (2) with the final achievable 4.5 wt% in equation (3)[2]. For $(LiBH_4)_{64}$.NaA, this ratio of percentages was observed with 1.8 wt% up to 600℃ and 1.3 wt% up to 420℃. This suggests that some of the third desorption may be achievable at a lower temperature, compared with that of bulk $LiBH_4$ which occurs in excess of 600℃. This reduction may be due to the reduced particle size and improved diffusion through a more lightly loaded zeolite.

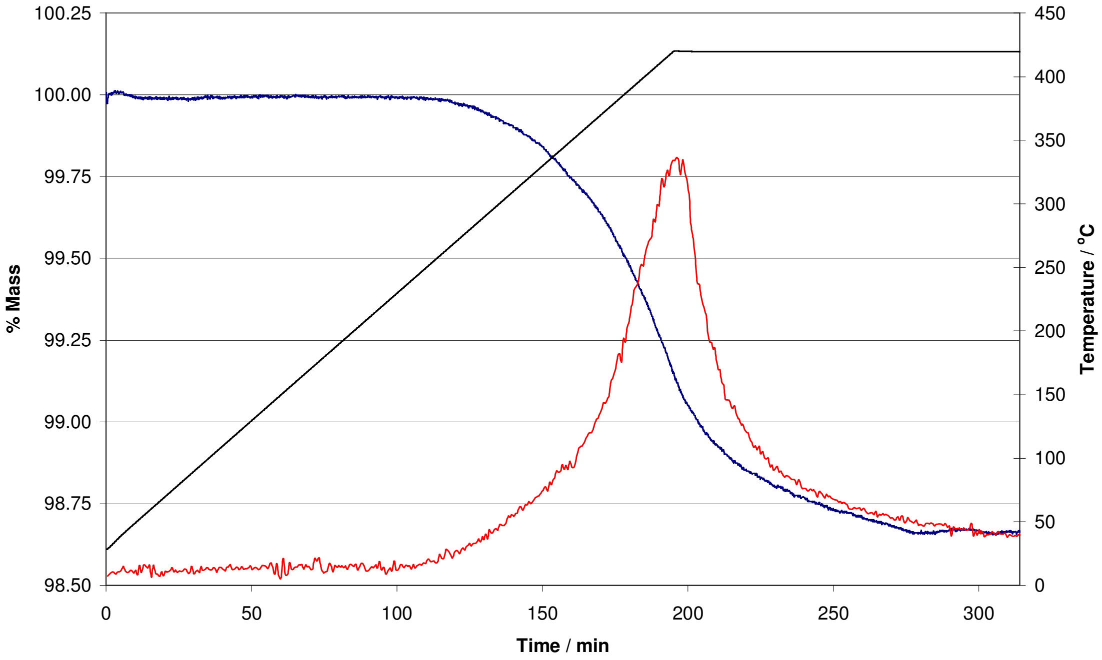

Figure 5.9 – TGA-MS desorption trace of $(LiBH_4)_{64}$.NaA from 30 to 420℃ with 2 hour dwell: temperature (-); % of initial mass (-). MS trace for hydrogen evolution (-) scaled to fit.

It was observed in chapter 4 that some sodium borohydride is present in the samples. Its onset temperature for desorption is approximately 565℃ which will not contribute to the hydrogen desorption in the temperature regime of 30 - 420℃. Between 30 - 600℃ it can be observed as a slight tail in figure 5.8 for $(LiBH_4)_{64}$, starting at approximately 560℃.

Both samples, 128 and 64 $LiBH_4$ PUC, were analysed in a vacuum desorption rig with RGA analyser. The runs were conducted from 30 to 450℃. The first desorption of $(LiBH_4)_{128}$.NaA, shown in figure 5.10, occurred at just below 100℃, with hydrogen being the major species observed.

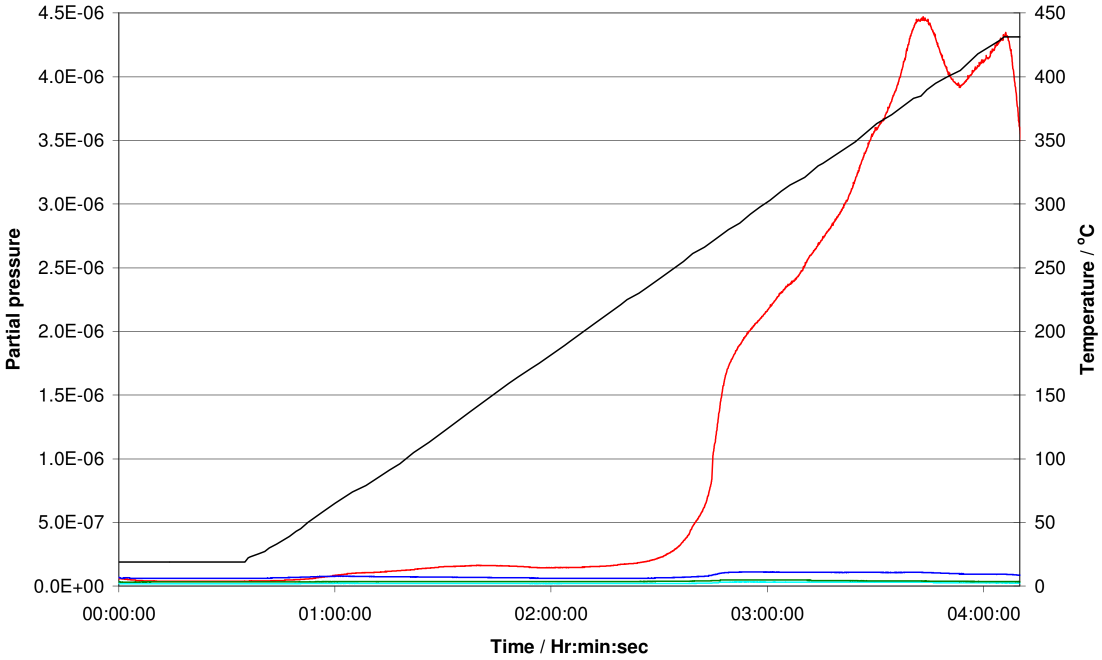

Figure 5.10 – TPD-MS into vacuum of $(LiBH4)_{128}$.NaA from 30 to 430℃: temperature (-); MS trace for hydrogen (-); H_2O (-); OH^- (-); and nitrogen (-).

After this two distinct desorptions were observed, the first at approximately 250℃, which had a sharp onset of desorption which continued steadily to a peak at 385℃. The second desorption occurred at around 410℃. The peaks were not clearly resolved and were exclusively composed of hydrogen. The poor resolution of peaks was probably due to the vacuum pump not being able to handle the increased gas flow at the time. The partial pressures did not return to their background value as the sample was not left isothermally to obtain the thermodynamic equilibrium. Other samples measured by vacuum desorption were found to do so after several hours.

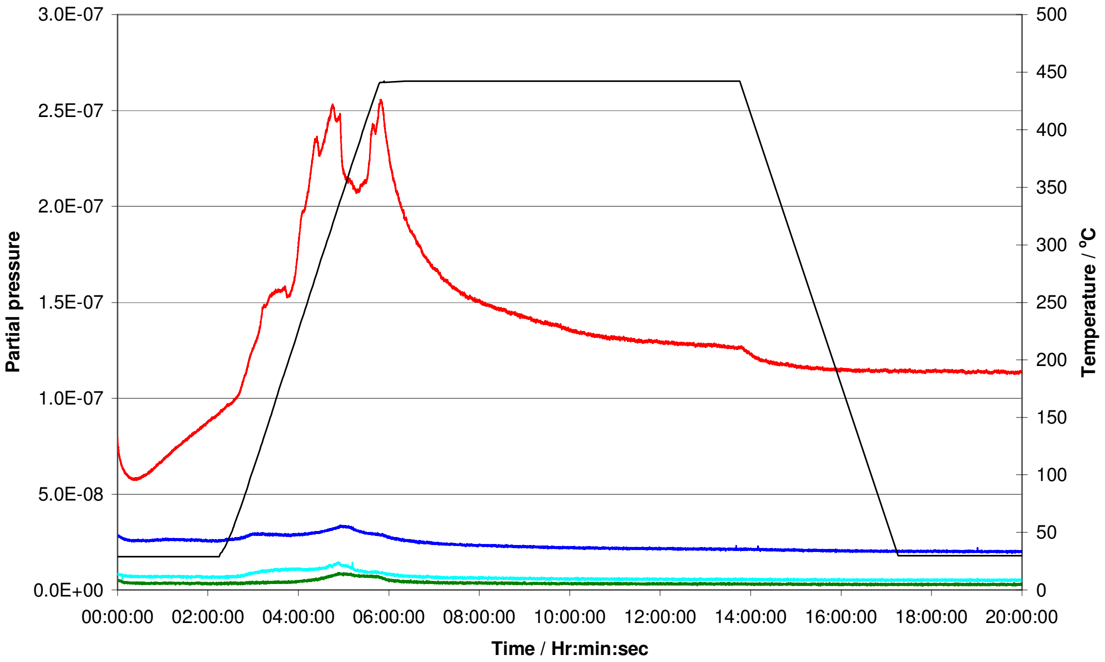

Figure 5.11 – TPD-MS into vacuum of $(LiBH_4)_{64}$.NaA from 30 to 450°C with an 8 hour dwell: Temperature (-); MS trace for hydrogen (-); H_2O (-); ^-OH (-); and Nitrogen (-).

For $(LiBH_4)_{64}$.NaA it was observed, in figure 5.11, that the onsets and peaks occurred at similar temperatures to those in the $(LiBH_4)_{128}$.NaA. The small desorption at around 100°C was present. Further desorptions occurred at 220 and 375°C, slightly lower than the fully loaded counterpart. The 8 hours isothermal data showed that eventually the hydrogen desorption signal declined, but not quite to zero. Lithium borohydride had a slight desorption below 100°C associated with a structure change, the major peak started at 225°C and peaked at 345°C, shown in figure 5.12 for comparison.

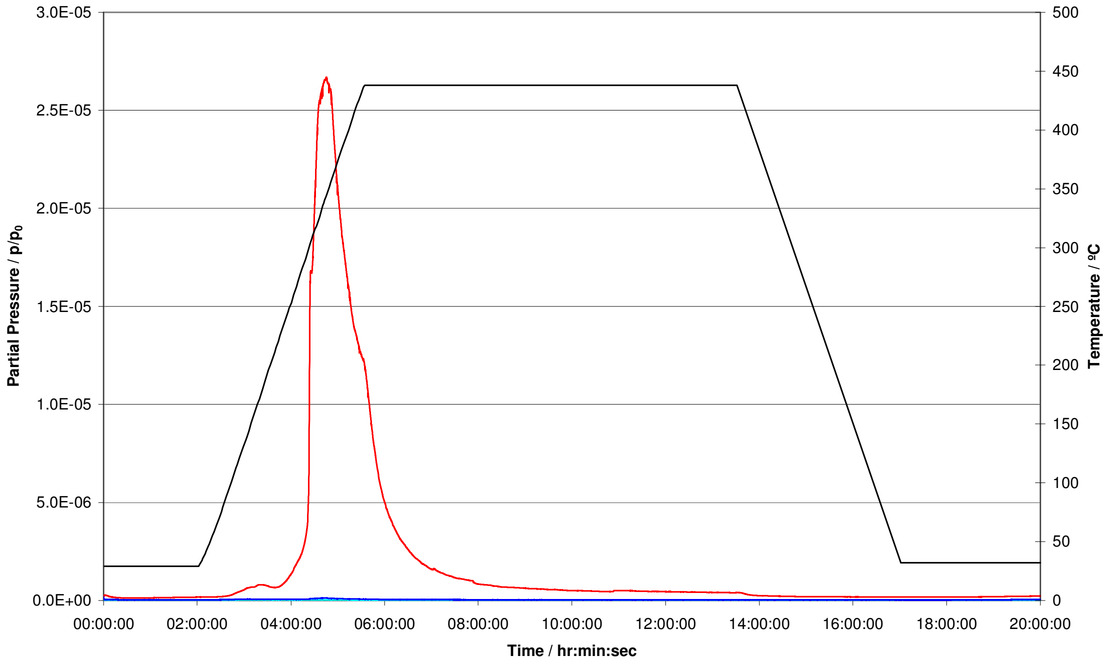

Figure 5.12 – TPD-MS into vacuum of $LiBH_4$ from 30 to 450℃ with an 8 hour dwell: Temperature (-); MS trace for hydrogen (-); H_2O (-); and ^-OH (-).

A noticeable difference between the vacuum desorption and TGA data is the lower onset temperatures for both samples, though more pronounced in $(LiBH_4)_{64}$.NaA. This is due to the more dynamic nature of gas removal in the vacuum system, helping drive the diffusion of gas from the pores, compared with the gentle flow of gas in the TGA.

5.3.1.4 Vibrational Spectroscopy

Section 4.3.1.3 showed the initial spectroscopic analysis on occlusion and tables 4.2 and 4.3 showed the key vibrations associated with lithium borohydride and zeolites[3-6]. With the IR data for $(LiBH_4)_{128}$.NaA, shown in figure 5.13, a radical change was observed on desorption of the sample, which generated a broadening of the peak to approximately 300 cm^{-1} and a shift of the maximum from 960 cm^{-1} to 902 cm^{-1}. In the region between 2150 and 2400 cm^{-1} containing the borohydride stretches, on desorption we observe the loss of this feature. The feature remaining is due to atmospheric CO_2 which has a peak at 2350 cm^{-1}.

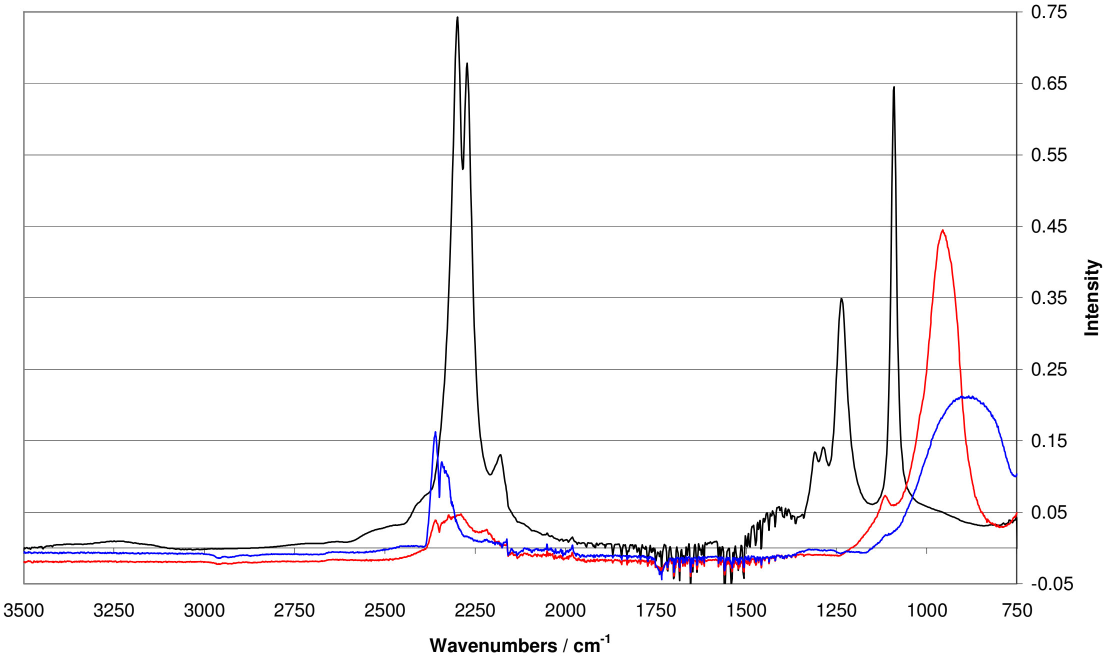

Figure 5.13 – IR spectra of $LiBH_4$ (-), $(LiBH_4)_{128}$.NaA (-) and after heating at 420°C (-).

Figure 5.14, showing the IR spectra of $(LiBH_4)_{64}$.NaA, showed little borohydride stretching for the region of 2150 to 2400 cm^{-1}, being masked by CO_2 at 2350 cm^{-1}, the diminished peak heights in comparison to the $(LiBH_4)_{128}$.NaA being due to there being less borohydride present. In contrast the zeolite peak at 960 cm^{-1} remained in roughly the same location between the occluded and desorbed samples, with the desorbed sample again having a larger peak width than the sample before desorption.

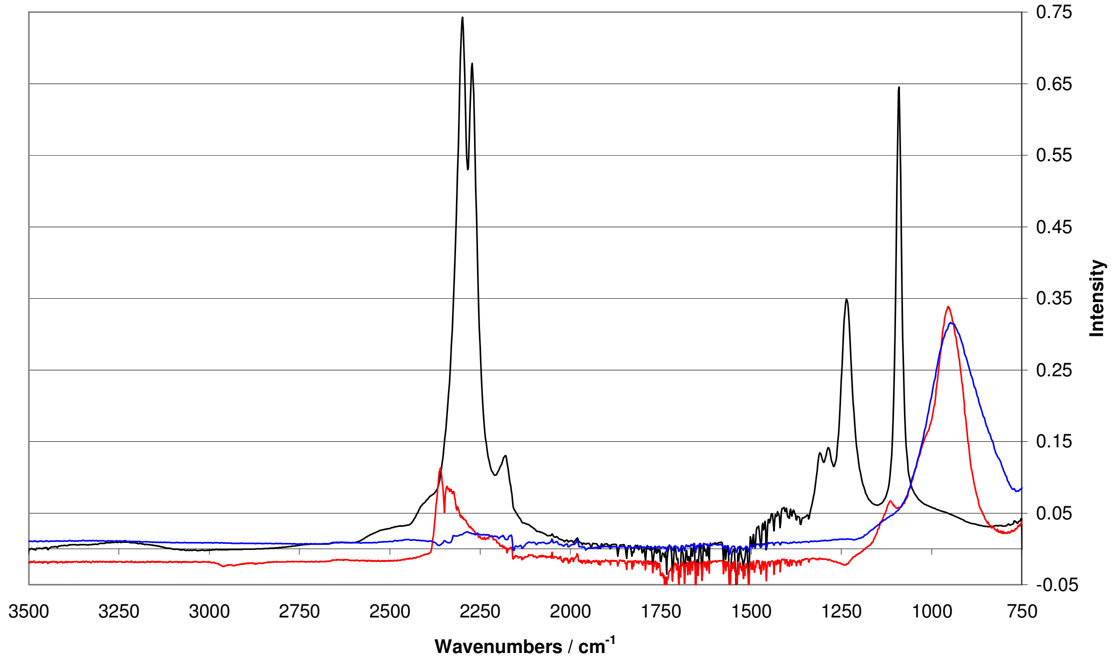

Figure 5.14 – IR spectra of $LiBH_4$ (-), $(LiBH_4)_{64}$.NaA (-) and after heating at 420°C (-).

The Raman spectra (figure 5.15) were virtually featureless after desorption. The peak at 494 cm^{-1}[5] in $(LiBH_4)_{128}$.NaA due to the zeolite framework (T-O bend) was removed completely on desorption. The broad borohydride peak at 2325 cm^{-1} in $(LiBH_4)_{128}$.NaA was also removed on desorption.

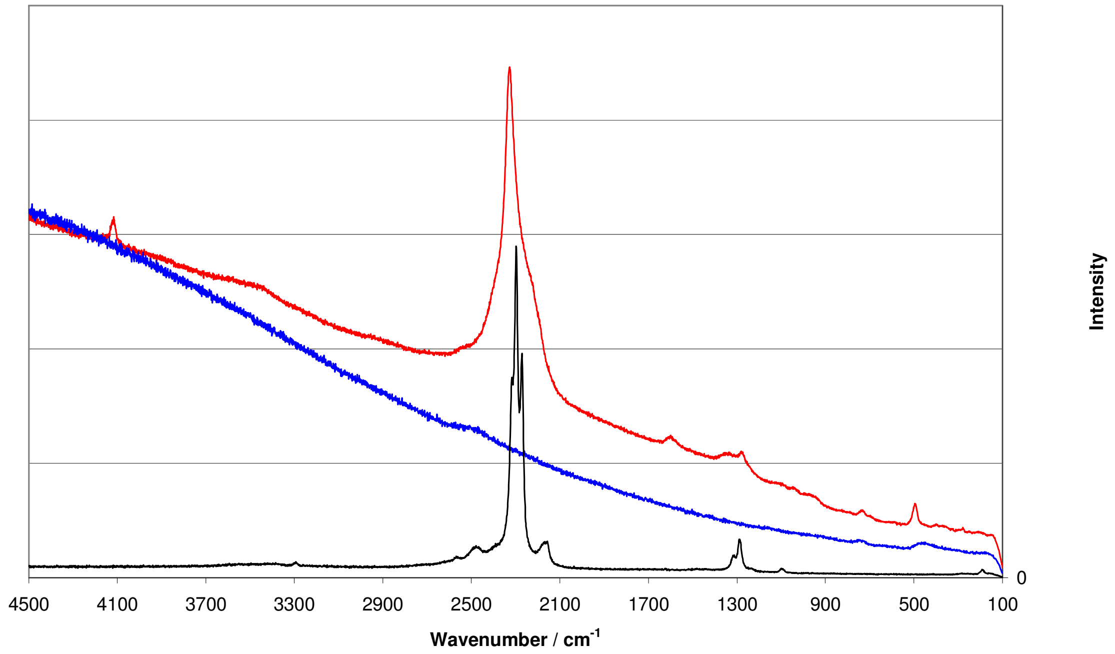

Figure 5.15 – Raman spectra of $LiBH_4$ (-), $(LiBH_4)_{128}$.NaA (-) and after heating at 420°C (-).

Similar results were observed in $(LiBH_4)_{64}$.NaA (Figure 5.16) to those observed for $(LiBH_4)_{128}$.NaA. Both the framework peak at 494 cm^{-1}[5] and the broad borohydride peak at 2328 cm^{-1} disappeared on desorption.

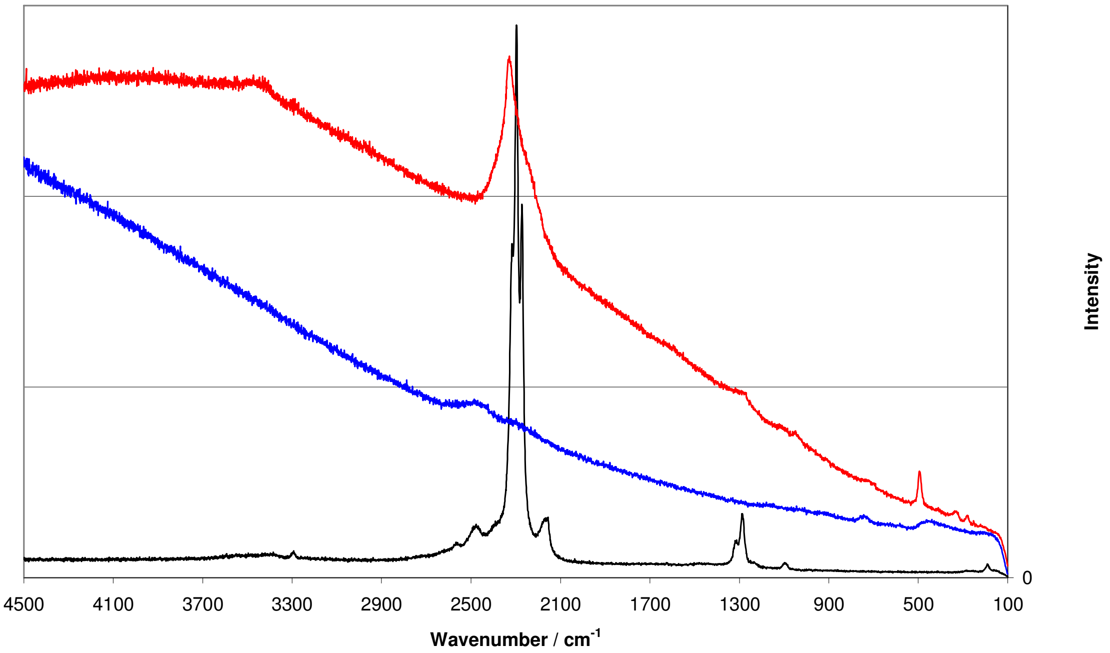

Figure 5.16 – Raman spectra of $LiBH_4$ (-), $(LiBH_4)_{64}$.NaA (-) and after heating at 420°C (-).

Raman and infra-red spectroscopy showed either a complete removal of peaks or a broadening and shift on desorption for framework peaks. Naturally BH vibrations disappear due to hydrogen no longer being present after desorption. The alteration to framework peaks may be caused by framework strain (or indeed collapse).

The strain effect on the framework can be analysed using the densities of lithium borohydride and its decomposition products, amorphous boron and lithium hydride. The densities of lithium hydride and amorphous boron, 0.82 and 2.37 g/cm^3 respectively, are greater than that of lithium borohydride, 0.666 g/cm^3. The molar densities of the desorption products are greater than that of lithium borohydride, the products, lithium hydride and boron in a one to one ratio, equalling 0.322 moles/cm^3 whilst the lithium borohydride occupies 0.0306 moles/cm^3. This would suggest that the guest will contract within the pore space on desorption, perhaps causing framework strain, evidence for which both from powder XRD and vibrational spectroscopy has been discussed. The effect may be similar to the desorption of water from the dehydrated zeolite.

5.3.1.5 Microscopy

SEM images after the decomposition of $(LiBH_4)_{128}$.NaA, figure 5.17b, showed that although signs of the basic cubic morphology were retained there was also evidence of deformation, which could be caused by a change in volume of the contents of the zeolite pores.

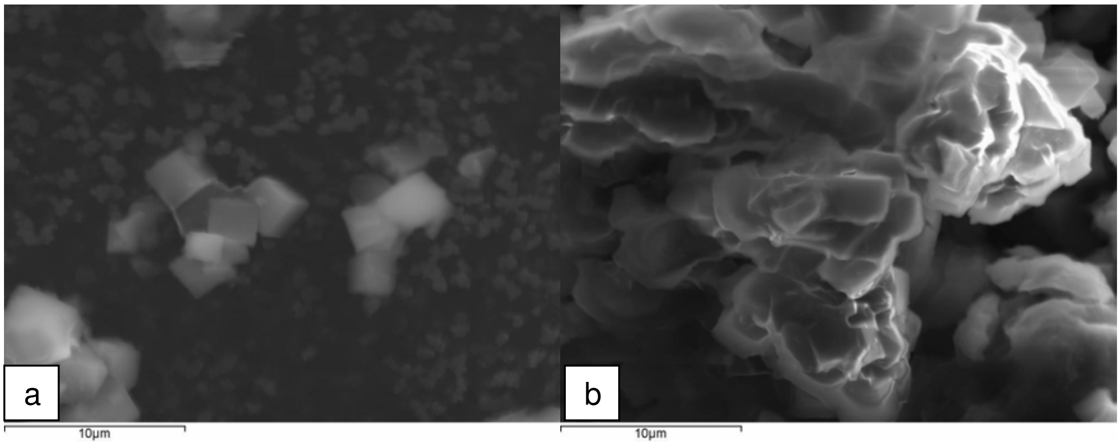

Figure 5.17 – SEM images of $(LiBH_4)_{128}$.NaA before (a) and after heating at 420℃ (b).

When the same analysis was performed on $(LiBH_4)_{64}$.NaA it was observed that the morphology was also retained on desorption and there was little sign of deformation to the particles or material on the surface.

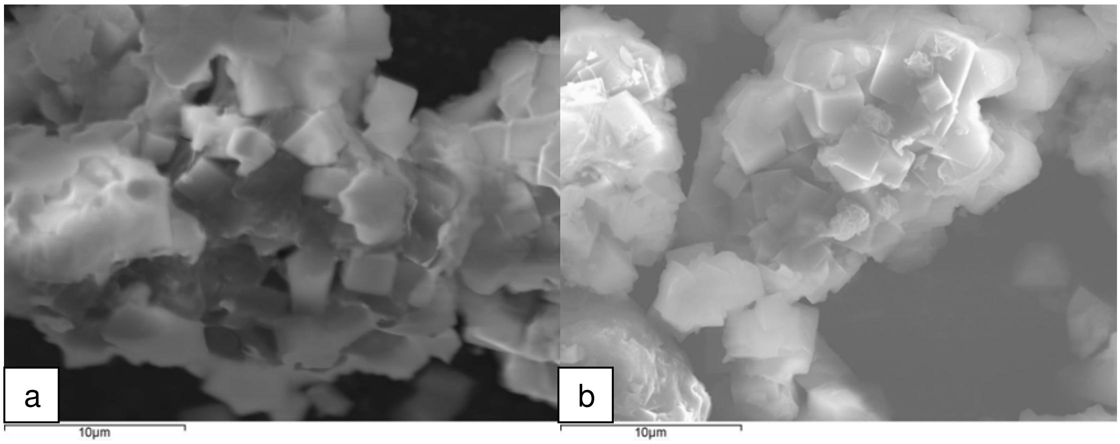

Figure 5.18 –SEM images of $(LiBH_4)_{64}$.NaA before (a) and after heating at 420℃ (b).

5.3.2 NaX with Lithium Borohydride

5.3.3.5 Desorption

Initial observations were obtained through TGA-MS. $(LiBH_4)_{224}$.NaX was run from 30 – 600℃ at 2℃ per minute. This run shown in figure 5.19 had a total desorption over the temperature range close to that expected from the original reaction mixture of 3.9 wt%. The onset occurred at around 280℃ and continued until 500℃, although a slight shoulder at around 460℃ was observed.

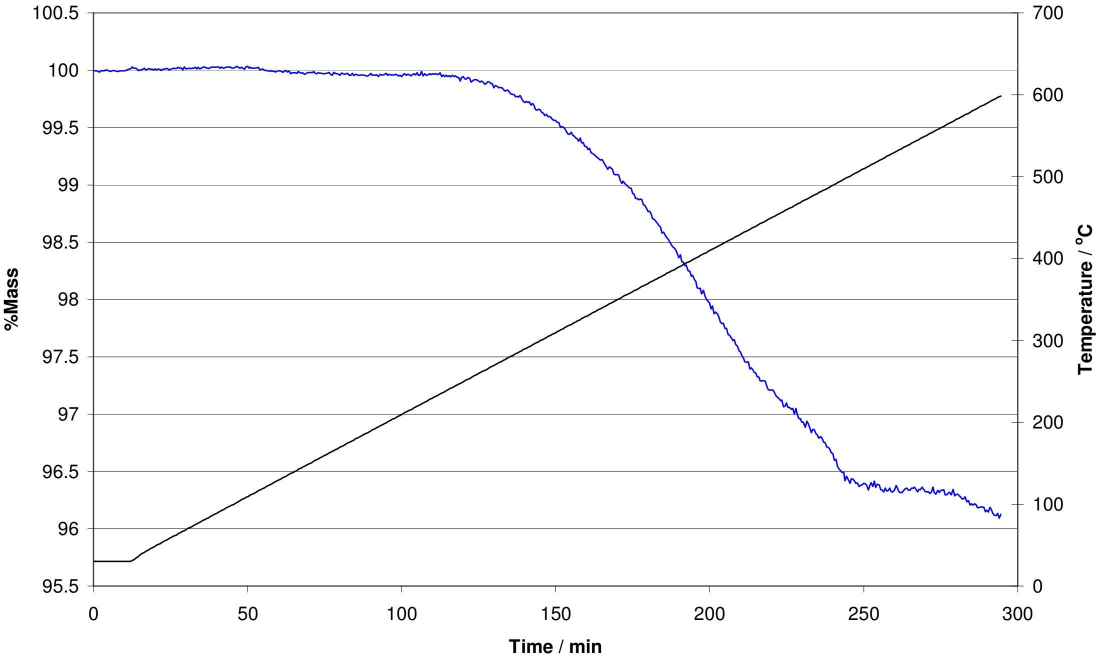

Figure 5.19 – TGA desorption trace of $(LiBH_4)_{224}$.NaX from 30 to 600°C: temperature (-); % of initial mass (-).

The framework of the loaded zeolite was shown to be destroyed at the high temperatures. Another run was performed between 30 and 420°C with a 2 hour dwell at temperature, the results are shown in figure 5.20.

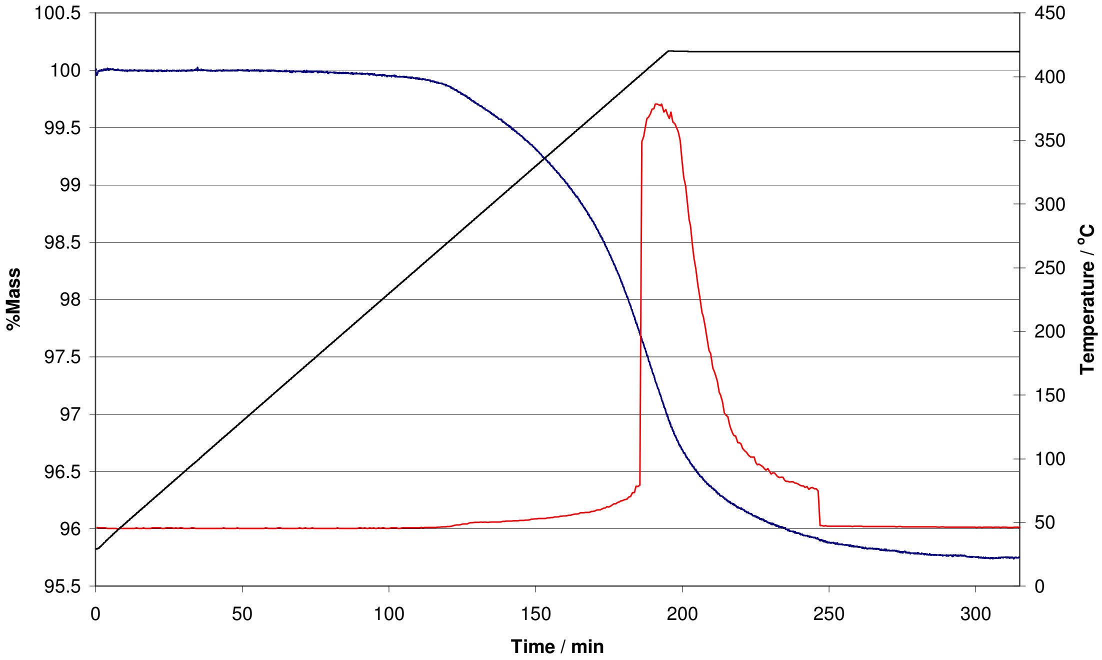

Figure 5.20 – TGA desorption trace of $(LiBH_4)_{224}$.NaX from 30 to 420℃ with 2 hour dwell: temperature (-); % of initial mass (-). Hydrogen release (-) scaled to fit.

This showed one desorption, again very slow over the period with a maximum weight loss of 4.2 wt% and no shoulder as observed in the previous run. Hydrogen provided the total weight loss with errors in correcting for the buoyancy most likely accounting for this difference in value from the 600℃ from the theoretical maximum. The ability of the sample to desorb completely beneath the second onset temperature and equilibrate over the 2 hours may be due to the increased pore vibrations at higher temperature which allow better diffusion. With NaA a reduction in the amount desorbed was observed when the temperature was reduced. This effect did not occur in NaX, which may be an effect of the wider pore aperture.

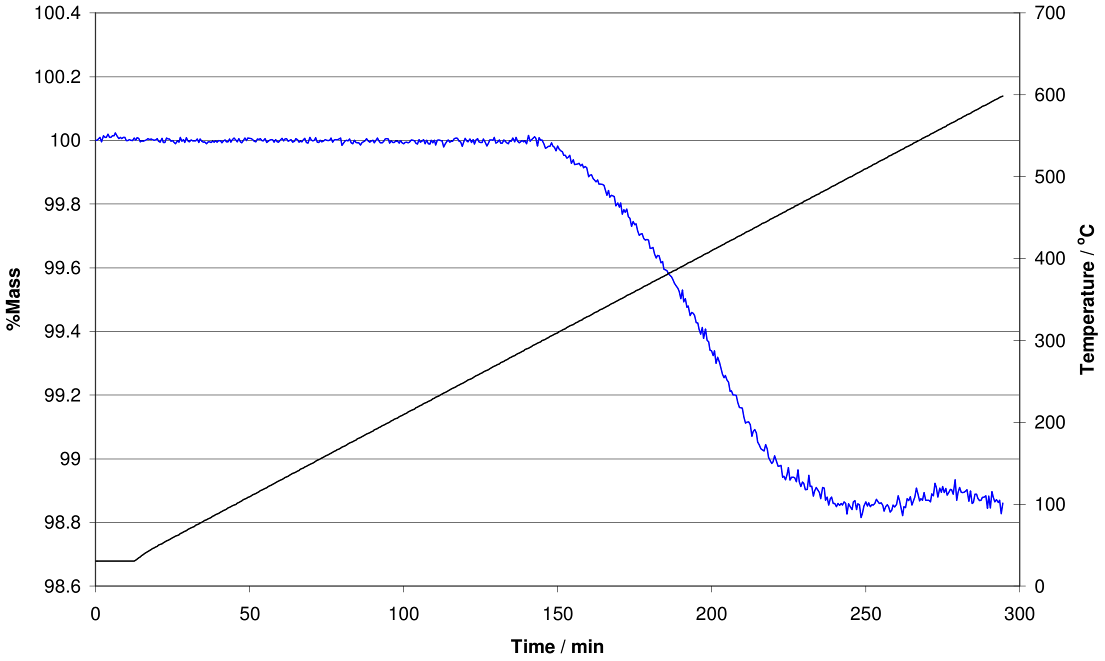

Figure 5.21 – TGA desorption trace of $(LiBH_4)_{96}$.NaX from 30 to 600°C: temperature (-); % of initial mass (-).

On analysis of $(LiBH_4)_{96}$.NaX, for the 600°C run shown in figure 5.21, a similar series of desorptions were observed to those in $(LiBH_4)_{224}$.NaX, except no shoulder was present, with a total weight loss of approximately 1.15 wt%.

When the temperature was reduced to 420°C (figure 5.22) a greater mass loss of 2.3 wt% was observed. The latter was more in line with the theoretical maximum for $(LiBH_4)_{96}$.NaX.

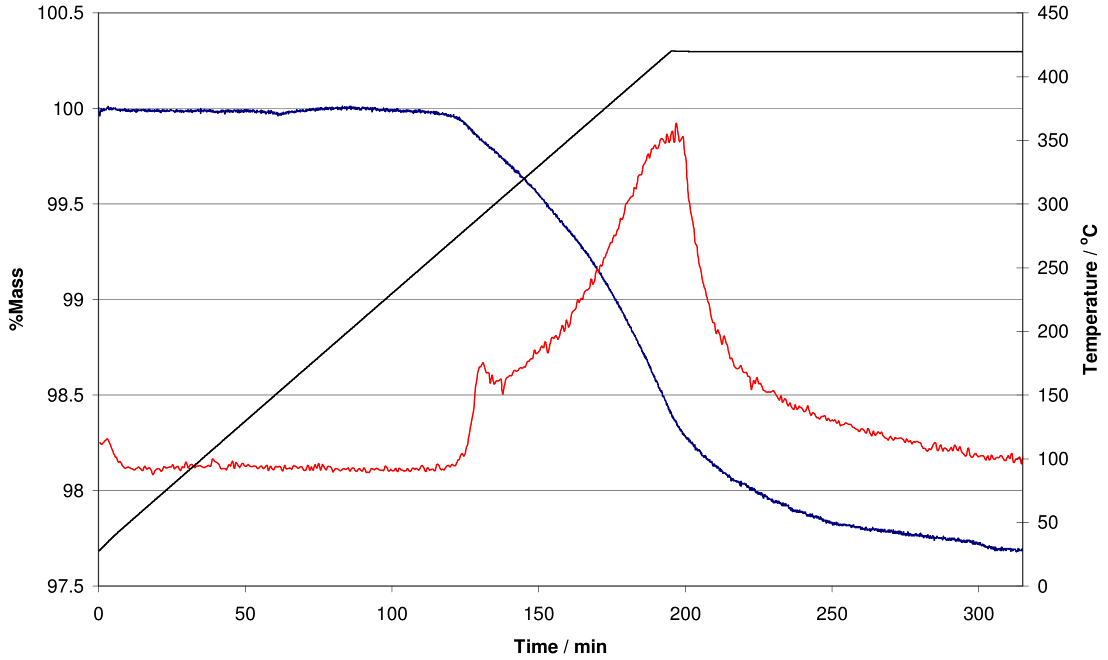

Figure 5.22 – TGA desorption trace of $(LiBH_4)_{96}$.NaX from 30 to 420℃: temperature (-); % of initial mass (-). Hydrogen release (-) scaled to fit.

The slope of this desorption appeared greater than that of $(LiBH_4)_{224}$.NaX, an indication of improved kinetics possibly caused by greater mobility of the hydrogen molecule in less congested pores.

5.3.2.4 Powder X-Ray Diffraction

Analysis was performed on the $(LiBH_4)_{224}$.NaX and $(LiBH_4)_{96}$.NaX, figures 5.23 and 5.24 respectively, after desorption at 420℃ for 18 hours. On desorption $(LiBH_4)_{224}$.NaX changed to a dark brown/orange powder, whilst $(LiBH_4)_{96}$.NaX went a slightly darker grey. The dark brown colour was from formation of amorphous boron on desorption. The light grey colour of $(LiBH_4)_{224}$.NaX suggests that the desorption didn't go to completion. The powder XRD showed that the zeolite diffraction pattern was still present, and the only crystalline phase observed. There was considerable damage to $(LiBH_4)_{224}$.NaX observed, with only short range order remaining, characterised by the weak broad peaks.

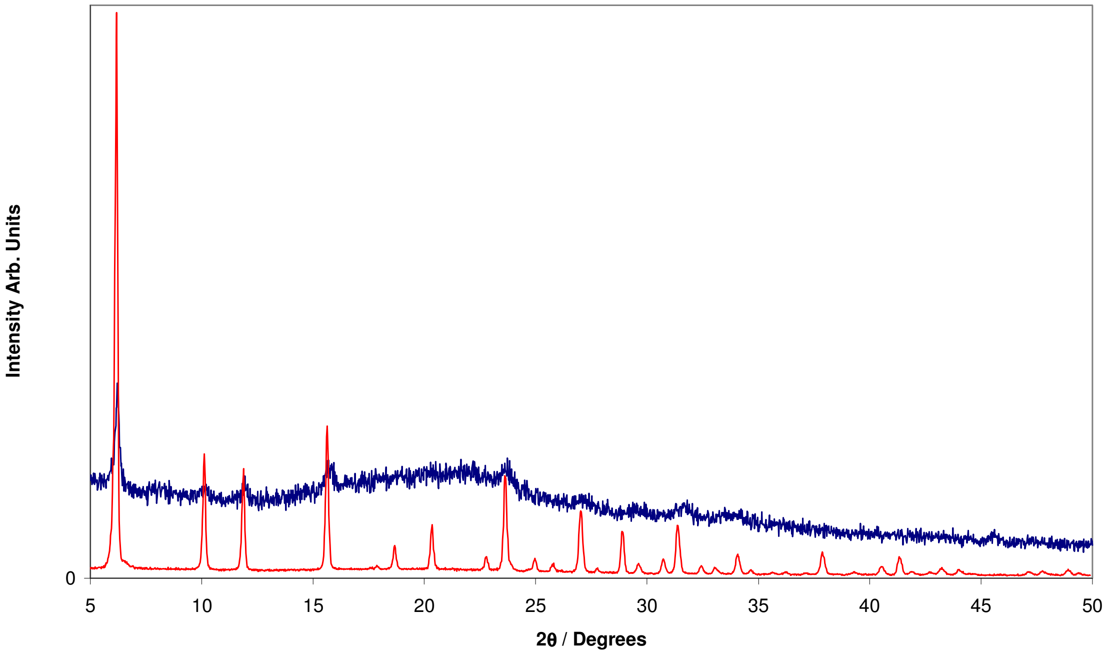

Figure 5.23 – Powder XRD pattern showing $(LiBH_4)_{224}$.NaX after synthesis (-) and after desorption at 420℃ (-).

For the half loaded sample $(LiBH_4)_{96}$.NaX, figure 5.24, only one set of broad lines was present which indicates that in desorption there may have been diffusion of the decomposition products to occupy the vacant zeolite. Observed lattice parameters after desorption of 24.67(9) and 24.90(8) Å for $(LiBH_4)_{224}$.NaX and $(LiBH_4)_{96}$.NaX, respectively, compare with the original as synthesised values of 24.70(6) and 24.66(2) Å.

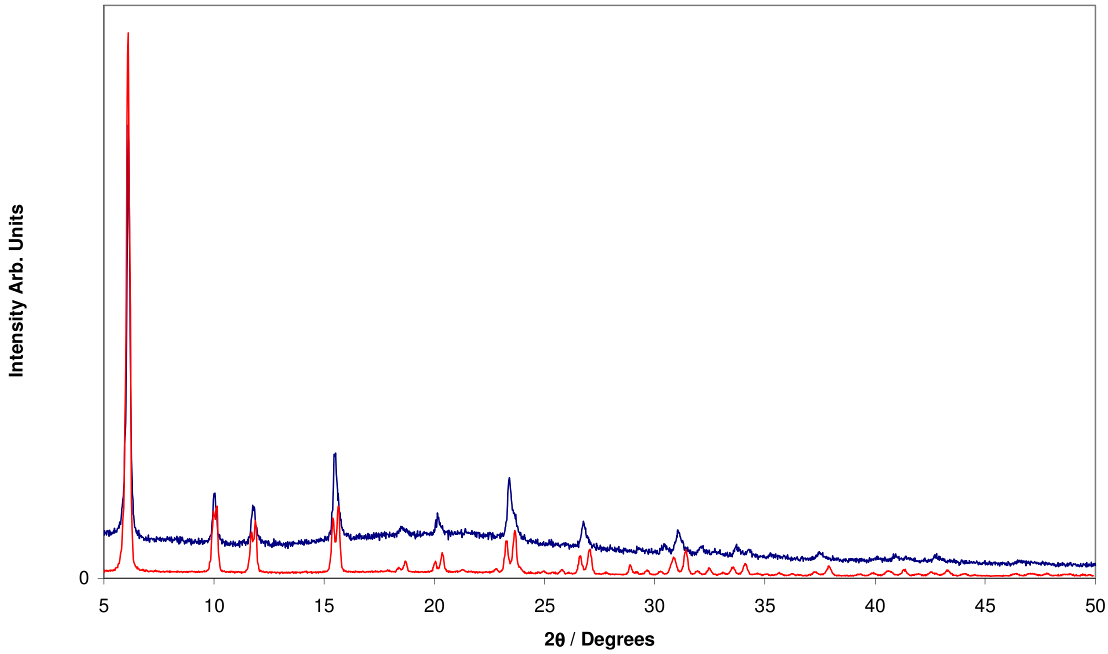

Figure 5.24 – Powder XRD Pattern showing $(LiBH_4)_{96}$.NaX after synthesis (-) and after desorption at 420°C (-).

The values remained near the contracted value of the “loaded” material for the $(LiBH_4)_{224}$.NaX rather than that of dehydrated zeolite, suggesting the zeolite was still occluded after desorption. The half loaded sample had an increased lattice parameter which was closer to that of the dehydrated zeolite. $(LiBH_4)_{96}$.NaX showed that only one phase was present after desorption, whilst two were present before. This could suggest a homogenisation during the desorption of the pore contents, or collapse of the “loaded” parts of the framework.

5.3.2.5 Vibrational Spectroscopy

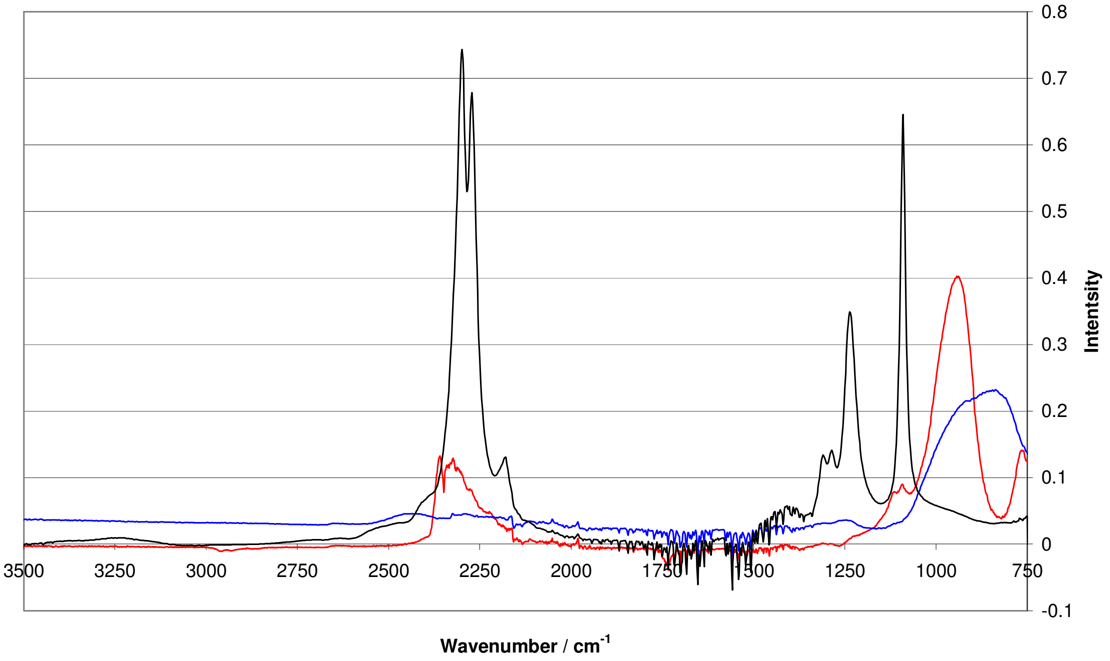

Figure 5.25 – IR spectra of LiBH$_4$(-), (LiBH$_4$)$_{224}$.NaX after synthesis (-) and after heating at 420°C (-).

Figure 5.25 shows borohydride stretches at 2300 cm^{-1} and 2271 cm^{-1}, which were removed on desorption.

The decomposition again brought a further broadening (to around 300 cm^{-1} in width) of the framework peak at approximately 870 cm^{-1}, which indicates strain in the framework. Two peaks were present in the spectrum of (LiBH$_4$)$_{224}$.NaX as shoulders on the main zeolite peak. One, at 1128 cm^{-1}, is a zeolite vibration associated with framework interactions with pore species. Another noticeable peak was that at 1098 cm^{-1}, which matches the ν_4 of lithium borohydride. Neither were present after desorption.

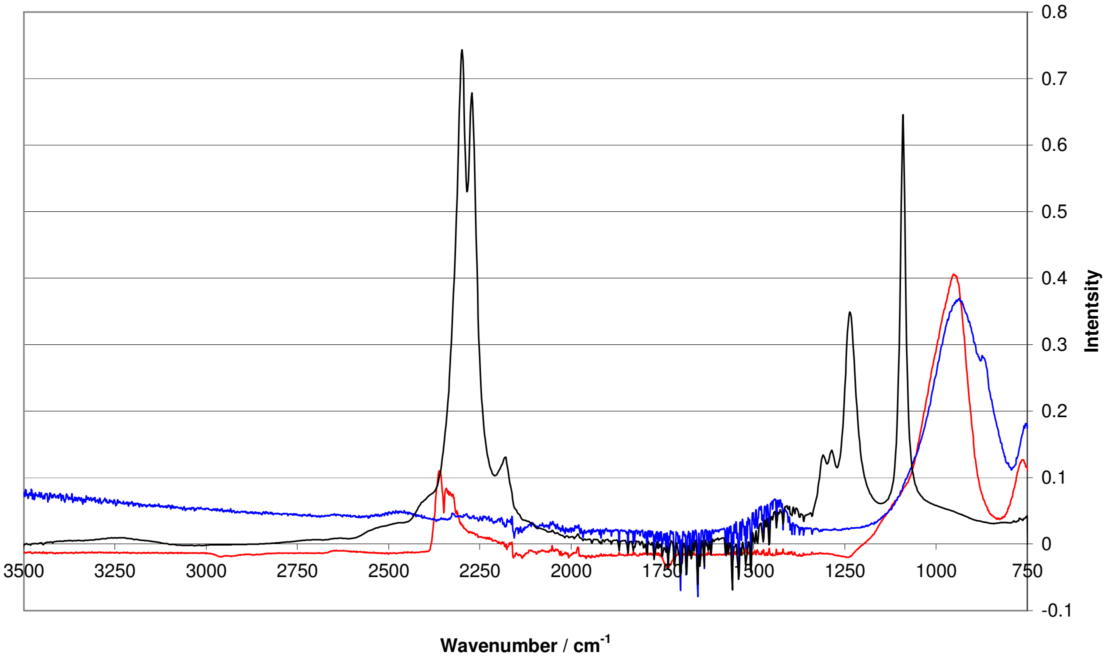

Figure 5.26 – IR spectra of $LiBH_4$ (-), $(LiBH_4)_{96}$.NaX after synthesis (-) and after heating at 420°C (-).

Figure 5.26 shows $(LiBH_4)_{96}$.NaX in which desorption shifted the framework peak from 945 to 930 cm^{-1}. This was a smaller shift, and the band was also far less broad, than in $(LiBH_4)_{224}$.NaX. The borohydride stretches at 2300 cm^{-1} and 2271 cm^{-1} were affected by atmospheric CO_2, as with $(LiBH_4)_{224}$.NaX, but were not present on desorption. Noticeably there were no shoulder peaks at ~1100 cm^{-1}.

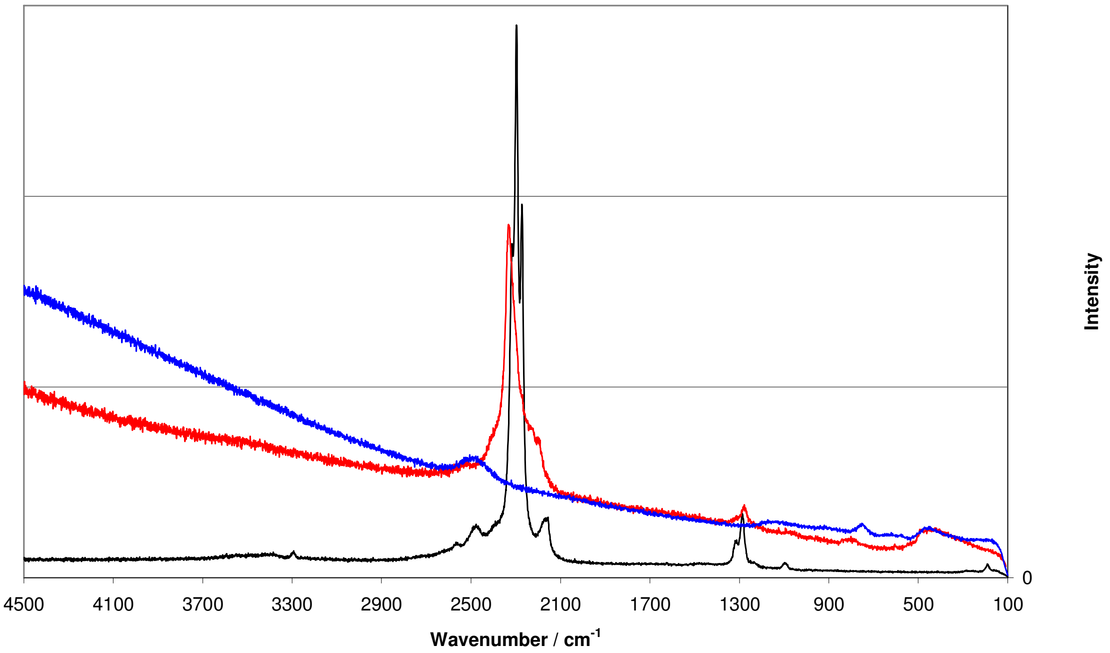

Figure 5.27 – Raman spectra of $LiBH_4$ (-), $(LiBH_4)_{224}$.NaX after synthesis (-) and after heating at 420°C (-).

For $(LiBH_4)_{224}$.NaX the broad main stretch had a maximum at 2327 cm^{-1}. A single framework peak at 500 cm^{-1} was present in the spectrum of $(LiBH_4)_{224}$.NaX.

In $(LiBH_4)_{96}$.NaX, figure 5.28, the borohydride region showed two broader peaks at 2323 and 2265 cm^{-1}. The framework peak was shifted to 542 cm^{-1}. Desorption resulted in the removal of all these peaks, in both half and fully loaded samples.

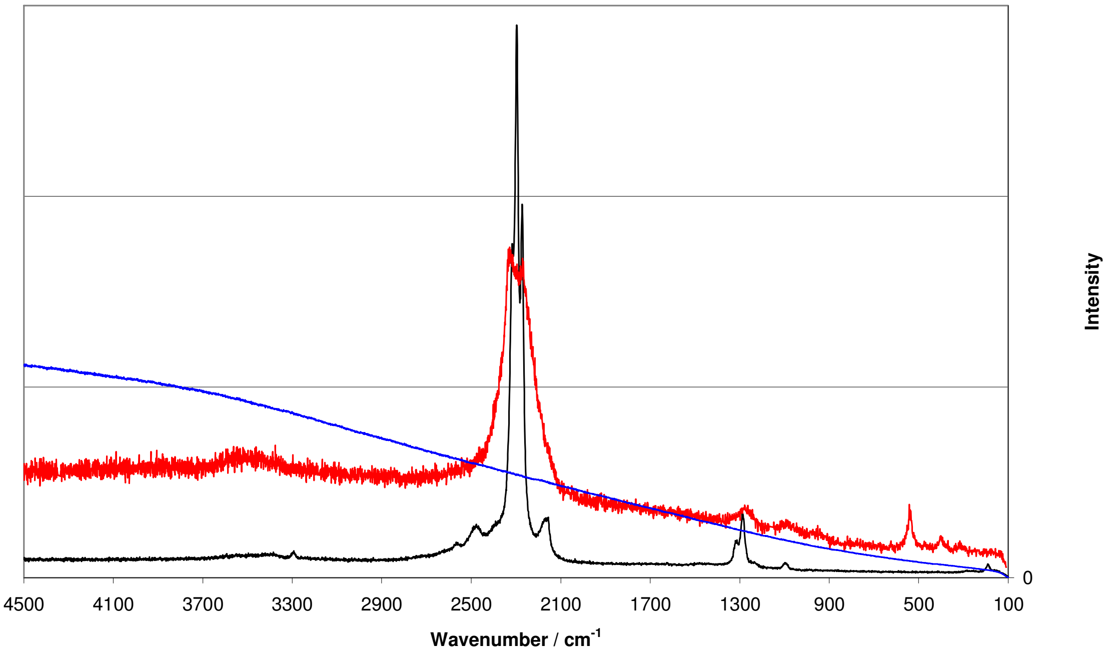

Figure 5.28 – Raman spectra of $LiBH_4$ (-), $(LiBH_4)_{96}$.NaX after synthesis (-) and after heating at 420℃ (-).

5.3.2.5 Microscopy

On analysis of SEM images of $(LiBH_4)_{224}$.NaX before and after desorption, figure 5.29a and 5.29b respectively, traces of the original octahedral crystal morphology were observed, though the particles look highly fused or perhaps coated in an amorphous material.

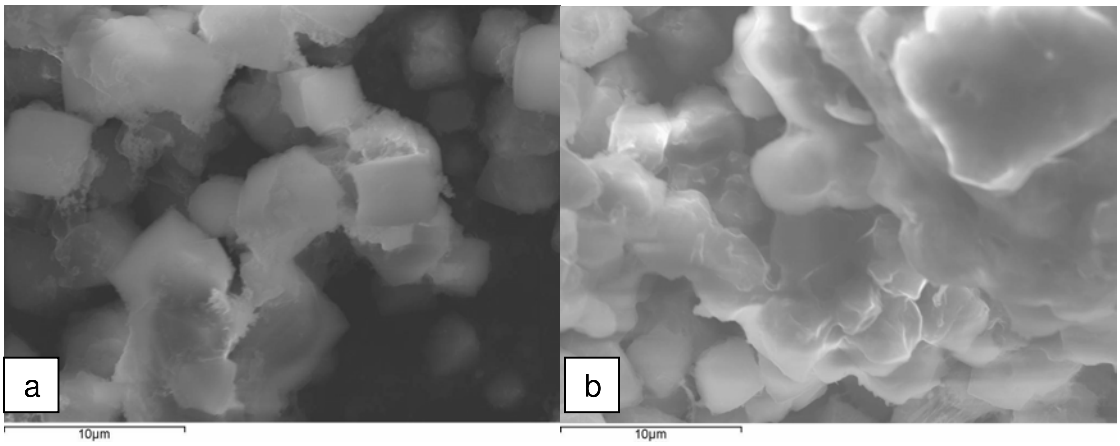

Figure 5.29 – SEM images of $(LiBH_4)_{224}$.NaX before (a) and after heating at 420℃ (b).

After desorption of $(LiBH_4)_{96}$.NaX, figure 5.29b, the regular octahedral morphologies were retained. There appeared to be some material on the surface, perhaps a desorption product.

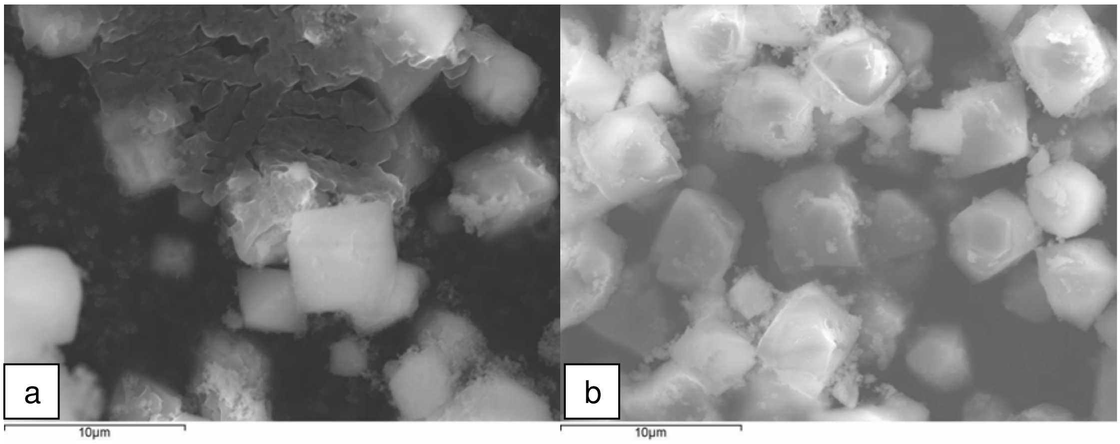

Figure 5.30 – SEM images of $(LiBH_4)_{96}$.NaX before (a) and after heating at 420℃ (b).

5.3.4 NaY with Lithium Borohydride

5.3.4.1 Desorption

Initial analysis was done by TGA-MS from 30 - 600℃ with a heating rate of 2℃ per minute. The fully loaded sample showed a mass loss of 3.5 wt%, with the onset occurring at 280℃ and continuing above 600℃ (Figure 5.31). There appeared to be a change in the rate of desorption above 400℃.

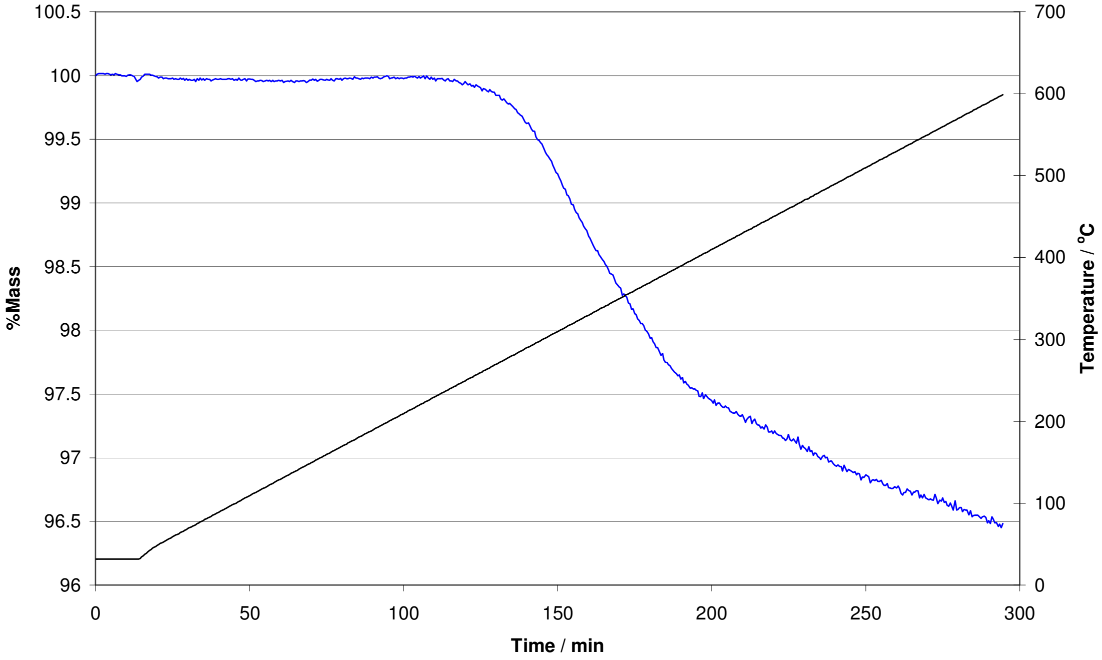

Figure 5.31 – TGA desorption trace of $(LiBH_4)_{192}$.NaY from 30 to 600℃: temperature (-); % of initial mass (-).

The weight loss was slightly lower than expected from the loading level (~3.97 wt%). The continuing desorption suggests that at 600℃ the desorption was still not complete. This could be due either to slow diffusion kinetics, or the thermal desorption of sodium borohydride. When heated to this temperature, the samples became denser and glassy, and it was decided to repeat the analysis under conditions designed to ensure the survival of the host framework.

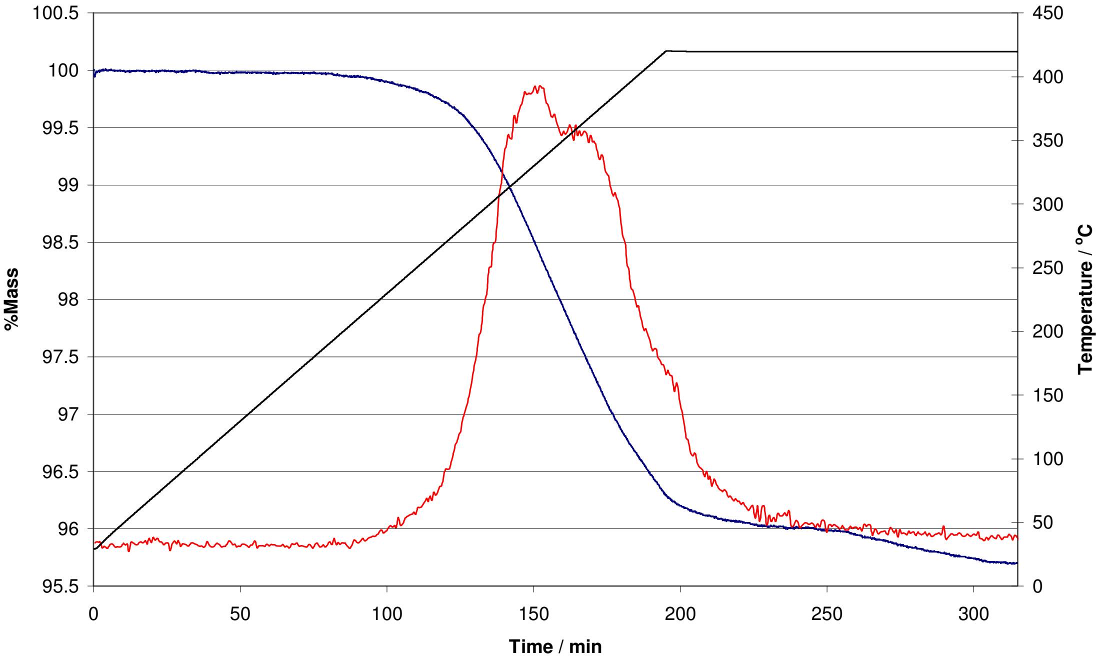

Figure 5.32 – TGA desorption trace of $(LiBH_4)_{192}.NaY$ from 30 to 420°C: temperature (-); % of initial mass (-). Hydrogen release (-) scaled to fit is also shown.

To this effect the TGA-MS was repeated between 30 and 420°C with a heating rate of 2°C per minute and a 2 hour dwell at temperature; the results are shown in figure 5.32. The fully loaded sample showed a single desorption of 4.2 wt% with an onset of 275°C. Again the greater overall desorption indicates that the decomposition of the framework observed above these temperatures may, in fact, inhibit desorption.

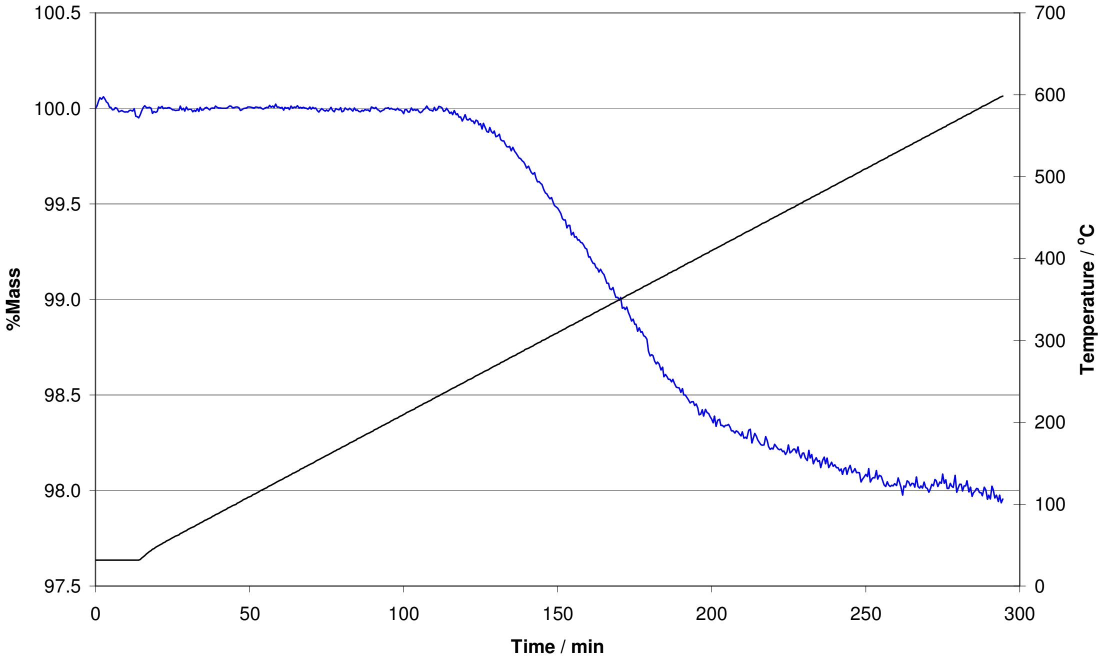

Figure 5.33 – TGA desorption trace of $(LiBH_4)_{96}$.NaY from 30 to 600℃: temperature (-); % of initial mass (-).

When the half loaded sample $(LiBH_4)_{96}$.NaY was heated to 600℃, a similar desorption, figure 5.33, was observed with an onset at 280℃ and total weight loss of 2.0 wt% by 600℃. This is again the approximate value we would expect based on the initial loading level.

Figure 5.34 shows the trace when the maximum temperature was reduced to 420℃; the half loaded sample also showed a single broad desorption of 1.4 wt% with an onset at 275℃.

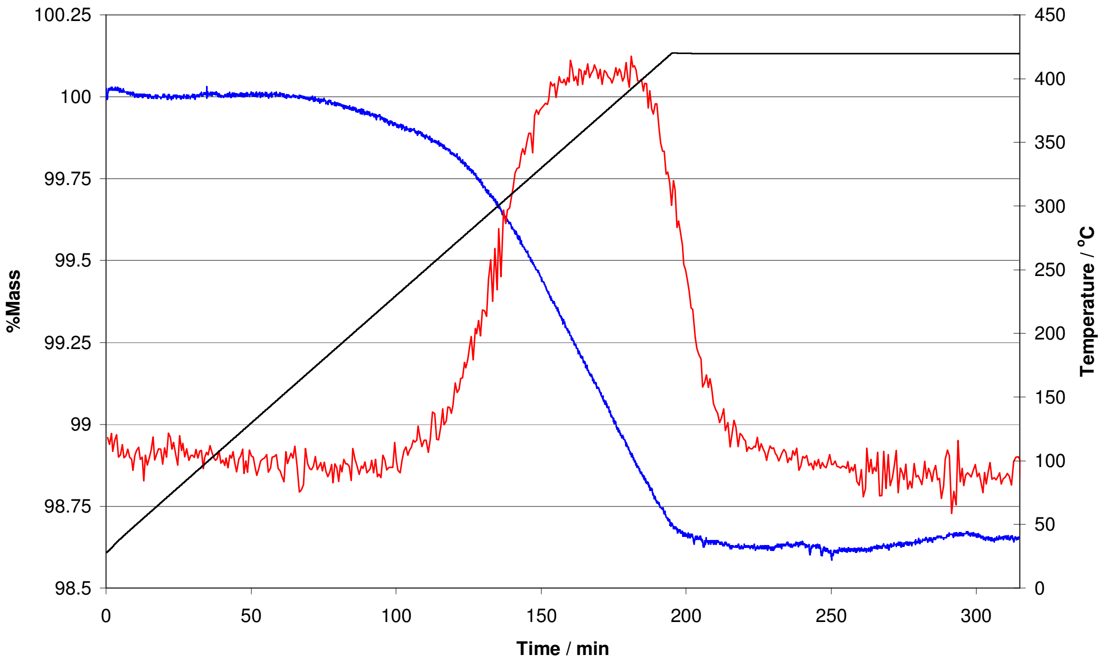

Figure 5.34 – TGA desorption trace of $(LiBH_4)_{96}$.NaY from 30 to 420°C: temperature (-); % of initial mass (-). Hydrogen release (-) scaled to fit is also shown.

5.3.4.2 Powder X-ray Diffraction

As with the previous cases the samples were analysed after desorption of the guest material. $(LiBH_4)_{192}$.NaY and $(LiBH_4)_{96}$.NaY were heated at 420°C for 18 hours to bring desorption to completion. Both samples were grey in contrast to the previous cases (NaA and NaX) where the samples were often brown, most likely due to the presence of amorphous boron.

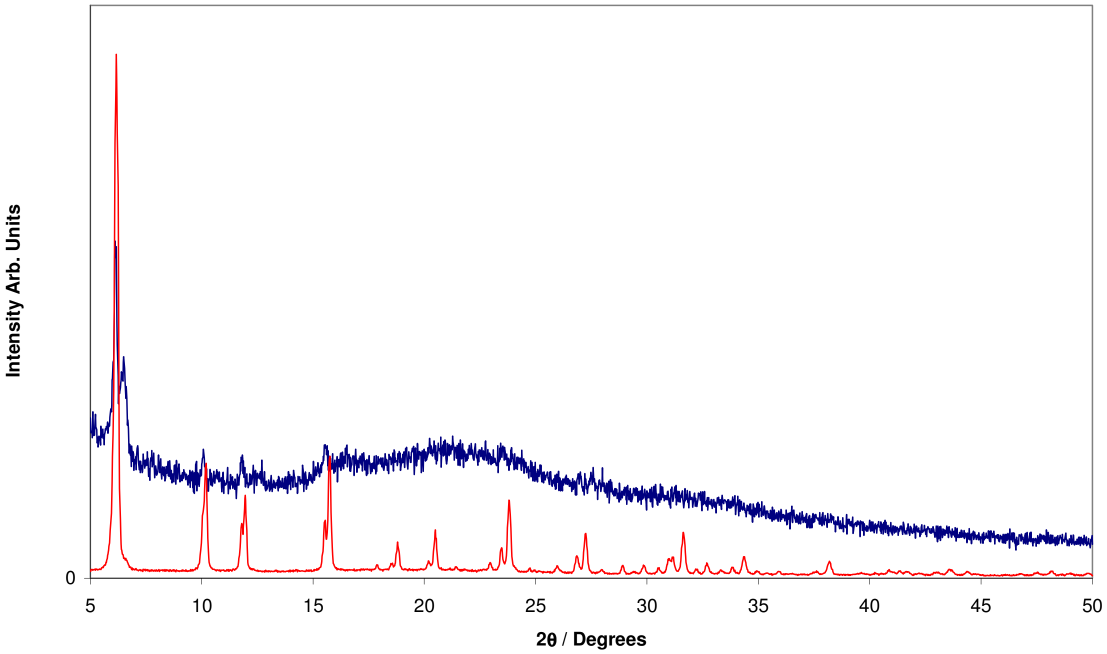

Figure 5.35 – Powder XRD pattern showing $(LiBH_4)_{192}$.NaY after synthesis (-) and after desorption at 420°C (-).

These desorbed samples had rather poor diffraction patterns which showed poor long range order in $(LiBH_4)_{96}$.NaY and little or no remaining crystalline material in $(LiBH_4)_{192}$.NaY (Figures 5.35 and 5.36 respectively). On comparison of the XRD patterns a single phase was estimated at 24.8 (1) Å and observed at 24.76(7) Å for $(LiBH_4)_{192}$.NaY and $(LiBH_4)_{96}$.NaY, respectively. This compares with the original loaded phase lattice parameters of 24.44(3) and 24.58(4) Å for $(LiBH_4)_{192}$.NaY and $(LiBH_4)_{96}$.NaY, respectively. Again the values of the desorbed sample tended towards those of the dehydrated zeolite.

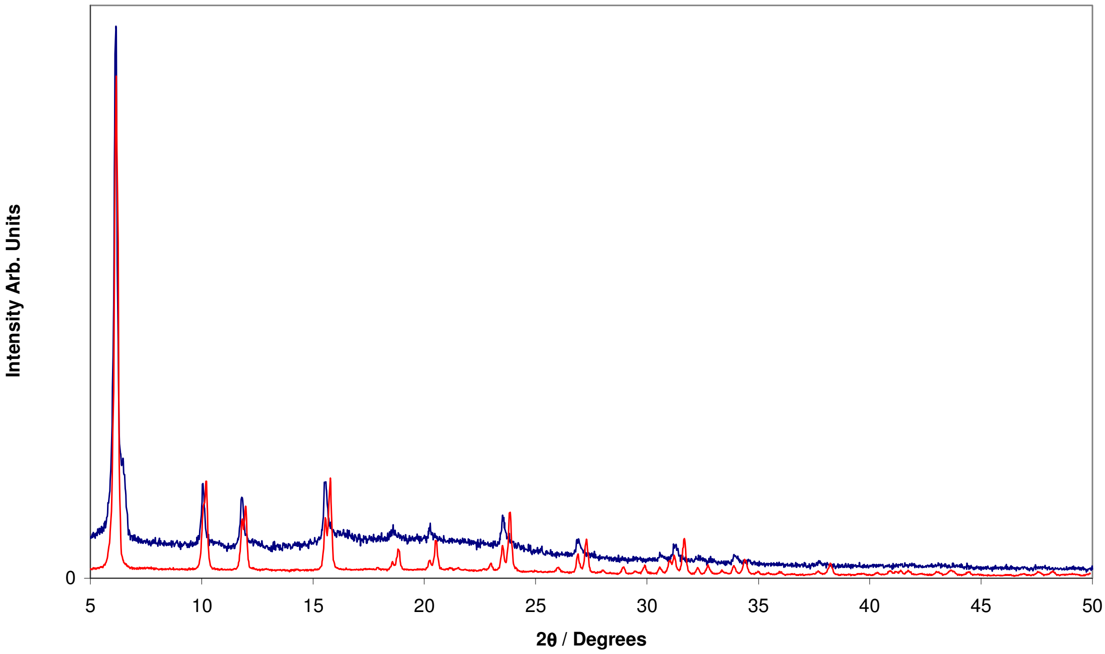

Figure 5.36 – Powder XRD pattern showing $(LiBH_4)_{96}$.NaY after synthesis (-) and after desorption at 420°C (-).

$(LiBH_4)_{96}$.NaY showed only one phase after desorption, indicating homogenisation within the zeolite pores.

5.3.4.3 Vibrational Spectroscopy

Figure 5.37 shows IR spectra of $(LiBH_4)_{192}$.NaY before and after desorption. On desorption the framework peak peak was broadened and shifted in its position to 906 cm^{-1} from 966 cm^{-1}, indicating a significant change in structure. There was a broad borohydride feature peaking at 2310 cm^{-1}, which disappeared on desorption. On desorption the entire spectrum was featureless, showing that the borohydride was no longer present. The removal of the small peak at 495 cm^{-1} indicates the disappearance of any interactions with the framework, possibly due to the collapse of the framework.

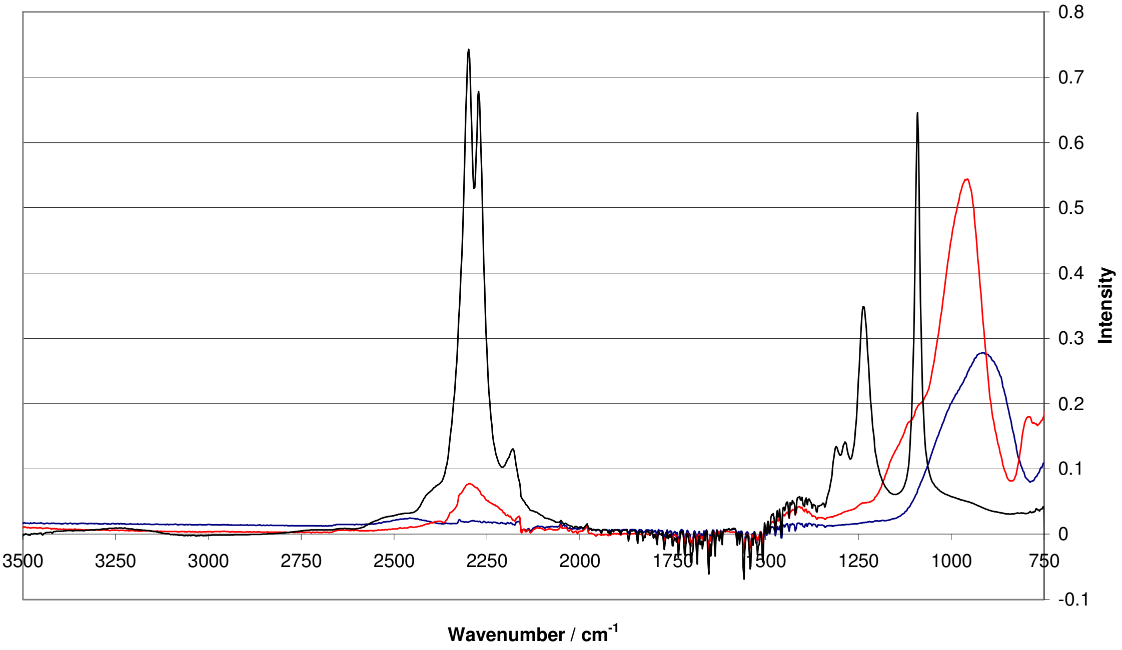

Figure 5.37 – IR spectra of $LiBH_4$ (-), $(LiBH_4)_{192}$.NaY before (-), and after (-) heating at 420°C.

The half loaded sample $(LiBH_4)_{96}$.NaY showed a similar set of effects (Figure 5.38). The feature at 2300 cm^{-1} was completely removed on desorption, indicating the decomposition of borohydride. The effect on the framework after desorption was less in comparison to $(LiBH_4)_{192}$.NaY with a reduced broadening of the peak at 996 cm^{-1}. The broadening and shift confirm that the framework was under strain and collapsing, but to a slightly lesser extent than $(LiBH_4)_{192}$.NaY.

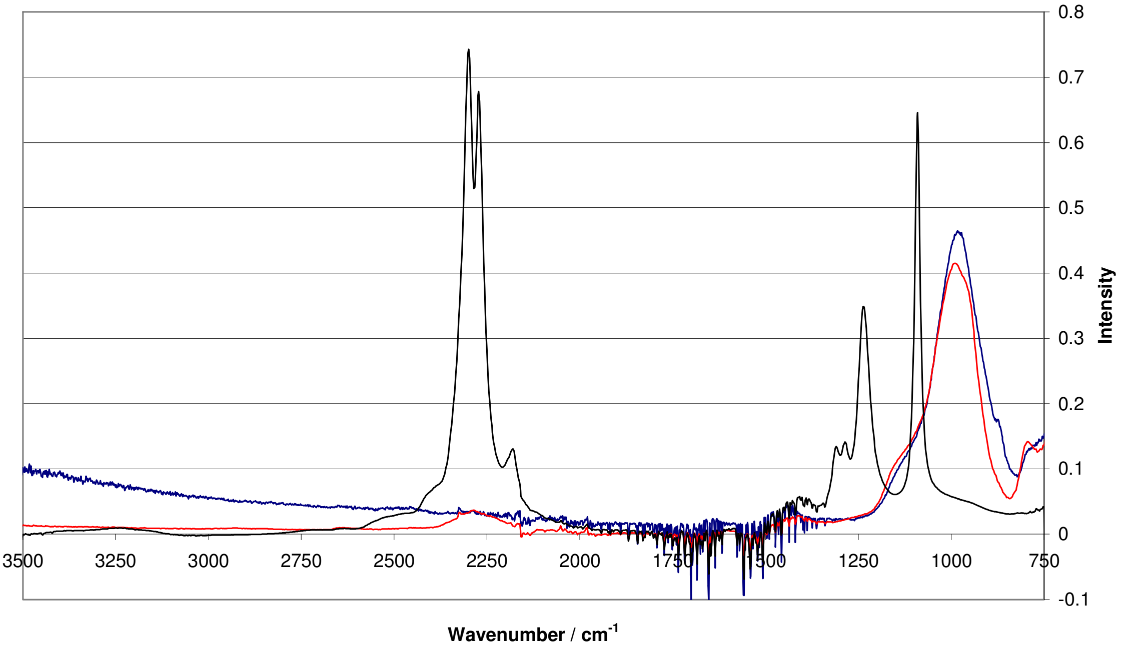

Figure 5.38 – IR spectra of $LiBH_4$ (-), $(LiBH_4)_{96}$.NaY before (-), and after (-) heating at 420°C.

The Raman spectra (Figures 5.39 & 5.40) of the zeolite Y samples were similar to those of the other zeolites, with the borohydride peak at 2325 cm^{-1}.

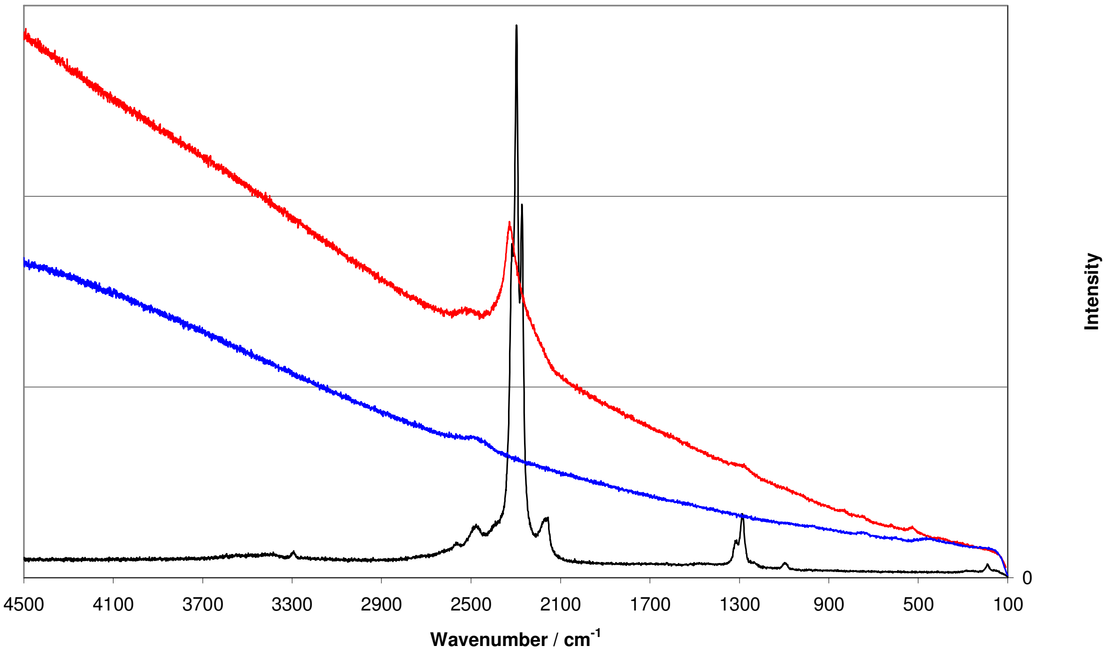

Figure 5.39 – Raman spectra of $LiBH_4$ (-), $(LiBH_4)_{192}$.NaY before (-), and (-) after desorption at 420°C.

The $(LiBH_4)_{96}$.NaY sample (figure 5.40) in contrast to all the other samples showed only a small broad feature at 2300 cm^{-1}, and again the small framework peak at 495 cm^{-1}. These features again disappeared on desorption.

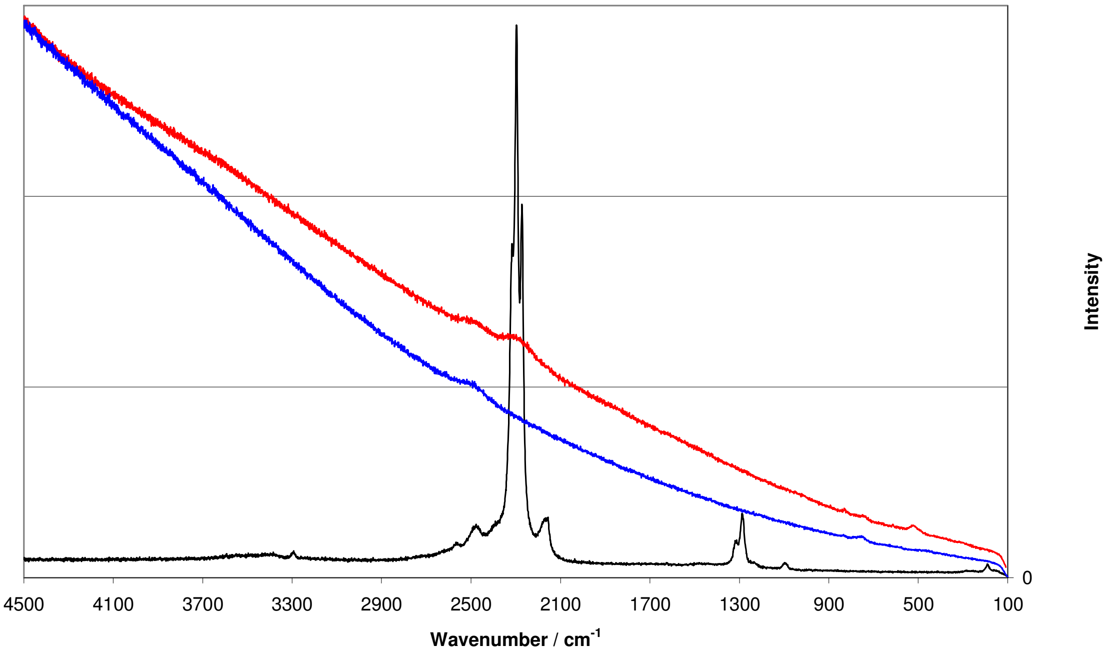

Figure 5.40 – Raman spectra of $LiBH_4$ (-), $(LiBH_4)_{96}$.NaY before (-),and after desorption at 420°C (-).

5.3.4.4 Microscopy

SEM images for $(LiBH_4)_{192}$.NaY (Figure 5.41) showed fine octahedral particles as expected from a faujasite-type zeolite. On desorption of the sample the morphology was retained.

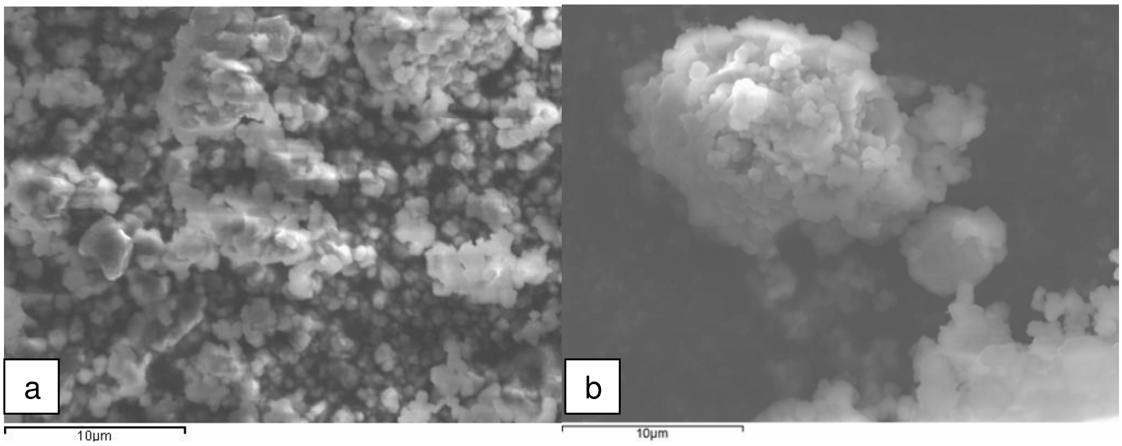

Figure 5.41 – SEM images of $(LiBH_4)_{192}$.NaY before (a) and after desorption at 420°C (b).

Analysis of the half loaded sample showed similar results in figure 5.42, with the morphology again retained on desorption.

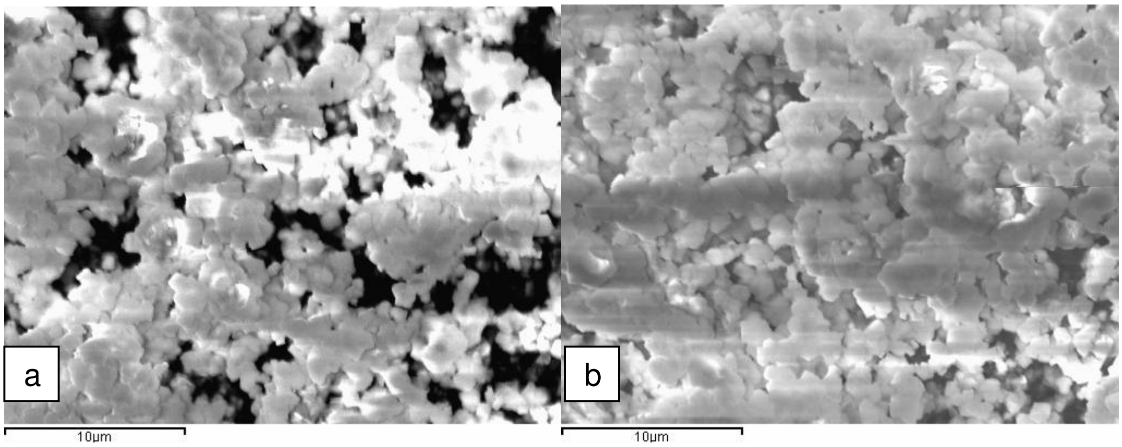

Figure 5.42 – SEM images of $(LiBH_4)_{96}$.NaY before (a) and after desorption at 420°C (b).

5.4 Conclusion

Desorption of occluded lithium borohydride was shown to break apart the host framework, reducing its stability compared with an unloaded dehydrated zeolite.

The effect of desorption on the zeolite framework was also apparent in IR spectra, which showed a shift and broadening in the framework peaks. On desorption the Raman spectra were featureless indicating that the borohydride had decomposed; removal of the framework peaks corroborated the framework collapse.

SEM analysis showed that the morphology of the host crystals remained largely unchanged after desorption.

The desorption profiles obtained from TGA-MS and by vacuum desorption of the loaded samples were significantly different from those of bulk lithium borohydride. Although the initial onset of desorption occurred at the same temperature, the overall desorption appeared to be slower, with the second desorption peak overlapping the first. This second desorption step was shown to be concurrent with the decomposition of the framework, and is associated with the framework collapse. When repeated at lower temperatures the host structure was maintained, and only one desorption was observed. In some cases the reduction of temperature for desorption resulted in no reduction in hydrogen desorbed, suggesting that the framework can lower the desorption temperature relative to bulk lithium borohydride. Higher temperatures causing framework collapse may result in reduced desorption by inhibiting diffusion.

5.5 References

1. Breck D. W., Eversole W. G., Milton R. M., Reed T. B., Thomas T. L., *J. Am. Chem. Soc.*, **1956**, 78, 5963
2. Züttel A., Rentsch S., Fisher P., Wenger P., Sudan P., Mauron Ph., Emmenegger Ch., *J. Alloys Comp.*, **2003**, 356-357, 515
3. Harvey K. B., McQuaker N. R., *Canadian J. Chem.*, **1971**, 49, 3282
4. Gomes S., Hagemann H., Yvon K., *J. Alloys Comp.*, **2002**, 346, 206
5. No K. T., Seo B. H., Jhon M. S., *Theor. Chim. Acta*, **1989**, 75, 307
6. Auerbach S. M., Carrado K. A., Dutta P. K., *Handbook of Zeolite Science and Technology*, **2003**.

CHAPTER 6

ADSORPTION OF HYDROGEN BY SODIUM ZEOLITES A, X & Y, CONTAINING LITHIUM BOROHYDRIDE.

6.1 Introduction

Chapter 4 showed the structural changes that occur when lithium borohydride is successfully occluded in zeolites NaA, NaX and NaY. Chapter 5 showed that there were some changes to the desorption of lithium borohydride and with it there were effects on the framework. This chapter follows the adsorption properties of the host–guest material and hydrogenation at elevated temperature to show the potential uptake of the guest after desorption. Low temperature adsorptions were performed for comparison with the host framework. Heats of adsorption were obtained on a sample to determine changes in physisorption properties due to the presence of a guest species.

6.2 Experimental

Samples NaA and NaX were synthesised as detailed in the experimental chapter; NaY (13Y) and $LiBH_4$ (>90%) were obtained from Sigma-Aldrich.

Sample preparation was performed as outlined in Section 4.2.

Samples were analysed by gravimetric methods. The hydrogen uptake measurements were performed above room temperature and at 77 K using high purity hydrogen.

6.3 Results and Discussion

This section is broken down into three parts starting with the high temperature hydrogenation of the desorbed guest. The second part will focus on the adsorption at 77 K, with the final part showing heat of adsorption data collected for $(LiBH_4)_{96}$.NaX.

6.3.1 High Temperature Hydrogenation

Lithium borohydride when desorbed under suitable conditions yields LiH and boron as its products[1]. Research has shown that hydrogenation of lithium borohydride is achievable at 600℃ and 155 bar[2]. The fully loaded and half loaded samples were analysed using ramped temperature isobars at elevated temperature of samples outgassed at above 275℃ but no higher than 420℃, to investigate hydrogenation of decomposed samples.

6.3.1.1 NaA with Lithium Borohydride

$(LiBH_4)_{128}$.NaA was outgassed at 375℃ for 36 hours and was shown to lose approximately 4 wt%.

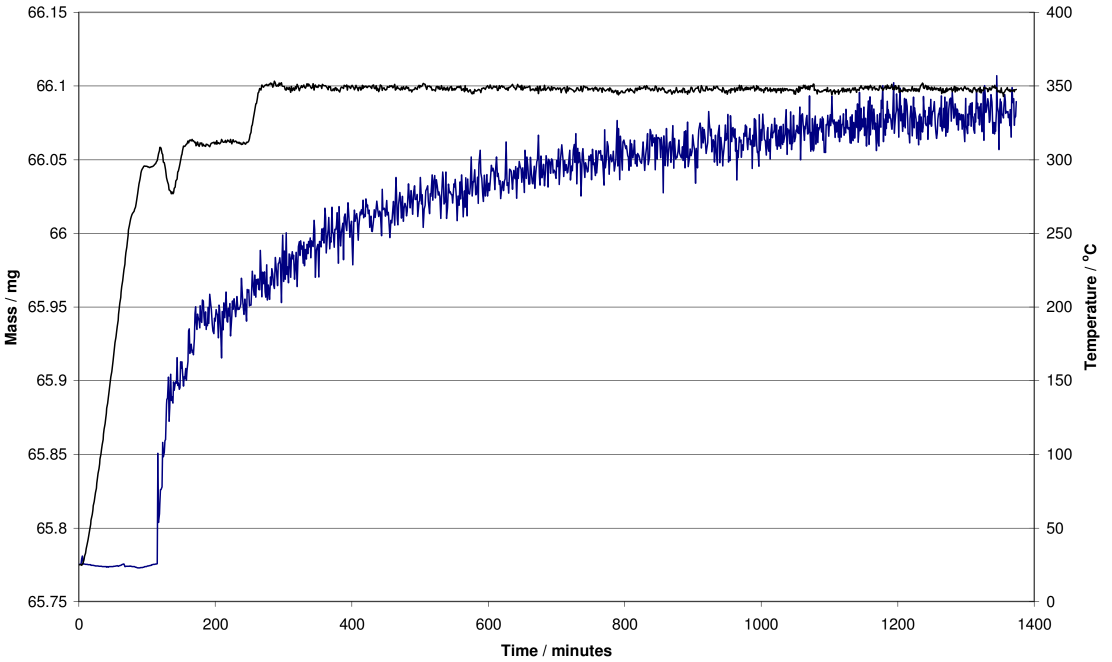

Figure 6.1 – Adsorption isobar at 18 bar between 25 and 350°C for $(LiBH_4)_{128}$.NaA after degassing for 36 hours at 375°C; (-) denotes temperature in Celsius and (-) denotes the mass in milligrams (buoyancy corrected).

$(LiBH_4)_{128}$.NaA was treated under 18 bar hydrogen, whilst the temperature was ramped to a maximum of 350°C, shown in figure 6.1. This was to determine if the lithium borohydride desorption products (lithium hydride and boron) could be hydrogenated at above ambient pressure and temperature. We observed here a weight increase of approximately 0.50 wt% at temperatures up to 348°C over an 18 hour period. The sample required elevated heating (360°C) and vacuum to observe the same weight in loss, physisorption of hydrogen would not require these increased temperatures to see the desorption of hydrogen. This showed the sample was hydrogenating at lower temperatures and lower pressures than expected for bulk $LiBH_4$, which occurs at 600°C and 155 bar. Interestingly, 350°C was above the temperature at which this sample began to desorb hydrogen, but the rehydrogenation appeared to starts at 300°C. It appears that the segregation of the desorption products on a nanoscale rather than into bulk phases may aid rehydrogenation.

$(LiBH_4)_{64}$.NaA was desorbed at 360℃ for 48 hours, to generate the desorbed guest material; this was accompanied by a weight loss of 0.6%. The adsorption was performed with an isobaric run at 18 bar up to 350℃ (Figure 6.2). The slight upward trend shown is typical of drift in the system, and could be caused by minor impurities. The observed mass gain was removed on evacuation and cooling of the sample implying no hydrogenation had occurred. Further heating to 360℃ for 36 hours showed no further weight loss

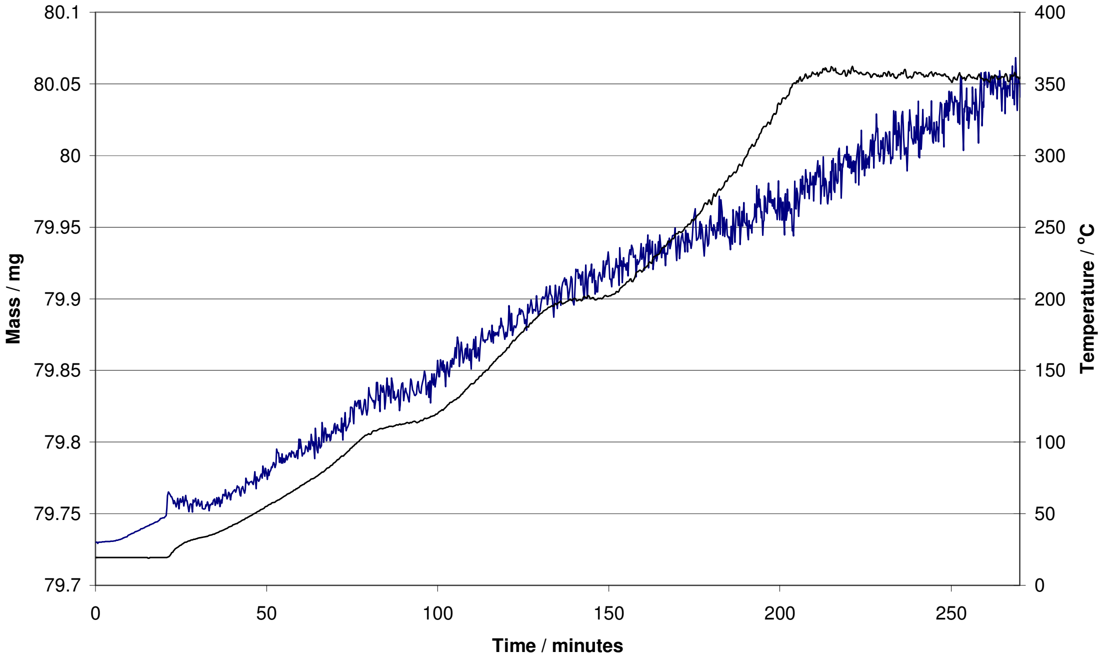

Figure 6.2 – Adsorption isobar at 18 bar between 25 and 350℃ for $(LiBH_4)_{64}$.NaA after degassing for 36 hours at 375℃; (-) denotes temperature in Celsius and (-) denotes the mass in milligrams (buoyancy corrected).

This would indicate that even though the lithium hydride and boron were intimately mixed, there was no reaction. The initial desorption showed only around 30% of the expected desorption from the half loaded sample, ~2 wt%. It could be possible that the $LiBH_4$ is only partly desorbed and very little would be expected to re-hydrogenate.

6.3.1.2 NaX with Lithium Borohydride

$(LiBH_4)_{224}$.NaX was outgassed at 410℃ for 24 hours and a weight loss of 4 wt% was observed. When the outgassed sample was treated at 18 bar of hydrogen whilst ramping in temperature to 360℃ a small uptake of 0.2 wt% was observed, shown in figure 6.3. This uptake was slightly less than NaA under similar conditions (at 348℃ and 18 bar for 18 hours), where 0.50 wt% was absorbed.

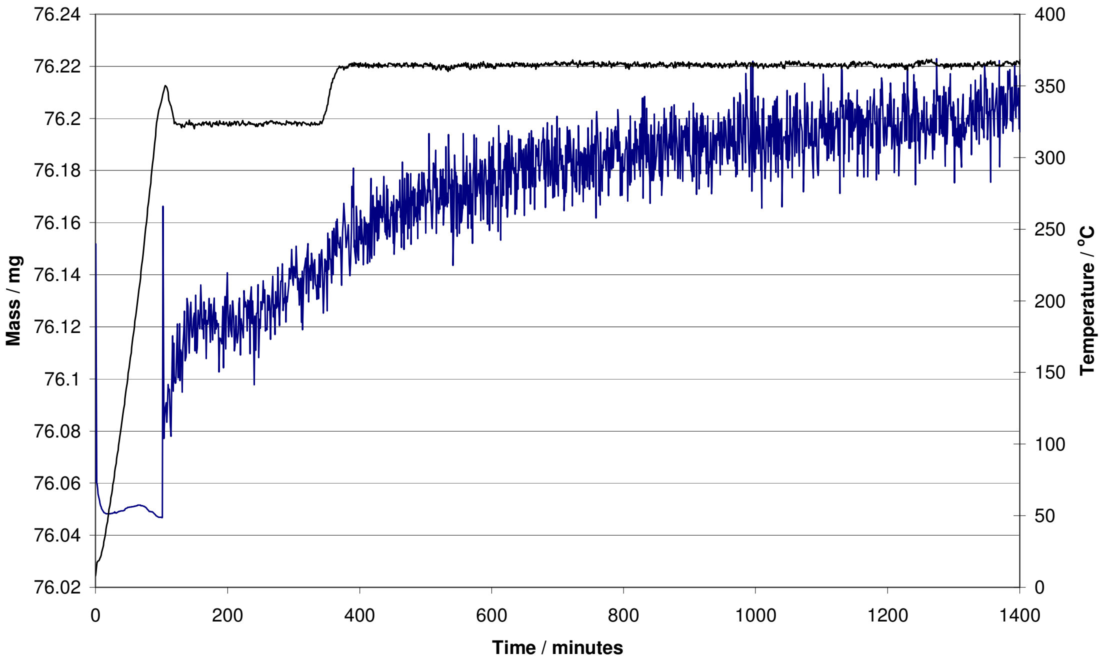

Figure 6.3 – Adsorption isobar at 18 bar between 25 and 350℃ for $(LiBH_4)_{224}$.NaX after degassing for 36 hours at 375℃, (-) denotes temperature in Celsius and (-) denotes the mass in milligrams (buoyancy corrected).

The lower uptake than NaA at high temperature, may revolve around the fact that powder XRD suggests that the structure of zeolite A was not quite so badly damaged on desorption as zeolite X (shown in section 5.3.2.2).

$(LiBH_4)_{92}$.NaX was outgassed at 350℃ over 48 hours resulting in a mass loss of 1.0 wt%.This sample when treated at 18 bar from room temperature up to 360℃ showed no measureable uptake. Some framework degradation from the desorption hay have been inhibiting the access to allow hydrogenation.

6.3.1.3 NaY with Lithium Borohydride

On degassing at 364℃ for 36 hours, $(LiBH_4)_{192}$.NaY desorption showed a weight loss corresponding to 3.0 wt%. This was followed by an isobaric measurement at 18 bar, with temperature ramped to 350℃, which showed no detectable uptake. $(LiBH_4)_{96}$.NaY was heated at 366℃ for 24 hours and showed a small desorption of approximately 1.5 wt%. The subsequent isobaric measurement at 18 bar between room temperature and 345℃ saw no uptake, with only buoyancy effects being observed.

6.3.2 Low Temperature Adsorption

The next task was to investigate the adsorption potential of these systems. Zeolites are usually considered as cryogenic storage materials. With this in mind two different regimes were used for adsorption experiments on the IGA:

- 77 K isotherms of parent sample outgassed at no higher than 120℃, to investigate physisorption on loaded samples;
- 77 K isotherms of sample outgassed at above 275℃ but no higher than 420℃, to investigate physisorption on samples after desorption at elevated temperature.

6.3.2.1 NaA with Lithium Borohydride

After outgassing at room temperature, $(LiBH_4)_{128}$.NaA showed no uptake up to 15 bar at 77 K. This confirms that the pores were essentially filled with loaded materials. The sample was then degassed at 375℃ for 36 hours and was shown to lose approximately 4 wt%. The isotherm of $(LiBH_4)_{128}$.NaA after degassing at 375℃ also showed an negligible uptake.

$(LiBH_4)_{64}$.NaA showed no weight loss, after an initial outgas at room temperature for 48 hours, and minimal uptake was observed. It was decided to outgas the sample at 120℃ for 24 hours, in case impurities had contaminated the surface of the sample; a weight loss of approximately 0.4 wt% was observed.

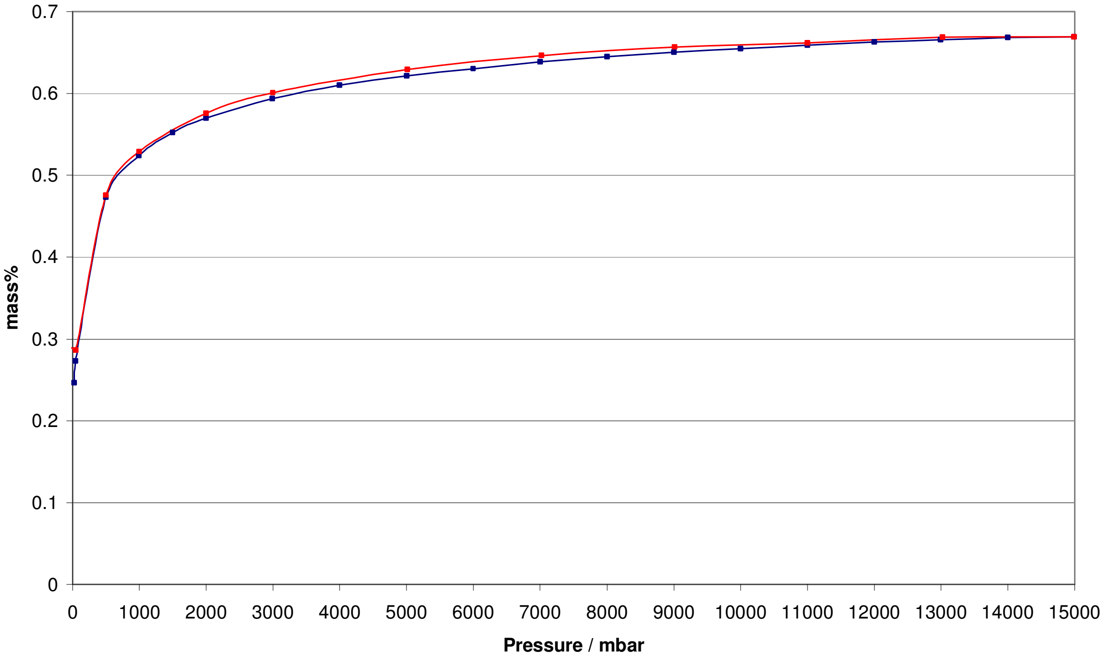

Figure 6.4 – Adsorption and desorption isotherm at 77 K $(LiBH_4)_{64}$.NaA after degassing for 24 hours at 120℃; (-) shows the adsorption whilst (-) shows the desorption.

Figure 6.4 shows the isotherm after the outgas at 120°C for $(LiBH_4)_{64}$.NaA. This time a significant adsorption was observed, showing an uptake of approximately 0.65 wt% to 15 bar at 77 K. This corresponds to 42% of that of the parent host zeolite[3].

A further desorption was performed at 360°C for 48 hours, to generate the desorbed guest material; this was accompanied by a weight loss of 0.6%. The resulting compound adsorbed 0.35 wt% at 77 K (Figure 6.5).

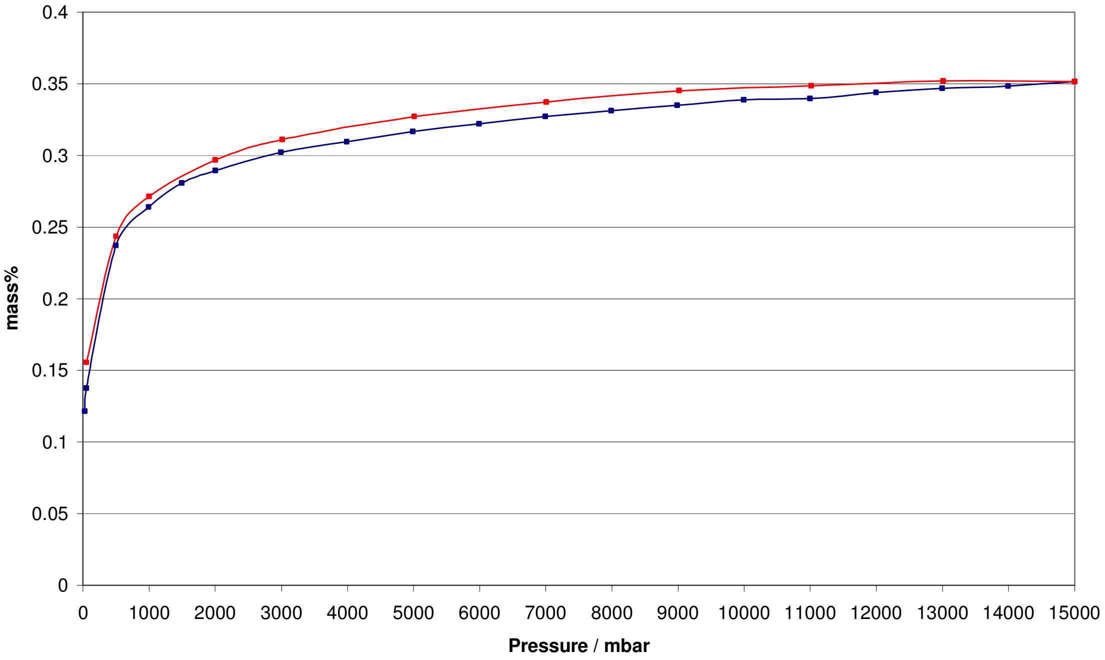

Figure 6.5 – Adsorption and desorption Isotherm at 77 K of $(LiBH_4)_{64}$.NaA after degassing for 48 hours at 360°C, (-) shows the adsorption whilst (-) shows the desorption.

There was a reduction in uptake between the low temperature and high temperature outgas, figures 6.7 and 6.8 respectively. Between these two measurements the $LiBH_4$ had been desorbed. The desorption process may cause some previously available pores to be blocked by the products of decomposition or loss of structure from the host material, thus reducing the uptake.

6.3.2.2 NaX with Lithium Borohydride

After an initial outgas at room temperature over 24 hours, which showed no weight loss, an isotherm was performed at 77 K from 50 mbar to 15 bar and a negligible adsorption was observed. This result is largely unsurprising as the zeolite pores were completely blocked by the guest material.

On further degassing at 410℃ for 24 hours, a weight loss of 4 wt% was observed. The adsorption isotherm at 77 K which followed again showed insignificant uptake.

$(LiBH_4)_{96}$.NaX was treated in a similar fashion. After an initial degassing at room temperature for 24 hours an isotherm was performed. Figure 6.6 shows a deviation between adsorption and desorption, several kinetic points timed out through mass drift, whilst the isotherm suggested an uptake of 0.6 wt%.

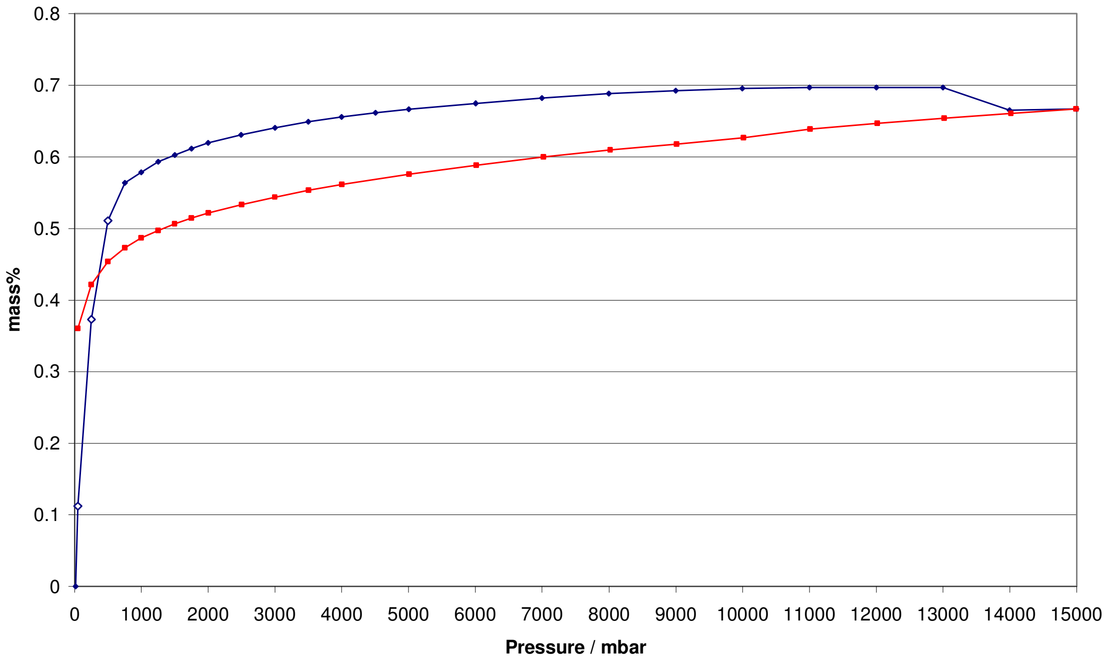

Figure 6.6 – Adsorption (-) and desorption (-) isotherms at 77 K of $(LiBH_4)_{96}$.NaX after degassing for 24 hours at room temperature.

The suggestion that the adsorption may be hindered or interfered with by contaminants, resulting in the deviation between adsorption and desorption, led to a repeat measurement with an outgas at higher temperature. This was performed at 95°C for 48 hours and resulted in a weight loss of 0.3 wt%.

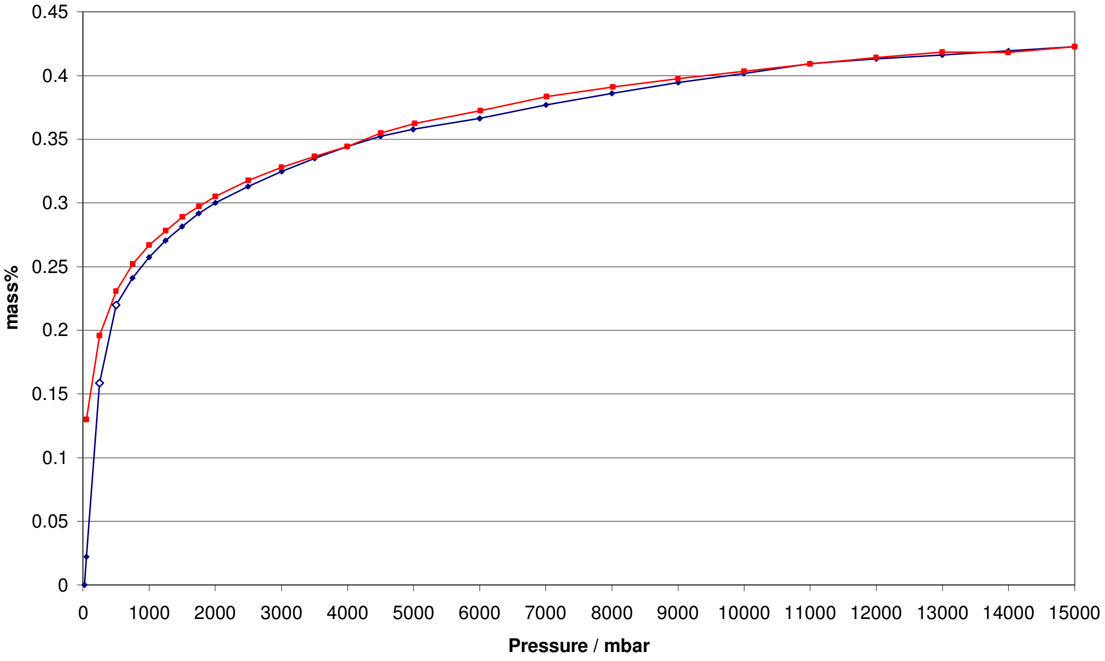

Figure 6.7 – Adsorption (-) and desorption (-) isotherms at 77 K of $(LiBH_4)_{96}$.NaX after degassing for 24 hours at 95°C.

The isotherm, figure 6.7, showed a reversible uptake of 0.42 wt%; this indicates that there was some form of impurity present in the previous isotherm, possibly a small amount of water. The parent zeolite showed an uptake of 1.79 wt% so this sample actually showed a capacity of around 24% of the original zeolite. This greatly reduced amount can be put down to pore blocking or loss of structure.

The sample was outgassed at 350°C over 48 hours resulting in a mass loss of 1.0 wt%.

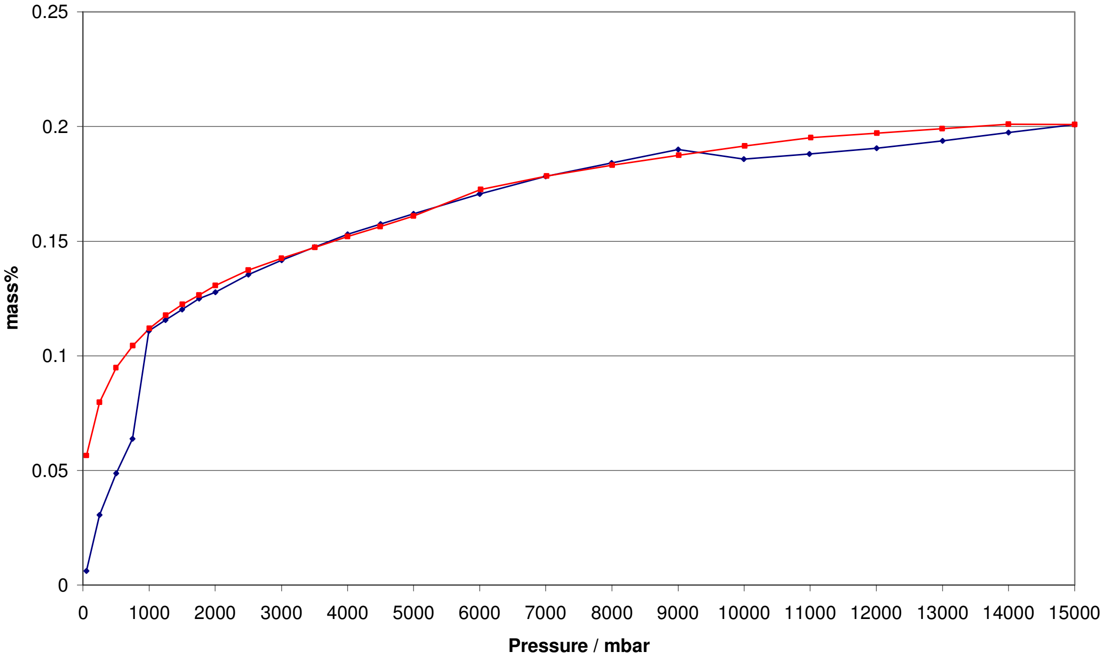

Figure 6.8 – Adsorption (-) and desorption (-) isotherms at 77 K of $(LiBH_4)_{96}$.NaX after degassing for 48 hours at 350°C.

Figure 6.8 shows the isotherm after degassing. An uptake of 0.20 wt% was observed, a marked reduction on the previously desorbed sample. This is likely due to desorption of the hydrogen from the guest lithium borohydride leading to a lower internal surface area due to pore blocking or through loss of structure.

6.3.2.3 NaY with Lithium Borohydride

$(LiBH_4)_{192}$.NaY was outgassed initially at 45°C for 36 hours, with a negligible weight loss over this period. Figure 6.9 shows the isotherm at 77 K showed an uptake of about 0.18 wt% with a little noise.

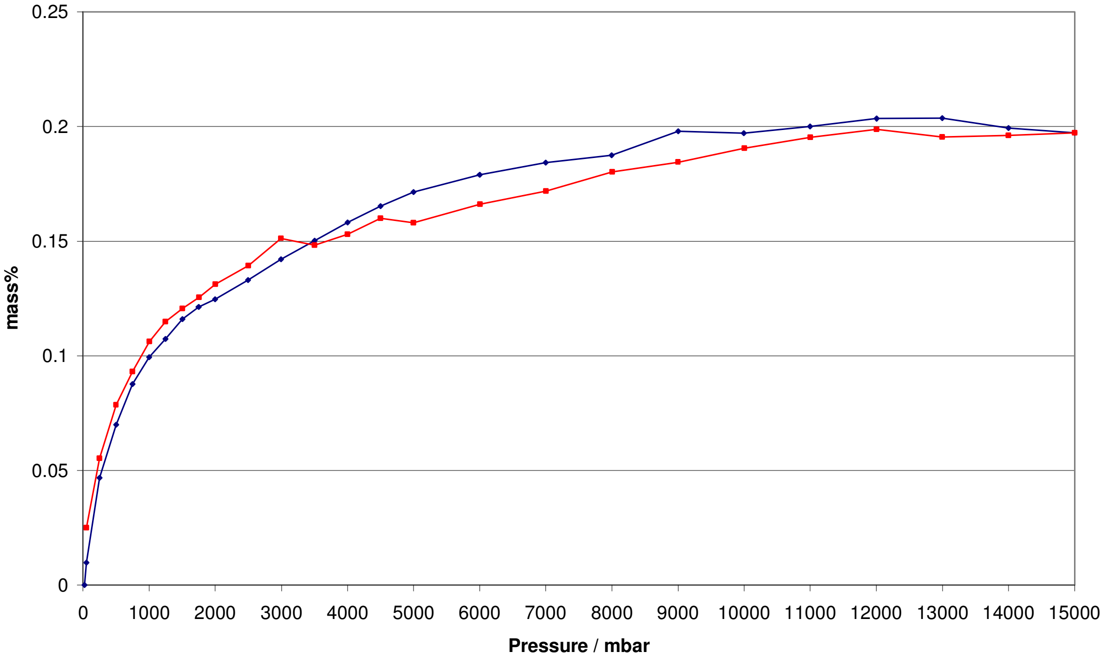

Figure 6.9 – Adsorption and desorption isotherms at 77 K of $(LiBH_4)_{192}$.NaY after degassing for 36 hours at 45℃; (-) shows the adsorption whilst (-) shows the desorption.

On further desorption at 364℃ for 36 hours, a weight loss corresponding to 3.0 wt% was observed. This sample was again measured at 77 K and no adsorption was observed.

The decrease in measured adsorption was probably due to the blocking of some pores following the desorption, as has been observed with the other zeolites. One noticeable difference was that there was measurable adsorption, unlike the other fully loaded samples where no significant adsorption was observed. This could suggest the sample was not fully loaded but the diffraction pattern suggested otherwise. Clearly, however, some of the framework pore space remained empty after loading.

$(LiBH_4)_{192}$.NaY was treated in a similar fashion. The initial outgas at 55℃ for 36 hours produced a negligible weight loss.

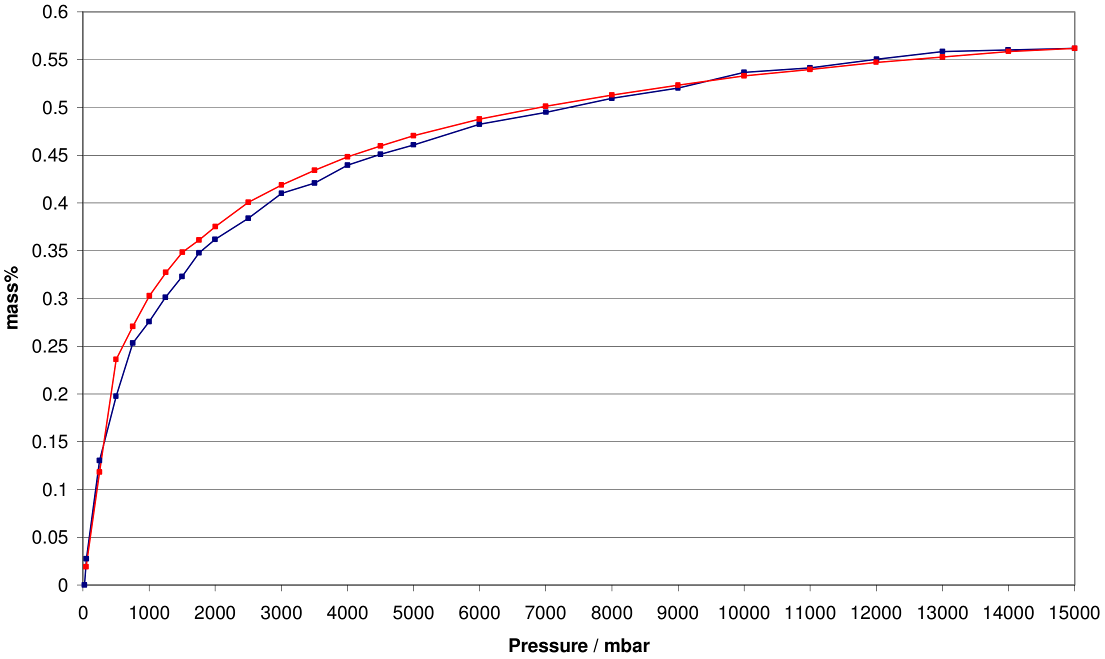

Figure 6.10 – Adsorption and desorption isotherms at 77 K of $(LiBH_4)_{96}$.NaY after degassing for 36 hours at 55°C; (-) shows the adsorption whilst (-) shows the desorption.

The adsorption (figure 6.10) at 77 K that followed showed an uptake of 0.57 wt%, corresponding to 32% of capacity of the parent NaY (1.81 wt%).

Heating at 366°C for 24 hours showed a small desorption of approximately 1.5 wt%.

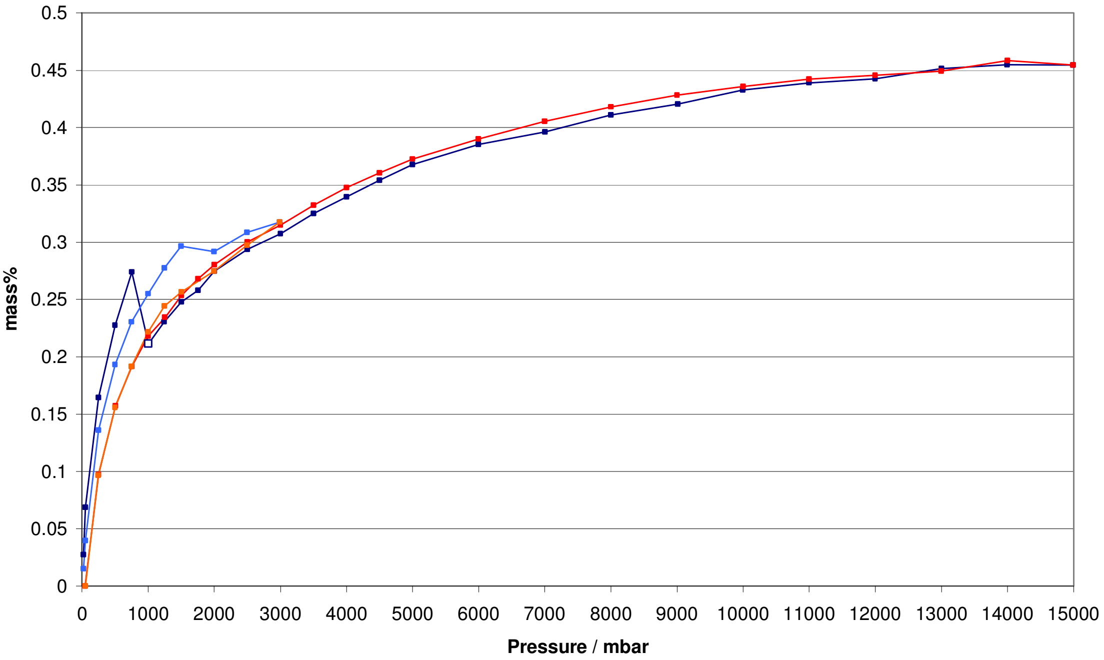

Figure 6.11 – Adsorption and desorption isotherms at 77 K of $(LiBH_4)_{96}$.NaY after degassing for 24 hours at 366℃; (-) shows the adsorption whilst (-) shows the desorption. A short adsorption (-) and desorption (-) followed.

The isotherm of $(LiBH_4)_{96}$.NaY at 77K after degassing at 366℃ showed an uptake of 0.45 wt%. This reduced quantity is indicative of the pore blocking that has been observed when the guest lithium borohydride is desorbed. There appeared to be some deviation between the adsorption and desorption. The experiment was repeated and showed that there was a buoyancy effect causing increased uptake at lower pressures.

6.3.3 Heats of Adsorption in $(LiBH_4)_{96}$.NaX

$(LiBH_4)_{96}$.NaX exhibited adequate uptake values for both before and after desorption to permit exploration of the ability of the guest to enhance the binding of hydrogen to the zeolite measuring the heat of adsorption (ΔH_{ads}). For this, measurements were performed at 77 and 87 K as follows:

- 77 and 87 K isotherms of parent sample outgassed at no higher than 120℃;
- 77 and 87 K isotherms of sample outgassed at above 275℃ but no higher than 420℃.

The isotherms at 77 and 87 K for desorption at 50℃ and 360℃ are shown in figures 6.12 and 6.13, respectively.

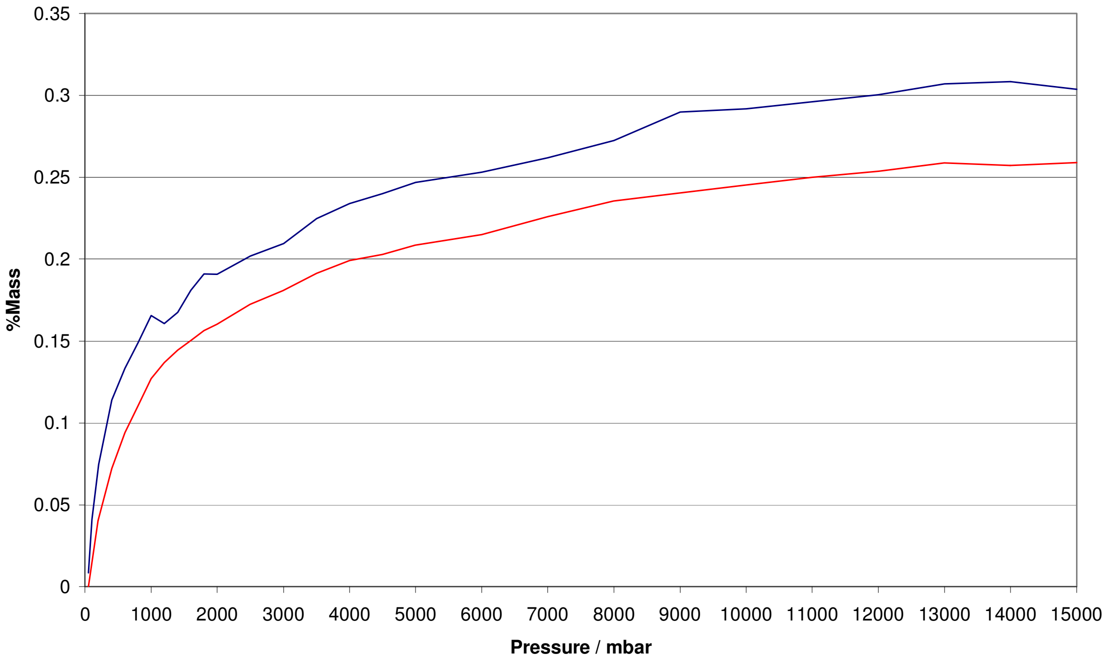

Figure 6.12 – Adsorption isotherms at 77 K (-) and 87 K (-) of $(LiBH_4)_{96}$.NaX after degassing for 24 hours at 50℃.

The uptakes showed a reduction in the adsorption of hydrogen between the 77 and 87 K in both cases as expected, with a further reduction after desorption at 360℃, which has been previously observed.

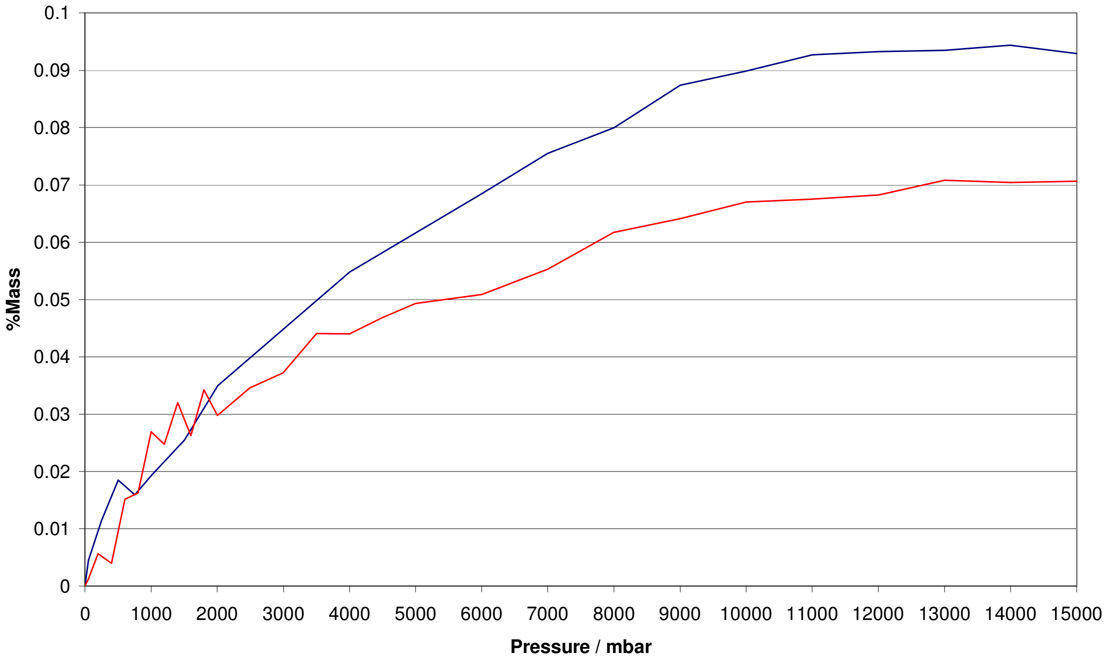

Figure 6.13 – Adsorption isotherms at 77 K (-) and 87 K (-) of showing $(LiBH_4)_{96}$.NaX after degassing for 24 hours at 365°C.

The initial measurements suffered from a certain amount of noise in the isotherms, so direct conversion using the Clausius–Clapeyron equation would have yielded poor results. In figure 6.13, for example, between 1500 and 2000 mbar the pressure points jump around and would give rise to positive and negative ΔH within a short region, and multiple values at the same coverage. It was necessary to use curve fitting to these isotherms.

Two different methods of analysis were tried: using the Clausius–Clapeyron and Virial equations for generating values for heats of adsorption[4,5]. Both methods generate their values from the isotherm, but as the isotherms were rather "noisy", it seemed sensible first to fit the data to adsorption models.

The Virial equation:

$$\ln\left(\frac{n}{p}\right) = A_0 + A_1 n + A_2 n^2 + \ldots$$

The Virial equation uses n as the amount adsorbed at a given pressure, p. A_0 is the 1st Virial coefficient used to describe adsorbent–adsorbate interactions; A_1 is the 2nd Virial coefficient which describes the adsorbate–adsorbate interactions. Higher coefficients are neglected due to their minimal contribution to the system at low fractional coverage. A plot of ln (n/p) versus n would yield A_0 as the intercept. The plotting of A_0 versus 1/T would allow the ΔH of adsorption to be estimated from the gradient. When this was performed the values produced were –3.5 and –2.1 kJ mol^{-1} for desorption at 50 and 360 °C respectively. ΔH_{ads} does, however, change with coverage.

The second method fitted data using adsorption models and ΔH_{ads} determined by using the Clausius–Clapeyron equation.

The Clausius–Clapeyron equation:

$$\ln\left(\frac{p_1}{p_2}\right) = \Delta H_{ads}\left(\frac{T_2 - T_1}{RT_1T_2}\right)$$

Here p_x denotes the pressure at the corresponding temperature, T_x; R is the molar gas constant (8.314 (4) J K^{-1} mol^{-1}). The ΔH_{ads} can be calculated at different coverages. Application of this method has been shown to be most accurate below 25% of the monolayer coverage. 25% provides a substantial coverage whilst minimising adsorbate–adsorbate interactions which would alter the perceived heat of adsorption.

Different methods for fitting of the datasets have been used. The Langmuir equation has been often used as a benchmark with its simple assumptions, whilst Langmuir–

Freundlich and Tóth have been shown to give better detailed fits to real adsorption data[4-8].

The Langmuir equation:

$$n = n_m \left(\frac{Kp}{1 + Kp} \right)$$

Here the pressure, p, relates to the amount adsorbed, n. n_m denotes the monolayer coverage and K is the adsorption coefficient specific to adsorbent–adsorbate interactions. The Langmuir model treats all binding sites equal with no adsorbate–adsorbate interactions.

The Langmuir–Freundlich equation:

$$n = n_m \left(\frac{(Kp)^x}{1 + (Kp)^x} \right)$$

This function fits n the amount adsorbed as a function of fitting parameters, K and x, whilst p is nominally the concentration or pressure of gas.

The Tóth equation:

$$n = n_m \left(\frac{(Kp)^{\frac{1}{x}}}{1 + (Kp)^{\frac{1}{x}}} \right)^{\frac{1}{x}}$$

Here each parameter is the same as those in the Langmuir–Freundlich model.

The fits for the sample data before desorption are shown in figure 6.14. For the 77 K plot the fits showed a good agreement with both the Tóth and Langmuir–Freundlich isotherms though, with the noise associated with the raw data, the errors understandably were higher than wanted. The Langmuir model did not appear to fit as well as the others, overestimating at low pressures and underestimating at high pressures. The 87 K fit for the Langmuir model appeared to be a closer fit, but the Tóth and Langmuir–Freundlich still appeared to follow the isotherm shape better. The errors obtained for the 87 K fit were smaller than those observed for the 77 K fitting.

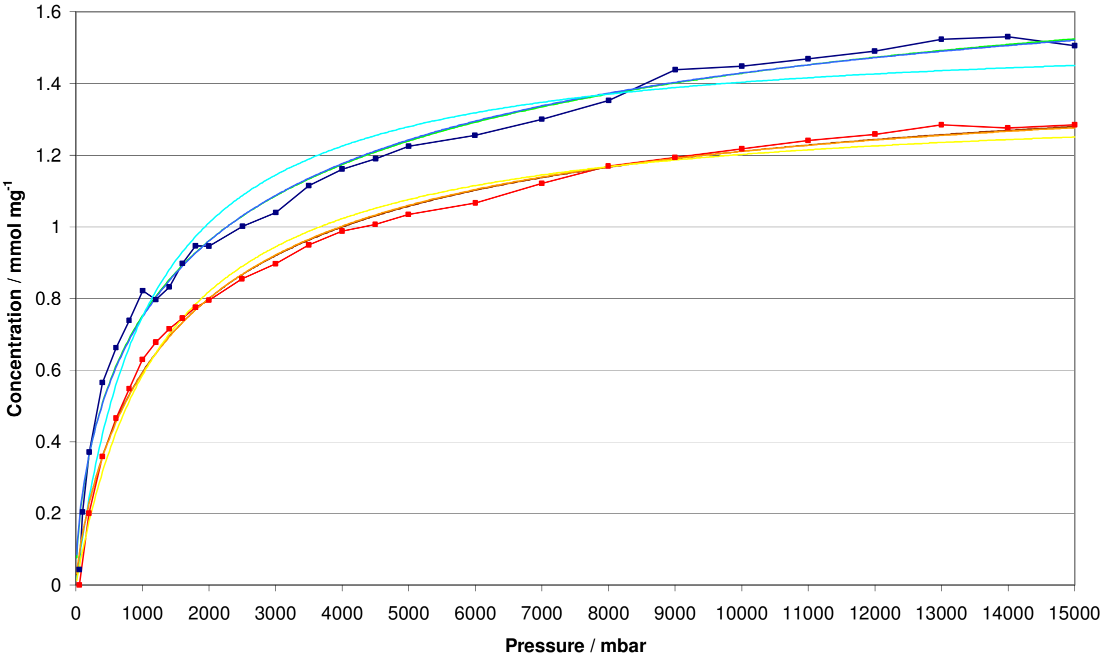

Figure 6.14 – Adsorption isotherms at 77 K (-) and 87 K (-) of $(LiBH_4)_{96}$.NaX after degassing for 24 hours at 50°C. The fits are shown for 77 K: Langmuir (-); Langmuir–Freundlich (-) and Tóth (-). Also for 87K: Langmuir (-); Langmuir–Freundlich (-) and Tóth (-).

Figure 6.15 outlines the fitting performed on the data after the sample had been desorbed at 365°C for 24 hours. Here the fits differed much less from each other at both 77 and 87 K. The 77 K fits showed a rather poor approximation towards higher pressure, with all behaving similarly. For 87 K, the high pressure Langmuir model fitted well, but again was less accurate than the Tóth and Langmuir–Freundlich at lower pressures.

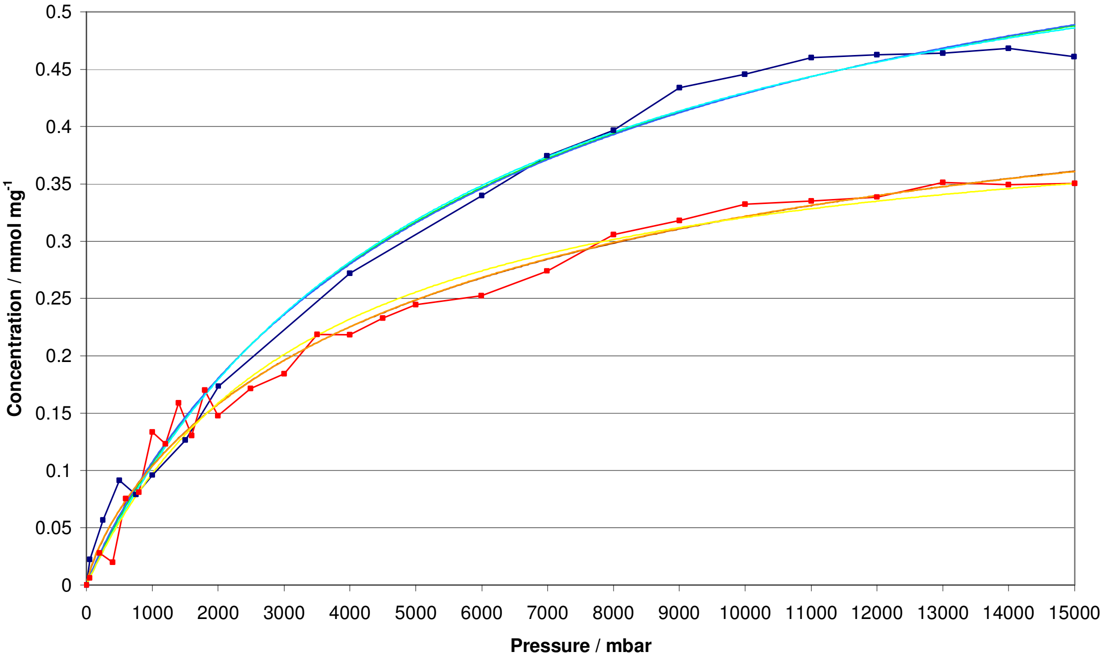

Figure 6.15 – Adsorption isotherms at 77 K (-) and 87 K (-) of $(LiBH_4)_{96}$.NaX after degassing for 24 hours at 365℃. The fits are shown for 77 K: Langmuir (-); Langmuir–Freundlich (-) and Tóth (-). Also for 87 K: Langmuir (-); Langmuir–Freundlich (-) and Tóth (-).

Another plot, figure 6.16, shows the low pressure region of the sample prepared at 365℃. This has been included as the fits at low pressures were poor. The overlap between 87 and 77 K fits show that for all the fitting models, the 87 K had a higher adsorption than that of the 77 K. It would be highly unlikely that the increase in temperature would actually result in improved adsorption at low temperatures. This is likely to be a by-product of the noisy data, and an artefact of the fitting.

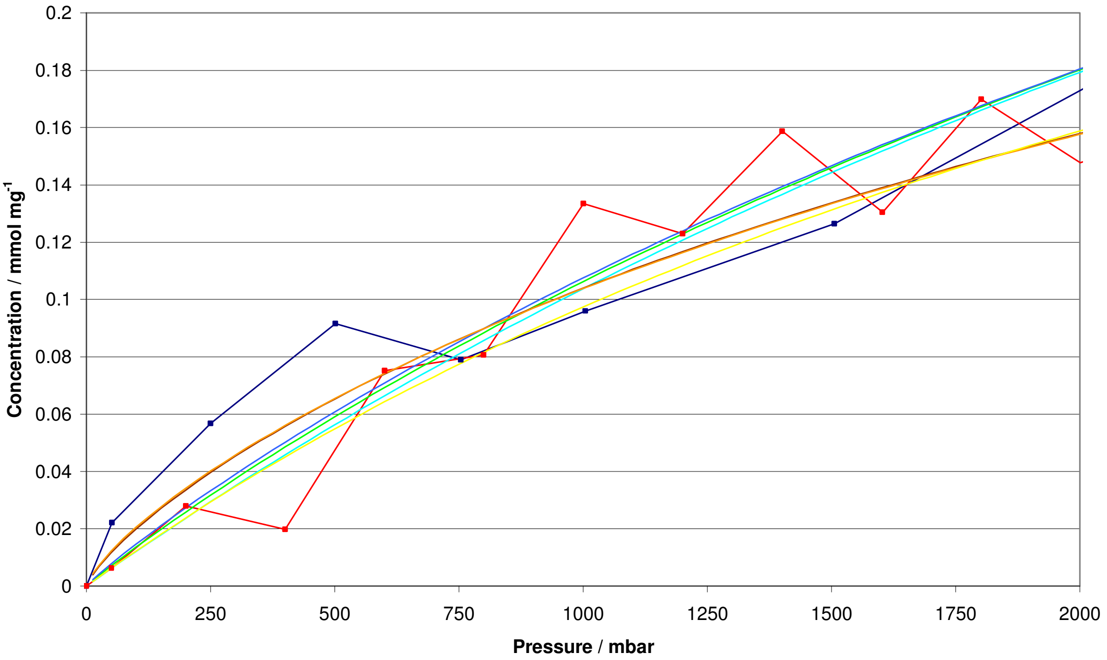

Figure 6.16 – Adsorption isotherms at 77 K (-) and 87 K (-) of showing $(LiBH_4)_{96}$.NaX after degassing for 24 hours at 365°C. The fits are shown for 77 K: Langmuir (-); Langmuir–Freundlich (-) and Tóth (-). Also for 87 K: Langmuir (-); Langmuir–Freundlich (-) and Tóth (-).

The data was fitted and minimised using Microsoft Excel's Solver program. The analyses were performed on the fitted data and at given fractional coverages the heats of adsorption were determined using the Clausius–Clapeyron relationship, the Virial values have also been shown on these plots. The results are shown for the 50°C outgassed sample in figure 6.17, with the sample outgassed at 360°C being shown in figure 6.18.

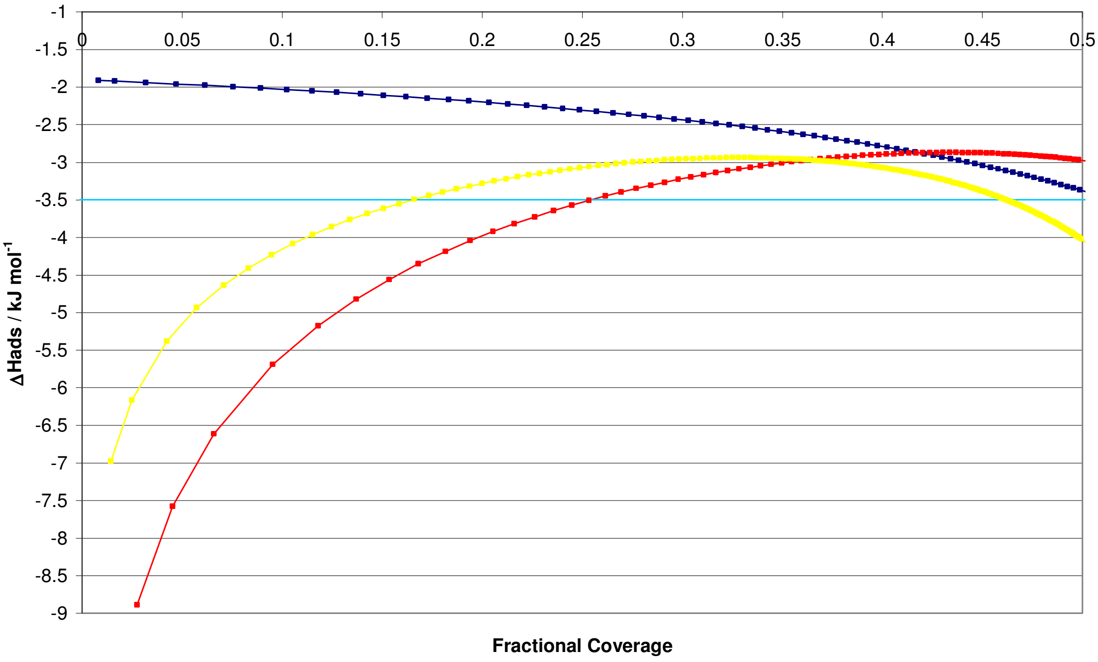

Figure 6.17 – Plot of the calculated heats of adsorption (in kJ mol^{-1}) against the fractional coverage for the sample degassed at 50°C for 24 hours. Models: Langmuir (-); Langmuir-Freundlich (-); Tóth (-) and Virial (-).

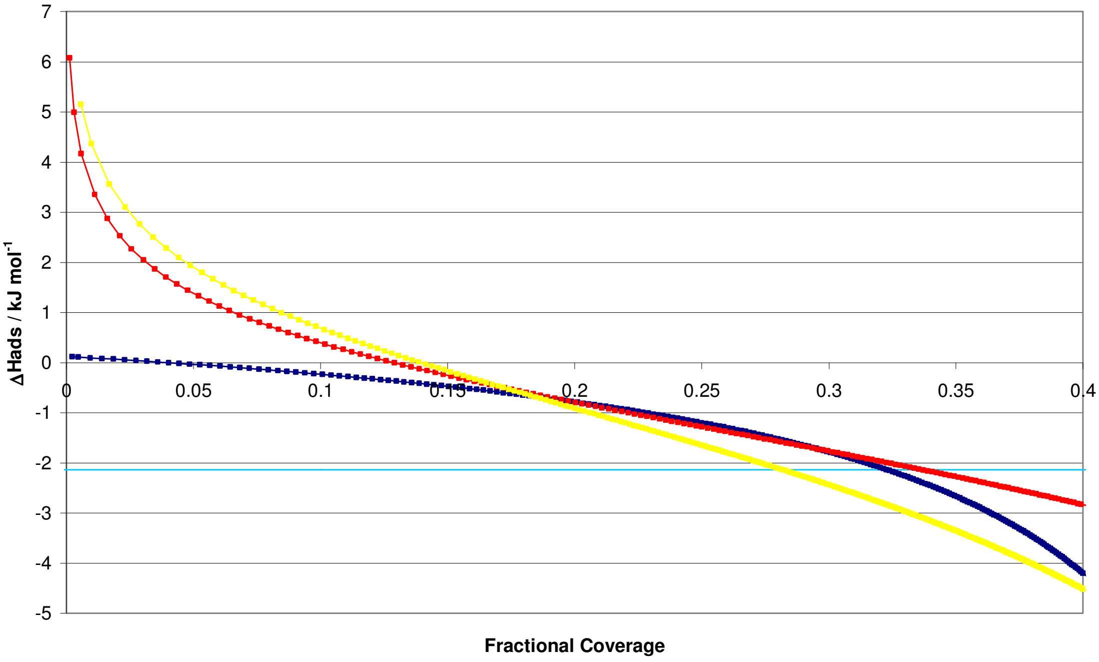

Figure 6.18 – Plot of the calculated heats of adsorption (in kJ mol^{-1}) against the fractional coverage for the sample degassed at 365°C for 24 hours. Models: Langmuir (-); Langmuir-Freundlich (-); Tóth (-) and Virial (-).

These two plots indicate that there was a reduction in the heat of adsorption associated with desorption of hydrogen from the system. Using the 25% coverage a range between -2.3 and -3.5 kJ mol^{-1} for the prepared sample was obtained. Because of the poor fitting of the Langmuir model this was disregarded. The other models sat between -3.1 and -3.5 kJ mol^{-1}.

On desorption of hydrogen a reduction in the heat of adsorption was observed. Acknowledging the inaccuracy of the fitting at low fractional coverage, the 25% coverage point was again taken as a guideline giving a spread between -1.2 and -2.1 kJ mol^{-1}.

We may speculate that a reduction may be associated with the removal of the zeolite framework as the predominant adsorption site, being replaced by the products of desorption. There was also a reduction in the enthalpy of adsorption upon occlusion. Previous studies on zeolites have shown a wide range of heats of adsorption. NaX was shown to have a heat of adsorption of between -4.7 and -10.4 kJ mol^{-1}, depending on the model used[9] whilst in magnesium ion-exchanged zeolites values as high as -17.5 kJmol^{-1} have been reported[10]. This indicates that the occlusion of lithium borohydride may reduce the capacity and ability of the host framework to adsorb hydrogen.

6.4 Conclusion

Limited rehydrogenation was possible in desorbed $(LiBH_4)_{128}$.NaA and $(LiBH_4)_{224}$.NaX at 350°C and 18 bar, far below the conditions for bulk hydrogenation. It was found that rehydrogenation was largely unsuccessful in half loaded samples and in NaY. Inhibition of uptake may occur through pore blocking, though mostly in half-loaded samples.

On analysis of low temperature adsorption properties by IGA no detectable uptake was observed in the fully loaded samples. The half loaded samples exhibited values slightly less than half those of the parent zeolites. This suggests that either the maximum loadings estimated from powder XRD were inaccurate, or that the guest material may block access to some empty pores. Upon desorption of the lithium borohydride guest, the available space in the half loaded samples appeared to decrease suggesting further pore blocking.

There was an apparent reduction in heat of adsorption in loaded $(LiBH_4)_{96}$.NaX, and after high temperature desorption. Both values were markedly lower than expected for unloaded zeolites.

6.5 References

1. Züttel A., Rentsch S., Fisher P., Wenger P., Sudan P., Mauron Ph., Emmenegger Ch., *J. Alloys Comp.*, **2003**, 356-357, 515
2. Mauron P., Buchter F., Friedrichs O., Remhof A., Bielmann M., Zwicky C. N., Zuttel A., *J. Phys. Chem. B*, **2008**, 112, 906
3. Langmi H. W., Book D., Walton A., Johnson S. R., Al-Mamouri M. M., Speight J. D., Edwards P. P., Harris I. R., Anderson P. A., *J. Alloys Comp.*, **2005**, 404-406, 637
4. Zhao X. B., Xiao B., Fletcher A. J., Thomas K. M., *J. Phys. Chem. B*, **2005**, 109, 8880
5. Kaye S. S., Long J. R., *J. Am. Chem. Soc.*, **2005**, 127, 6506
6. Langmuir I., *J. Am. Chem. Soc.*, **1918**, 40, 1361
7. Roquerol, F., Rouquerol J., Sing, K., *Adsorption by Powders and Solids: Principles, Methodology, and Applications*, **1999**.
8. Yang, R. T., *Gas Separation by Adsorption Processes*, **1997**
9. Personal Communication: Langmi H., Walton A., 2009

10. Palomino G. T., Llop Crayol M. R., Otero Areán C., *J. Mater. Chem.*, 2006, 16, 2884

CHAPTER 7

OCCLUSION OF AMMONIA BORANE AND LITHIUM BOROHYDRIDE AMIDE INTO ZEOLITES

7.1 Introduction

Chapter 4 showed that there were some interesting properties associated with the occlusion of lithium borohydride into zeolites. It seemed pertinent to try related systems that are known to desorb hydrogen at lower temperatures. For this ammonia borane [NH_3BH_3] and lithium borohydride amide [$Li_4BH_4(NH_2)_3$] were chosen[1,2].

7.2 Reactions with Ammonia Borane

Ammonia borane (AB) has previously been incorporated into a number of porous materials. Its high weight percentage of hydrogen and low thermal onset of desorption make it a prime candidate for use in hydrogen delivery applications[1,3-6]. The desorption of ammonia borane proceeds primarily to polymeric aminoborane. The chief concerns have been the undesired byproduct on desorption of borazine, c-$(NHBH)_3$ (an analogue of benzene), which is known to poison PEM fuel cells[1,6]. The difference in desorption products are caused by simultaneous competing reaction pathways occurring over the small range of desorption.

With desorption in the region of 77 - 112℃ AB also is a good contender for use in mobile applications. Certain key problems need to be overcome to make this a viable storage medium. The issue of the desorption of a potentially damaging species can be overcome through incorporation in a mesoporous silica, SBA-15, host[6-7]. This brought about two changes: a slight reduction in the temperature of the desorption maximum and more importantly a substantial reduction in the production of borazine. Similar reports have been shown within carbon aero gels, and in the milling to restrict particle size of ammonia borane[4,7]. When considering regeneration it is necessary to minimize desorption of any non-hydrogen components to improve reuse as a store, although AB can't be directly hydrogenated as the desorption is exothermic.

In the cases involving porous hosts the ammonia borane was incorporated into a degassed host using a solution (ether or THF) and the capillary effect. The solvent was then removed under vacuum. The use of solvents for the wet impregnation of zeolites would unfortunately lead to competing loading of the solvent with ammonia borane. The thermal occlusion of ammonia borane can be complicated due to its melting and desorption at similar temperatures around 77℃. What follows in this section is a brief look at the incorporation of ammonia borane into zeolites A and X by thermal methods, with preliminary analysis of the desorption properties of the products.

7.2.1 Experimental

Samples NaA and NaX were synthesised as detailed in the experimental chapter. NH_3BH_3 (>90%) was obtained from Sigma-Aldrich. Sample preparation began with dehydrating the zeolites (NaA and NaX).

Dried zeolites were then transferred to an argon glove box to allow for intimate mixing with the ammonia borane. Mixtures were formed in increments of 32 NH_3BH_3 per unit cell (PUC) from 64 – 256. For NaA the $Fm\overline{3}c$ space group with a 24 Å unit cell was used; for NaX the space group was $Fd\overline{3}m$ with a unit cell parameter of approximately 25 Å[8-10]. Samples were prepared as outlined in section 3.2.3.5.

The samples were then characterized using powder X-ray diffraction. These samples were also analysed by gravimetric and residual gas analysis methods. Thermogravimetric data was collected with temperature runs from 30 - 260°C with a ramp rate of 2°C per minute. The TGA data was coupled with mass spectrometry collecting m/z for hydrogen, water (OH^- and H_2O), ammonia, diborane (as $BH_3BH_2^-$), nitrogen, oxygen, argon and borazine (as $B_3N_3H_5^-$).

7.2.2 Results and Discussion

Initial reaction of the ammonia borane (white solid) with the white zeolites NaA at 80°C in sealed tubes yielded a slight over pressure within the tube. The sample collected was a white powder, which displayed slight signs of being electrostatic. On preparation of the same mixtures at 60°C there was no pressure, but at this temperature ammonia borane was still observed in the diffraction pattern (figure 7.1). When reheated up to 4 times for 12 hours at 60°C the ammonia borane peaks were removed. A slight complication in the analysis was caused by the overlap of the main (110) peak of ammonia borane with the (622) peak of NaA. The second most intense peak (101) for ammonia borane, with 53% intensity, didn't overlap. This could be used to determine if ammonia borane had disappeared from the sample.

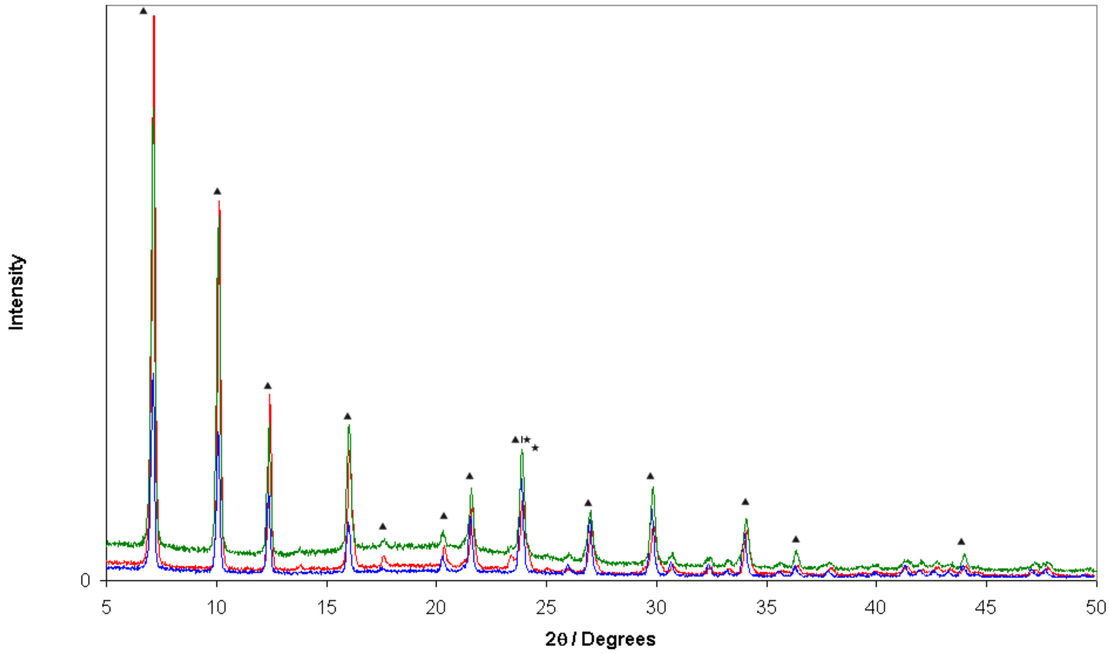

Figure 7.1 – Powder XRD pattern showing $(NH_3BH_3)_{128}$.NaA showing samples prepared: at 60℃ under vacuum (-); at 70℃ under flowing gas (-); at 80℃ under vacuum (-); with ▲ denoting zeolite and ★ denoting ammonia borane peaks.

When the same reactions were performed replacing NaA with NaX similar changes in the sample appearance and products of the reaction were observed.

It can be assumed that in both cases the over pressure observed on sample collection from a sealed evacuated tube reaction at 80℃ came from desorption of hydrogen, as this was above the reported desorption starting point of AB[1].

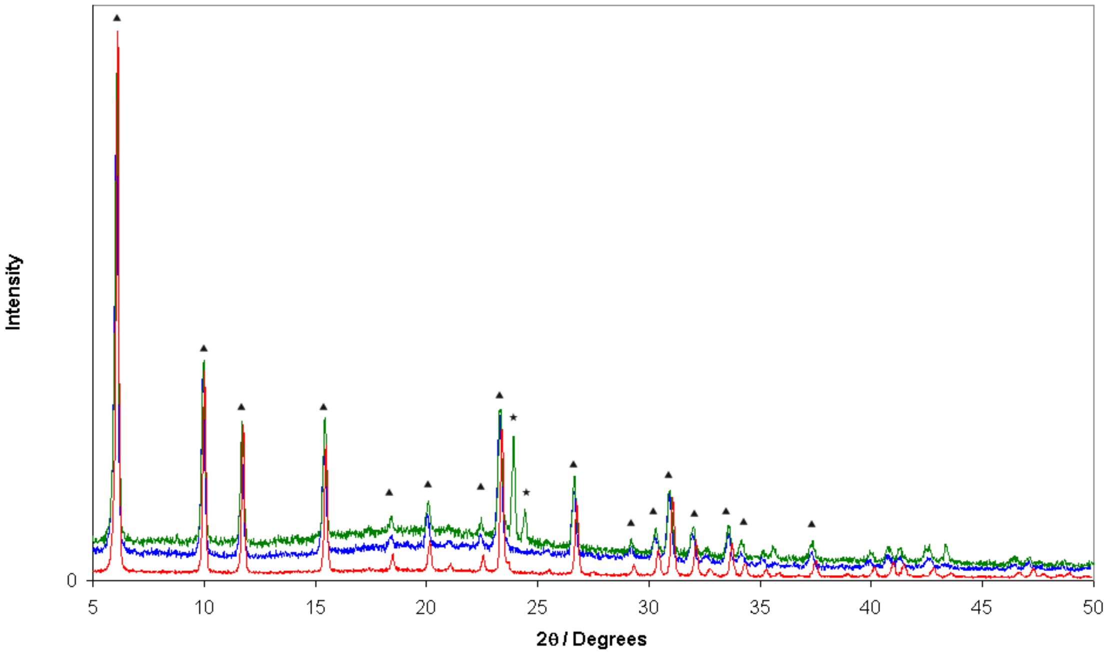

Figure 7.2 – Powder XRD pattern showing $(NH_3BH_3)_{128}$.NaX showing samples prepared: at 60°C under vacuum (-); at 70°C under flowing gas (-); at 80°C under vacuum (-); with ▲ denoting zeolite and ★ denoting ammonia borane peaks.

Unlike the case of lithium borohydride we appear to see only one zeolite pattern, in which the peaks were slightly shifted from that of the parent dehydrated zeolite.

Analysis of the lattice parameters produced the values shown in figures 7.3 and 7.4 for NaA and NaX, respectively. For NaA we see that in the case of samples at 80°C the lattice parameters are still within error for the dehydrated zeolite. This suggests that no occlusion has occurred. Given that 80°C is above the desorption temperature AB isn't expected in the XRD pattern. The samples prepared at 60°C similarly had values that did not differ significantly from that of the dehydrated zeolite, with a noticeable exception at 96 ammonia borane per unit cell. At this temperature the ammonia borane was present in all XRD patterns, even after being reheated several times. The samples prepared at 70°C had parameters significantly different from the value of dehydrated

NaA at low loadings only to revert to a very similar value at higher loading. At 256 ammonia borane's PUC, ammonia borane was still not present in the diffraction pattern. This suggests that the samples prepared at 70°C were decomposing slowly over the reaction period.

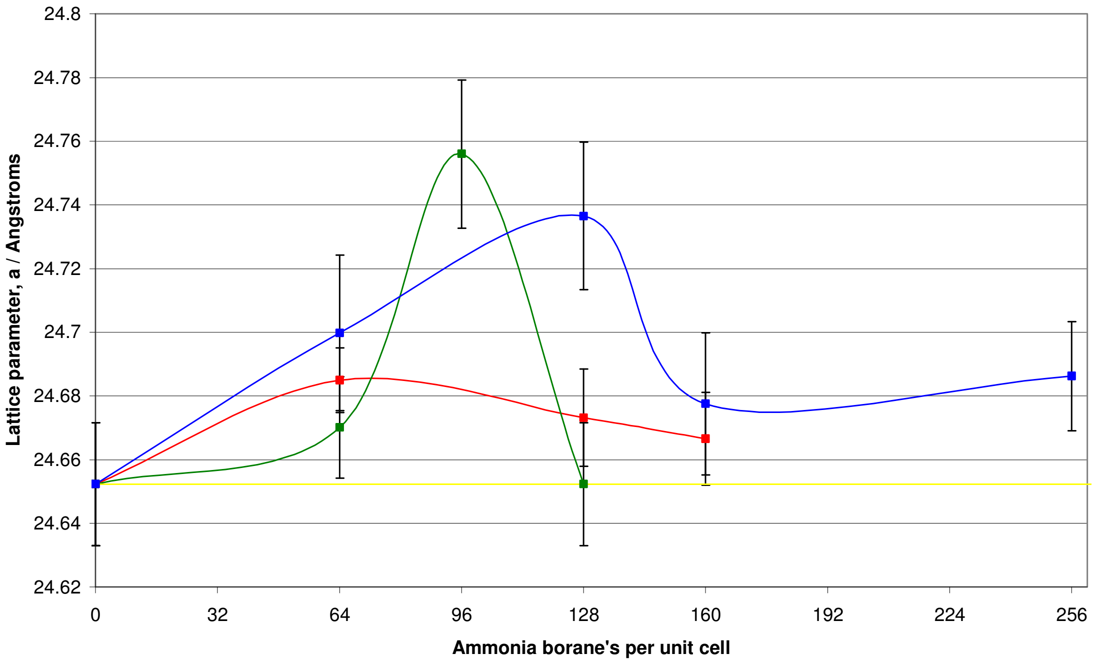

Figure 7.3 – Lattice parameter against loading for NaA with NH_3BH_3 showing samples prepared: at 60°C under vacuum (-); at 70°C under flowing gas (-); at 80°C under vacuum (-); and dehydrated NaA (-). Errors shown to 3ESD's.

For NaX it was observed that the lattice parameters for samples prepared at both 70 and 80°C were reduced compared to the dehydrated zeolite. The parameters of samples prepared at 80°C were much lower than those prepared at 70°C, and in both cases there was no evidence of ammonia borane in the XRD patterns after heating.

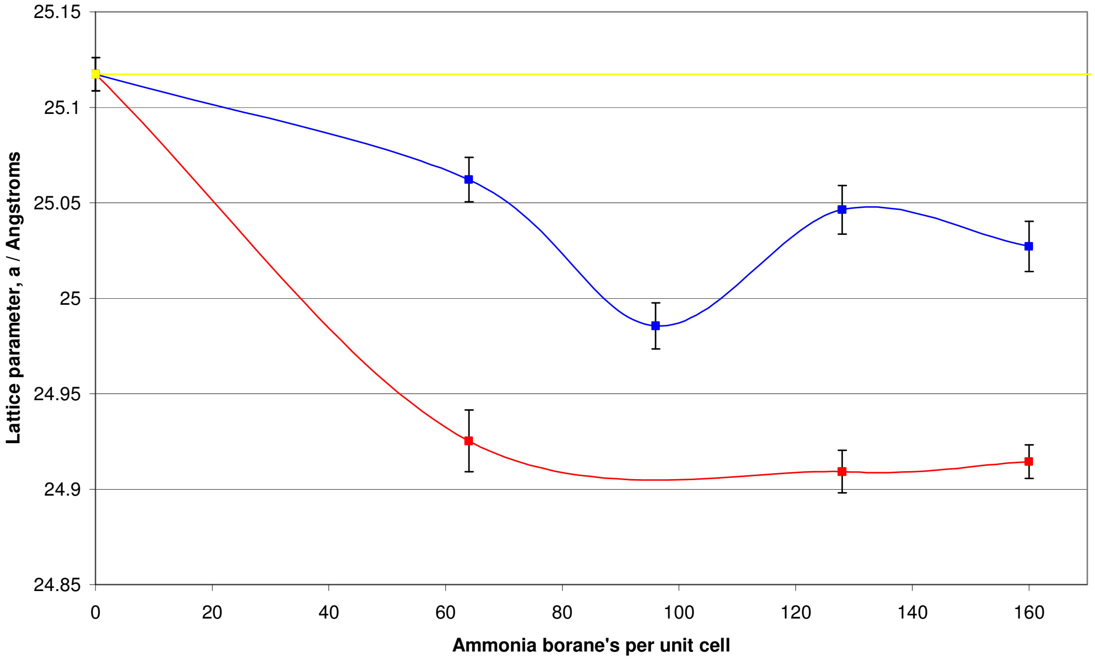

Figure 7.4 – Lattice parameter against loading for NaX with NH_3BH_3 showing samples prepared: at 70℃ under flowing gas (-); at 80℃ under vacuum (-); and dehydrated NaA (-). Errors shown to 3ESD's.

Clearly, there was a stark difference between the two different zeolites. In the case of NaA there was an expansion of the unit cell to accommodate any ammonia borane, whereas the lattice of NaX appeared to contract slightly. This may be due to the difference in the cage size and the nature of the interactions of ammonia borane with the exchangeable cations and the framework.

The fact that no ammonia borane was observed in the preparations, even at higher loadings, at 70℃ may indicate that the samples were decomposing. Other observations of ammonia borane generally show it to decompose and "foam" above 80℃. As this was not observed we may conclude that any desorption was relatively slow, and if desorption was occurring it could be the products which were incorporated into the zeolites instead of the starting material.

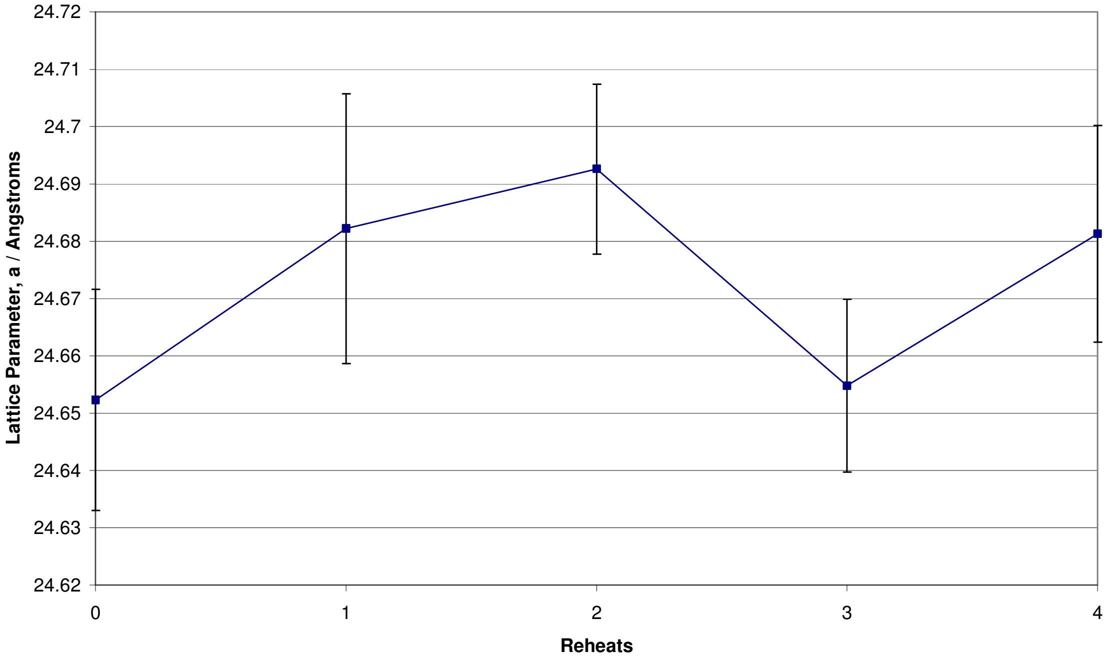

Figure 7.5 – Lattice parameter against the number of reheats at 60°C for $(NH_3BH_3)_{128}$.NaA PUC.

Reheat analysis was performed on samples of NaA and NaX with 128 AB's PUC at 60°C under vacuum. In the case of NaA (figure 7.5) no significant change was observed in lattice parameter over the course of the experiment. In all the preparations no pressure of gas was observed, suggesting no decomposition occurred at this temperature, yet over the course of the experiment the amount of ammonia borane in the XRD was reduced to zero by the 4th reheat, which should suggest incorporation.

In the case of NaX, AB was observed in the final XRD pattern, yet the lattice parameters showed a decrease, suggesting that some AB may have been occluded.

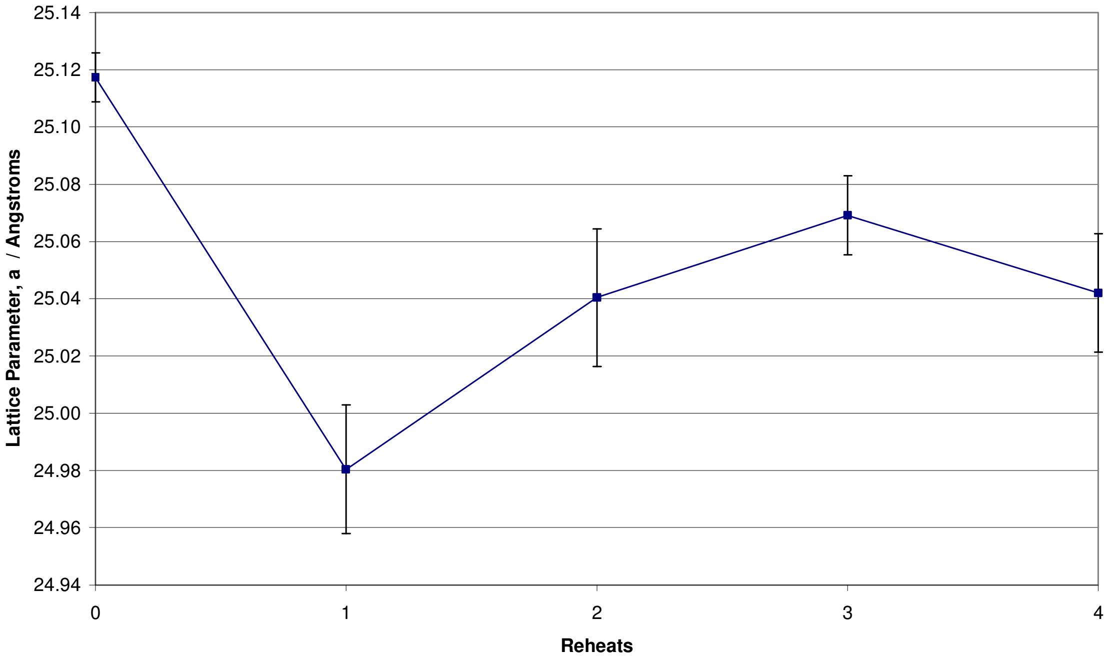

Figure 7.6 – Lattice parameter against the number of reheats at 60°C for $(NH_3BH_3)_{128}$.NaX PUC.

As has been observed before, the occlusion of materials in the vacant pore space alters the electron density. Variation in the relative peak intensities was observed for both zeolite NaA and NaX. Changes in peak ratios both against the different loadings at the three temperatures, and also during the reheat analyses at 60°C, are shown for both NaA (figures 7.7 and 7.8) and NaX (figures 7.9 and 7.10).

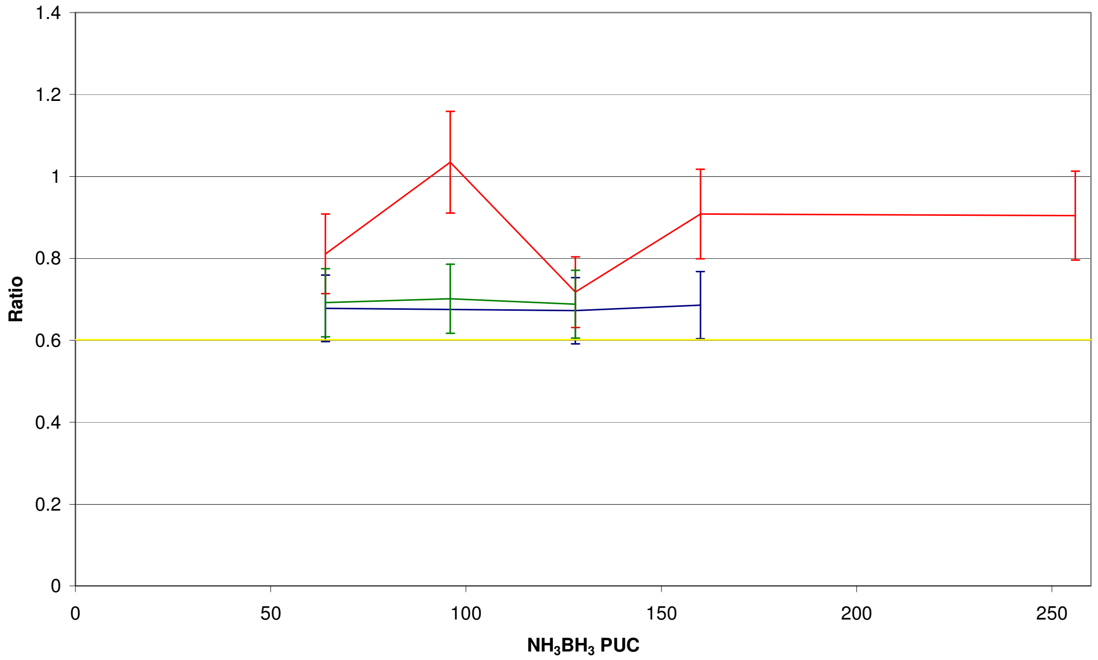

Figure 7.7 – Ratio of the intensities of the (220) to (200) peaks for NaA with NH_3BH_3 against the loading level, showing samples prepared at 60°C (-), 70°C (-) and 80°C (-), compared with dehydrated NaA (-).

The sample at 70°C (under flowing argon) was furthest away from the value for the dehydrated zeolite, indicating this could be the best condition for ammonia borane to be incorporated. In the case of the 60 and 80°C preparations (under vacuum) the values were close to those of the dehydrated zeolite. The successful incorporation of AB at these temperatures must therefore remain in doubt.

For $(NH_3BH_3)_{128}$.NaA the ratio remained similar regardless of the number of heatings, in spite of the reduction in the intensity of the ammonia borane peaks in the XRD patterns. These values were similar to those observed for samples heated singly at 60°C for various loadings (figure 7.7), and similar to the dehydrated zeolite.

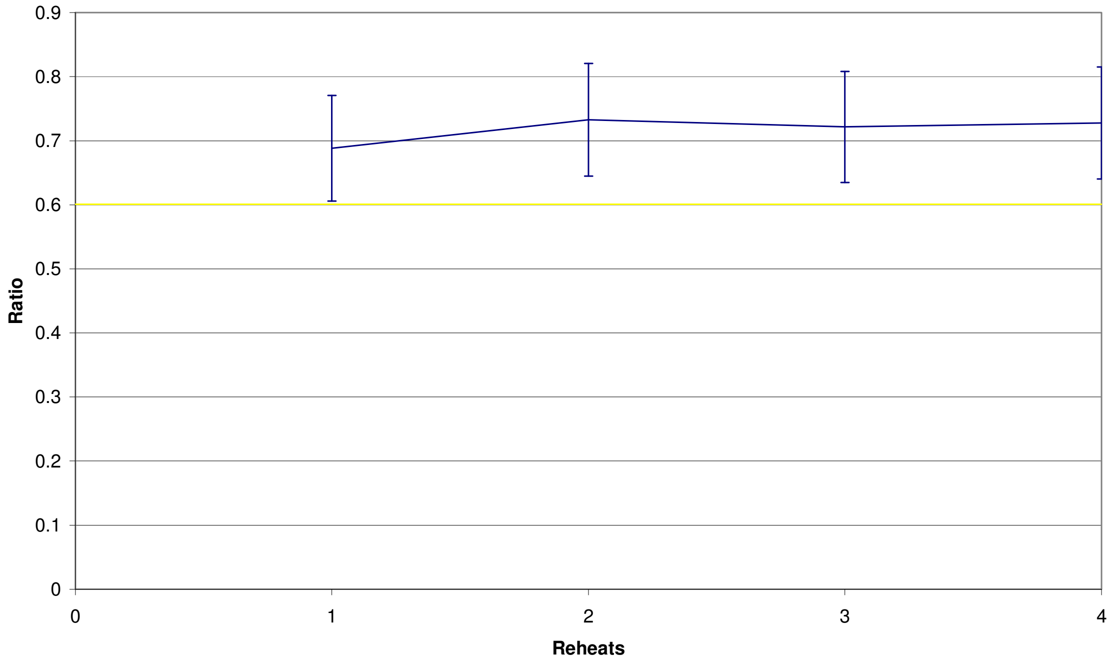

Figure 7.8 – Ratio of the intensities of the (220) to (200) peaks for $(NH_3BH_3)_{128}$.NaA against the number of reheats (-), compared with dehydrated NaA (-).

In NaX the ratio was in most cases quite different from the value of the dehydrated zeolite. Most of the values were very similar irrespective of the preparation temperature. The only exception was the $(NH_3BH_3)_{64}$.NaX prepared at 80℃, which was very close to the dehydrated value.

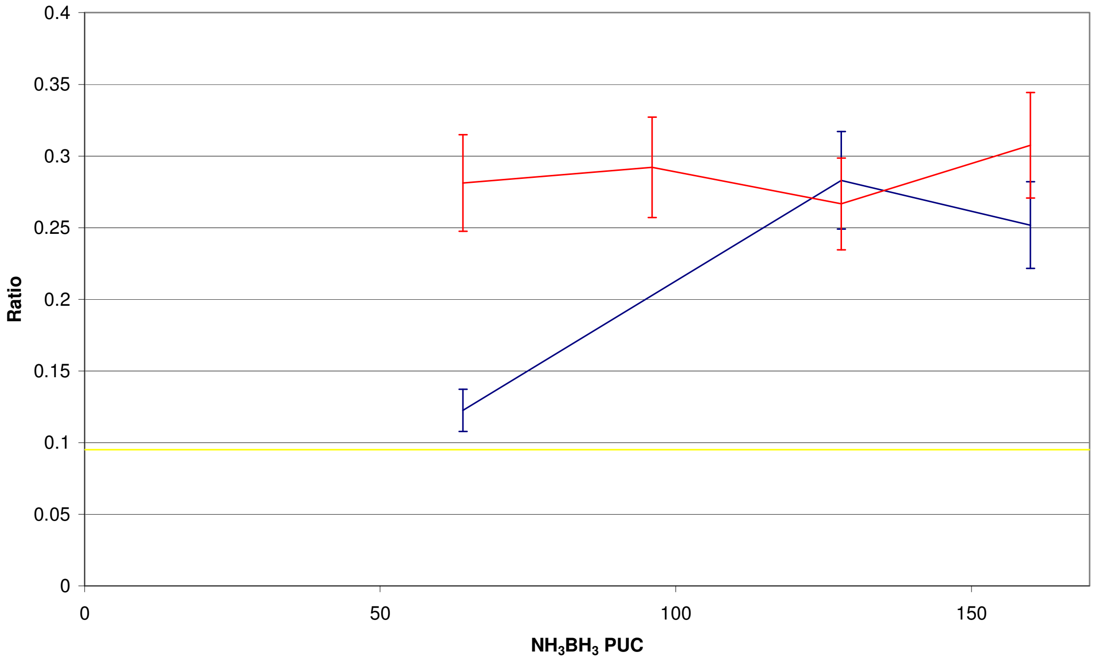

Figure 7.9 – Ratio of the intensities of the (311) to (111) peaks for NaX with NH_3BH_3 against the loading level, showing samples prepared at 70°C (-) and 80°C (-) compared with dehydrated NaX (-).

We can also see that the analysis of the reheated samples led to very similar results yielding a ratio well above that of the dehydrated zeolite. Again these values were similar to those found after a single heating at 70 and 80°C. This suggests that NaX successfully incorporated ammonia borane, although some was still present in the XRD pattern after the final reheat.

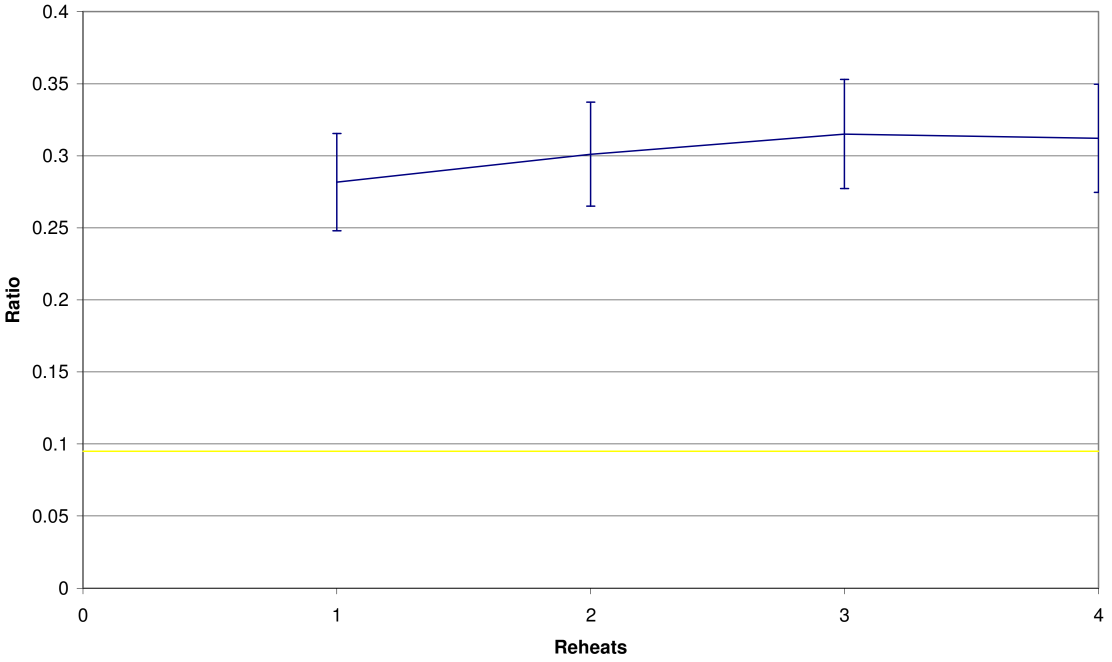

Figure 7.10 – Ratio of the intensities of the (311) to (111) peaks for NaX with 128 NH_3BH_3 PUC against the number of reheats (-), compared with dehydrated NaX (-).

The analysis of the powder XRD patterns has shown that that the incorporation of some ammonia borane did occur. If this was the case changes would be expected in the desorption characteristics of the samples. A sample was chosen where obvious differences were present in the XRD pattern showing a lack of bulk ammonia borane and a change in zeolite peak relative intensities to suggest that ammonia borane had been incorporated.

TGA was performed on the $(NH_3BH_3)_{128}$.NaA PUC, prepared at 60°C and reheated four times. Due to the lack of ammonia borane in the XRD, and a change in relative peak intensities it could be assumed that some ammonia borane had been incorporated.

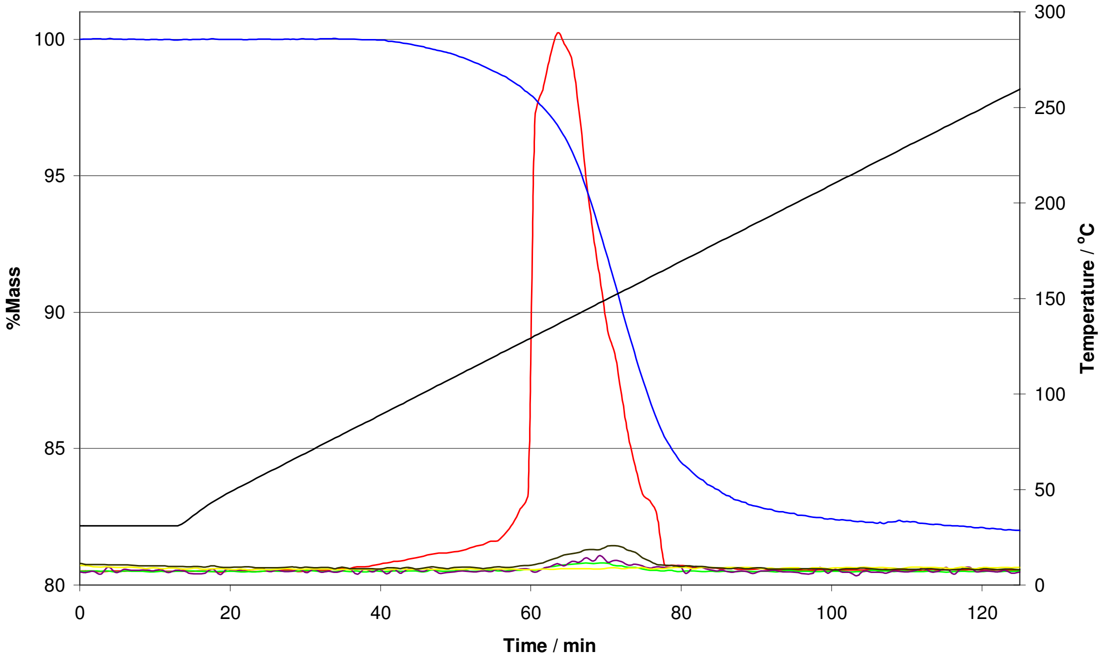

Figure 7.11 – TGA-MS plot for $(NH_3BH_3)_{128}$.NaA PUC after heating 4 times for X hours at 60℃. The change in percentage mass (-), and temperature (-) against time are shown, with the MS traces for hydrogen (-), ammonia (-), di-borane (-), nitrogen (-) and borazine (-).

There was is a single desorption which began around 87℃ and appeared to finish around 190℃, with a total mass loss of 18.0 wt%, up to 260℃. This mass loss corresponds to the complete desorption of the amount of ammonia borane from the original reaction mixture. Hydrogen formed the majority of the desorbed product, with trace amounts of diborane and borazine also present.

Other studies have outlined the reaction pathways by which AB decomposes within this temperature regime[11]:

$NH_3BH_3 \rightarrow n(NH_2BH_2) + H_2$ (1)

$n(NH_2BH_2) \rightarrow (NHBH)n + H_2$ (2')

$n(NH_2BH_2) \rightarrow c\text{-}(NHBH)_3 + H_2$ (2'')

In bulk AB reaction (1) occurs between 77 and 112°C, with reaction (2) desorbing above this finishing at approximately 155°C. Desorption of the incorporated ammonia borane may occur at a higher temperature due to a partial desorption occurring during the synthesis. This is unlikely as 18 wt% corresponds to the total amount of AB from the original mixture. It is possible that the occlusion stabilises the decomposition of AB increasing the overall temperature and causing a narrow single desorption, bulk AB is often a broad desorption. Overall this was a completely different desorption mechanism favouring the formation of small gaseous species over the polymeric amino-boranes often seen in bulk decomposition.

7.3 Reactions with Lithium Amide Borohydride

The lithium borohydride amide ($Li_4BH_4(NH_2)_3$) is a new mixed anion complex hydride that shows both a change in desorption pathway compared to $LiNH_2$, in favour of H_2 rather than NH_3, and a reduction in temperature for hydrogen desorptions compared to $LiBH_4$[2,12,13]. The desorption temperature is reduced to around 230°C with the majority product being hydrogen, although some ammonia is still produced[2]. The amount of ammonia appears to be dependent on the method by which desorption occurs and the original method of synthesis. The results point towards a possible desorption mechanism which may be directly influenced by the interaction with ammonia at a molecular level with the starting material. If this is the case occlusion could assist the intimate mixing required, and maximise the hydrogen production on desorption.

7.3.1 Experimental

Samples NaA and NaX were synthesised as detailed in the experimental chapter. The lithium borohydride amide was synthesised and purified by Dr Philip Chater, according to the procedure outlined in references 2 & 12.

Zeolite/lithium borohydride amide mixtures were formed in increments of 8 $Li_4BH_4(NH_2)_3$ per unit cell (PUC) from between 16 – 32. For NaA the $Fm\overline{3}c$ space group with a 24Å unit cell was used; the space group for NaX is $Fd\overline{3}m$, with a unit cell parameter of approximately 25Å[8-10]. Samples were prepared as outlined in section 3.2.3.4.

The samples were then characterized using powder X-ray diffraction. ESR spectra were collected at room temperature and 77K. Vacuum TPD on some samples was carried out with RGA to monitor desorption products in the temperature range of 30 – 450℃.

7.3.2 Results and Discussion

On reaction at 200℃ in the sealed tube it was observed that no pressure was generated. The reaction of the white crystalline lithium borohydride amide with the white zeolite NaA powder yielded a lilac coloured powder.

Inspection of the XRD patterns (Figure 7.12 being a representative pattern) showed a secondary zeolite phase at a higher 2θ. Repeated heating of the sample did not remove all the initial lithium borohydride amide. The dehydrated zeolite had a lattice parameter of 24.65 (2) Å with the new phase 24.15 (5) Å.

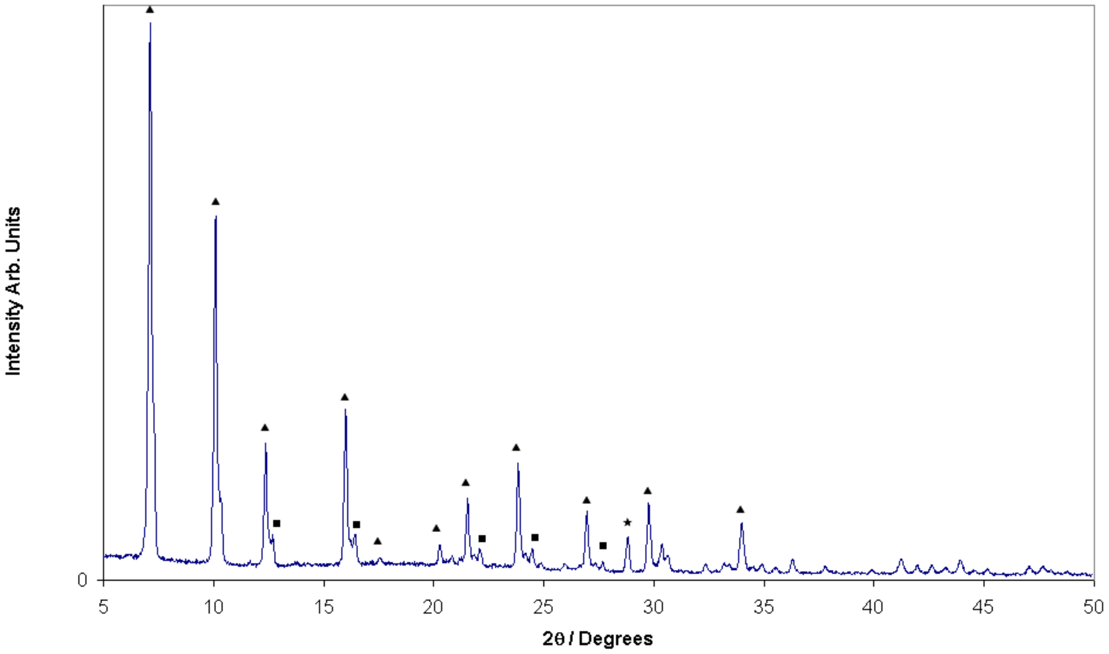

Figure 7.12 – Powder XRD pattern showing $(Li_4BH_4(NH_2)_3)_{24}$.NaA after heating at 200℃, with ▲ denoting zeolite; ■ the secondary phase and ★ denoting lithium borohydride amide peaks.

Elevated heating to 230℃ brought about a small pressure in the sealed tube, but both the secondary zeolite phase and lithium borohydride amide were retained in the XRD pattern.

Due to its coloured appearance, reminiscent of those observed on reaction of alkali metals with zeolites, the lilac sample was analysed by ESR at 77 K. The spectrum data showed a single sharp signal at g = 2.0020(5). Cluster formation is often done through metal vapour inclusions, some research has shown that reduction of dehydrated zeolites forms similar clusters. Reducing agents are often quite powerful such as n-butyllithium[14] and solvated electrons in liquid ammonia, lithium borohydride amide is probably acting as reducing agent under the conditions of reaction. The signal was from the formation of

Na_4^{3+} clusters, which in similar systems (sodalite cages of NaA and NaY) form lilac and pinkish grey samples[14-16].

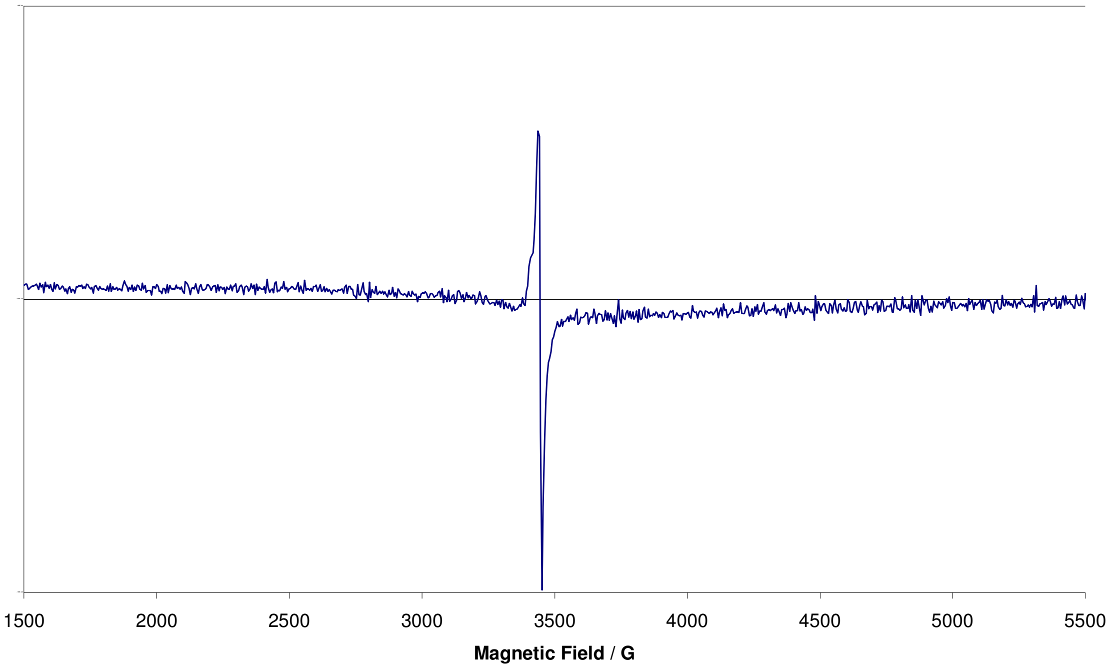

Figure 7.13 – ESR spectrum collected at 77 K for $(Li_4BH_4(NH_2)_3)_{24}$.NaA prepared at 200°C.

The narrow pore opening of NaA could be inhibiting the complete occlusion of $Li_4BH_4(NH_2)_3$ into it. Another possibility was that the reduction products of $Li_4BH_4(NH_2)_3$ could be unable to diffuse into the zeolite at these temperatures. These species could be a barrier to further reduction and occlusion mechanisms. The indication of a second phase and colour change suggests some occlusion has occurred, though clearly it is incomplete.

NaX would be a better candidate given its larger ring opening. Here, no pressure was generated during synthesis and the product was a white powder. Powder XRD showed in figure 7.14 that two of the samples contained a single phase of similar lattice parameter to that of the dehydrated zeolite. The 24 PUC phase contained a second phase at higher 2θ. Although this was the only composition to exhibit a second zeolite phase, the peak shape of the other loadings was broader and asymmetric with respect to the parent dehydrated zeolite. The (222) peak for lithium borohydride amide was visible just above the background at all loadings suggesting that the occlusion was not complete; further heating did not reduce this. The lattice parameter for all three reacted samples was 25.05(3) Å, suggesting a slight contraction in lattice parameter compared to the 25.11(1) Å of dehydrated NaX. In the case of 24 $Li_4BH_4(NH_2)_3$ PUC, the lattice parameter of the secondary phase was 24.73(5) Å.

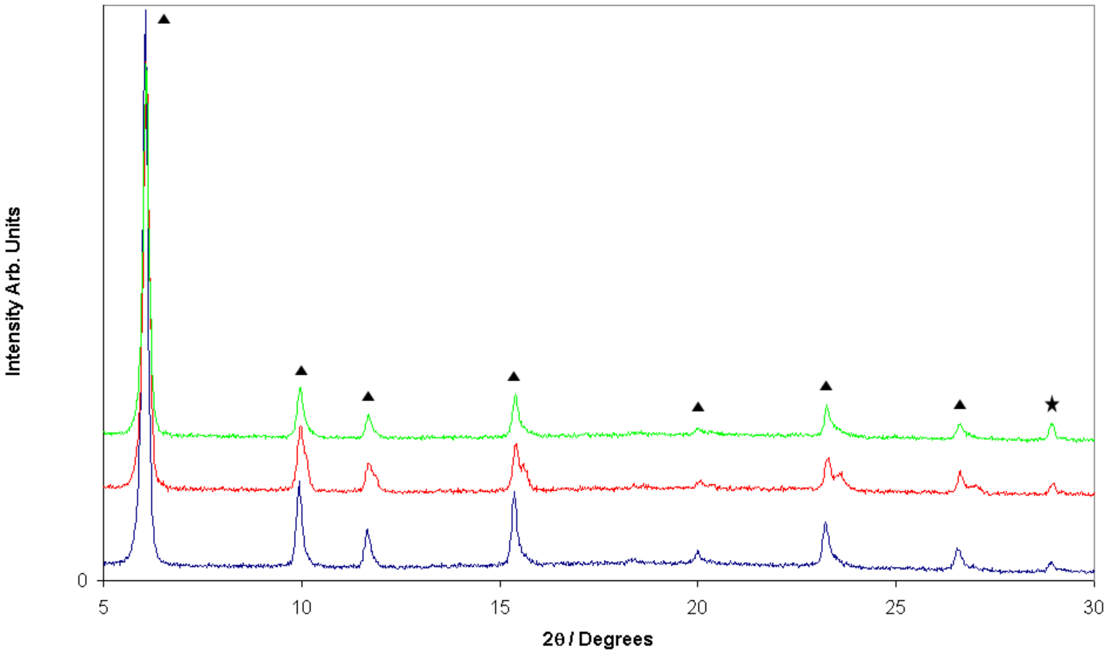

Figure 7.14 – Powder XRD pattern showing NaX with $Li_4BH_4(NH_2)_3$ after heating at 200℃ at loadings of 16 (-), 24 (-) and 32 (-) PUC. ▲ denotes zeolite and ★ denotes lithium borohydride amide peaks.

Relative peak intensities did not change much either with loading or on repeated heating. When the mixture was heated to temperatures above 200℃, pressures were observed. When the temperature was increased the changes in relative peak intensity were greater. This indicated that a greater change in the samples was seen on partial desorption.

When an elevated heating to 250°C was performed on two samples, one the original starting mixture and the other a previously heated mixture, it was found that the fresh mixture produced a pressure of gas in the sealed tube whilst the previously heated mixture did not. This phenomenon was explored further through vacuum TPD measurements.

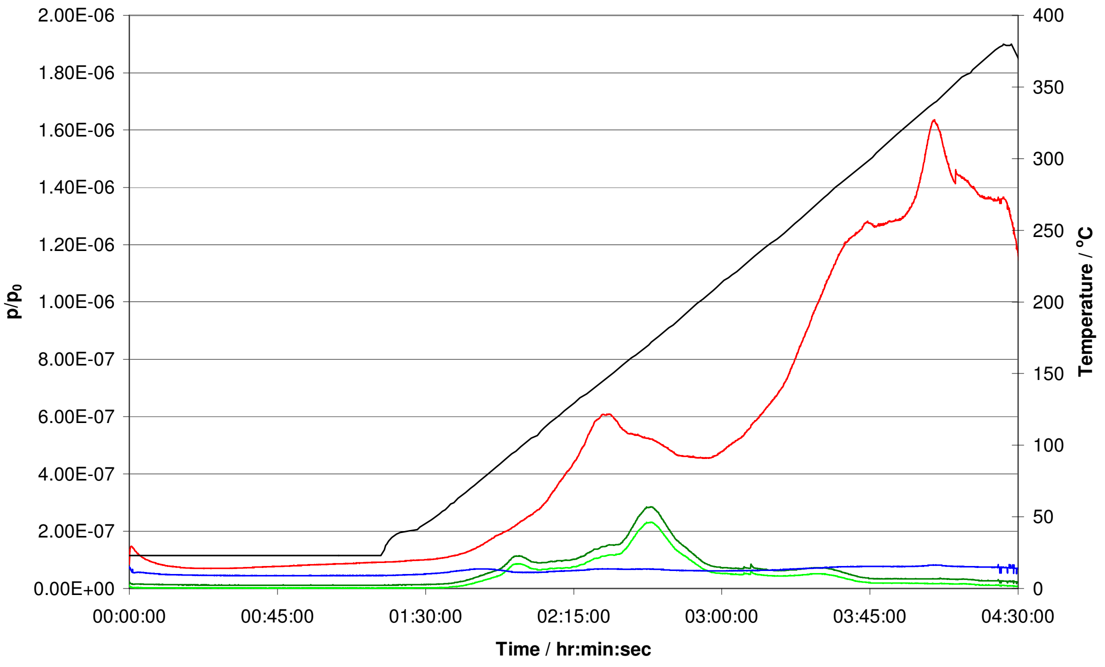

Figure 7.15 – Vacuum TPD of $(Li_4BH_4(NH_2)_3)_{16}$.NaX mixture from 30 to 400°C: temperature (-); and MS trace for hydrogen (-); H_2O (-); $^{\cdot}OH/NH_3$ (-); and $NH_2^{\cdot}$ (-).

The sample mixture when desorbed in figure 7.15, showed a very low onset to desorption with ammonia and hydrogen appearing at around 80°C, the hydrogen peaking at 150°C and ammonia at 175°C, with the majority of the hydrogen desorption occurring above 250°C, peaking at 325°C. Bulk $Li_4BH_4(NH_2)_3$ under similar conditions shows desorption of ammonia and hydrogen at 180°C with a further peak of hydrogen at

290°C. Differences between the bulk and mixture desorption could be attributed to the occlusion process occurring over the temperature range.

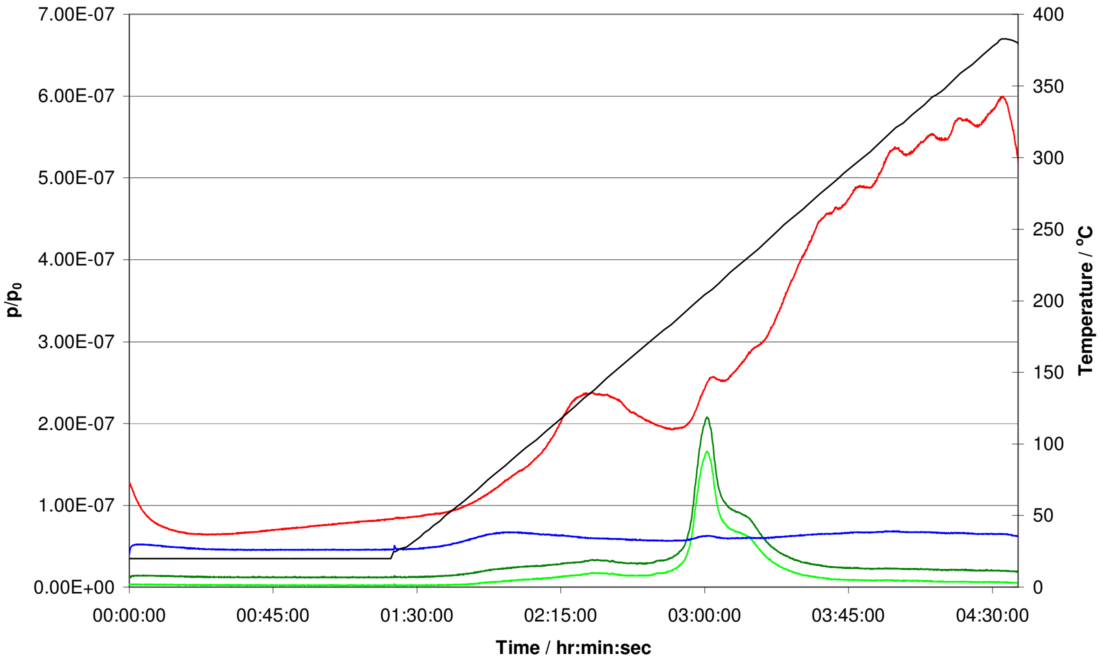

Figure 7.16 – Vacuum TPD from 30 to 400°C of $(Li_4BH_4(NH_2)_3)_{16}$.NaX after heating at 200°C: temperature (-); and MS trace for hydrogen (-); H_2O (-); $^{\cdot}OH/NH_3$ (-); and $NH_2^{\cdot}$ (-).

The sample after reaction (figure 7.16) behaved in a similar fashion with regard to hydrogen desorption with an initial peak at around 150°C. The ammonia desorption on the other hand was suppressed to 210°C. Again the final hydrogen desorption was broad above 250°C. The ammonia desorption occured at higher temperature over the mixture and bulk $Li_4BH_4(NH_2)_3$, conversely the hydrogen desorption occurs at lower temperature to the bulk and mixture. Some of the desorption could come from unoccluded $Li_4BH_4(NH_2)_3$. Hydrogen desorption also appears broad, which could indicate some desorption due to occluded material. It remains inconclusive as to whether occlusion has been successful, though changes to the desorption have occurred, they share some bulk characteristics.

7.4 Conclusion

A variety of different effects were observed on the incorporation of different materials into the zeolites. The ammonia borane samples showed some degree of successful guest incorporation, shown by gradual changes in lattice parameter and alterations to relative peak intensities. The generation of pure products through thermal reaction appeared to be problematic, but a complete desorption over a short period favouring completely gaseous products was observed. This implies that the alternative polymeric product is not particularly stable within the channel structure of the zeolites.

Reaction with lithium borohydride amide showed minimal experimental evidence to suggest incorporation within the zeolite, with lattice parameters and intensities not changing significantly. Nevertheless, changes observed in desorption data would indicate incorporation had occurred to some extent, though bulk desorptions properties were also observed. Both ammonia and hydrogen are observed on desorption. Coloured products formed suggest that sodium clusters may have been formed.

7.5 References

1. Baitalow F., Baumann J., Wolf G., Jaenicke-Rößler K., Leitner G., *Thermochim. Acta*, **2005**, 430, 9
2. Chater P. A., Anderson P. A., Prendergast J. W., Walton A., Mann V. S. J., Book D., David W. I. F., Johnson S. R., Edwards P. P., *J. Alloy Comps.*, **2007**, 446-447, 350
3. Parry R. W., Schultz D. R., Girardot P. R., *J. Am. Chem. Soc.*, **1958**, 80, 1
4. De Benedetto S., Carewska M., Cento C., Gislon P., Pasquali M., Scaccea S., Prosini P P., *Thermochim. Acta*, **2006**, 441, 184
5. Baumann J., Baitalow F., Wolf G., *Thermochim. Acta*, **2005**, 430, 9

6. Gutowska A., Li L., Shin Y., Wang C. M., Li X. S., Linehan J. C., Smith R. S., Kay B. D., Schmid B., Shaw W., Gutowski M., Autrey T., *Angew. Chem. Int. Ed.*, **2005**, 44, 3578
7. Feaver A., Sepehri A., Shamberger P., Stowe A., Autrey T., Cao G., *J. Phys. Chem. B.*, **2007**, 111, 7469
8. Breck D. W., Reed T. B., *J. Am. Chem. Soc.*, **1956**, 78, 5972
9. Baerlocher Ch., Meier W. M., Olson D. H., *Atlas of Zeolite Framework types*, **2001**
10. Olson D. H., *J. Phys. Chem.*, **1970**, 74, 2758
11. Wolf G., Baumann J., Baitalow F., Hoffmann F. P., *Thermochim. Acta*, **2000**, 343, 19
12. Chater P. A., David W. I. F., Johnson S. R., Edwards P. P., Anderson P. A., *Chem. Commun.*, **2006**, 2439
13. Filinchuk Y. E., Yvon K., Meisner G. P., Pinkerton F. E., Balogh M. P., *Inorg. Chem.*, **2006**, 45, 1433
14. Yoon K. B., Kochi J. K., *J. Chem. Soc. Chem. Commun.*, **1988**, 510
15. Edwards P. P., Harrison M. R., Klinowski J., Ramdas S., Thomas J. M., Johnson D. C., Page C. J., *J. Chem. Soc. Chem. Commun.*, **1984**, 982
16. Anderson P. A., Barr D., Edwards P. P., *Angew. Chem. Int. Ed. Engl.*, **1991**, 30. 1501

CHAPTER 8

ADSORPTION OF HYDROGEN BY SODIUM METAL IN ZEOLITES

8.1 Introduction

One area which could show interest would be the introduction of a compound or element with the capacity to absorb hydrogen into the pores to observe any modifications to the adsorption uptake compared with that of the bulk. It was important to look at simpler systems than the desorption products of mixed hydrides such as lithium hydride and boron as shown with lithium borohydride. Experimental data has shown that the introduction of magnesium into a porous carbon yielded improved uptake due to the fine dispersion and small particle sizes[1,2]. It was suggested that the small particle sizes improve the kinetics of diffusion within small particles or clusters allowing for easier hydrogenation.

In the case of lithium borohydride, highly loaded NaA and NaX showed limited hydrogenation of the desorbed product. Improved hydrogen uptake in $Li_3BN_2H_8$ after desorption has also been reported after inclusion in carbon scaffolds[3].

The main reason for this is likely to be the relative lack of reactivity of the desorption products. Therefore it was decided to examine the hydrogenation of zeolites containing more reactive guest species. Two sodium metal containing Y-type zeolites were chosen: a highly loaded Na_{64}/Na_{56}-Y and a slightly less loaded Na_{44}/Na_{56}-Y. The samples were analysed to determine the effects of the adsorption of hydrogen.

8.2 Experimental

The samples of Na_{64}/Na_{56}-Y and Na_{44}/Na_{56}-Y were prepared by Dr Lee Woodall. The samples were prepared from the reaction of dehydrated zeolite (Na_{56}-Y) with a measured amount of sodium metal, in the vapour phase. The reactions were performed at 200℃ for up to 72 hours to produce a homogeneous product[4,5].

The samples were characterized using powder X-ray diffraction (PXRD) and ESR spectra of a sample were collected at room temperature and 77 K. Gravimetric methods were used to determine uptakes of high purity hydrogen at 77 K and room temperature.

8.3 Results and Discussion

The adsorption properties of the samples were analysed with the IGA. The samples were initially outgassed at 50℃. Under these conditions no weight loss or gain was observed, indicating that the sample remained unchanged.

An isotherm measurement was performed on Na_{64}/Na_{56}-Y at 77 K; the results are shown in figure 8.1.

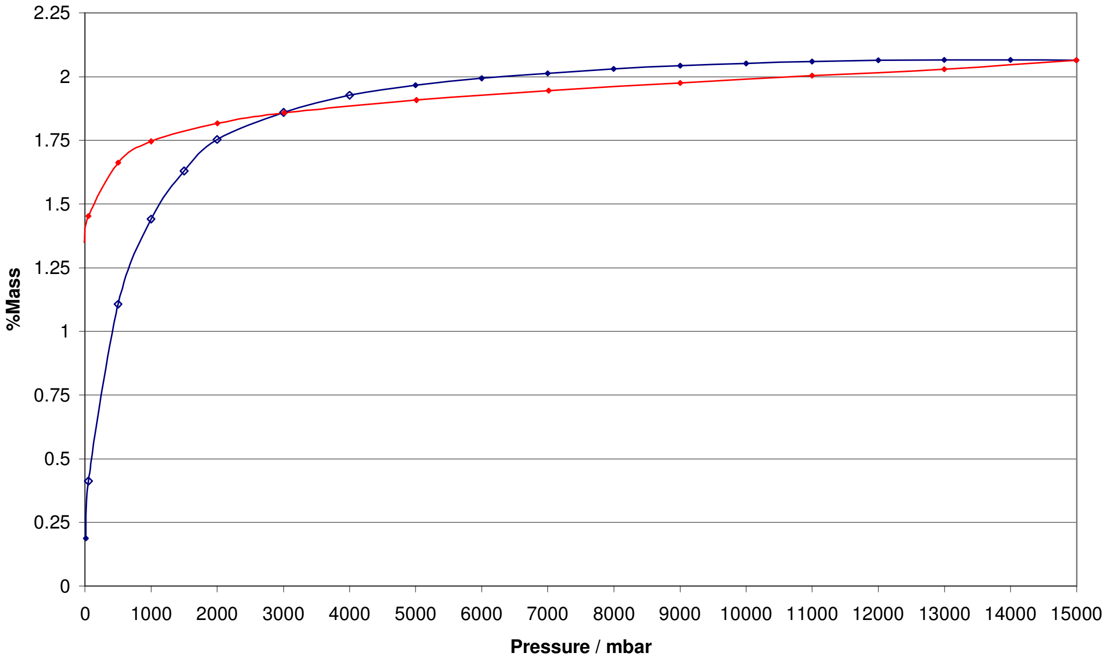

Figure 8.1 – Isotherm at 77 K of Na_{64}/Na_{56}-Y showing both adsorption (-) and subsequent desorption(-). Open symbols denote points timed out.

There were several things which were interesting about this isotherm. The uptake of 2.08 wt% was 15% greater than that for the unloaded NaY (1.81 wt%). The increased uptake of hydrogen, in spite of the presence of sodium in the zeolite pores, appeared counterintuitive as a reduced pore volume would be expected.

At each kinetic point parameters for fitting of the adsorption are used, minimum and maximum times, a required percentage completion as well as error margins for fitting parameters. When a point timed out, there was adsorption which was not completed within the maximum allotted time. These cases occurred at low pressures where adsorption and diffusion were slow.

Another noticeable feature was the hysteresis between the adsorption and desorption curves. There were several possible reasons for this: reactions with impurities; trapping;

and irreversible adsorption. If there were impurities reacting with the sample, the perceived mass increase would continue at high pressures in the desorption cycle. As the mass was clearly reduced on desorption this cannot be the case. A further isotherm was performed at 77 K to observe possible changes after a re-evacuation of sample at 50°C, again with no perceived weight loss.

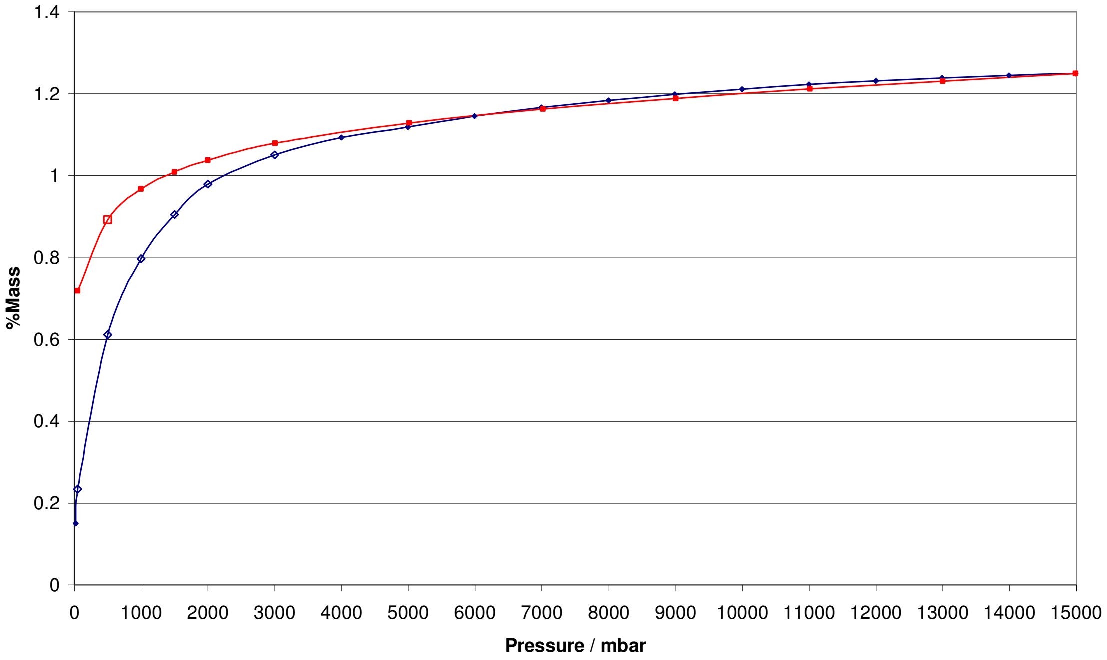

Figure 8.2 – Second isotherm at 77 K of Na_{64}/Na_{56}-Y showing both adsorption (-) and subsequent desorption(-). Open symbols denote points timed out.

A reduction in the amount adsorbed was observed, only 1.25 wt%. This value was slightly (0.25 wt%) greater than the measured desorption in the first isotherm. The similarity between these values suggests that there may be irreversible adsorption or trapping of hydrogen which was reducing the uptake capacity. The remaining presence of hysteresis would suggest that there may still be some trapping occurring. The reaction between hydrogen and sodium may still be occurring, given the timing out of some low pressure points.

It seemed appropriate to check whether a similar phenomenon happened in a slightly less loaded sample. Na_{44}/Na_{56}-Y was chosen and treated in a similar fashion.

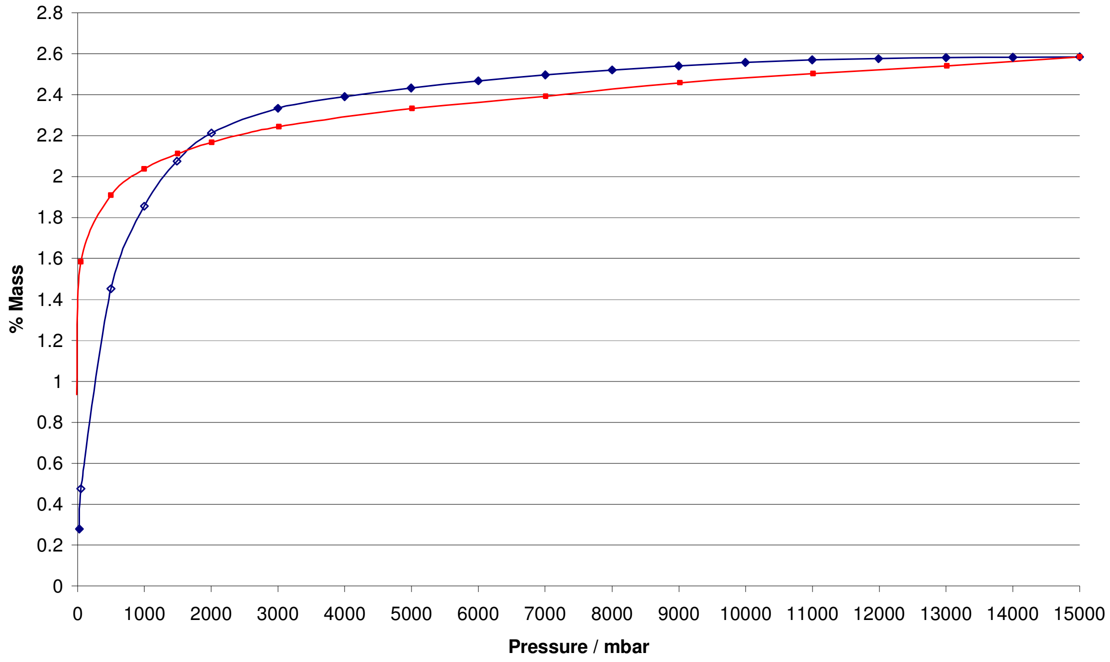

Figure 8.3 – Isotherm at 77 K of Na_{44}/Na_{56}-Y showing both adsorption (-) and subsequent desorption(-). Open symbols denote points timed out.

As we can see in figure 8.3, the uptake was again significantly improved to 2.59 wt%, an increase of 43% over the unloaded zeolite. This suggests that the reduced loading of sodium allows for extra volume to be occupied by hydrogen, observed as an increase in adsorption. The molar densities of sodium and sodium hydride are 0.0421 and 0.0582 mol/cm^3 respectively, suggesting that the hydrogenation would cause a contraction allowing further adsorption of hydrogen. Again the hysteresis was present suggesting irreversible interaction at 77 K, with a difference of around 1 wt% at the end of the isotherm.

This sample also was evacuated at 50℃ and the isotherm repeated under the same conditions.

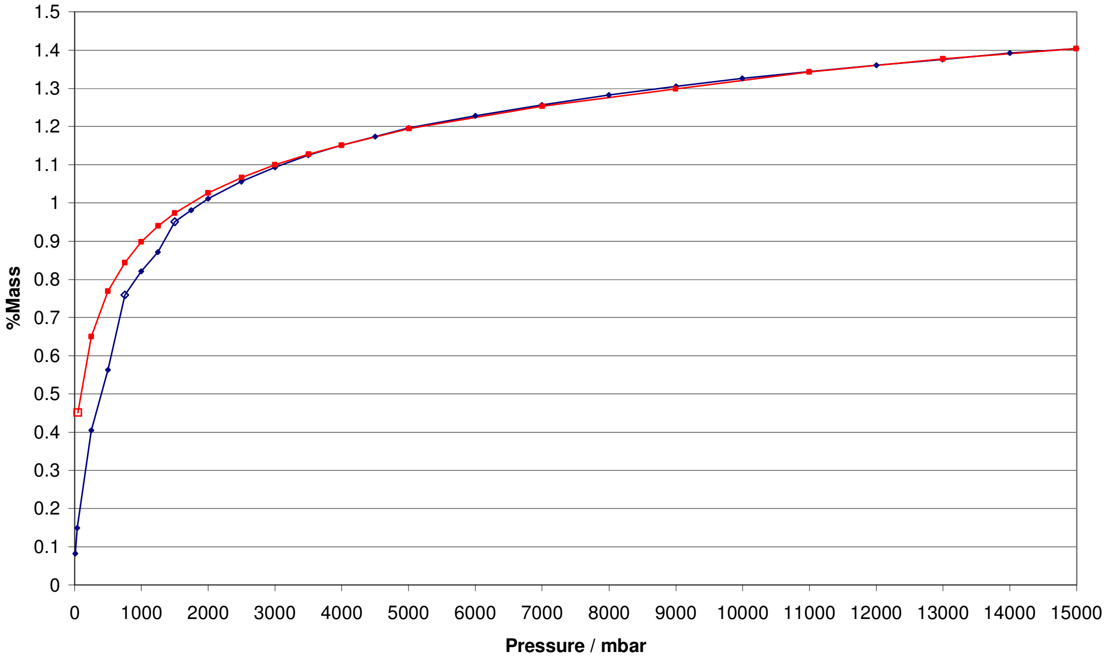

Figure 8.4 – Second isotherm at 77 K of Na_{44}/Na_{56}-Y showing both adsorption (-) and subsequent desorption(-). Open symbols denote points timed out.

The behaviour was similar to the more highly loaded sample where there was a diminished uptake of 1.40 wt% after the outgassing. This corresponds to a 1.19 wt% discrepancy of uptakes between the two isotherms of Na_{44}/Na_{56}-Y. A slight hysteresis was still observed between adsorption and desorption. There was a slight “kink” in the adsorption between 1 and 2 bars, though it was defined by two timed out points. It may be indicative of some form of enhanced adsorption interaction occurring at lower pressures, probably due to low population of preferred adsorption sites.

These results lead to further isotherms being performed, in an attempt to understand better the nature of any distinct adsorptions occurring, in particular the possible low pressure “kink” that appeared in the isotherms for Na_{44}/Na_{56}-Y. A second goal was to perform several room temperature isotherms prior to a liquid nitrogen isotherm, to ascertain whether the irreversible portion of the isotherms was due to the formation of the hydride.

The “back to back” isotherms in figure 8.5, showed that the second adsorption at 77 K retraced almost exactly the first desorption. The kink in the adsorption must be due to some form of reversible trapping which was not present in the second adsorption, which was confirmed by desorption at room temperature under vacuum.

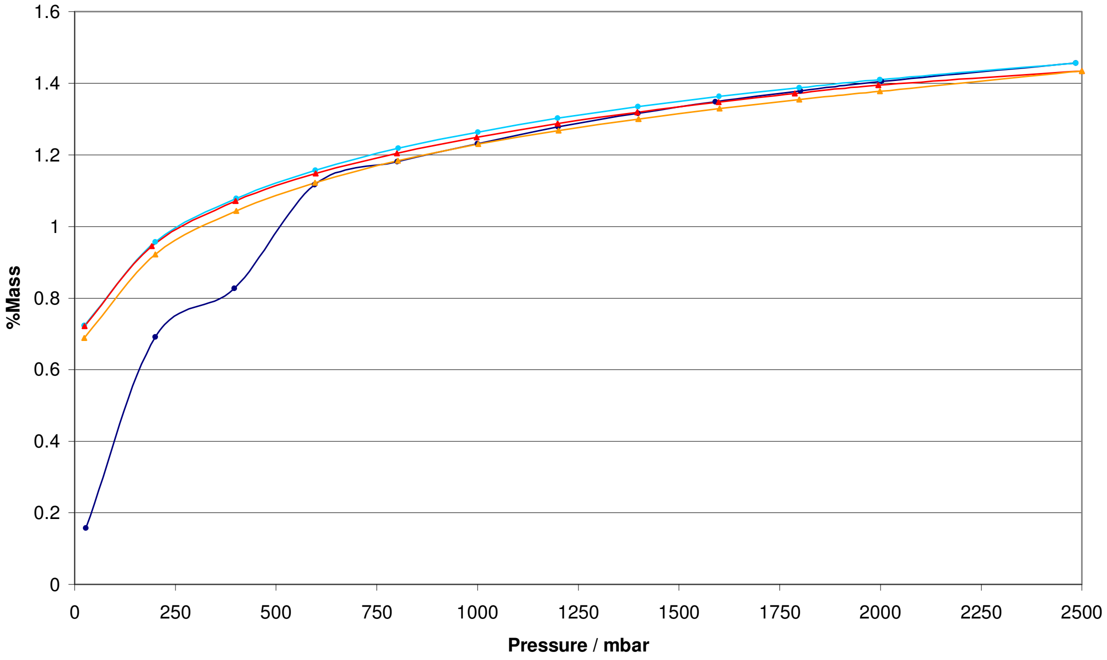

Figure 8.5 – Back to back isotherms at 77 K of Na_{44}/Na_{56}-Y showing the first adsorption (-) and desorption(-); the second adsorption (-) and desortion (-).

The kink region showed a quick initial uptake in the kinetic data, yet a slower further uptake taking up to 8 hours was observed on the first adsorption in figure 8.5. In the second run only the type 1 isotherm was observed, completing in 20 minutes. This confirmed the presence of several adsorption mechanisms.

The sample subjected to room temperature isotherms to start with showed slow adsorptions. The 500 mbar point didn't equilibrate over a 48 hour period, and the 1 bar point couldn't over 24 hours. The mass traces of these two kinetic points look as if they were adsorbing impurities, but this problem would continue and get more pronounced at higher pressures. As it doesn't, this can be assumed to be caused by the hydrogen interacting with the zeolite. Clearly this was an irreversible process as can be observed from the desorption.

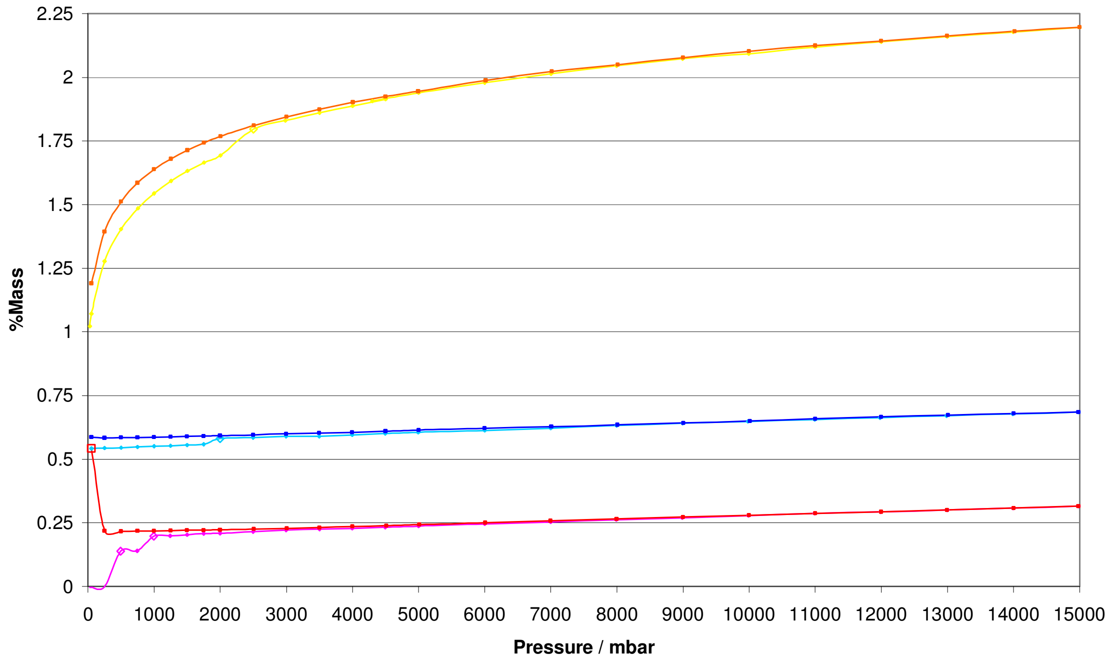

Figure 8.6 – Room temperature isotherms of Na$_{44}$/Na$_{56}$-Y showing the first room temperature adsorption (-) and desorption(-); the second room temperature adsorption (-) and desortion (-); the third adsorption (-) and desorption (-) at 77K. Open symbols denote points timed out.

The final point on this desorption showed a great uptake at low pressure. This behaviour could be indicative of a hydrogenation of the sodium in the zeolites, accounting for the lack of reversibility. This effect occurring at low pressure could be due to favoured adsorption sites which are preferentially occupied at low pressures, at higher pressures the competition for these sites may inhibit the hydrogenation of the clusters. The second room temperature isotherm showed a greatly reduced uptake, implying that the hydrogenation had run to completion. The final 77 K isotherm shows some hysteresis, but far less than previously observed in this sample. This further suggests a third adsorption process which is reversible but only slowly. This could be a form of trapping of hydrogen.

Collectively, these results show that there were several adsorption processes occurring. During the isotherms the samples themselves went from a rich black colour, to a grey colour. A similar colour change was observed on oxidation/hydration, from the rich black to red, to a light grey.

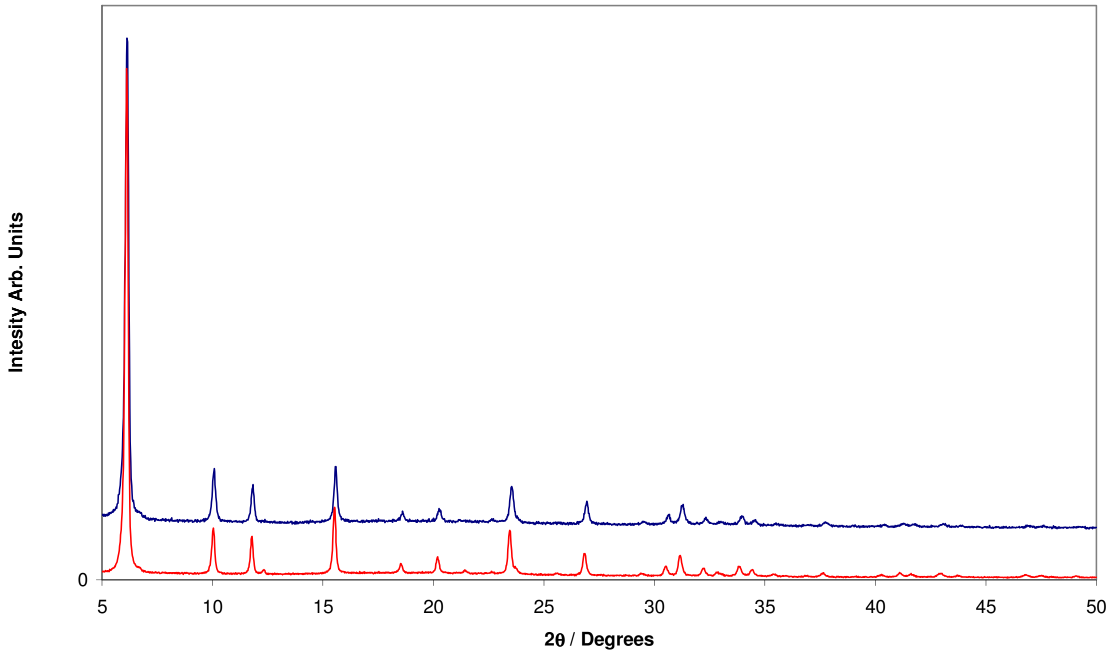

Figure 8.7 – Powder XRD patterns showing Na_{44}/Na_{56}-Y before (-) and after (-) treatment on the IGA.

The samples were checked by powder XRD (Figure 8.7) and showed a change from 24.856(5) to 24.768 (7) Å in the lattice parameters after IGA treatment. Importantly the framework was retained. Only the zeolite phase was present in the XRD, suggesting any sodium hydride present remained within the framework. Evidence for a change in the contents of the zeolite can be found in small changes in relative peak intensities.

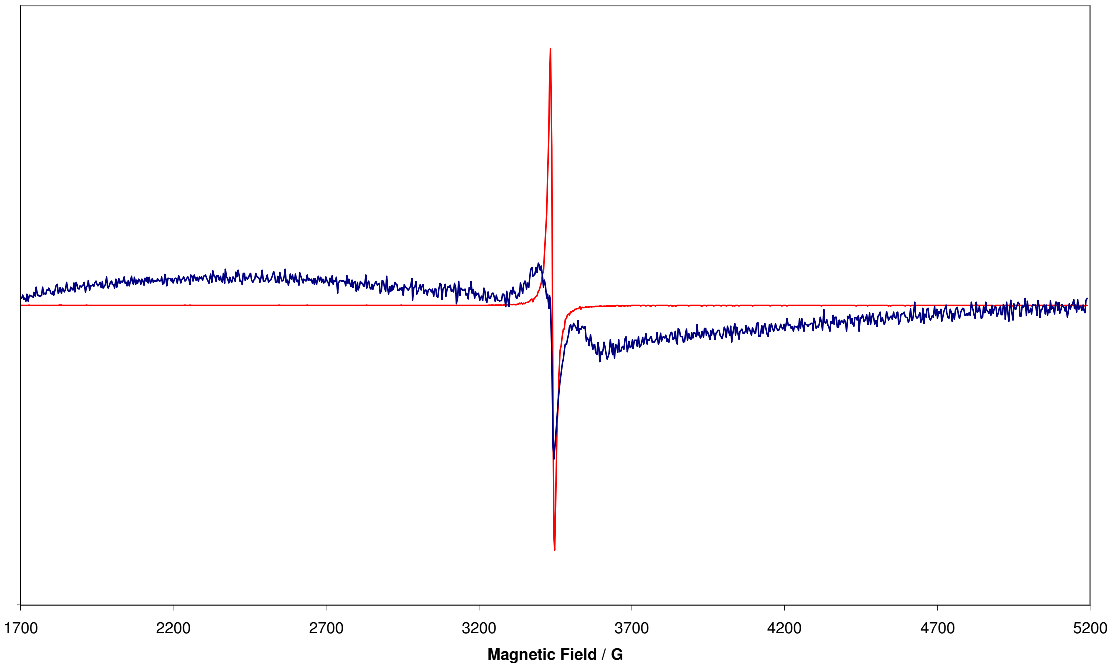

Figure 8.8 – ESR spectra collected at 77 K showing Na_{44}/Na_{56}-Y before (-) and after (-) treatment on the IGA.

ESR also indicated a change to the zeolite contents. Na_4^{3+} clusters were observed on loading sodium metal into NaY, filling the sodalite cages. Sodium is expected in the supercages, but its format remains uncertain. At lower loadings hyperfine lines would be observed when the clusters are well separated, but these were not observed. The intensity of the ESR signal was greatly reduced after IGA treatment suggesting a reduction in the number of clusters present, also an indication that some clusters have reacted. The g values were 2.0010(1) for the as synthesised sample, whilst the post IGA sample showed a g value of 2.025(1) for the broader signal overlaid with a less sharp signal with g = 2.0009(1). Removal of the dominant sharp signal is caused by the formation of sodium hydride type clusters, which are not paramagnetic.

8.4 Conclusion

Sodium loaded zeolites showed that the adsorption of hydrogen could occur through different mechanisms. Initial reactions with hydrogen appear to show irreversible adsorption occurring which was likely to result from the hydrogenation of sodium within the zeolite pores. Two different modes of reversible adsorption were also observed: one which appeared irreversible unless the sample was evacuated, suggesting a trapping mechanism; the final reversible mode was typical of physisorption. The zeolite structure remained intact whilst changes were observed in sodium clusters within the cages.

8.5 References

1. Gross A.F., Ahn C. C., Vajo J. J., Van Atta S. L., Liu P., *Nanotechnology*, **2009**, 20, 204005
2. Vajo J. J., Olson G. L., *Scripta Materialia*, **2007**, 56, 829
3. Wu H., Zhou W., Wang K., Udovic T. J., Rush J. J., Yildirim T., Bendersky L. A., Gross A. F., Vajo J. J., Van Atta S. L., Pinkerton F. E., Meyer M. S., *Nanotechnology*, **2009**, 20, 204002
4. Woodall L. J., *Inorganic electrides: Spin-pairing and cluster states in alkali-doped zeolites*, Thesis awarded by the University of Birmingham, **1995**.
5. Edwards P. P., Harrison M. R., Klinowski J., Ramdas S., Thomas J. M., Johnson D. C., Page C. J., *J. Chem. Soc. Chem. Commun.*, **1984**, 982

CHAPTER 9
OCCLUSION OF LITHIUM BOROHYDRIDE IN ION-EXCHANGED ZEOLITES

9.1 Introduction

Ion exchange of different cations into zeolites can serve a wide variety of purposes[1-3]. When considering the benefits for hydrogen storage we have a potential for minimising the zeolite mass by using lower weight cations. To avoid the competing solid state ion exchange observed in chapter 4, lithium zeolites could be used. The introduction of ions containing hydrogen could modify the desorption characteristics of the composite materials, whilst increasing weight percentages, and potentially modifying adsorption properties[4,5]. The last group of potential ion-exchange candidates are those which offer catalytic properties. The use of milled transition metals has found catalytic success with a range of hydrides, serving to improve reaction kinetics and reduce desorption temperatures[6-8].

9.2 Lithium Ion-Exchanged Zeolites

Lithium ion exchange was initially identified as a means of minimising the zeolite weight and to avoid the solid state ion exchange which was occurring in the sodium zeolites, outlined as a problem in chapter 4. In the case of cryogenic adsorption of hydrogen, ion exchange of lithium for sodium has been shown to result in an increased uptake of hydrogen (2.17 *vs* 1.79 wt%) in the case of zeolite X with zeolite Y showing a similar uptake (1.80 *vs* 1.81 wt%) after ion-exchange[4,9]. After lithium exchange, in contrast, zeolite A samples showed a negligible uptake of hydrogen (at 77K under 15 bar). This reduction in radius also facilitates occupation of other sites, dependent on the framework, which can inhibit adsorption by blocking pores, explaining the variety of results[10]. LiA and LiX were chosen as candidates for study because of their very different behaviour in cryogenic adsorption.

9.2.1 Experimental

The ion exchange with lithium nitrate was performed as outlined in the experimental chapter.

The dried zeolites were then transferred to an argon glove box to ensure that they did not rehydrate and allow for intimate mixing with the lithium borohydride. Mixtures were formed in increments of 32 $LiBH_4$ per unit cell (PUC) from 64 – 128 for LiA and 32 – 256 for LiX. For LiA the full $Fm\bar{3}c$ space group (24 Å unit cell), and for LiX the $Fd\bar{3}m$ space group with a unit cell parameter of approximately 25 Å, were used for determination of unit cell loadings[11]. The samples were prepared as outlined in section 3.2.3.3.

The samples were then characterized using powder X-ray diffraction. Vacuum TPD data was collected over the temperature range of 30 – 450℃

9.2.2 Results and Discussion

Lithium ion exchange of zeolite A resulted in a solid with a lower lattice parameter (24.018(3) Å) compared with that of the original NaA (24.652(6) Å). Reaction between the off-white powder LiA and the crystalline lithium borohydride at 250℃ over 12 hours resulted in no pressure within the sealed tube and produced a light grey powder.

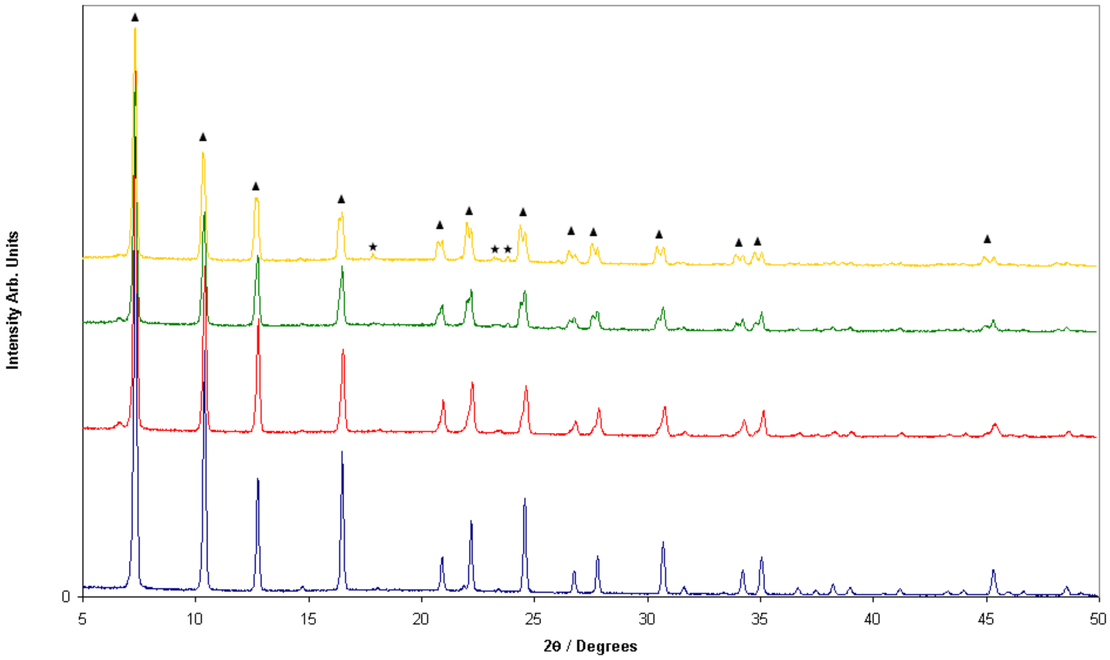

Figure 9.1 – Powder XRD patterns of LiA heated with different loadings of $LiBH_4$ PUC showing: LiA (-); 64 PUC (-); 96 (-) and 128 (-).▲ denotes zeolite and ★ denotes lithium borohydride peaks.

On inspection of the XRD patterns in figure 9.1 a new phase at lower 2θ was observed after reaction. Initially present as shoulders on the main zeolite peaks at the lowest loading, these became distinguishable at higher loadings. This is similar behaviour to that observed in chapter 4 with the sodium zeolites and lithium borohydride. The second phase appeared to increase in intensity as the loading was increased. The lattice parameters, in figure 9.2, showed two distinct lattice parameters, one of similar value to the dehydrated LiA, the other a new 'loaded' phase.

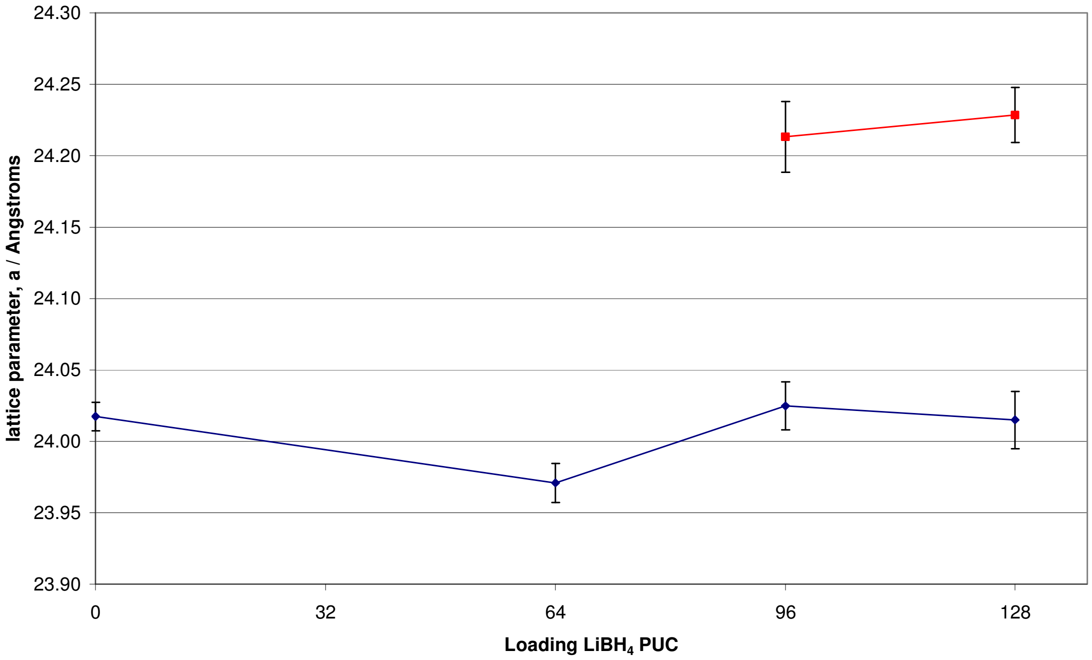

Figure 9.2 – Lattice parameter against loading for LiA with lithium borohydride, showing the LiA type phase (-) and the new loaded phase (-). Errors are to 3ESD's.

Lithium borohydride was not observed in the patterns at loadings of 64 and 96 PUC, but at a loading of 128 lithium borohydride PUC it was observed in the XRD pattern. At this loading two distinct zeolite phases were still observed. Further heating of this sample up to 48 hours increased the majority loaded phase, but did not remove the lithium borohydride entirely. The two zeolite phases in the reheated samples had lattice parameters consistent with the values of the samples with dehydrated LiA at 24.018(3) Å and 24.213(8) Å for the loaded phase. Relative intensities were the same as dehydrated LiA for both phases.

After ion exchange LiX was found to have a lattice parameter of 24.780(4) Å, smaller than that of its sodium counterpart at 25.117(3) Å. On reaction of the off-white LiX with lithium borohydride at 250℃ over 12 hours no pressure was produced within the sealed tube, the products appearing as a light grey powder.

In contrast with the LiA sample only one zeolite phase was observed in the diffraction patterns over the range of loading.

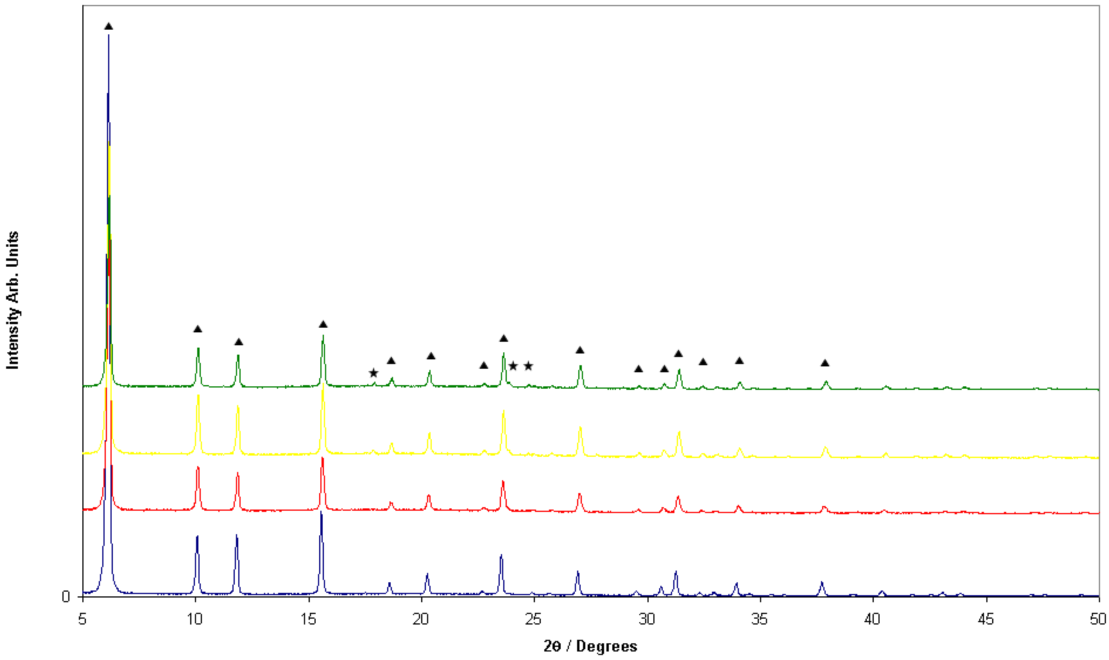

Figure 9.3 – Powder XRD patterns of LiX heated with different loadings of LiBH$_4$ PUC showing: LiX (-); 96 PUC (-); 160 (-) and 256 (-). ▲ denotes zeolite and ★ denotes lithium borohydride peaks.

Inspection of the XRD patterns, figure 9.3, showed that above (LiBH$_4$)$_{160}$.LiX lithium borohydride remained in the diffraction pattern after reaction. The sample at a loading of 192 PUC was reheated, and whilst the most intense peak at 18° 2θ, corresponding to the (101), was diminished after heating it was still present.

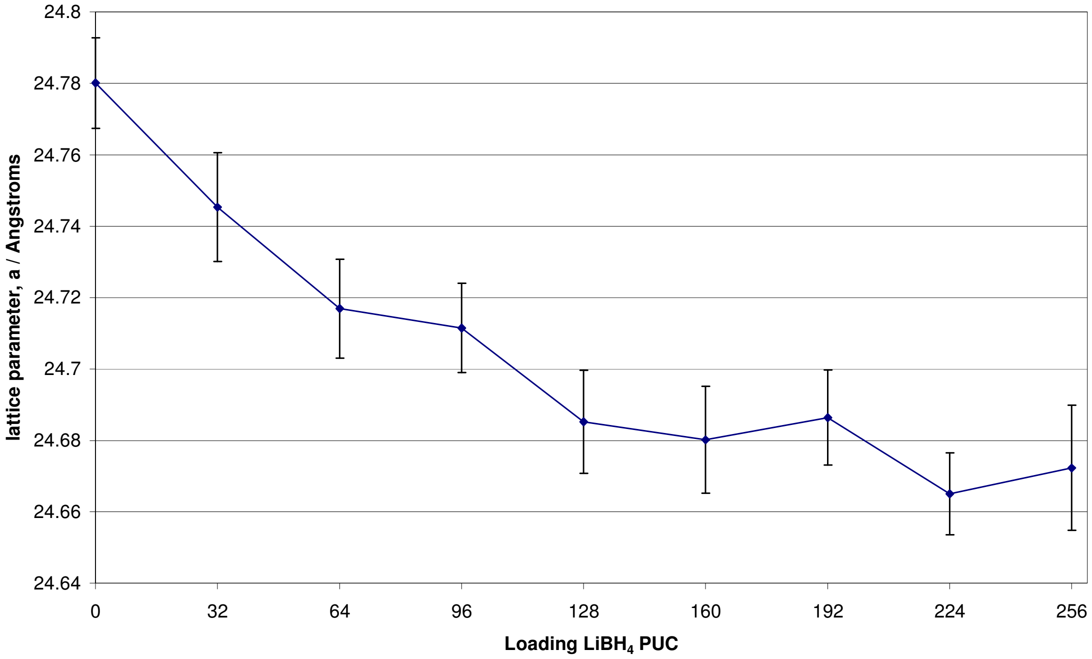

Figure 9.4 – Lattice parameter against loading for LiX with lithium borohydride. Errors are to 3ESD's.

We see in figure 9.4 that as the loading was increased a corresponding reduction was seen in the zeolite lattice parameter. These values tend towards a value of approximately 24.67 Å within error at high loading. The lattice parameters levelled out around 160 lithium borohydrides per unit cell, correlating well with the perceived maximum occupancy from the appearance of $LiBH_4$ in the diffraction pattern.

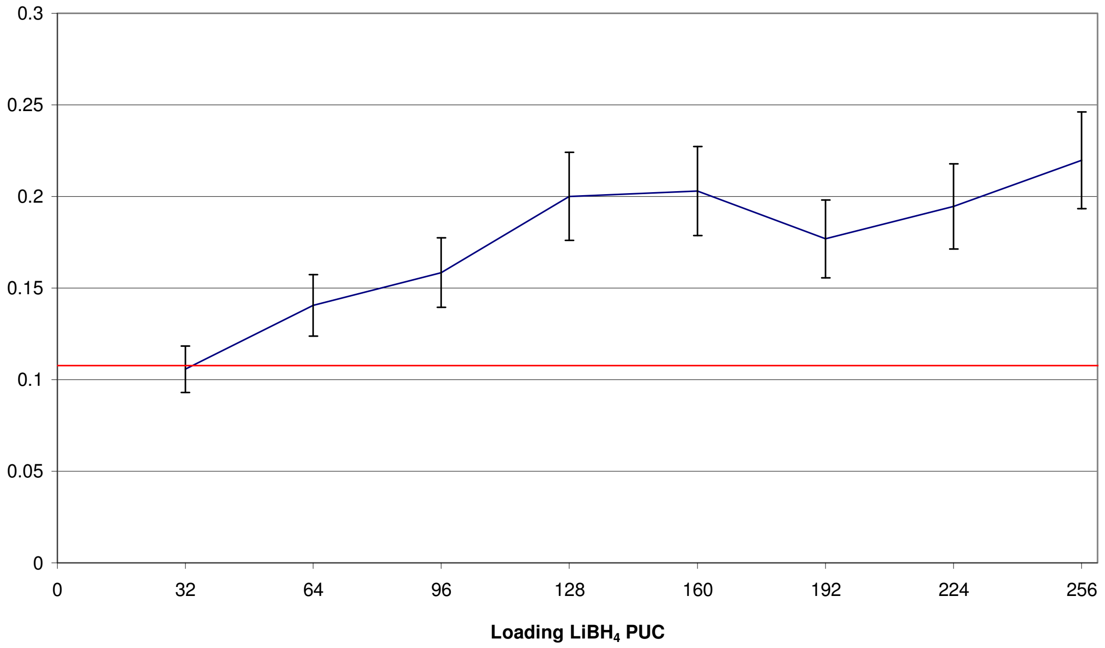

Figure 9.5 – The relative ratio of the (220) to the (111) peaks over a range of compositions for LiX with lithium borohydride, showing: LiA dehydrated (-) and the range of sample compositions (-).

The general trend away from the ratio value for the dehydrated zeolite, shown in figure 9.5, with the increase in loading provides additional evidence for the incorporation of lithium borohydride in the zeolite. Again the values appeared to plateau around 160 lithium borohydrides per unit cell.

$(LiBH_4)_{128}$.LiX was chosen for vacuum TPD–MS measurements, shown in figure 9.6, as it contained the highest loading without signs of starting material present. The desorption was performed up to 440℃.

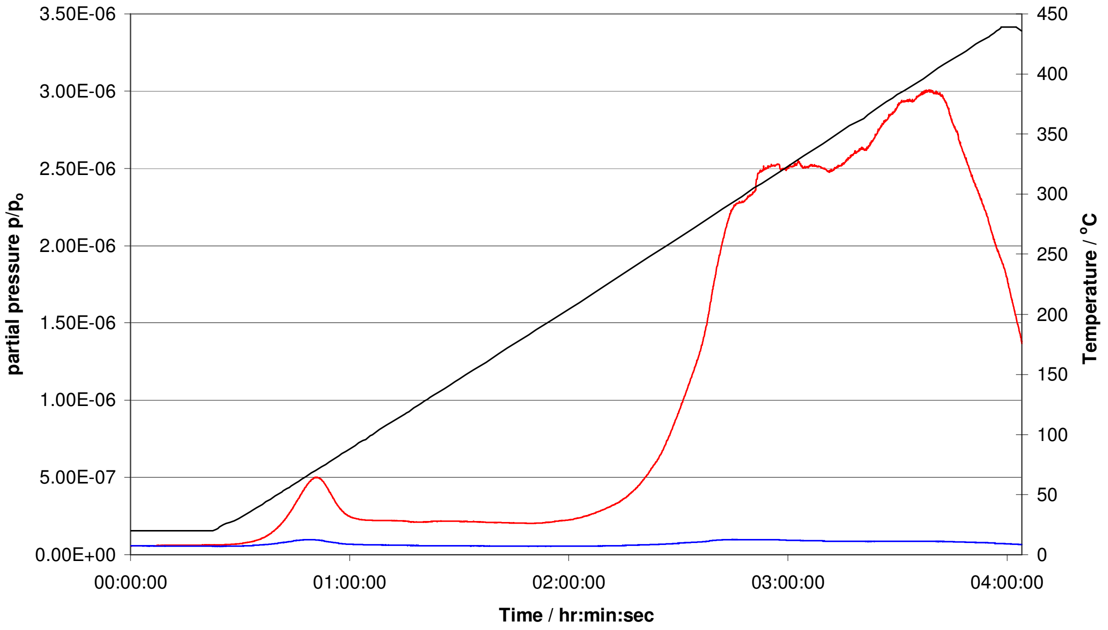

Figure 9.6 – TPD–MS trace of $(LiBH_4)_{128}$.LiX, showing the temperature (-) and the MS signal for hydrogen (-) and water (-).

Two main desorptions were observed. The first started at 50°C and peaked at 65°C, which may be the low temperature desorption of lithium borohydride associated with its bulk structure change[12]. In bulk $LiBH_4$ the change from orthorhombic phase to its tetragonal phase is typically accompanied by a small (0.3wt% hydrogen) desorption causing a slight defect in the structure. Desorbed surface moisture could react with some borohydride to yield this low temperature peak. The second desorption started at 220°C, peaking between 310 and 400°C. This compares with the desorption of bulk $LiBH_4$ which starts desorbing at 225°C and peaks at 345°C and decreases, returning to the background value within 2 hours at 438°C. The NaX system desorbed at 220°C, peaking at 375°C. The broad nature of the desorption is likely to result from poor diffusion kinetics through the framework, possibly due to pore blocking. There appears to be minimal difference between the sodium and lithium zeolite systems.

9.3 Ammonium Ion-Exchanged Zeolites

Interest in ammonium ion-exchanged zeolites initially centred on increasing the amount of hydrogen present in the system. With regard to hydrogen storage in metal hydrides, a similarity may be drawn with the lithium amide and lithium hydride system. On heating pure amide, gas desorption occurs at approximately 300℃ with the major gaseous product being ammonia. This changes when the amide is mixed with lithium hydride, altering the major product to hydrogen, with desorption starting at around 200℃[13,14]. This change has been ascribed to the interaction between protic and hydridic hydrogens from amide and hydride, respectively[13,14]. The mechanism has also been proposed to be an “ultra fast” reaction between ammonia and hydride[15]. Subsequent research was carried out into reactions between lithium amide and lithium borohydride, which also led to the reduction, and in some cases removal, of ammonia as a reaction product[16]. It was thought that a similar interaction might be exploited between the ammonium cations of the zeolite and lithium borohydride, once occluded within the zeolite pores.

Ammonium zeolites are traditionally used as a route to hydrogen zeolites, where the frameworks can accommodate this[17]. HY is used in this case because HX is unstable. We were interested examining the properties of both compounds, so the dehydration of the sample required two different circumstances. The major use of hydrogen zeolites is in acid catalysis[18]. The use of HY in hydrogen storage has been explored: it showed a slight increase to 1.85 wt% from 1.81 wt% (77 K at 15 bar) observed for the NaY parent zeolite[4,9].

9.3.1 Experimental

NaY (13Y) and $LiBH_4$ (>90%) were obtained from Sigma-Aldrich. Ion exchange with ammonium chloride was performed as outlined in the experimental chapter.

Dried zeolites were then transferred to an argon glove box to ensure that they did not rehydrate and allow for intimate mixing with the lithium borohydride. Mixtures were formed in increments of 32 $LiBH_4$ per unit cell (PUC) in the range 96 – 160. For NH_4Y the $Fd\overline{3}m$ space group with a unit cell parameter of approximately 25 Å was used for determination of unit cell loadings[11]. Samples were prepared as outlined in section 3.2.3.3.

The samples were then characterized using powder X-ray diffraction data. These samples were also analysed by TPD–MS collected over the temperature range of 30 – 450℃.

9.3.2 Results and Discussion

The ion exchange was successful showing a change of lattice parameter from 24.889(3) Å to 24.782(5) Å for NH_4Y. This is a good indicator that the ion-exchange had occurred and agrees with literature values[19].

Two methods of dehydration were used. The first method for dehydration was performed at 50℃ to avoid de-ammoniation, whilst the other at 350℃ was designed to allow the removal of ammonia. Dehydration at 50℃ over a week yielded a product with only the zeolite phase present with a lattice parameter of 24.845(5) Å. The dehydration performed at 350℃ also yielded only a single zeolite phase, but the lattice parameter was 24.714(5) Å.

9.3.2.1 NH_4Y after Dehydration at 50°C

The samples dehydrated at 50°C were heated with $LiBH_4$ under flowing line conditions at 250°C. Previous attempts with the equivalent sodium zeolite showed that reduced temperatures of below 100°C did not result in occlusion. This implied that temperatures closer to those of the melting point were imperative, but at these temperatures there was a possibility that gas might be released, so the reactions were performed under flowing argon. This procedure had earlier been shown to produce samples identical to those prepared in sealed evacuated tubes when performed with the parent zeolite and lithium borohydride. The creamy coloured zeolite when reacted with the white crystalline lithium borohydride at 250°C resulted in off-white/grey products. Analysis of the XRD patterns showed that a secondary zeolite phase was present at a higher angle, shown in figure 9.7

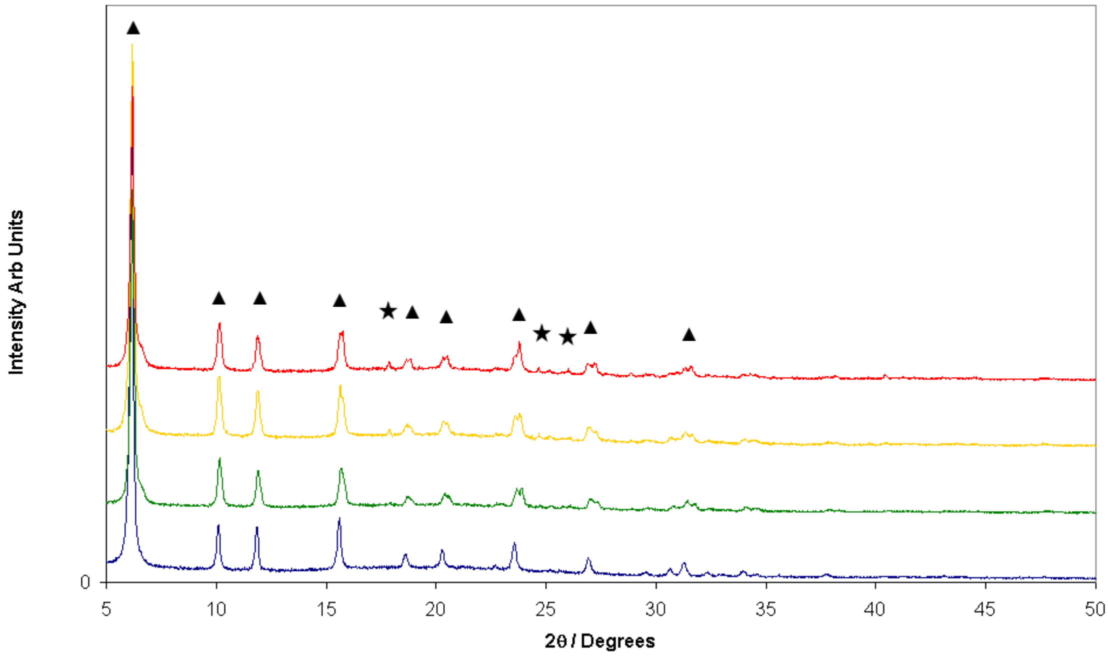

Figure 9.7 – Powder XRD patterns of NH_4Y (dehydrated at 50°C) heated with different loadings of $LiBH_4$ PUC showing: NH_4Y (-); 96 PUC (-); 128 (-) and 160 (-).▲ denotes zeolite and ★ denotes lithium borohydride peaks.

The new phase appeared at smaller d-spacings, suggesting a lattice contraction on reaction, and its intensity appeared to increase to some degree with an increase in loading. At 128 lithium borohydride PUC some lithium borohydride remained even after heating, although the new phase appeared to increase in intensity between 128 and 160 lithium borohydride PUC.

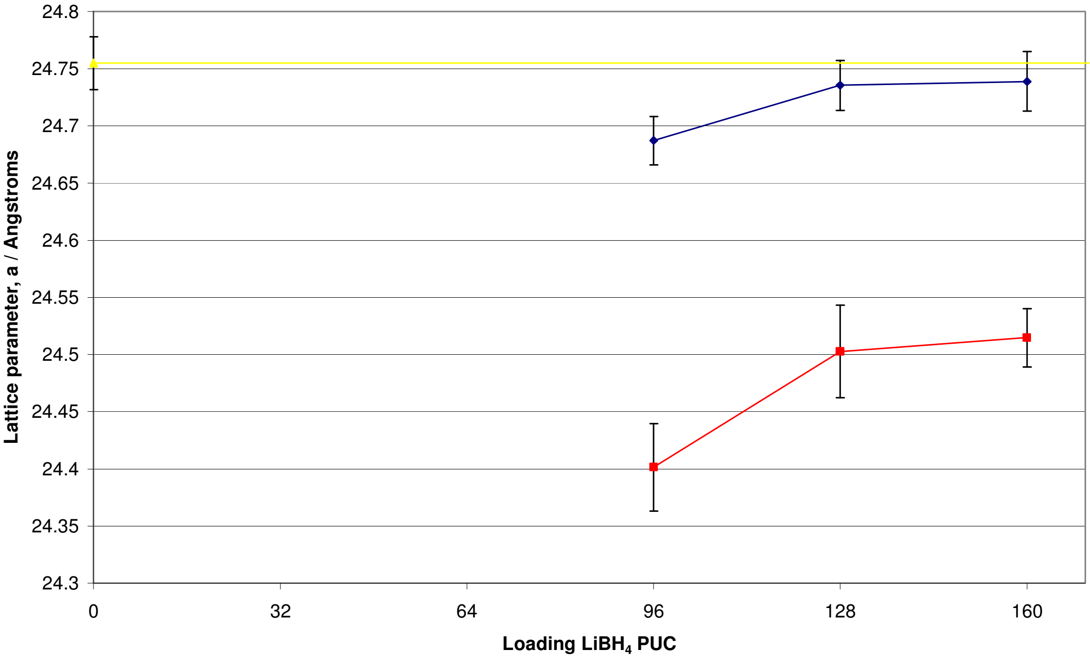

Figure 9.8 – Lattice parameter against loading for NH_4Y (dehydrated at 50°C) with lithium borohydride showing: NH_4Y dehydrated (-); NH_4Y phases (-) and the new loaded phases (-). Errors are to 3ESD's.

The lattice parameters are shown in figure 9.8. Of the two distinct zeolite phases present, one showed a similar lattice parameter to that of the dehydrated zeolite. The other phase at a smaller lattice parameter was distinct, and increased slightly with loading. This most likely indicates the presence of both loaded and unloaded regions as observed in the case of NaY.

9.3.2.2 NH_4Y after Dehydration at 350°C

Further reaction with the white crystalline lithium borohydride at 250°C for 12 hours yielded a creamy brown product. Powder XRD showed one zeolite phase present, though some peak broadening was observed, and maybe the result of deammoniation. The creamy brown colour of the solid may have been caused by some boron formation during the reaction. No pressure was generated in the evacuated tube. Any ion exchange would result in the formation of ammonium borohydride, which decomposes at –20°C[20], and within the temperature range of the reaction its decomposition product, ammonia borane, would also decompose. This observation indicates that there was no side reaction.

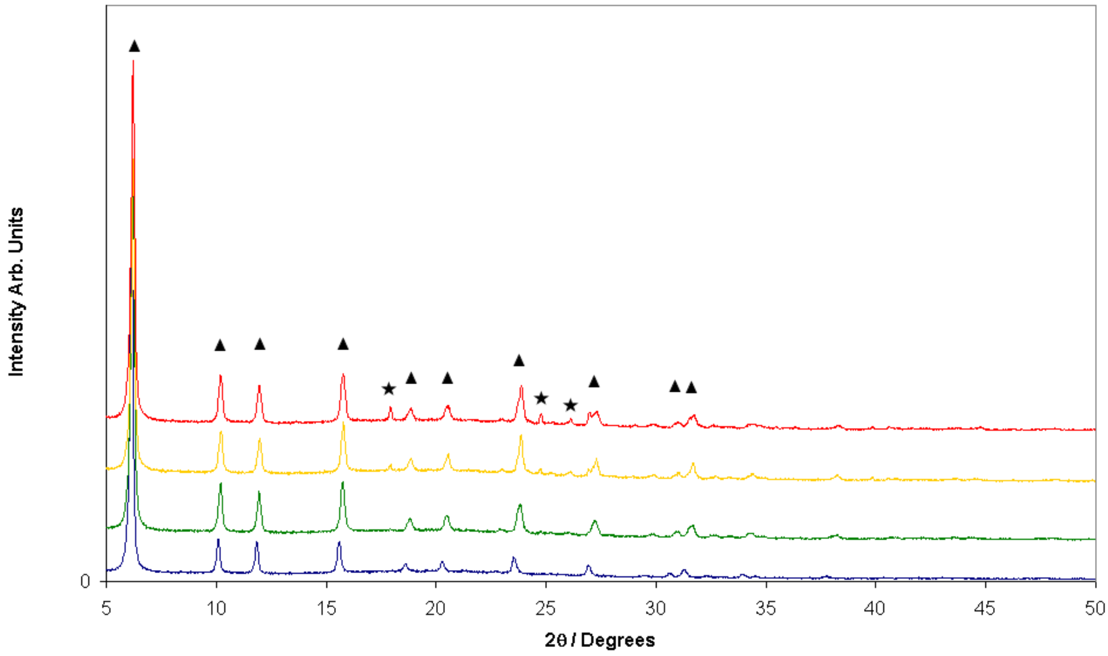

Figure 9.9 – Powder XRD patterns of NH_4Y (dehydrated at 350°C) heated with different loadings of $LiBH_4$ PUC showing: NH_4Y (-); 96 PUC (-); 128 (-) and 160 (-). ▲ denotes zeolite and ★ denotes lithium borohydride peaks.

Clearly the peaks were shifted to a higher angle indicating a contraction in the unit cell. Lithium borohydride remained at loadings above 128 per unit cell, and was found to persist upon reheating.

In this case, the lattice parameter values, figure 9.10, for the loaded samples differed greatly from that of the dehydrated zeolite. The values of 24.45 Å were similar to those for the loaded phase in the samples obtained from NH_4Y dehydrated at 50℃. This suggests that the two phases could be of similar composition.

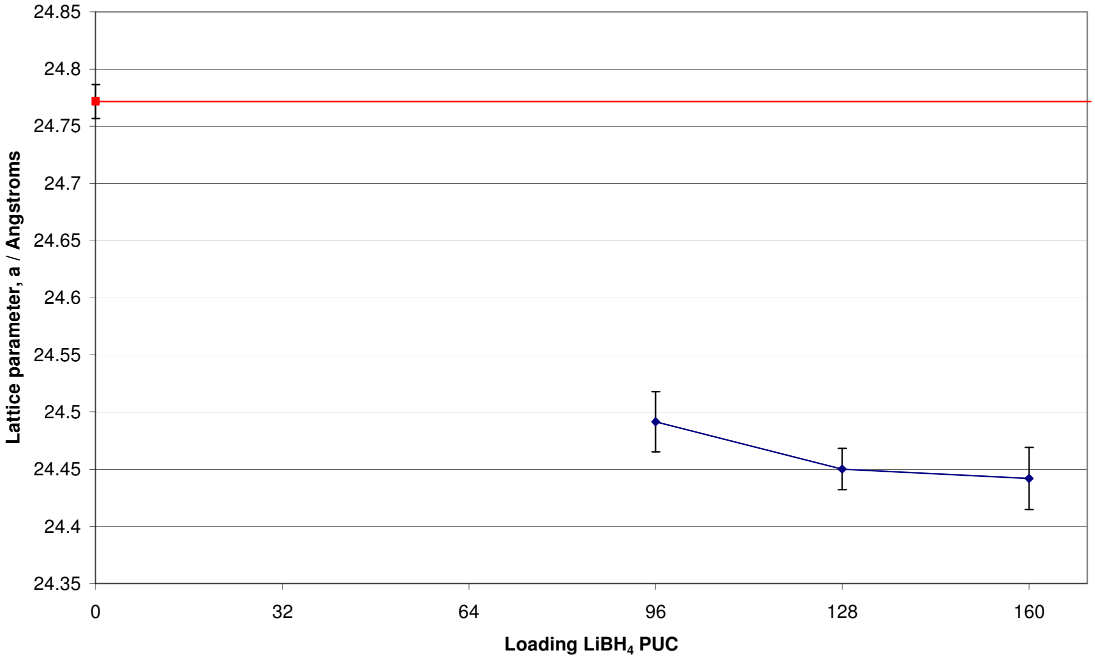

Figure 9.10 – Lattice parameter against loading for NH_4Y (dehydrated at 350℃) with lithium borohydride, showing: NH_4Y dehydrated (-) and the heated series (-). Errors are to 3ESD's.

The analysis of the relative peak intensity ratios, shown in figure 9.11, showed that the loaded samples gave values very similar to that of the dehydrated zeolite.

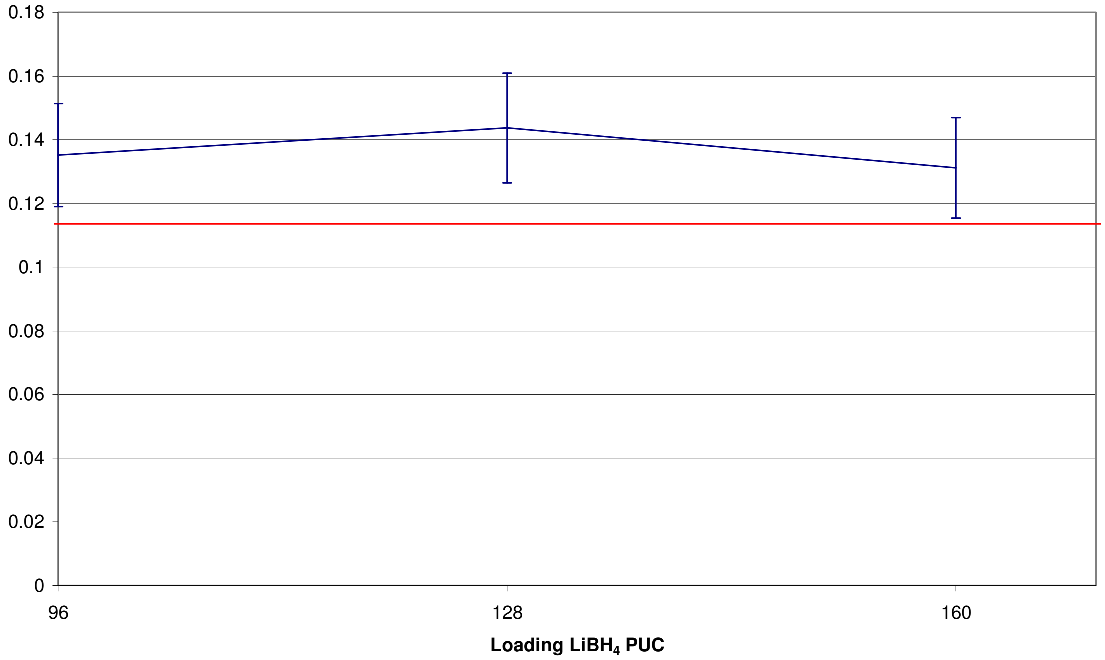

Figure 9.11 – The relative ratio of the (311) to the (111) peaks over a range of compositions for NH_4Y with lithium borohydride, showing the NH_4Y dehydrated (-) and the loaded samples (-).

From diffraction data alone it appears that the samples prepared by the different degassing regimes were very similar. Heating at 250℃ under argon may result in deammoniation, though the direct deammoniation resulted in only a single phase product after occlusion. The deammoniation at slightly lower temperature under occlusion conditions may not be complete, indicating occlusion into both ammoniated and deammoniated zeolite, suggesting that both these phases are in fact HY.

9.3.2.3 Vacuum TPD-MS

TPD–MS data for $(LiBH_4)_{96}$.HY dehydrated at 50℃ is shown in figure 9.12.

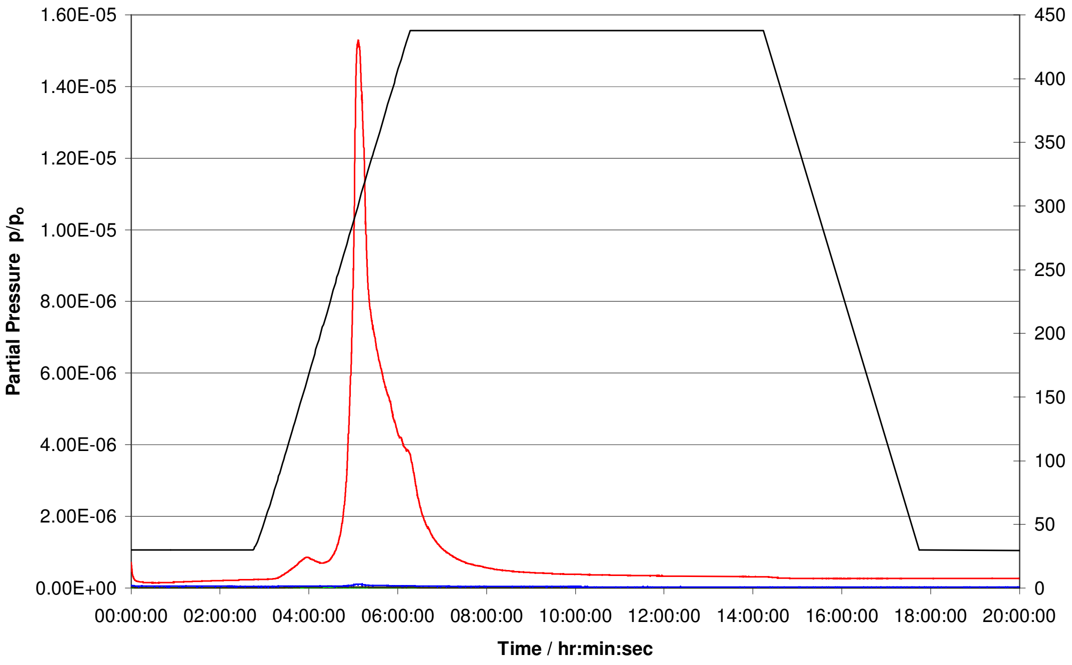

Figure 9.12 – TPD–MS trace of $(LiBH_4)_{96}.NH_4Y$ (50℃) showing the temperature (-) and the MS signal for hydrogen (-), NH_2^- (-), NH_3/OH^- (-) and water (-).

Two desorptions were observed, a small one starting at 85℃ peaking at 158℃, which could again be associated with the low temperature desorption of bulk $LiBH_4$ occurring on a phase transition at ~100℃[12], and a second starting at 220℃ and peaking at 305℃. This contrasts with the desorption of lithium borohydride which desorbed at 225℃ and then peaked at 345℃, collected under the same conditions, shown in figure 5.12. The main desorption peak of the loaded sample was far narrower, with a reduced temperature of peak desorption, than that of bulk lithium borohydride. The longer time to reach equilibrium again gives an indication of slow diffusion kinetics through the pore structure. No evidence for ammonia was observed in the desorption trace, indicating that only hydrogen was being desorbed during this process.

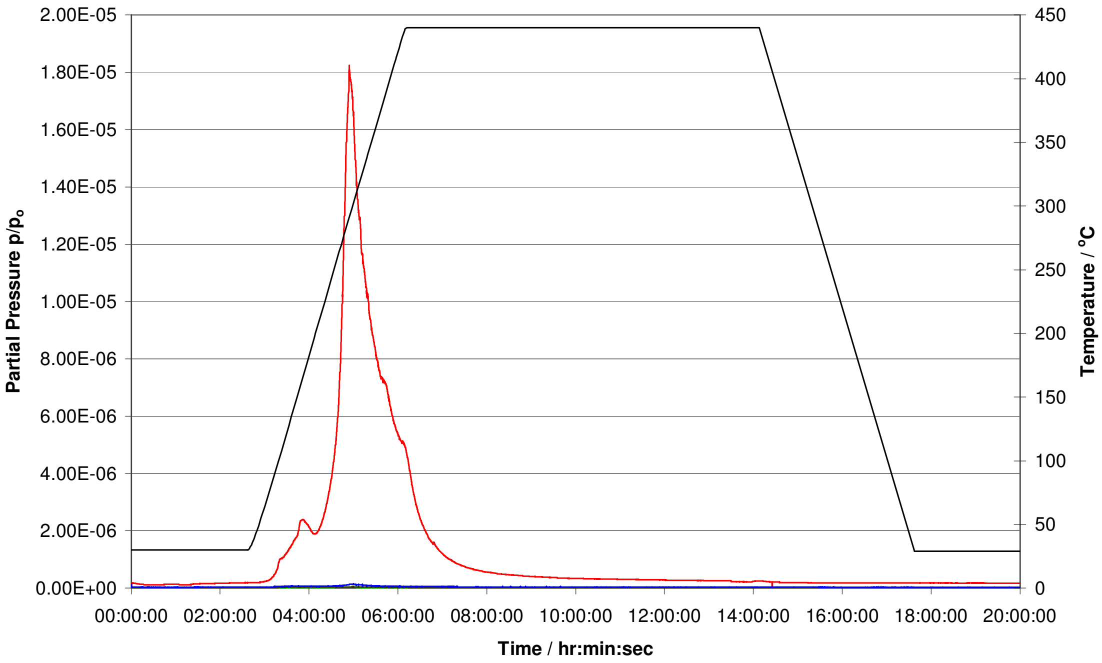

Figure 9.13 – TPD–MS Trace of $(LiBH_4)_{96}.NH_4Y$ (350°C) showing the temperature (-) and the MS signal for hydrogen (-), NH_2^- (-), NH_3/OH^- (-) and water (-).

The TPD–MS data (Figure 9.13) from the sample dehydrated at 350°C showed a very similar desorption trace. Again two desorptions were observed, the first beginning at 85°C and peaking at 175°C, and the second starting at 206°C (though the onset may be masked by the previous desorption) and peaking at 292°C. This was a reduced desorption onset and maximum with the 50°C sample and bulk $LiBH_4$.

The main difference in these samples was the second phase in the sample prepared at 50°C. This could suggest that the loaded phases are of different compositions. The similarity between the 50°C sample and lithium borohydride, may suggest some finely dispersed lithium borohydride remained in the sample. Inspection by XRD did not show $LiBH_4$ peaks, though fine dispersal may be undetectable by powder XRD.

The comparison with the desorption from lithium zeolites showed far narrower desorption ranges in the ammonium ion-exchanged materials. This could suggest that the zeolite cations can alter the desorption kinetics as well, and in this case reduce the blocking effect of diffusion through the pores. H^+ does not obstruct the pores in the way in which other cations would, explaining the broader features in both lithium and sodium zeolites.

9.4 Copper Ion-Exchanged Zeolites

Transition metal catalysts have been widely used to improve the kinetics of hydrogen adsorption and desorption in many systems such as MgH_2[7,8] and $NaAlH_4$[6]. The catalytic additives do not inherently need to be hydrogen stores themselves. In the case of catalysed desorption of sodium aluminium hydride it has been shown that the addition of titanium reduced desorption temperatures[6,8].

The addition of transition metals to the lithium amide/lithium hydride system has also been explored[13,14]. The addition of nickel, iron and cobalt produced alterations in the desorption characteristics, marginally reducing the onset temperatures, whilst also reducing the amount of ammonia generated.

In many areas of chemistry transition metals have been preferred as catalysts, with the precious and noble and metals often being at the forefront of heterogeneous redox catalysis. Their practical utility in this field has been ascribed to their unique coordination chemistry, multiple valance states and labile nature. They have been combined with zeolites in several forms with including simple ion-exchanged materials[18,21] or dispersed nanoparticles[22,23]. Copper was chosen to use in this case due to its straightforward ion exchange behaviour. Other transition metals often hydrolyse on ion exchange to form oxide/hydroxide clusters, complicating the system.

In this section the loading of $LiBH_4$ into copper-exchanged zeolites is investigated to explore whether the copper cations could act as a potential catalyst within the zeolite for the dehydrogenation of lithium borohydride.

9.4.1 Experimental

NaX was synthesised as detailed in the experimental chapter. $LiBH_4$ (>90%) was obtained from Sigma-Aldrich. Ion exchange with copper (II) nitrate was performed as outlined in the experimental chapter.

The dried zeolite was transferred to an argon glove box to ensure that the zeolites did not rehydrate and allow for intimate mixing with the lithium borohydride. Mixtures were formed in increments of 32 $LiBH_4$'s per unit cell (PUC) in the range 96 – 256. For CuX, the $Fd\bar{3}m$ space group with a unit cell parameter of approximately 25 Å was used for determination of unit cell loadings[11]. Samples were prepared as outlined in section 3.2.3.3.

The samples were then characterized using powder X-ray diffraction. These samples were also analysed by gravimetric analysis: thermogravimetric data were collected for temperature runs from 30 – 600°C at a ramp rate of 2°C per minute.

9.4.2 Results and Discussion

Copper (II) ion exchange produced a change in lattice parameter from 25.117(3) Å for NaX to 24.937(3) Å for the copper ion-exchanged material. The change was well in excess of errors, and the diffraction pattern showed significant changes in relative intensities. The final product from ion-exchange was a pale blue solid.

After dehydration the sample retained the pale blue colour and the lattice parameter changed to 24.853(3) Å. When the first sample was heated, with a high loading of 256 lithium borohydride PUC, under vacuum at 250°C, a large overpressure was generated. This implied that the sample had decomposed under this temperature regime. When the experiment was repeated under vacuum at 100°C, with a lower loading, the same result was obtained.

All samples prepared, upon reaction became darker, producing dark grey blue solids. When left for 48 hours at room temperature instead of reaction at temperature the samples showed a similar level of discolouration.

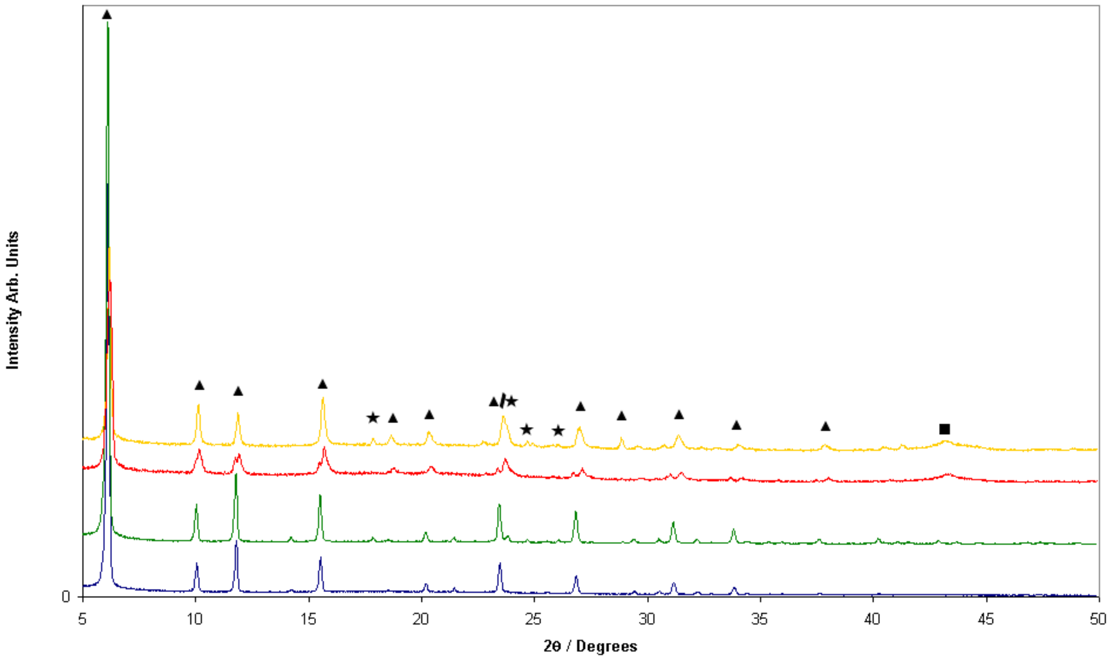

Figure 9.14 – Powder XRD patterns of CuX heated with different loadings of LiBH$_4$ PUC at different temperatures showing: dehydrated CuX (-); 160 LiBH$_4$ PUC at 100°C (-); 96 LiBH$_4$ PUC at 250°C (-) and 256 LiBH$_4$ PUC at 250°C (-). ▲ denotes zeolite, ★ denotes lithium borohydride and ■ denotes copper metal peaks.

Inspection of the diffraction patterns, figure 9.14, revealed a number of things. Lithium borohydride was not present at the lowest loading (96 PUC) when the sample was prepared in a sealed tube, but was present in a similar sample prepared under flowing gas. Also present in some samples was a low broad peak at 43° 2θ. This peak corresponds to the (111) of bulk copper metal. The lack of intensity and broad width of the line suggest it originated from relatively small particles. This feature appeared in the high temperature and vacuum prepared samples. The particles are likely to have been formed by the reductive properties of lithium borohydride. This is unsurprising as sodium borohydride has been used in the generation of cobalt particles in zeolite Y[23], as well as an enormous variety of chemical reductions. The samples prepared at a loading of 96 PUC also showed a second zeolite phase manifest as shoulders on the main zeolite peaks at low angle, regardless of preparation method. Table 10.1 shows some of the information collected from the diffraction patterns.

Loading Level PUC	Temperature / °C	Preparation	Major Phase lattice parameter / Å	Minor Phase lattice parameter / Å	Ratio of (311)/(111) of Major Phase	Copper peaks Y/N
0	N/A	Dehydrated	24.853(3)	N/A	0.130	N
96	250	Vacuum	24.619(7)	24.97(1)	0.158	Y
96	250	Gas	24.593(9)	24.925(7)	0.158	Y
160	100	Vacuum	24.869(5)	N/A	0.137	N
256	250	Vacuum	24.726(6)	N/A	0.213	Y
256	Room	Gas	24.807(4)	N/A	0.142	N

Table 9.1 – Lattice parameters and relative ratios of the (311) to (111) peaks of $LiBH_4$ containing CuX samples prepared under various conditions.

It can be seen that the reaction conditions had a large effect on lattice parameters and relative peak intensities. The greatest change in lattice parameter occurred with the most lightly loaded samples, which showed a framework contraction. The second zeolite phase that appeared in some samples had a lattice parameter closer to that of hydrated CuX suggesting that it might have arisen through contamination. The relative intensities showed the sample prepared at 100℃ had a similar value to that of the parent dehydrated zeolite, whilst the other samples prepared at elevated temperatures showed larger values. Meaningful information was difficult to obtain from these values, as desorption was clearly occurring. Lithium borohydride is likely to have been desorbing hydrogen, leaving the products lithium hydride and boron, which may be unable to enter the zeolite at these temperatures. Taken together the observations were indicative of changes occurring within the zeolite pores, though there were no obvious trends.

The $(LiBH_4)_{96}.CuX$ samples, shown in figure 9.15, were both heated on a TGA up to 600℃, to note whether any further desorption occurred and whether it was different to that of bulk lithium borohydride. The extent to which the samples desorbed during synthesis is an unknown, though perhaps can be inferred from these seemingly random results.

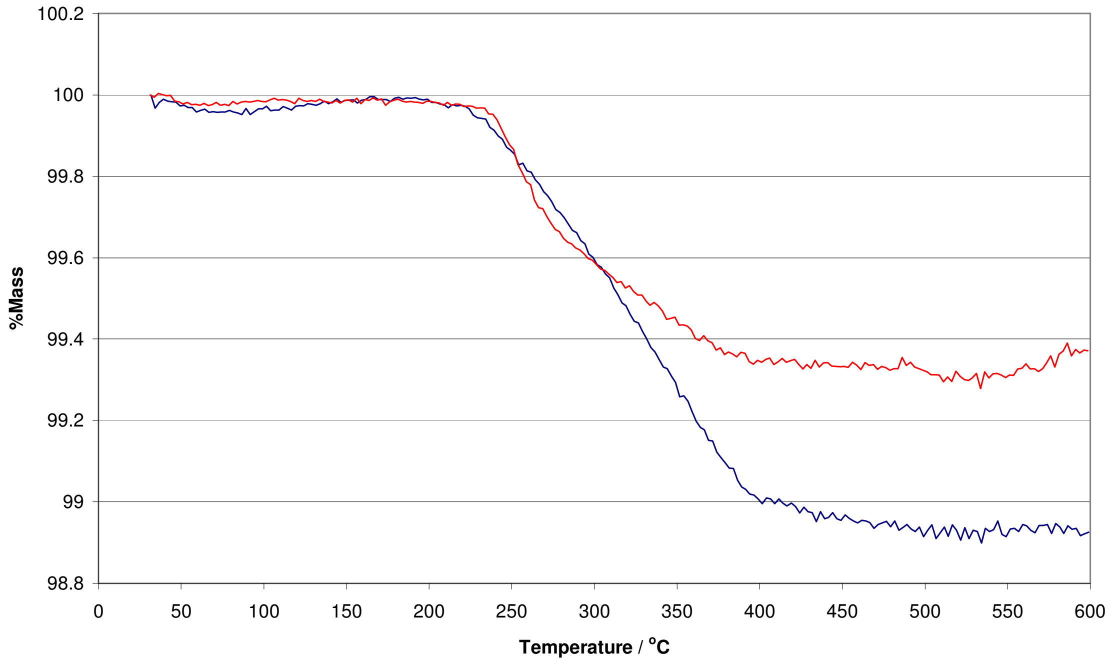

Figure 9.15 – TGA traces of mass loss against temperature showing CuX with 96 $LiBH_4$ PUC prepared under vacuum (-) and flowing gas (-).

The data from the TGA showed relatively small weight loss in both cases starting at around 235℃. This is a far lower onset temperature than observed in the sodium zeolite with lithium borohydride systems under a gas atmosphere. The amounts desorbed, 1.08 and 0.70 wt% for the samples prepared in vacuum and flowing gas respectively, were relatively low. A zeolite loaded with 96 $LiBH_4$ PUC could in theory desorb a maximum of 2.35 wt% hydrogen, clearly indicating that some desorption occurred during the reaction. Assuming only hydrogen was lost, the vacuum- and gas-synthesised samples lost 1.27 wt% and 1.65 wt% respectively during synthesis. The sample heated under flowing gas released more hydrogen, as the gas was removed as formed pushing the equilibrium towards hydrogen formation. All the desorption was complete by 380℃ in the flowing gas sample and 400℃ in the vacuum prepared sample. As the second desorption of bulk lithium borohydride starts at around 400℃, clearly the zeolite reduced the desorption temperature in both cases, also apparent in the desorption on synthesis.

9.5 Conclusion

Lithium borohydride was incorporated into ion-exchanged zeolites and altered desorption properties were observed as a result.

In lithium zeolites, a single phase was observed on incorporation of $LiBH_4$ in LiX, with LiA exhibiting distinct loaded and unloaded phases. This difference most likely stems from the easier diffusion through the 12-ring window of zeolite X, versus the 8-ring window of zeolite A. The desorption of lithium borohydride in this case showed a similar onset temperature to the NaX analogue and bulk $LiBH_4$. A broader desorption than bulk $LiBH_4$ was observed, suggesting diffusion through the pores was restricted.

Clear evidence of incorporation of $LiBH_4$ in NH_4Y/HY was obtained by powder XRD for samples dehydrated in two different ways. Desorption in both cases showed a reduction in onset temperature and peak maxima, with hydrogen being the sole desorption product. The sharp desorptions showed improved diffusion compared with the sodium analogue.

Copper exchanged X showed low temperature catalytic desorption of lithium borohydride at room temperature; this generated a gas pressure most probably from hydrogen. Alterations were observed in the lattice parameters and relative peak intensities suggesting that changes were occurring within the zeolite pores. This could result from incorporation of lithium borohydride and/or the generation of fine copper particles within the pores. Further desorption of the samples showed a reduction in desorption temperature compared with that of lithium borohydride and the sodium zeolite systems. This indicates that the presence of copper acted as a catalyst to reduce desorption temperatures.

9.6 References

1. Dyer A., *An Introduction to Zeolite Molecular Sieves*, Wiley, Chichester, **1988**
2. Inglezakis V. J., *J. Colloid Interface Sci.*, **2005**, 281, 68
3. Frising T., Leflaive P., *Micropor. Mesopor. Mater.*, **2008**, 114, 27
4. Langmi H. W., Book D., Walton A., Johnson S. R., Al-Mamouri M. M., Speight J. D., Edwards P. P., Harris I. R., Anderson P. A., *J. Alloys Comps.*, **2005**, 404-406, 637
5. Hedström A., *J. Environ. Eng.*, **2001**, 127, 673
6. Jensen C. M., Zidan R., Mariels N., Hee A., Hagen C., *Int. J. Hydrogen Energy*, **1999**, 24, 461

7. Gross A.F., Ahn C. C., Vajo J. J., Van Atta S. L., Liu P., *Nanotechnology*, **2009**, 20, 204005
8. Fichtner M., *Adv. Eng. Mater.*, **2005**, 7, 443
9. Langmi H. W., *Hydrogen Storage in Zeolites and Carbon Materials*, Thesis awarded by the University of Birmingham, **2004**.
10. Porcher F., Souhassou M., Dusausoy Y., Lecomte C., *C. R. Acad. Sci. Paris, Série IIc*, **1998**, 12, 701
11. Baerlocher Ch., Meier W. M., Olson D. H., *Atlas of Zeolite Framework Types*, **2001**
12. Züttel A., Rentsch S., Fisher P., Wenger P., Sudan P., Mauron Ph., Emmenegger Ch., *J. Alloys Comp.*, **2003**, 356-357, 515
13. Ichikawa T., Isobe S., Hanada N., Fujii H., *J. Alloys Comps.*, **2004**, 365, 271
14. Chen P., Xiong Z., Luo J., Tan K. L., *Nature*, **2002**, 420, 302
15. Hu Y. H., Ruckenstein E., *J. Phys. Chem. A*, **2003**, 107, 9737
16. Chater P. A., Anderson P. A., Prendergast J. W., Walton A., Mann V. S. J., Book D., David W. I. F., Johnson S. R., Edwards P. P., *J. Alloy Comps.*, **2007**, 446-447, 350
17. Kühl G. H., Schweizer A. E., *J. Catal.*, **1975**, 38, 469
18. Armor J. N., *Micropor. Mesopor. Mater.*, **1998**, 22, 451
19. Ćeranić T. S., Radak V. M., Lukić T. M., Nikolić D., *Zeolites*, **1985**, 5, 42
20. Parry R. W., Schultz D. R., Girardot P. R., *J. Am. Chem. Soc.*, **1958**, 80, 1
21. Seidel A., Kampf G., Schmidt A., Boddenberg B., *Catal. Lett.*, **1998**, 51, 213
22. Seidel A., Loos J., Boddenberg B., *J. Mater. Chem.*, **1999**, 9, 2495
23. Wang Y., Wu H., Zhang Q., Tang Q., *Micropor. Mesopor. Mater.*, **2005**, 86, 38

CHAPTER 10

OCCLUSION OF LITHIUM BOROHYDRIDE IN ZEOLITIC CARBON

10.1 Introduction

In zeolite samples containing lithium borohydride the major limiting factor on the gravimetric hydrogen capacity has been shown to be the framework weight.

The use of one type of porous material to template another has been used as a method for generating mesoporous carbons amongst others[1,2]. This technique involves the deposition of a material which through further reaction can form its own stable framework based upon the host structure, which is then removed. The remaining material is a “negative” of the original structure. The values of surface area from the templated material often reflect those of the original host material, but variations to this can be caused through the synthesis.

The favoured material to be templated is often carbon, usually introduced as either glucose or acetylene. A pyrolysis step forms the carbon structure, with most by-products as gaseous species. At higher temperature it is possible to dope the carbon via reactions with nitrogen. This causes possible internal structure defects, modifying the “graphitic” electronic structure. The introduction of interstitial nitrogens has resulted in most cases in a negligible difference in hydrogen uptake measurements. This suggests that the physisorption in the case of carbon materials is only subtly altered by this defect structure.

The ability to modify the content of these samples during synthesis allows some degree of control, with catalytic metals potentially being placed within the templated material. It has also been observed that metals can be deposited onto the surfaces of these materials, but the interpore distances and loading quantity define the ability to generate either discrete sites, or the formation of clusters and aggregates[3]. These factors have been explored in mesoporous materials and their application in catalysis reactions. Increased loading of metals affects diffusion by blocking channels, whilst still retaining catalytic behaviour.

The use of carbon materials as hosts for hydrides has been attempted with mesoporous systems. Lithium borohydride occluded in carbon nano-scaffolds showed reduced desorption temperatures with increased kinetics. It was reported that the heats of adsorption were also reduced upon particle size reduction when occluded[4,5]. Carbon aerogels with magnesium hydride showed evidence of nano-scaled hydride particles[6]. The samples behaved with improved kinetics far better than those exhibited in milled hydride samples. The improved kinetics were also observed on hydrogenation with a 75% reversibility of the initial uptake over 10 cycles. Some of these improvements are attributed to the inability of the guest material to aggregate and behave like the bulk material.

It could be argued that even smaller guest material particles, while maintaining separation might be attained in microporous materials. Ammonia borane has also been investigated in a carbon aerogel, and showed the typical response of a reduced desorption temperature along with a reduction in the production of borazine[7].

Carbon materials templated from zeolites have been developed[8,9]. Unsurprisingly these zeolitic carbons have shown improved gravimetric uptakes of hydrogen compared with the original parent zeolites, with values as high as 4.5 wt% at 77K observed in a zeolite X based material[10]. Higher values were achieved in materials templated from zeolite β[8]. High surface areas are recorded for these materials, between 900 and 1300 m^2/g. The formation conditions have been found to be of great importance; although long range zeolite ordering is not observed, materials prepared at higher temperatures form graphitic linkages, whilst lower temperatures generally afford an amorphous product.

This chapter is concerned with the incorporation of lithium borohydride in zeolitic carbons formed from NaY.

10.2 Experimental

Zeolitic carbons CY-9 and CY-5 were synthesised by the Mokaya group at Nottingham University[8,9]. $LiBH_4$ (>90%) was obtained from Sigma-Aldrich.

The degassed carbons were transferred to an Argon glove box to ensure that they did not come into contact with the atmosphere and adsorb any gaseous species especially water. This allowed for intimate mixing with the lithium borohydride. A ratio of 1.2:1 of carbon to lithium borohydride was prepared by mass. Samples were then prepared as outlined in section 3.2.3.3.

The samples were then characterized using powder X-ray diffraction. Raman spectra of a sample were collected. These samples were also analysed by vacuum TPD collected over the temperature range of 30 – 450℃.

10.3 Results and Discussion

Two different zeolitic carbons were used: CY-9 and CY-5. During the initial synthesis they were pyrolysed under oxygen at varying temperatures, CY-9 at 900℃ and CY-5 at 950℃. The reactions of both of these carbon materials with lithium borohydride resulted in no pressure, indicating that no desorption occurred. The carbon based materials usually have structures related to either graphite or amorphous carbons. Mesoporous carbon materials are often formed of graphene sheets, and characterization data reflects this with diffraction patterns often showing similar peaks to those of graphite.

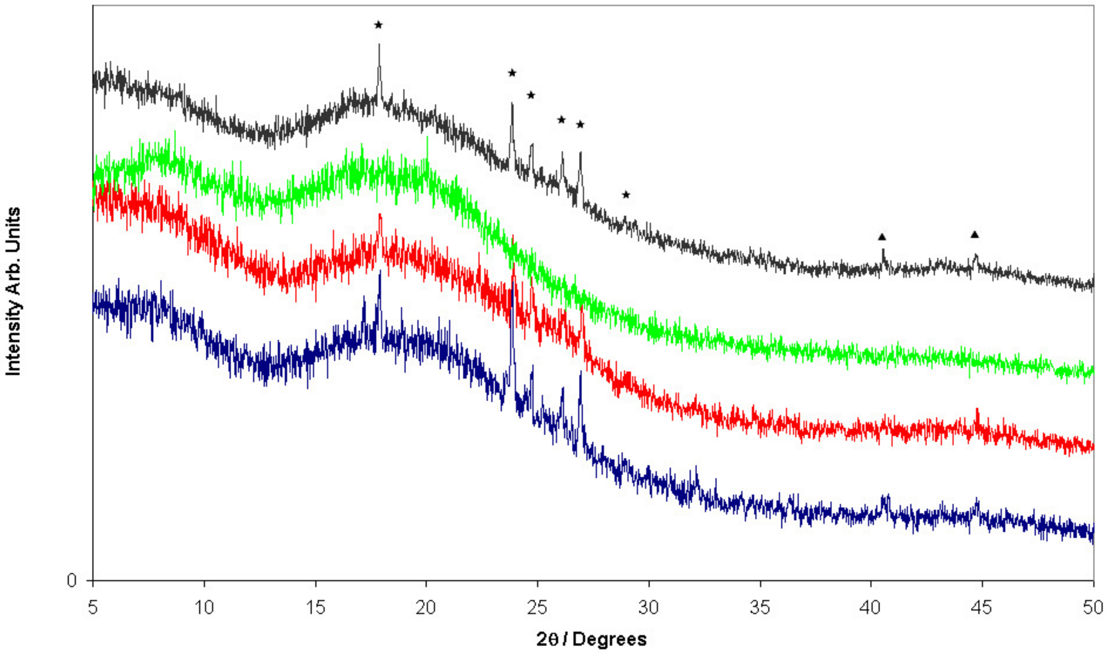

Figure 10.1 – Powder XRD patterns of samples prepared using zeolitic carbon CY-9 showing: the initial sample mixture (-); and after heating for 12 hours (-); 72 hours (-) and 144 hours (-). ▲ denotes carbon based material and ★ denotes lithium borohydride peaks.

Zeolitic carbon CY-9, prepared at the lower temperature, did not show many graphitic peaks in figure 10.1. The presence of the (010) and (011) at higher angle suggest the possibility that the zeolitic carbon has graphitic nature. The (010) was shifted to higher 2θ compared with that of graphite. It can be readily observed that the reaction still left the diffraction pattern associated with lithium borohydride, although at reduced intensity. The sample prepared for 72 hours showed no $LiBH_4$, although the one heated for 144 hours did; disappearance of the lithium borohydride maybe due to sample inhomogeneity.

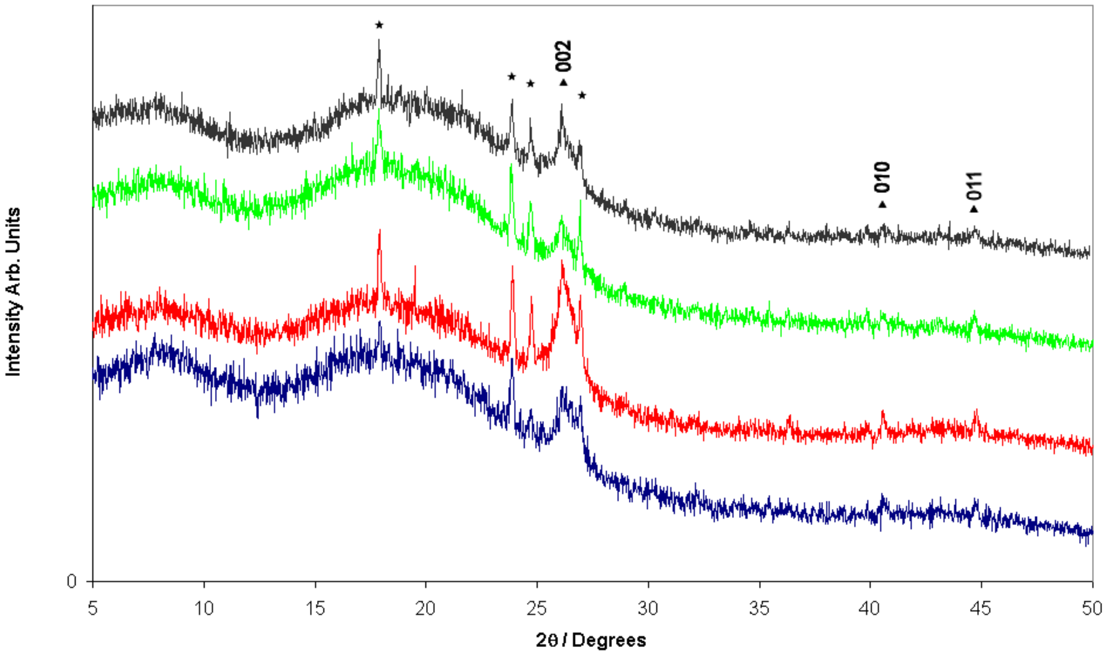

Figure 10.2 – Powder XRD patterns of samples prepared using zeolitic carbon CY-5 showing: the initial sample mixture (-); and after heating at 250°C for 12 hours (-); 72 hours (-) and 144 hours (-). ▲ denotes carbon based material and ★ denotes lithium borohydride peaks.

Figure 10.2 showed patterns from the reactions with carbon CY-5. In this case the formation of zeolitic carbon generated a diffraction pattern with graphitic peaks, showing the (002), (010) and (011). Figure 10.3 showed a pattern for Lonza graphite for comparison. In this case the (002) showed a lower and broader peak than that expected for graphite, this is expected given that there would only be small graphitic regions in the zeolitic carbon. The zeolitic carbon peaks' position was not changed over the range of heating times. The peaks associated with lithium borohydride remained in all cases, with their relative intensities unchanged, but reduced in intensity from the starting mixture. This reduction of peak intensity in both samples would indicate some occlusion has occurred.

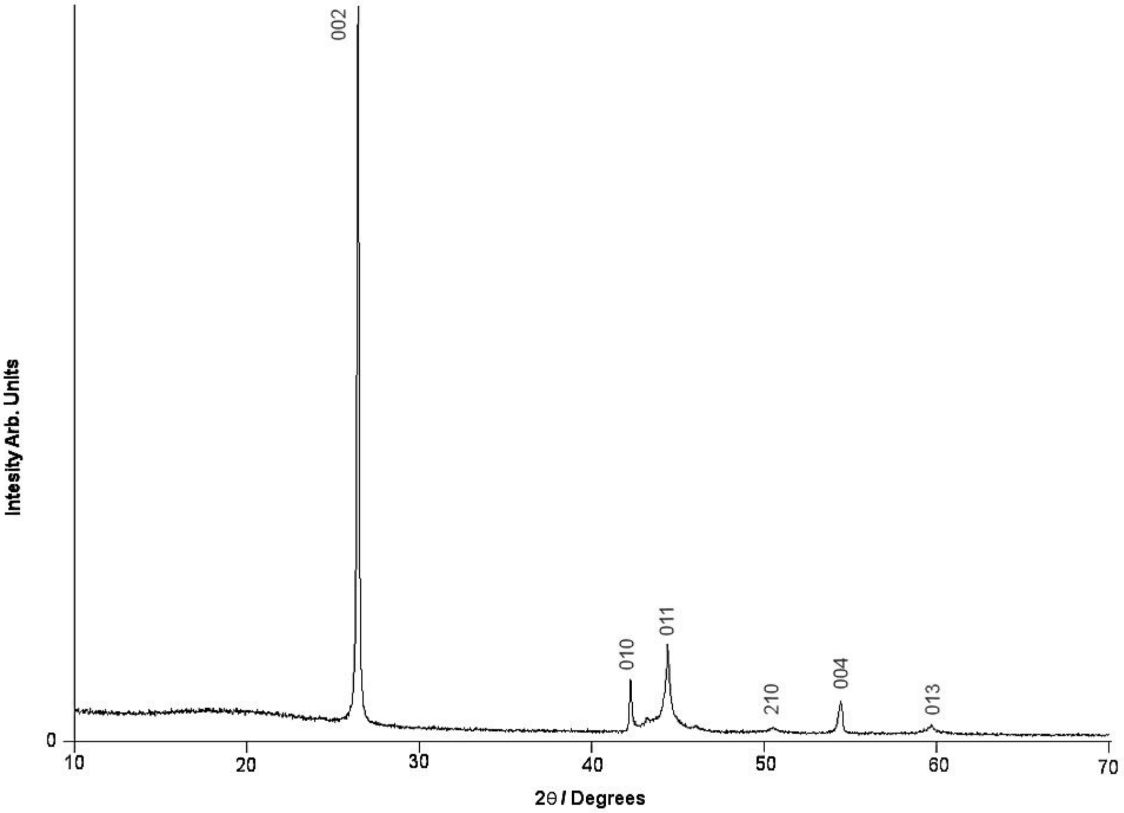

Figure 10.3 – Powder XRD pattern of Lonza graphite.

Raman spectroscopy has been used to frequently categorise graphitic carbon materials. The samples showed some graphitic nature in the XRD and this was further corroborated by Raman spectroscopy. Figure 10.4 shows the Raman spectrum recorded from the sample mixture for CY-9, before and after heating for 12 hours. Also shown for reference is the spectrum of lithium borohydride. Typically, highly ordered graphitic carbon materials contain a single band above 1500 cm^{-1} referred to as the “G-band”, with a second order of this appearing above 2500 cm^{-1}. In most other graphitic structure types another peak was typically observed at lower wave number brought about by the disorder between the graphitic layers, this is referred to as the “D-band”. Both of these features related to the $e_{2g}^{(2)}$ vibration, an asymmetric vibration of *sp*^{2} carbons coupled with a mirrored interaction between neighbouring layers[11,12].

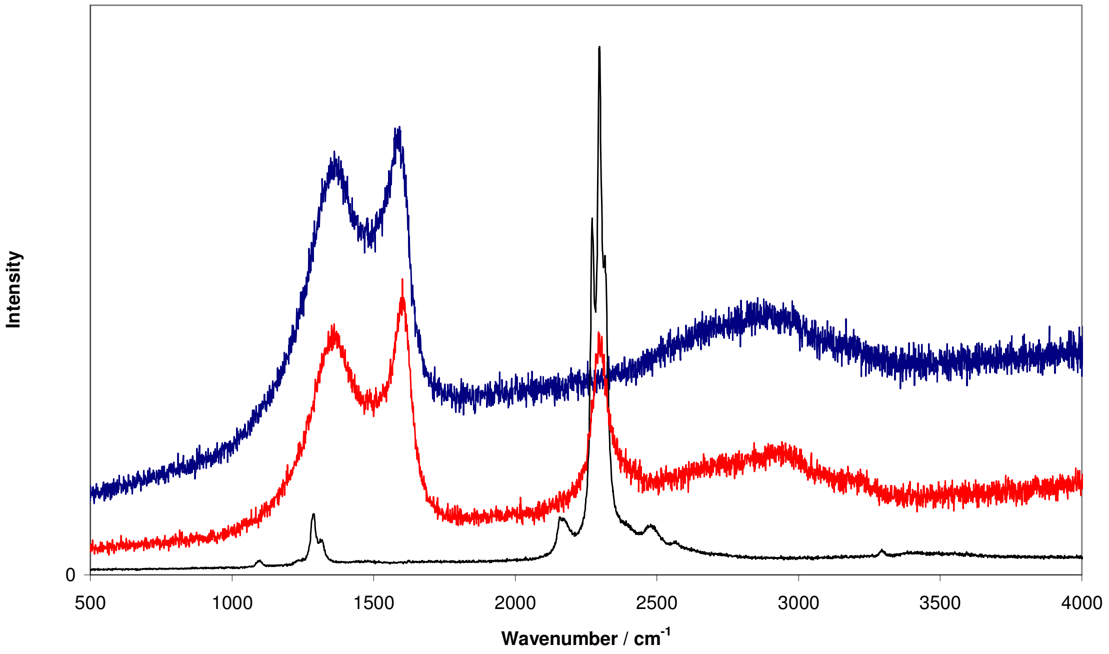

Figure 10.4 – Raman spectra showing CY-9 with lithium borohydride before (-) and after being heated for 12 hours at 250°C (-), with lithium borohydride for reference (-).

We can see that the D- and G-band for the sample mixture occur at 1360 and 1601 cm^{-1}, respectively. After reaction we see a shift in these values to 1364 and 1585 cm^{-1}, respectively. The disorder peak unsurprisingly remained at a similar value, indicating that the degree of disorder is little affected by the incorporation of new species. The G-band was more affected by the introduction of new species onto the surface of pores, and this indicated a slight change in chemical environment between the graphene layers. It is possible that some intercalation of guest ions such as Li^+ may occur. Possibly the most surprising difference was observed on the lithium borohydride ν_1 and ν_3' stretch occurring at 2300 cm^{-1}. Within the mixture this was present, although as a broader feature than in the pure borohydride[13,14]. On heating to 250°C these sets of vibrations disappeared completely as if to suggest the complete removal of borohydride, but no decomposition was experienced on synthesis (as a pressure in the sealed tubes). This result was observed at several sites within the sample suggesting that it was representative of the bulk sample. This curious effect could be attributed to a complete change in geometry of the borohydride ion upon incorporation into the zeolitic carbon. The reduction in lithium borohydride intensity by powder XRD and removal of distinct stretches in the Raman spectra would indicate some occlusion has occurred.

TPD was performed on the same sample prepared using CY-9 heated with lithium borohydride for 12 hours; the trace is shown in figure 10.5.

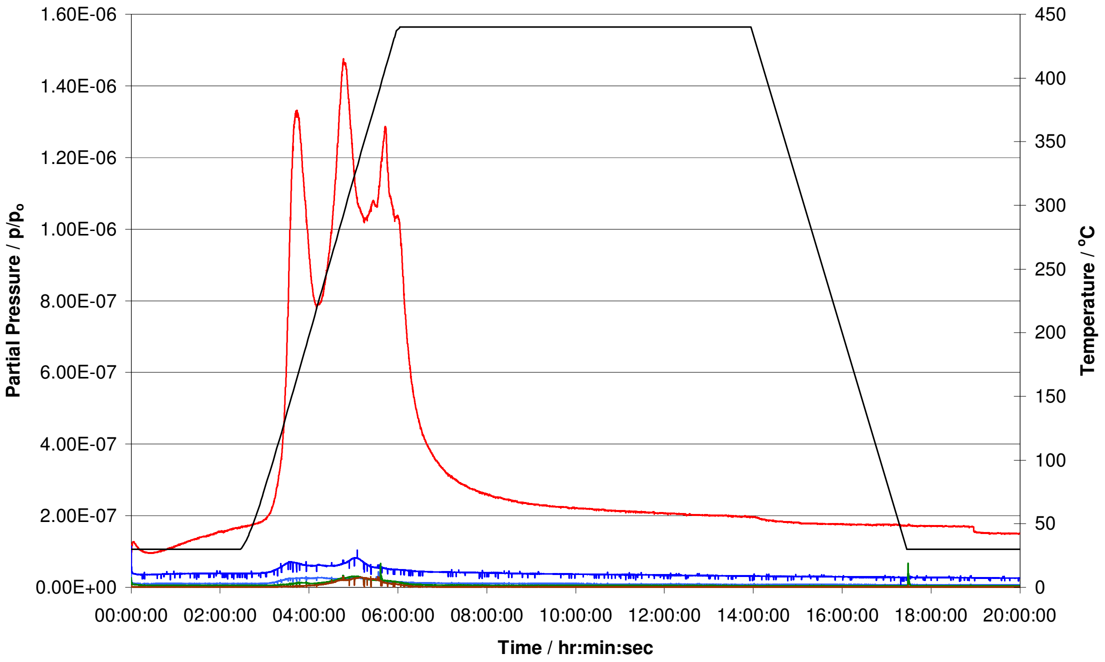

Figure 10.5 – TPD-MS of CY-9 with LiBH$_4$ heated for 12 hours from 30 to 450℃: temperature (-) and MS trace for hydrogen (-); H$_2$O (-); $^-$OH (-); N$_2$ (-) and CO$_2$ (-).

The data showed a more complicated trace than expected for plain lithium borohydride, as shown in chapter 5 (figure 5.12). The first large desorption of CY-9 with lithium borohydride had initial onset at 84℃ and peaked at 168℃. A second major peak started at 220℃ and peaked at 299℃, with a further smaller peak at around 408℃. Here the onset could be masked as the two desorption peaks appear to overlap. Lithium borohydride had a slight desorption below 100℃ with the majority starting at around 225℃ and peak at 345℃.

The initial temperature of desorption decreased on introduction to the zeolitic carbon. The second high temperature peak of the reacted mixture was accompanied by a slight desorption of carbon dioxide, which could be bound to the zeolitic carbon. The only other possible source of carbon dioxide would be slight burning of the sample at this temperature, which could be possible if oxygen was adsorbed by the carbon.

10.4 Conclusion

Some evidence of incorporation was seen in reactions between zeolitic carbon and lithium borohydride, shown through powder XRD and Raman spectroscopy. The loaded sample showed modified desorption properties, with lower onsets and peak temperatures compared to $LiBH_4$ and an additional high temperature desorption also observed.

10.5 Reference

1. Yue W., Zhou W., *Chem. Mater.*, **2007**, 19, 2359
2. Armandi M., Bonelli B., Bottero I., Otero Areán C., Garrone E., *Micropor. Mesopor. Mater.*, **2007**, 103, 150
3. Langmi H. W., McGrady G. S., *Coord. Chem. Rev.*, **2007**, 251, 925
4. Gross A. F., Vajo J. J., Van Atta S. L., Olson G. L. *J. Phys. Chem. C*, **2008**, 112, 5651

5. Zhang Y., Zhang W.-S., Wang A.-Q., Sun L.-X., Fan M.-Q., Chu H.-L., Sun J.-C., Zhang T., *Int. J. Hydrogen Energy*, **2007**, 32, 3976
6. Gross A.F., Ahn C. C., Vajo J. J., Van Atta S. L., Liu P., *Nanotechnology*, **2009**, 20, 204005
7. Feaver A., Sepehri A., Shamberger P., Stowe A., Autrey T., Cao G., *J. Phys. Chem. B.*, **2007**, 111, 7469
8. Yang Z., Xia Y., Mokaya R., *J. Am. Chem. Soc.*, **2007**, 129, 1673
9. Yang Z., Xia Y., Sun X., Mokaya R., *J. Phys. Chem. B*, **2006**, 110, 18424
10. Takagi H., Hatori H., Soneda Y., Yoshizawa N., Yamada Y., *Mater. Sci. Eng. B*, **2004**, 108, 143
11. Eklund P. C., Holden J. M., Jishi R. A., *Carbon*, **1995**, 33, 959
12. Armandi M., Bonelli B., Bottero I., Otero Areán C., Garrone E., *Micropor. Mesopor. Mater.*, **2007**, 103, 150
13. Harvey K. B., McQuaker N. R., *Canadian J. Chem.*, **1971**, 49, 3282
14. Gomes S., Hagemann H., Yvon K., *J. Alloys Comp.*, **2002**, 346, 206

CHAPTER 11
GENERAL CONCLUSIONS AND FURTHER WORK

11.1 General Conclusions

A variety of analytical methods has shown that active hydrogen storage guest materials can be successfully incorporated into zeolites.

Powder X-ray diffraction provided evidence for the incorporation of lithium borohydride into a range of as-synthesised and ion-exchanged zeolites. In nearly all cases the products contained two zeolite phases denoted ‘loaded’ and ‘unloaded’, on account of the strong similarity of the latter to the starting dehydrated zeolite, but evidence for slight variations in the chemical composition of both phases was observed in some cases.

The loading of lithium borohydride in the three sodium zeolites resulted in mixtures of loaded and unloaded phases, with no apparent intermediate compositions. The ratio between the loaded and the unloaded phase increased with increased loading. Initially sodium zeolite systems showed the formation of some sodium borohydride, indicating the possibility of some solid state ion-exchange. The effects of occlusion in sodium zeolites could also be tracked through changes in the spectroscopy of the guest and host constituents. Loading in lithium zeolite A showed a similar two phase result, but although lithium zeolite X also showed evidence of occlusion it was observed with a single phase.

All the systems studied exhibited altered desorption mechanisms, resulting from the occlusion of the material in the zeolite pores, but in most cases the onsets and maxima were only a few degrees celsius lower. The copper system saw the most significant change with partial decomposition of lithium borohydride at room temperature, accompanied by the reduction of Cu^{2+} to copper metal within the zeolite. The low temperature desorption was not complete, with gravimetric data showing further desorption above 250℃. Lithium borohydride also showed a 20℃ reduction in the temperature of vacuum desorption after loading in ammonium exchanged zeolite Y. In most cases the desorption profiles were broad, probably due to the issues of diffusion of hydrogen and pore blocking within the zeolites.

After thermal desorption the products of loaded sodium A rehydrogenated to the extent of 0.50 wt% at 350℃ and 18 bar hydrogen. This was only a small proportion of the desorbed hydrogen, possibly due to pore blocking and framework collapse inhibiting full hydrogenation, but conditions were significantly less extreme in terms of temperature and pressure than those observed for bulk $LiBH_4$.

Adsorptions at cryogenic temperatures showed reduced uptakes compared to the parent zeolites. This was attributed to the loss of pore volume, as expected from the incorporation of guest material. Half loaded samples showed greater uptake than their fully loaded counterparts, which often showed no uptake at all.

The thermodynamic heats of adsorption for lithium borohydride within zeolites showed a slightly smaller value than those recorded for the pure zeolites. These reductions are likely due to removal of the interaction with framework sites, and replacement with interaction to the borohydride which appear weaker.

The incorporation of other guest materials also resulted in altered desorption properties. Ammonia borane showed complete desorption in one step, starting at a similar temperature to that of bulk ammonia borane. The confinement in micropores inhibited the long range connectivity that allows for the formation of polymeric aminoborane. This was corroborated by the desorption of smaller molecules like borazine and diborane, but also the observation of ammonia by mass spectrometry. Conversely the use of lithium borohydride amide ($Li_4BH_4(NH_2)_3$) showed that on successful loading in NaX, it was possible to suppress to some degree the production of ammonia as a major desorption product, whilst also reducing desorption temperature. Some bulk desorption was still observed, suggesting incomplete reactions. NaA showed no incorporation of lithium borohydride amide, presumably due to small pore windows. Some evidence for the reduction of the sodium cations in the zeolite and sodium cluster formation was observed.

When sodium metal was used as a guest, increased uptakes were observed. These were attributed to an irreversible hydrogenation to form sodium hydride within the framework. Upon completion of this phenomenon a hysteresis was observed in the sample on adsorption and desorption at 77 K and 15 bar, suggesting trapping hydrogen, which could be reversed on outgassing at room temperature. This was thought to be a trapping effect. Normal low temperature physisorption was also observed suggesting a highly varied internal surface area and pore space with multiple binding modes and sites.

The use of zeolitic carbons with a much lighter framework composition suggests that increased loadings by weight can be achieved. Reduction of the intensity of the XRD peaks of lithium borohydride and observation of a broad borohydride stretch from Raman spectroscopy suggest that some material was occluded. The desorption trace showed a greatly reduced and improved mechanism. The peak desorption was reduced by 45°C, showing the best reduction using lithium borohydride as a guest species.

11.2 Further Work

With such a large number of variables which could be changed in these the host–guest systems, there are limitless possible avenues of further work.

Key areas that could be elaborated on include:

- Initial observations of desorption and adsorption suggest that larger pore materials are important. Though maintaining the intrinsic microporosity would prove useful as seen in the rehydrogentation of guest materials. Use of framework materials such as ZSM-5 (MFI structure type) might afford a clearer diffusion path way allowing improved desorptions to be observed.

- Further crystallographic and spectroscopic methods, such as neutron diffraction and nuclear magnetic resonance spectroscopy (NMR), to determine the locations of the guest species within the pore structure of the host. This would allow elucidation of the role of the host in the changing the desorption properties. Understanding the surface binding sites would allow for better selection of host materials and an improved degree of tuning in these systems.

- Further analysis of the heats of adsorption should be performed on other host–guest systems, particularly the alkali metal systems, to quantify the perceived improvements to the system. Further analysis of this system is required corroborate the postulation of hydride formation.

- More hydrogenation work needs to be performed to investigate apparent improvements in reversibility of these systems. The product of room temperature desorption of lithium borohydride with copper zeolite requires hydrogenation to determine whether the system is reversible, and also to see if a stable material can be maintained at room temperature, after the initial cycle is complete.